



TECHNISCHE
UNIVERSITÄT
DARMSTADT

NUCLEAR MASSES AND THEIR IMPACT IN R-PROCESS NUCLEOSYNTHESIS

Vom Fachbereich Physik
der Technischen Universität Darmstadt
zur Erlangung des Grades
eines Doktors der Naturwissenschaften
(Dr. rer. nat.)

genehmigte Dissertation von

Joel de Jesús Mendoza-Temis, M.Sc.

aus Huatusco, Veracruz; México

Referent : Prof. Dr. Gabriel Martínez-Pinedo
Korreferent : Prof. Dr. Karlheinz Langanke

Tag der Einreichung: 29.01.2014
Tag der Prüfung: 17.02.2014

Darmstadt 2014
D 17



So here it is, another chance

Wide awake, you face the day

Your dream is over...

Or has it just begun?



la memoria de mi abuelita Sra. Rosa Temis
(In loving memory to my beloved grand mother)
09.06.1915 – 25.08.2013 †



mi familia :
(To my family)
Inés (Tía),
María Gozos (Mamá),
Agustín (Papá),
Andrés y Germán (Hermanos)

Acknowledgments

To my advisors Prof. Dr. Gabriel Martínez-Pinedo, Prof. Dr. Karlheinz Langanke and Prof. Dr. Andrés Zuker for all their unlimited patience and all the tips that you gave me during my PhD. Thanks for give me the opportunity to be part of your research team and for share your expertise with this humble student.

To my colleagues from the theoretical nuclear astrophysics group at the university of Darmstadt: Andreas Lohs (for all his support and encouragement), Lutz Huther (For all his unlimited friendliness and support), Heiko Möller (For his honesty and support), Andrea Idini (For his support and advice), Hans-Peter Loens (For sharing with me part of his knowledge), Tobias Fischer (For making me smile and all his advices), Tomás Rodriguez, Tomislav Marketin and Meng-Ru Wu (For all their time and advices), Alex Arzhanov, David Volk, Andre Siever and Samu Giuliani (For their friendly style). Everyone of you, gave me the necessary support in the most difficult moments of my life...honestly without you guys, I will probably wouldn't manage to finish.

Last but not least, to all my Darmstadtians friends (From both German and non-German citizenships) for make my empty life a little better. Because of the lack of space I won't mention all of you, however you have an special place in my heart and thoughts.



Erklärung zur Dissertation

Hiermit versichere ich, die vorliegende Dissertation ohne Hilfe Dritter nur mit den angegebenen Quellen und Hilfsmitteln angefertigt zu haben. Alle Stellen, die aus Quellen entnommen wurden, sind als solche kenntlich gemacht. Diese Arbeit hat in gleicher oder ähnlicher Form noch keiner Prüfungsbehörde vorgelegen.

Darmstadt, den 29.01.2014

(Joel de Jesús Mendoza-Temis, M.Sc.)

Zusammenfassung

Im Rahmen der vorliegenden Thesis wurde die Bedeutung der Kernmassen für Berechnungen der Nukleosynthese im Rahmen des r-Prozess untersucht. Zu diesem Zweck haben wir für alle relevanten Kerne entlang des r-Prozess-Pfads die Neutroneneinfangraten gemäß dem statistischen Modell [152] berechnet. Dabei handelt es sich um Isotope von Zn ($Z = 30$) bis Bi ($Z = 83$) innerhalb der modellabhängigen Neutronen-Abbruchkante. Wir haben jene der gegenwärtig verfügbaren Kernmassenmodelle benutzt welche die experimentell bekannten Massen am besten reproduzieren, wobei die mittlere quadratische Abweichung geringer als 600 keV ist. Es handelt sich hierbei um das Finite-Range-Droplet-Modell (FRDM) [18], das Weizsäcker-Skyrme-Modell (WS3) [19] und zwei Varianten des Duflo-Zucker-Massenmodells [20], DZ10 und DZ31.

Diese Arbeit widmet sich hauptsächlich folgenden Aufgabenstellungen:

1. Identifikation der charakteristischen Eigenschaften der unterschiedlichen Kernmassenmodelle bezüglich bekannter Kernstruktur-Größen, wie der Ein- und Zwei-Neutronen-Separationsenergie ($S_{1n}(Z, N)$ und $S_{2n}(Z, N)$), oder den Schalen-Abständen ($\Delta(Z, N)$). Z und N beziffern dabei jeweils die Protonen- bzw. Neutronenzahl. Darüber hinaus wurden für die einzelnen Modelle die Differenzen zu experimentell bekannten Massen und die Schalen-Korrekturen (Differenzen zum Tröpfchenmodell) bestimmt.
2. Berechnung der Neutroneneinfangraten im Rahmen des statistische Modells [17] für alle Kernmassenmodelle. Die dabei erhaltenen Raten wurden für Netzwerkrechnungen im Rahmen des r-Prozess verwendet.
3. Dynamische Netzwerkrechnungen entlang des r-Prozess-Pfads für thermodynamische Bedingungen wie sie in Neutrino-getriebenen Winden von Kernkollaps-Supernovae (SNe) oder bei der Verschmelzung zweier Neutronensterne (NSM) erwartet werden. Diese Bedingungen wurden in hydrodynamischen Simulationen dieser Szenarien bestimmt. Für den Fall des Neutrino-getriebenen Winds wurde auch der Einfluss des Rückwärtsschocks auf die Dynamik und die Häufigkeiten des r-Prozess untersucht. Dazu wurden drei unterschiedliche Trajektorien studiert, die sich im Wesentlichen in der Position des Schocks unterscheiden. Diese Fälle sind repräsentativ für den heißen r-Prozess, den kalten r-Prozess und den r-Prozess ohne Rückwärtsschock. Bei den Neutronenstern-Verschmelzungen musste aufgrund der niedrigen Entropie die Energieerzeugung durch Kernreaktionen berechnet und berücksichtigt werden. Die

Berechnungen der Nukleosynthese wurden mit einem großen Reaktions-Netzwerk bestimmt, welches 7000 Isotope von Kernen bis $Z = 110$ zwischen der Neutronen-Abbruchkante und dem Tal der Stabilität beinhaltet.

Bei der Untersuchung der Charakteristika und der Neutroneneinfangraten hat sich gezeigt, dass sich die einzelnen Modelle im Übergangsbereich zwischen sphärischen und deformierten Kernen bei $N \sim 90$ am deutlichsten unterscheiden. Um den Einfluss dieser besonderen Region genauer zu untersuchen wurden “Hybrid-Raten” nach folgender Methode konstruiert: Im FRDM-Modell werden die Massen der Isotopen-Ketten von Pd ($Z = 46$) bis Xe ($Z = 54$) durch die Werte eines der anderen Modelle (WS3, DZ10, DZ31) ersetzt. Die so erhaltenen Modelle werden als “Hybrid-Massenmodell” bezeichnet. Basierend auf diesen “Hybrid-Massenmodellen” werden dann die Neutroneneinfangraten wieder nach dem statistischen Modell berechnet.

Es ist dabei zu erwähnen, dass bis zum Zeitpunkt dieser Arbeit nur Neutroneneinfangraten basierend auf den Kernmassen des erweiterten Thomas-Strutinsky-Integrals (ETFSI), auf dem FRDM-Modell berechnet mit dem Statistischen Modell [17] und auf dem HFB-Massenmodell berechnet mit dem TALIS-Code [?] verfügbar waren. Unsere Berechnung haben dem drei weitere Sätze für Neutroneneinfangraten basierend auf den Modellen WS3, DZ10 und DZ31 hinzugefügt. Im Vergleich zu früheren Studien, die den Einfluss unterschiedlicher Massenmodelle untersucht haben (siehe z.B. [178]), wurden in dieser Arbeit selbstkonsistente Ergebnisse ermittelt indem wir die gleichen Massenmodelle für die Neutroneneinfangraten benutzt haben.

Im Anschluss an die r-Prozess-Berechnungen bestimmen wir die Sensitivität der Entwicklung und finalen Verteilung der r-Prozess-Häufigkeiten bezüglich der kernphysikalischen Eingangsgrößen. Die wichtigsten Erkenntnisse sind im Folgenden zusammengefasst:

ν -getriebener Wind bei hoher Entropie. Unabhängig von der benutzten Trajektorie zeigen alle r-Prozess-Häufigkeiten, basierend auf den neuen Raten der Modelle (abgesehen von FRDM), keine Ansammlung von Materie um $A \sim 140$. Wir führen dies darauf zurück, dass in den anderen Modellen die charakteristische Anomalie bei $N \sim 90$ fehlt oder abgeschwächt ist.

Bei der Entwicklung des heißen r-Prozess mit Rückwärtsschock bei Temperaturen um 1 GK wird das System während der Hauptphase des r-Prozess in ein (Quasi-) $(n, \gamma) - (\gamma, n)$ -Gleichgewicht verlagert. Unter diesen Bedingungen hängt der Verlauf des r-Prozess ausschließlich von den Kernmassen in Form der Separationsenergie ab. Dadurch lassen sich interessante Rückschlüsse aus der Analyse der Charakteristika ziehen. Es zeigt sich unter anderem, dass die Bereiche der Verformung, die vor dem Schalenabschluss bei $N = 82$ bzw. nach dem Abschluss bei $N = 126$ liegen, von großer Bedeutung für die finalen Häufigkeitsverteilungen sind. So ist der Ursprung des nach rechts verschobenen dritten r-Prozess-Maximums, das bei WS3 und FRDM zu beobachten ist, verbunden mit dem Verhalten der Modelle nahe $A \approx 180$ ($N \approx 118$), da dort die Materie akkumuliert wird. Da in den Duflo-Zucker-Massenmodellen dieses Merkmal fehlt, kann dann Materie dort durch Neutroneneinfang zu größeren Massenzahlen gelangen, so dass in der Folge das dritte r-Prozess-Maximum breiter wird.

Für den Fall des kalten r-Prozess ist obige Analyse nicht möglich. Hier wird die explizite Kenntnis der Raten für Neutroneneinfang, $N_n \langle \sigma v \rangle^*$, und β -Zerfall, λ_β , benötigt, um

die Entwicklung und die finale Häufigkeitsverteilung des r-Prozess zu verstehen. Der r-Prozess-Pfad verläuft durch weniger stabile Regionen, da das System sich hauptsächlich bei niedrigeren Temperaturen kleiner als 1 GK bewegt. Dort kann die Neutronenemission durch Photodissoziation vernachlässigt werden.

Wie in [10] finden auch wir, dass beim kalten r-Prozess noch nach dem Ausfrieren der Materie Neutroneneinfänge stattfinden. Diese erzeugen signifikante Änderungen in den finalen Häufigkeiten. Tatsächlich finden wir für das FRDM-Modell, dass die Häufigkeiten wegen den späten Neutroneneinfängen in der Region $A > 195$ zu höheren Massenzahlen verschoben werden ($A = 185 - 195$). In den anderen Modellen dominiert der β -Zerfall gegenüber dem Neutroneneinfang, sodass diese Kerne ohne substantielle Änderungen der Massenzahl zerfallen.

Die Bildung des sogenannten “Seltene-Erden-Maximums“ bei $A \sim 165$ hängt von der Häufigkeitsverteilung zu späten Zeiten (nach dem Ausfrieren), hervorgerufen durch die Konkurrenz dreier Prozesse ab, nämlich des Neutroneneinfangs, der Neutronenemission durch Photodissoziation und des β -Zerfalls.

Die finalen Häufigkeiten basierend auf den “Hybrid-Raten“ zeigen eine Reihe interessanter Eigenschaften: Verschwinden oder Abschwächung des künstlichen Haltepunkts bei $A \sim 140$, korrekte Reproduktion der Breite des dritten r-Prozess-Maximums, sowie in manchen Fällen die Reproduktion des “Seltene-Erden-Maximums“ bei $A \sim 165$. Dies alles lässt sich auf das Verhalten der Modelle um $N \sim 90$ herum zurückführen.

Trajektorien von Neutronenstern-Verschmelzungen (NSM). Für den Großteil der in dieser Arbeit untersuchten Trajektorien ist die Zeitskala der Expansion langsam genug, sodass die hohen Heizraten das System bis auf eine Temperatur von $T \sim 1$ GK bringen kann. Dies ähnelt dem heißen r-Prozess, jedoch gibt es Unterschiede in Zusammenhang mit den Dichten und den Expansions-Zeitskalen der beiden Szenarien. In einer Neutronenstern-Verschmelzung werden eine Größenordnung höhere Dichten erreicht und die Zeitskala ist schneller im Vergleich zum Neutrino-getriebenen Wind.

Im Rahmen der untersuchten Trajektorien erscheinen die finalen r-Prozess-Häufigkeiten robust, d.h. weitestgehend unabhängig von den Anfangsbedingungen. Als Ursache werden Zyklen von Kernspaltungen vermutet, welche die Materie umverteilen. In den untersuchten Trajektorien werden bis zu drei solcher Zyklen durchlaufen.

Da die Anzahldichte der Neutronen nach dem Ausfrieren der Materie immer noch hoch ist, sind späte Neutroneneinfänge nicht vernachlässigbar. Dadurch wird die finale Häufigkeitsverteilung gewissermaßen geglättet.

Die Physik hinter dem zweiten r-Prozess-Maximum ist verbunden mit der Spaltung von Kernen um $A \sim 280$. Es muss bedacht werden, dass das System in einer NSM-Trajektorie sogar zu frühen Zeiten in Regionen verschoben wird, in denen, unabhängig vom gewählten Kernmassenmodell, bereits Kernspaltungen stattfinden können.

Die meisten der untersuchten Modelle, abgesehen von FRDM, zeigen gute Übereinstimmung bezüglich der Breite und Position des dritten r-Prozess-Maximums. Dies ist wieder auf das Verhalten bei $N \approx 90$ zurückzuführen. Dort unterscheiden sich alle anderen Modelle signifikant von FRDM.

Schließlich ist festzuhalten, dass die Übereinstimmung bezüglich der Position des “Seltene-Erden-Maximums“ schwieriger zu analysieren ist. Sie hängt ab vom Zusammenspiel der dominanten Prozesse in der Spätphase des r-Prozesses.

Abschließend gibt es einige Fragestellungen mit denen sich zukünftige Arbeiten auseinandersetzen könnten:

- In bestimmten NSM-Trajektorien läuft der r-Prozess bei niedrigeren Separationsenergien ab ($S_{1n} < 1$ MeV). Dort könnte die Beschreibung von Neutroneneinfängen anhand des statistischen Modells zusammenbrechen und man müsste stattdessen direkte Neutroneneinfänge berücksichtigen.
- In dieser Arbeit wurden β -Zerfallsraten von Moeller et al. [162] verwendet. Für folgende Arbeiten wäre es aufschlussreich, zusätzliche Sätze von β -Zerfallsraten zu untersuchen.
- Die Implementierung der Verteilung diverser Spaltfragmente steht noch aus.
- Schließlich könnte untersucht werden, inwiefern das Verhältnis von Uran und Thorium als nukleares Kosmochronometer sensitiv ist auf die kernphysikalischen Eingangsparameter und die unterschiedlichen astrophysikalischen Szenarien.

Contents

1. INTRODUCTION	1
1.1. Physical context	2
1.2. Goals of the thesis	3
1.3. Outline	4
I Theoretical background	5
2. Nuclear physics Input	7
2.1. Nuclear mass models	7
2.1.1. Liquid drop Model (LDM)	7
2.1.1.1. The semi-empirical mass formula	8
2.1.2. Mac-Mic models	9
2.1.2.1. Finite Range Drop Model (FRDM)	10
2.1.2.1.1. Macroscopic part of FRDM.	10
2.1.2.1.2. Microscopic part of FRDM.	10
2.1.2.1.3. Final form of FRDM.	11
2.1.2.1.4. Fitting procedure.	12
2.1.2.2. Weizsäcker-Skyrme mass formula (WS)	12
2.1.2.2.1. Macroscopic sector.	12
2.1.2.2.2. Microscopic sector.	13
2.1.2.2.3. Final form.	13
2.1.3. Skyrme-Hartree-Fock-Bogoliubov (HFB) mass formulas	13
2.1.4. Duflo-Zuker mass formula (DZ)	14
2.1.4.1. Master terms. Asymptotic behaviour	15
2.1.4.2. Origin of the master terms. Scaling	17
2.1.4.3. The HO-EI transition	18
2.1.4.4. Macroscopic sector	19
2.1.4.5. Microscopic sector	19
2.1.4.6. Spherical nuclei	19
2.1.4.7. Deformed nuclei	20
2.1.4.8. Final form	20
2.2. Exploring systematics	20
2.2.1. Tests of reliability	21
2.2.1.1. Results	22
2.2.1.2. Remarks	22

2.2.2.	Global trends	23
2.2.3.	Residuals patterns	24
2.2.4.	Shell corrections	26
2.2.4.1.	Region of deformation	26
2.2.5.	Shell gaps	28
2.2.5.1.	Behaviour of the shell gaps near experimental region	28
2.2.5.1.1.	N=50 shell gap	28
2.2.5.1.2.	N=82 shell gap	28
2.2.5.1.3.	N=126 shell gap	29
2.2.5.2.	Behaviour of the shell gaps for regions far away from stability	30
3.	<i>r</i>-process Nucleosynthesis	35
3.1.	Requirements for the <i>r</i> -process	36
3.2.	Astrophysical sites for the <i>r</i> -process	38
3.2.1.	Massive star evolution and explosion	38
3.2.2.	Neutrino-driven winds from protoneutron stars	39
3.2.2.1.	Observational constrains and current status	41
3.2.3.	Neutron star mergers	41
3.2.3.1.	Observational constrains and current status	41
4.	Rates	43
4.1.	Nuclear reaction cross sections	43
4.1.1.	Compound nucleus (formation and conservation laws)	46
4.1.1.1.	Compound nucleus cross section (spin dependence)	46
4.1.2.	Statistical model	47
4.1.2.1.	Hauser-Feshbach Model	47
4.1.2.2.	Reaction rates from Statistical model	50
4.1.2.3.	Applicability of the Statistical Model	51
4.1.2.4.	Level densities	52
4.2.	Astrophysical Reaction Rates	53
4.2.1.	Reactions with particles of similar mass	53
4.2.2.	Photodissociation, decays and weak interaction rates	53
4.2.3.	Stellar enhancement factor	54
4.3.	Results: MOD-SMOKER	55
4.3.1.	Preliminary details	55
4.3.2.	Analytic neutron capture rate fits	55
4.3.3.	Parameters for the photodissociation rates	56
4.3.4.	Computed rate sets	56
4.3.4.1.	Global features	57
4.3.4.2.	Local features	59
5.	Nuclear reaction network	61
5.1.	Application: <i>r</i> -process nucleosynthesis	62
5.1.1.	The waiting point approximation	63
5.1.2.	Steady flow approximation	65
5.1.3.	Dynamic calculations	66
5.1.3.1.	Numerical solution of the reaction network	66
5.2.	Application: Energy generation	67

II	Results	69
6.	r-process network calculations: General features	71
6.1.	Description of the network	71
6.2.	Hydrodynamical trajectories	71
6.2.1.	Extrapolation to late times	72
6.3.	Performing network calculations	72
6.3.1.	Expansion from NSE	72
6.3.2.	Relevant variables and stages of the evolution	73
7.	r-process network calculations: ν-driven wind conditions	77
7.1.	<i>r</i> -process dynamics	79
7.1.1.	General features	80
7.1.1.1.	Evolution of a hot <i>r</i> -process	80
7.1.1.2.	Evolution of a cold <i>r</i> -process	82
7.1.1.3.	Evolution of an <i>r</i> -process without a reverse shock	84
7.1.2.	Sensitivity to the nuclear physics input	85
7.2.	Final <i>r</i> -process abundance pattern	87
7.2.1.	General features	87
7.2.2.	Sensitivity to the nuclear physics input	87
7.2.2.1.	Anatomy of a hot <i>r</i> -process	90
7.2.2.2.	Anatomy of a cold <i>r</i> -process	95
7.2.2.3.	Formation of the rare earth peak ($A \sim 165$)	97
7.2.3.	Relevance of the deformation region at $N \sim 90$	100
8.	r-process network calculations: NSM conditions	105
8.1.	<i>r</i> -process heating	106
8.2.	Evolution of an <i>r</i> -process under NSM conditions	108
8.3.	Distribution of abundances for NSM trajectories at various stages	110
8.3.1.	Fission cycles	115
8.4.	Robustness in the observed final pattern of abundances	115
III	Summary and Outlook	117
9.	Summary and Outlook	119

List of Figures

1.1.	Negative value of the binding energies per nucleon (MeV) as a function of the number of nucleons $A = N + Z$	1
2.1.	Residual differences between $BE_{EXP} - BE_{LDM}$ in units of MeV. On the l.h.s., along isotopic (bluish lines) and isotonic chains (reddish lines displaced by -15 MeV) only even-even nuclei are shown. On the r.h.s., along the plane NZ for all nuclei included in AME12 [32].	9
2.2.	(a) Harmonic oscillator and extruder-intruder (EI) shells. (b) The evolution from HO (dots) to EI (squares) shell effects for $N - Z = 24$. Heavier marks for existing data.	18
2.3.	Nuclear Landscape for the binding energies. The lime color area corresponds to the measured nuclei taken from [32], the yellow region represents extrapolations based on the Finite Range Drop Model (FRDM) [18] up to its drip lines (blue boxes). The red boxes denote the valley of stability.	21
2.4.	Set of nuclei used for the reliability test. The blue region represent the fitted ones and red dots the predicted ones.	22
2.5.	Residuals differences between $BE_{EXP} - BE_i$ for all nuclei included in AME12 [32] (l.h.s.). Residuals differences between $S_{2n}^{EXP} - S_{2n}^i$ for all nuclei included in AME12 (r.h.s.). The results for the different mass models used in the present work are displayed in the above panels as follows: a,b \rightarrow FRDM; c,d \rightarrow HFB21; e,f \rightarrow DZ10; g,h \rightarrow DZ31; i,j \rightarrow WS3.	25
2.6.	Shell corrections for even-even nuclei for a number of Isotopic chains ($30 < Z < 83$) for the set of nuclear masses based on AME12 up to the nuclear drip lines for the following theoretical models: FRDM, HFB21, DZ10 and DZ31 (black lines). The set of deformed nuclei predicted for a number of models is displayed by red lines (for further details see section 2.2.4.1).	27
2.7.	Shell gaps for the neutron shell closures at $N= 50$ (upper panel), 82 (middle panel) and 126 (bottom panel). For the mass models used in present work: FRDM (red lines), WS3 (blue line), DZ10 (green lines), DZ31 (cyan lines), HFB21 (orange lines) and also for the set of experimentally available nuclei, AME12 (black empty boxes).	29

2.8.	$S_{2n}/2$ for a number of isotonic (isotopic) chains $40 < N < 184$ ($30 < Z < 83$) on the l.h.s. (r.h.s.) based on the Finite Range Drop Model (FRDM) up to the neutron drip lines. Experimental data is always shown with red lines. Nuclei for which $\beta_2 \geq 0.2$ are displayed with green lines. On the l.h.s. only isotonic chains with N even are shown. The neutron shell gaps at $N=50, 82$ and 126 are represented by bluish shadowed regions with labels on top of the same. On the l.h.s. blue lines are added every five isotopic chains to guide the eye.	31
2.9.	Same as in Fig 2.8 but for the HFB21 model.	31
2.10.	Same as in Fig 2.8 but for the WS3 model.	32
2.11.	Same as in Fig 2.8 but for the DZ10 model.	33
2.12.	Same as in Fig 2.8 but for the DZ31 model.	33
3.1.	Solar system abundances of heavy elements produced by r-process and s-process neutron captures. Plotted values are $12 + \log_{10}$ of abundance relative to hydrogen. Taken from [7] (Adapted from [91]).	35
3.2.	Solar r-process abundances. These abundances are obtained by subtracting the s-process contributions calculated from (a) the phenomenological approach and (b) models of two AGB stars. See [101, 102, 103] for details.	36
3.3.	Combinations of Y_e , S , and τ_{dyn} giving rise to an initial neutron-to-seed ratio of $R_{n/s}(t_0) \approx 100$ for the r-process in adiabatically expanding matter. Production of nuclei with $A \sim 195$ is expected. Plot taken from [115].	38
3.4.	Structure of a massive star at the end of its evolution. Taken from [121].	39
3.5.	ν -driven wind from surface of the recently born proto neutron star (PNS). Taken from [97].	40
3.6.	Merger and mass ejection dynamics of the $1.35\text{-}1.35 M_{\odot}$ binary with the DD2 EoS, visualized by the color-coded conserved rest-mass density (logarithmically plotted in g/cm^3) in the equatorial plane. The dots mark SPH particles which represent ultimately gravitationally unbound matter (taken from [16]).	42
4.1.	Geometry of the scattering problem.	44
4.2.	Schematic view of the transitions (full arrows denote particle transitions, dashed arrows are γ -transitions) in a compound reaction involving the nuclei A and F , and proceeding via a compound state (horizontal dashed line) with spin J_C^k and parity π_C^k in the compound nucleus C . The reaction Q values for the capture reaction (Q_{cap}) and the reaction $A \rightarrow F$ ($Q_F = Q_{Aa}$) are given by the mass differences of the involved nuclei. Above the last state, transitions can be computed by integrating over nuclear level densities (shaded areas). Taken from [138].	48
4.3.	Ratio of n-capture rates of 4 investigated mass models (FRDM, WS3, DZ10 and DZ31) to those from [155] at a temperature $T = 1\text{GK}$. Experimental masses were used when available.	58
4.4.	Comparison of the n-capture rates for a number of representative isotopic chains in the region of relevance for the r-process nucleosynthesis calculations, the rates are based on different mass models. The previously n-capture rates computed in [155] are shown by dashed lines.	60

6.1. Evolution of the temperature T , the neutron number density n_n , the neutron-to-seed-ratio Y_n/Y_h , the average one-neutron separation energy $\langle S_n \rangle$ and the characteristic time-scales involving in the r-process, i.e., n-capture $\langle \tau_{(n,\gamma)} \rangle$ (dotted lines), photodissociation $\langle \tau_{(\gamma,n)} \rangle$ (dashed lines) and β -decay $\langle \tau_\beta \rangle$ (continuous lines). This results correspond to an arbitrary trajectory and an arbitrary mass model. Symbols are added on top of the lines that follow the evolution of the relevant variables to denote relevant stages in the evolution of the r-process (for further details see text).	73
7.1. Temperature and density evolution	78
7.2. Initial composition obtained via a network calculation (see section 6.3.1) for a temperature $T=3$ GK and a density of the order of 10^4 g cm^{-3} . The initial composition favours nuclei in the region of $A \sim 90$	79
7.3. Evolution of the temperature T , the neutron number density n_n , the neutron-to-seed-ratio Y_n/Y_h , the average one-neutron separation energy $\langle S_{1n} \rangle$ and the characteristic time-scales involving in the r-process, i.e., n-capture $\langle \tau_{(n,\gamma)} \rangle$ (dotted lines), photodissociation $\langle \tau_{(\gamma,n)} \rangle$ (dashed lines) and β -decay $\langle \tau_\beta \rangle$ (continuous lines). These results correspond to a hot r-process for the different mass models used in the present work: FRDM (black lines on all the panels), DZ31 (bluish lines), DZ10 (reddish lines) and WS3 (orange lines), we choose to used FRDM as a reference. Symbols are added on top of the lines to denote relevant stages in the evolution of the r-process.	81
7.4. Evolution of the temperature T , the neutron number density n_n , the neutron-to-seed-ratio Y_n/Y_h , the average one-neutron separation energy $\langle S_{1n} \rangle$ and the characteristic time-scales involving in the r-process, i.e., n-capture $\langle \tau_{(n,\gamma)} \rangle$ (dotted lines), photodissociation $\langle \tau_{(\gamma,n)} \rangle$ (dashed lines) and β -decay $\langle \tau_\beta \rangle$ (continuous lines). These results correspond to a cold r-process for the different mass models used in the present work: FRDM (black lines on all the panels), DZ31 (bluish lines), DZ10 (reddish lines) and WS3 (orange lines), we choose to used FRDM as a reference. Symbols are added on top of the lines to denote relevant stages in the evolution of the r-process.	83
7.5. Same as in Fig. 7.3 but this time, the evolution is referring to an r-process without a reverse shock (for further details see text).	84
7.6. Final r-process abundances as a function of the mass number A , for various conditions in the ν -driven wind scenario: hot r-process (Black lines), cold r-process (orange lines) and for an r-process without a reverse shock (red lines). Bullet symbols representing the solar r-process abundances are added to guide the eye. The displayed results correspond to a set of rates based on: FRDM, WS3, DZ10 and DZ31 mass model.	88
7.7. Final r-process abundances as a function of the mass number A , for a number of mass models: FRDM (Black lines), WS3 (orange lines), DZ10 (red lines), DZ31 (blue lines). Bullet symbols representing the solar r-process abundances are added to guide the eye. The uppermost panel shows the results corresponding to a hot r-process, the middle panel exhibits the results of a cold r-process and the lower one, results for an r-process without a reverse shock.	89

7.8.	Behaviour around the second minimum in the average neutron separation energy $\langle S_{1n} \rangle$ (See triangular shape symbols in Fig. 7.3) for a hot r-process (see Fig. 7.1). From the left hand to the right hand side panels, one can distinguish results involving rates based on FRDM, WS3, DZ10, DZ31 masses. The Uppermost panel display the $S_{2n}/2$ surface of the different models (the experimental information is always displayed), the middle zone shows the current abundances as a function of A and the bottom panel display the same on the N-Z landscape.	92
7.9.	Behaviour at the time of the neutron exhaustion, i.e. when $Y_n/Y_h \approx 1$ (See diamond shape symbols in Fig. 7.3) for a hot r-process (see Fig. 7.1). From the left hand to the right hand side panels, one can distinguish results involving rates based on FRDM, WS3, DZ10, DZ31 masses. The Uppermost panel display the $S_{2n}/2$ surface of the different models (the experimental information is always displayed), the middle zone shows the current abundances as a function of A and the bottom panel display the same on the N-Z landscape.	93
7.10.	Behaviour at the time of end of the r-process, i.e. when $\tau_{n,\gamma} \gg \tau_\beta$ (See pentagon shape symbols in Fig. 7.3) for a hot r-process (see Fig. 7.1). From the left hand to the right hand side panels, one can distinguish results involving rates based on FRDM, WS3, DZ10, DZ31 masses. The Uppermost panel display the $S_{2n}/2$ surface of the different models (the experimental information is always displayed), the middle zone shows the current abundances as a function of A and the bottom panel display the same on the N-Z landscape.	94
7.11.	Evolution of the abundances $Y_i(A)$, and the fluxes (defined in Eqs. 7.6 and 7.7) vs A and Z for a cold r-process at the neutron-exhaustion stage (see bluish lines) and at the so-called end of the r-process stage (see reddish lines). The net neutron capture flux is represent by solid lines and the β -decay flux by dashed lines. The set of rates are based on the: a) FRDM mass model, b) WS3 mass model, c) DZ10 mass model and d) DZ31 mass model.	96
7.12.	Understanding the formation of the rare earth peak (REP). Behaviour of the r-process path, distribution of abundances and the fluxes for neutron-capture (F_n) and β -decay (F_β) at various stages of the evolution of a hot r-process for rates based on the FRDM mass model.	98
7.13.	Understanding the formation of the rare earth peak (REP). Behaviour of the r-process path, distribution of abundances and the fluxes for neutron-capture (F_n) and β -decay (F_β) at various stages of the evolution of a hot r-process for rates based on the WS3 mass model.	99
7.14.	Same as Fig. 7.8, Impact of the region $N \sim 90$ under hot r-process conditions, at the time of the neutron exhaustion, i.e. when $Y_n/Y_h \sim 1$	101
7.15.	Same as in Fig. 7.7, but this time to explore the impact of the region $N \sim 90$ in the final r-process abundances.	102
8.1.	Density evolution of the NSM trajectories, starting when density has dropped below ρ_{drip} (see text).	105
8.2.	Initial composition based on the set of masses from the WS3 model for various NSM trajectories. Labels are added to identify the physical conditions, i.e., Temperature, T, density, ρ , neutron number density, n_n , neutron to seed ratio, Y_n/Y_h , entropy, S, and the electron fraction, Y_e	107

LIST OF FIGURES

8.3. Evolution of relevant variables for the r-process.	109
8.4. Distribution of abundances at various stages of the r-process as a function of the mass number A , for the FRDM mass model. Empty boxes symbols representing the solar r-process abundances are added just to guide the eye. Labels denote the electron fraction, Y_e , of a given trajectory.	111
8.5. Distribution of abundances at various stages of the r-process as a function of the mass number A , for the WS3 mass model. Empty boxes symbols representing the solar r-process abundances are added just to guide the eye. Labels denote the electron fraction, Y_e , of a given trajectory.	112
8.6. Distribution of abundances at various stages of the r-process as a function of the mass number A , for the DZ10 mass model. Empty boxes symbols representing the solar r-process abundances are added just to guide the eye. Labels denote the electron fraction, Y_e , of a given trajectory.	113
8.7. Distribution of abundances at various stages of the r-process as a function of the mass number A , for the DZ31 mass model. Empty boxes symbols representing the solar r-process abundances are added just to guide the eye. Labels denote the electron fraction, Y_e , of a given trajectory.	114
8.8. Robust pattern in the final r-process abundances for $A > 120$ due to fission cycling.	116



List of Tables

2.1.	Recent fit of the coefficients of the liquid drop model (Eq. 2.3).	9
2.2.	RMSD in MeV, for the fits and predictions for different mass models.	22
2.3.	Number of nuclei predicted in various intervals of the one-neutron separation energy S_n for all mentioned number of mass models	24
8.1.	number of fission cycles for a number of NSM trajectories, for n-capture rates based on: FRDM, WS3 and two variants of the DZ mass model.	115

INTRODUCTION

The intimate relationship between nuclear masses and astrophysics seems to go back to the earliest years of the 20th century, thanks to both Aston and Eddington. Aston on the one hand, measured the mass $M(N,Z)$ of a nucleus and found that its value was unexpectedly smaller than the sum of the masses of its constituent free nucleons [1]. Eddington on the other hand, interpreted this "mass defect" [2] in terms of the nuclear binding energy $BE(N,Z)$ which is the energy required to split an atomic nucleus into its component parts,

$$BE(N, Z) = [NM_n + ZM_H - M(N, Z)]c^2, \quad (1.1)$$

where M_n is the mass of the neutron and M_H that of hydrogen atom.

When plotting the experimental binding energy per atomic nuclei, $BE(N, Z)/A$, against the atomic number, A , a lot of features of nuclear physics become apparent (see Figure 1.1).

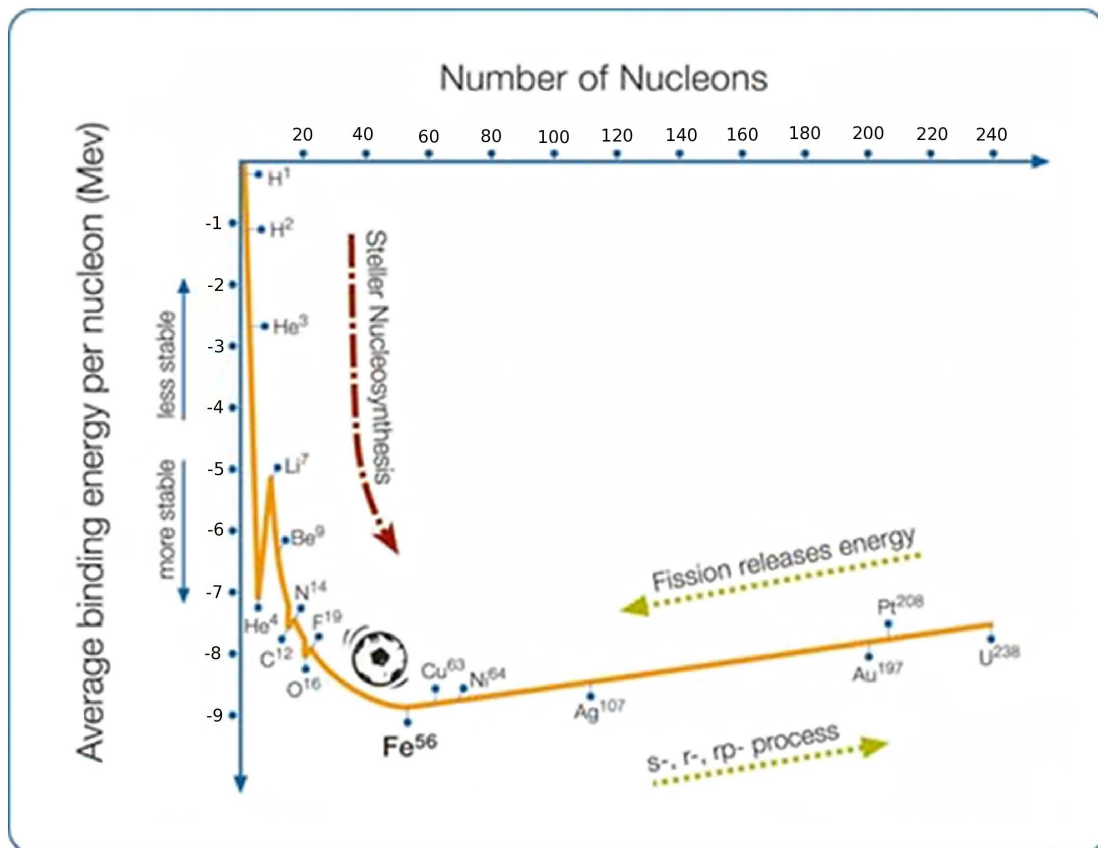


Figure 1.1: Negative value of the binding energies per nucleon (MeV) as a function of the number of nucleons $A = N + Z$

The most conspicuous feature of nuclei is that their binding energy per particle is nearly constant, in other words the nuclear force saturates and has its minimum around $A \approx 56$. The peaks in binding energy at 4, 12 and 16 nucleons are a consequence of the large stability of the α like nuclei (an α particle corresponds to a nucleus of ${}^4\text{He}$ which is nothing but a combination of two protons and two neutrons). Interestingly, one can also notice that energy must be released by the fusion of light elements into heavier ones. In fact Eddington showed that nuclear transmutations of hydrogen into helium could serve as an adequate source of stellar energy. A long standing puzzle was thereby resolved, since no other known source of energy being sufficient to account for the estimated luminosity of the sun over the necessary time scale [3]. This fusion process continues up to the most tightly bound nucleus ${}^{56}\text{Fe}$ from which no more energy can be released. Elements heavier than ${}^{56}\text{Fe}$ release energy when splitting into smaller fragments in the so-called nuclear fission process. This effect is responsible for the release of energy in nuclear reactors and atomic bombs.

Given this inherent connection with the binding energy, the mass of a nucleus must be regarded as one of its basic characteristics[3]. In fact, understanding nuclear masses provides a test of our basic knowledge of the underlying nuclear structure. Its accurate knowledge is relevant for the description of various nuclear and astrophysical processes [4]. Though great progress has been made in the challenging task of measuring the mass of short-lived nuclei which are far from the region of stable, naturally occurring isotopes, theory is needed to predict their properties and guide experiments that search, for example, for regions far from stability [5].

1.1. Physical context

In nuclear astrophysics there is no doubt that one of the most intriguing problems yet to be solved is the origin of the heaviest elements (those beyond the iron group). They cannot be produced in thermonuclear reactions in the interior of stars because fusion reactions are no longer exothermic processes (the most tightly bound nuclei lies around the iron group, see Figure 1.1). Additionally, the Coulomb barrier grows with proton number, hindering fusion reactions induced by charged particles at stellar temperatures. Indeed since the work of Burbidge et al. [6], it is well known that trans-iron elements must be produced through successive neutron captures followed by β -decays; these neutron capture processes are divided into rapid (r-process) and slow (s-process) depending on the time it takes a nucleus to capture a neutron (τ_n) compared to the time it takes the same nucleus to undergo a β -decay (τ_β). While τ_β depends only on the nuclear species, τ_n depends crucially on the ambient neutron flux [7]. The s-process isotopes remain near to the valley of stability and are long lived. For that reason their properties can be measured in the laboratory. On the other hand r-process isotopes involve extremely neutron rich (highly unstable) species which are lying farther away from the valley of stability; their properties cannot be reached in the laboratory and the emergence of a theoretical description of their properties is required. However, different theoretical models predict completely different properties for the same r-process nuclei. In this thesis a number of different theoretical models for the description of nuclear masses have been used, to explore the sensitivity of the nucleosynthesis to the nuclear physics input.

Up to date it has not been able to establish an astrophysical site for the production of r-process elements that simultaneously meets the physical conditions and observational constraints. In r-process nucleosynthesis, a high neutron flux is mandatory in order to move matter farther away from stability; therefore the favorite astrophysical scenarios involve the most violent and spectacular explosions that occur in nature, the so called "core-collapse supernova explosion" (CCSNe) and the subsequent formation of either a black hole (BH) or a "neutron star" (NS). In this thesis both high entropy ν -driven winds from CCSNe [8, 9, 10] and the matter that becomes gravitationally unbound from neutron star merger (NSM) [11, 12, 13, 14, 15, 16] have been explored as possible sites for r-process nucleosynthesis.

1.2. Goals of the thesis

The relevance of the present work relies on the role of the nuclear physics input and its interplay with different astrophysical scenarios for the production and the final yield distribution of heavy elements. In particular we focus our attention on the subject of nuclear masses, as they are among the most fundamental properties of the nucleus. Their knowledge is required to understand several astrophysical processes, from energy generation inside the stars up to the nucleosynthesis of heavy elements under high neutron flux environment. To this end neutron capture rates are computed in the framework of the statistical model approach [17] for different sets of nuclear masses based on the finite range droplet model (FRDM) [18], the Weizsäcker-Skyrme model (WS3) [19] and the Duflo-Zuker model (DZ) [20]. Then we incorporate the previous results in a REACLIB file. Nucleosynthesis calculations are performed starting from nuclear statistical equilibrium (NSE) conditions. After the freeze-out from NSE the use of a full reaction network is required. We follow the thermodynamical conditions taken from hydrodynamical simulations corresponding to either high entropy ν -driven winds from core collapse supernovae (CCSNe) [21] or Neutron star merger (NSM) [22].

In particular, the following questions will be addressed in this thesis:

- What can we learn from the systematics of nuclear masses?
- Can we identify which physical ingredients are missing in a given theoretical model, i.e., can we improve its description when compared with experimental data?
- Is there a way to test the reliability of the different theoretical nuclear mass models in the experimentally unknown regions?
- To what extent can we identify from the theoretical point of view possible key r-process nuclei in order to guide experiments?
- How to quantify the impact of nuclear masses on the r-process abundances?
- Can we constrain the astrophysical conditions assuming that nuclear masses are known?

1.3. Outline

We have decided to split the thesis in three parts. In the first part, we present the theoretical background, i.e., the tools required to perform r-process nucleosynthesis calculations and the theory behind the nuclear astrophysics concepts required to interpret such results. The second part of this thesis deals with our results of r-process nucleosynthesis calculations. The third part gives an summary and outlook.

The first part of this work is structured as follows:

- Chapter 2, is divided in two parts. The first part, introduces the different theoretical approaches to be used in the present work for the calculation of the nuclear masses. In particular the physics behind the so-called “liquid drop model” (LDM), the “finite range droplet model” (FRDM), the “Weizsäcker-Skyrme model” (WS3), the “Hartree-Fock-Bogoliubov” mass model (HFB) and the “Duflo and Zuker mass formula” (DZ) is explained. The second part, discusses the systematical properties (residuals, shell corrections and shell gaps) behind the aforementioned set of nuclear mass models.
- Chapter 3, presents a short introduction to the subject of r-process nucleosynthesis, focusing mainly in the required physical conditions needed for a successful r-process nucleosynthesis and the possible astrophysical scenarios, in particular two sites are described in more detail; the one of the ν –driven wind and the one of NSM.
- Chapter 4, is also divided in two parts. On the first part, we present a discussion of several aspects of the calculation of astrophysical reaction rates in the framework of the statistical model. Focusing in the calculation of neutron-capture rates, $N_A \langle \sigma v \rangle_{n,\gamma}^*$, and their inverse processes, the neutron-emission via photodissociation, $\lambda_{\gamma,n}$. On the second part, results concerning to the calculation of the aforementioned neutron capture rates and their inverse processes computed in the framework of the statistical model approach for a set of nuclear masses based on the FRDM, WS3 and DZ model are shown.
- Chapter 5, reviews the general aspects concerning nuclear reaction network calculations. The first part deals with applications to r-process calculations, and the second one with applications to energy generation from nuclear reactions.

The second part of the thesis, present the outcome of our r-process nucleosynthesis calculations.

- A general introduction to the results is given in Chapter 6.
- Chapter 7, presents results of the interplay between the ν –driven wind scenario with the different sets of neutron capture rates already shown in Chapter 4.
- In Chapter 8, results dealing with the NSM are explored.

Finally, in the third part of the thesis.

- In Chapter 9, the consequences of our findings are summarised, we draw conclusions and mention some directions for future work.

Part I

Theoretical background

Nuclear physics Input

The final goal of every theoretical model is not only to reproduce different observables that can be measured but to provide reliable information about those that can not be reached by up-to-day experimental facilities. There has been much work in developing mass formulas with both microscopic and macroscopic input, on one side, and on the derivation of masses in a fully microscopic framework, on the other [3]. Advances in the calculation of nuclear masses starting from first principles (*ab initio* calculations, based on realistic forces adjusted to reproduce nucleon-nucleon scattering) have been hampered due to the difficulties inherent to quantum many-body techniques. At present, the best choice for the calculation of nuclear masses is either to start from effective interactions or purely semi-empirical approaches fitted to ground state properties of nuclei, i.e., all measured binding energies. During the present work, we have been exploring the most successful approaches to compute nuclear masses. In the first part of this chapter, we briefly re-visited a number of mass models. For historical reasons our starting point is the so-called liquid drop model (LDM), which represents the first attempt to describe the nucleus with its analogy to a liquid drop. Then, we describe two models denoted as macroscopic-microscopic global mass formulas, firstly, the Finite Range Droplet Model (FRDM) [18], which has become the *de facto* mass model and secondly, the so-called Weizsäcker-Skyrme mass formula (WS) [19], which is the best available model to fit all measured binding energies taken from [47]. Afterwards, a short summary on the Skyrme-Hartree-Fock-Bogoliubov (HFB) mass formula [23] is presented and finally, the building blocks behind the shell model inspired Duflo-Zuker mass formula (DZ) [20] are explored. In the second part of this chapter, the systematic trends of the above mentioned models are explored in more detail.

2.1. Nuclear mass models

2.1.1. Liquid drop Model (LDM)

Historically George Gamow [24, 25, 26] was the first to suggest that the nucleus can be pictured as a drop of incompressible "nuclear fluid" in which its constituents are held together by surface tension, however all the developments are due to von Weizsäcker [27], Bethe and Bacher [28]. In fact the last ones reworked and simplified von Weizsäcker's calculations up to the version which is most familiar to the nuclear physics community. The idea of considering the nucleus as a liquid drop originally came from considerations about its saturation properties and from the fact that the nucleus has a very low compressibility and well defined surface [29]. The binding energy $BE(N,Z)$ was previously defined in Eq. 1.1, as the energy required to split an atomic nucleus into its component parts. A fact that can

be extracted from observations(see Fig. 1.1) is that the binding energy per particle stays fairly constant for nuclei with more than twelve nucleons:

$$\left. \frac{BE(N, Z)}{A} \right|_{A>12} \approx 8.0[\text{MeV/nucleon}]. \quad (2.1)$$

This is because the saturation property of the nuclear forces, which allows one nucleon in the nucleus to interact only with its nearest neighbours. This has its origin in the short-range nuclear force and the combined effect of the Pauli and uncertainty principles [29]. The saturation property also explain the roughly constant density of nucleons inside the nucleus and the nucleus relatively sharp surface, properties experimentally found by electron scattering, μ -mesonic x-rays, etc. If we assume an spherical shape nucleus with a constant density, the radius of such nucleus should go as

$$R = r_0 A^{1/3}, \quad \text{where } r_0 = 1.2 \text{ fm}. \quad (2.2)$$

2.1.1.1. The semi-empirical mass formula

In Bethe's own words [30]: "the nucleus is conceived as filling a compact volume, spherical or other shape, and its energy is the sum of an attractive term proportional to the volume, a repulsive term proportional to the surface (this effect is analogous to that of the surface tension of a liquid drop), and another term due to the mutual electric repulsion of the positively charged protons (the Coulomb repulsion energy is proportional to the number of proton pairs $Z(Z - 1)$ and inversely proportional to the radius $R \propto A^{1/3}$)". If there were no Coulomb interaction between protons, we would expect, from symmetry arguments applied to a Fermi gas, to find equal numbers of protons and neutrons. The Coulomb interaction implies that neutrons are energetically favoured respect to protons, in this way a neutron excess is introduced in heavier nuclei. Since nuclei are formed by two Fermi gases, any asymmetry will imply filling progressively more Fermi orbitals in only one of the two gases. The asymmetry energy reduces the nuclear binding. To lowest order, we can expect the energy to vary as $(N - Z)^2$; in addition, the Fermi gas energy level spacing varies as $1/A$. An empirical term to take into account the observed coupling in pairs of nucleons goes as follows:

$$\delta(N, Z) = \left\{ \begin{array}{l} +1 \text{ } N \text{ even, } Z \text{ even} \\ 0 \text{ } N+Z \text{ odd} \\ -1 \text{ } N \text{ odd, } Z \text{ odd} \end{array} \right\} \text{ nuclei.}$$

A combination of the above mentioned terms leads to the Weiszäcker semi-empirical formula for the binding energy of the atomic nucleus [31],

$$BE(N, Z)_{LDM} = a_v \cdot A - a_s \cdot A^{2/3} - a_c \cdot \frac{Z(Z - 1)}{A^{1/3}} - a_a \cdot \frac{(N - Z)^2}{A} + a_p \cdot \frac{\delta(N, Z)}{\sqrt{A}}. \quad (2.3)$$

We have performed a recent fit of the coefficients a_i of Eq. 2.3 based on the set of nuclei given by [32] with a root mean square deviation $RMS \approx 3 \text{ MeV}$ (see Table 2.1).

Finally, the pattern of the residuals between measured binding energies BE_{EXP} (taken from the brand new atomic mass evaluation [32]) and those calculated by fitting the coefficients (see table 2.1) in Eq. 2.3 is shown in Figure 2.1. In left hand side the systematic is displayed as a function of the neutron number N (proton number Z) connecting isotope lines

2.1. NUCLEAR MASS MODELS

Table 2.1: Recent fit of the coefficients of the liquid drop model (Eq. 2.3).

COEFFICIENT	(MeV)
a_v	15.64
a_s	17.58
a_c	0.71
a_a	23.07
a_p	13.59

(isotone lines) for even-even nuclei. In the right hand side the same systematic is shown in the nuclear Landscape but in this case for all nuclei.

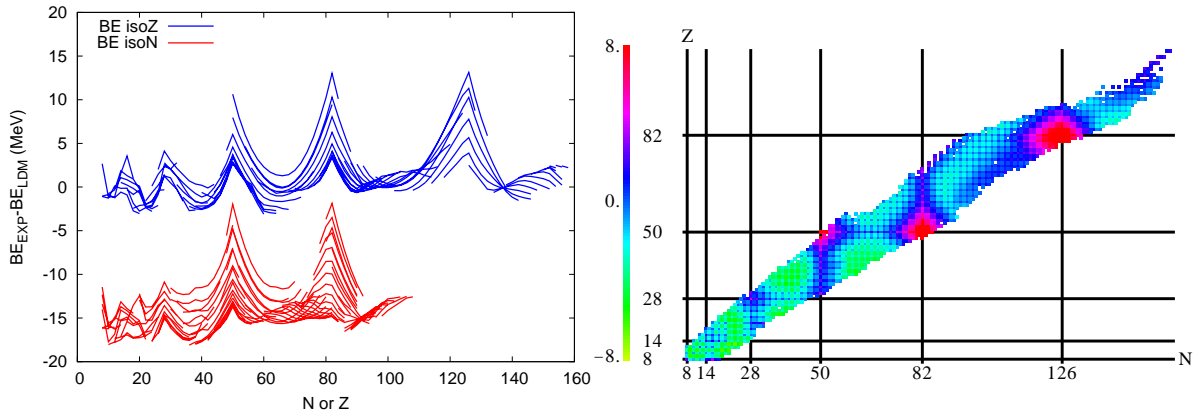


Figure 2.1: Residual differences between $BE_{EXP} - BE_{LDM}$ in units of MeV. On the l.h.s., along isotopic (bluish lines) and isotonic chains (reddish lines displaced by -15 MeV) only even-even nuclei are shown. On the r.h.s., along the plane NZ for all nuclei included in AME12 [32].

It's worth to be mentioned that by displaying the systematics of the residuals one can notice a regular pattern, i.e., the discrepancies grow up significantly at well located regions, in particular around $N=8,14,28,50,82,126$ and $Z=8,14,20,28,50,82$ indicating the presence of shell structure. In fact that was the origin of a major revolution in nuclear physics, the so-called the shell model.

2.1.2. Mac-Mic models

This section deals with the so-called mac-mic models (an abbreviation for macroscopic-microscopic models), on the one hand the "mac" part of the name is because all of them contain a macroscopic sector which resembles the Liquid Drop Model (LDM), including volume and surface terms, the Coulomb interaction between protons and asymmetry terms, linear and quadratic in the neutron excess $N-Z$; on the other hand the "mic" part of the name refers to a microscopic sector (a touch of quantum) by adding shell corrections via the so-called "Strutinsky method" [49, 50], BCS pairing corrections [33, 34] and a wigner term.

2.1.2.1. Finite Range Drop Model (FRDM)

All started back to 1966 when Myers and Swiatecky proposed a liquid drop formula including shell corrections and deformation effects the so-called "droplet model" [35], which evolve after a fruitful collaboration with Möller, Nix and Treiner into a macro-micro global nuclear mass formula the so-called Finite Range Drop Model (FRDM) [18]. Since this model has become not only the de facto standard for nuclear mass formulas but also the usual point of reference for experimentalists, in what follows a brief description of the FRDM is given, presenting some recent updates.

2.1.2.1.1. Macroscopic part of FRDM. The evolution of FRDM can be described in three stages [3]:

1. In the first stage the LDM was replaced by the so call "droplet model" [51, 52]. This version considers deformation effects, allowing a finite nucleus being compressed by the surface tension and dilated under the influence of the Coulomb force, so that it provides a useful framework for the description of dynamic phenomena, i. e. giant dipole resonances [53].
2. The second stage was manifested by introducing surface effects of finite range N-N interaction, i.e. multiply the surface sector of the droplet model by a factor depending on the shape of the nucleus; but since it must take into account the finite range effects, such factor wont gave a unit value in the case of spherical nuclei [54].
3. The last step was the addition of an exponential compressibility term from purely phenomenological origin [55], it was required because the droplet model used to overestimate the central density.

2.1.2.1.2. Microscopic part of FRDM. In FRDM, the microscopic sector is given by the shell-plus-pairing correction E_{s+p} , which is the sum of the proton shell-plus-pairing correction (E_{s+p}^Z) and the neutron shell-plus-pairing correction (E_{s+p}^N), namely

$$E_{s+p}(Z, N, \beta) = E_{s+p}^Z(Z, \beta) + E_{s+p}^N(N, \beta), \quad (2.4)$$

where β stands for the shape dependence (deformation effects). In general one have:

$$E_{s+p}^k(k, \beta) = E_{shell}^k(k, \beta) + E_{pairing}^k(k, \beta) \quad k = Z, N \quad (2.5)$$

a) Shell corrections

The Strutinsky theorem([49, 50]) made possible to add shell corrections to a purely macroscopic model. One can realize that the total energy of a nucleus can be divided in a smooth contribution given by the LDM and an oscillatory component due to the occurrence of shell closures, i.e. they have their maxima in the magic numbers (see Figure 2.1). It was the decisive idea of Strutinsky to calculate only the fluctuating part E_{osc} within the shell model and take the rest from the LDM.

$$E(Z, N, \beta) = E_{LDM}(Z, N, \beta) + E_{osc}^Z(Z, \beta) + E_{osc}^N(N, \beta), \quad (2.6)$$

where E is the negative value of the binding energy. The main assumption is that the fluctuating part E_{osc} is well approximated by the fluctuating part of the shell model energy,

2.1. NUCLEAR MASS MODELS

then the problem reduces to divide up the shell model energy into an oscillating part, E_{osc} and a smoothly varying part, $\langle E_{shell} \rangle$,

$$E_{SM}^k(k, \beta) = \sum_{i=1}^{N_k} \epsilon_i^k(\beta) = E_{osc}^k(k, \beta) + \langle E_{shell}^k(k, \beta) \rangle \quad k = Z, N \quad (2.7)$$

where Identifying E_{osc} with Eq. 2.5,

$$E_{shell}^k(k, \beta) = E_{osc}^k(k, \beta) = \sum_{i=1}^{N_k} \epsilon_i^k(\beta) - \langle E_{shell}^k(k, \beta) \rangle \quad k = Z, N \quad (2.8)$$

where ϵ_i are the single-particle energies of the deformed shell model potential.

b) Pairing corrections

The pairing model used in FRDM is that of the seniority force, pairing force with all matrix elements having the same value, $-G$ treated in the Lipkin-Nogami approximation of the BCS method, $G \equiv G(N, Z, \beta_i)$ where β_i stands for all the deformation parameters. The value of G is determined by first postulating an effective-interaction pairing gap Δ_G , which represents an average trend over all nuclei of the pairing gap, as deduced from the experimentally observed even-odd differences.

c) Wigner term

FRDM employs the following term to correct its tendency to underbind nuclei with $N \approx Z$,

$$E_W(Z, N) = +W \left\{ \begin{array}{l} |I| + \frac{1}{A} \quad N \text{ and } Z \text{ odd and equal} \\ 0 \quad N+Z \text{ otherwise} \end{array} \right\} \quad (2.9)$$

where $I = (N - Z)$.

2.1.2.1.3. Final form of FRDM. Finally in the FRDM, the total potential energy can be written as [18]:

$$E_{pot}(Z, N, \beta) = E_{mac}(Z, N, \beta) + E_{s+p}(Z, N, \beta) \quad (2.10)$$

In an earlier version of 1995 (see [18]) the model contained a total of 31 independent mass related parameters but only 19 were determined by performing a fit over all the nuclei, the remaining ones were obtained by heavy ion scattering data and from measured systematics of single-particle levels [3].

A quantity of interest is the so-called microscopic correction E_{mic} , which is different from the E_{s+p} . For a specific deformation β_i the microscopic correction is given by

$$E_{mic}(Z, N, \beta_i) = E_{s+p}(Z, N, \beta_i) + E_{mac}(Z, N, \beta_i) - E_{mac}(Z, N, \beta_{sphere}), \quad (2.11)$$

which implies that the potential energy E_{pot} of a nucleus at a certain deformation, for example, the ground state deformation β_{gs} , is simply

$$E_{pot}(Z, N, \beta_{gs}) = E_{mac}(Z, N, \beta_{sphere}) + E_{mic}(Z, N, \beta_{gs}) \quad (2.12)$$

2.1.2.1.4. Fitting procedure. In the FRDM mass calculation [18], the potential energy was calculated on a coarse two-dimensional grid in the quadrupole β_2 and hexadecapole β_4 shape parameters, the ground-state (gs) deformations were then determined by interpolation. With the gs values of β_2 and β_4 fixed, the octupole β_3 and hexacontatetrapole β_6 deformation parameters were varied separately and the lowest energy obtained was identified as the ground-state mass. The fits were performed over the set of 1654 nuclei contained in the atomic mass evaluation of 1989 [56] obtained a root mean square deviation (rms) of 0.669 MeV, predicting a total of 8979 nuclei ranging from ^{16}O to $A = 339$ lying between the proton and neutro driplines [18].

In a recent update, Moeller et al. [57] performed the minimisation procedure simultaneously varying the 4 shape parameters ($\beta_2, \beta_3, \beta_4, \beta_6$) to determine the ground-state shape and shell corrections obtaining an rms of 0.570 MeV over the set of 2149 nuclei contained in the atomic mass evaluation of 2003 [47].

2.1.2.2. Weizsäcker-Skyrme mass formula (WS)

Following the same lines of the mac-mic global FRDM, the next mass model to be discussed is a recent mac-mic formula developed by Wang & Liu ([58, 59, 60, 19]), the so-called Weizsäcker-Skyrme mass formula (WS).

2.1.2.2.1. Macroscopic sector. The Weizsäcker-Skyrme mass formula (WS) contains a LDM with a slightly modified Coulomb, pairing and asymmetry energy coefficients (for more details see [58, 59, 60]) and a Wigner like term (see [19]). In order to go beyond the LDM description of the nucleus, they employ a Skyrme energy density functional to incorporate the deformation, but only considering axially deformed cases

$$E_{mac}(Z, N, \beta) = E_{LDM}(Z, N) \prod_{k \geq 2} (1 + b_k \beta_k^2) \quad (2.13)$$

The trick is to recognise that there is a dependance of the β_k multipolarities on the mass number A . Given a density functional $\rho(\mathbf{r})$, one can calculate the corresponding energy via $E(\beta_k) = \int \mathcal{H}[\rho(\mathbf{r})] d\mathbf{r}$ under the extended Thomas-Fermi approximation. At first the negative value of the binding energy, $E(\beta = 0)$, is computed, using a spherical Wood-Saxon density distribution [61]. Afterwards, $E(\beta_k)$ is calculated, using a β_k deformed Wood-Saxon density distribution. Finally, using the following relation,

$$E(\beta_k)/E(\beta_0) = 1 + b_k \beta_k^2, \quad (2.14)$$

where the coefficients, b_k , can be approximately described by the following empirical formula[58]:

$$b_k = \left(\frac{k}{2}\right) g_1 A^{1/3} + \left(\frac{k}{2}\right)^2 g_2 A^{-1/3}, \quad (2.15)$$

This form of mass dependence of b_k is therefore adopted in the proposed mass formula and the optimal values of g_1 and g_2 are finally determined by the 2149 measured nuclear masses [47]. In this way a lot of computational time is saved at the time of the calculation of deformed nuclei.

2.1. NUCLEAR MASS MODELS

2.1.2.2.2. Microscopic sector. In their microscopic sector the shell corrections are obtained by the traditional Strutinsky procedure [49, 50], but this time they consider the shell corrections of a nucleus E_{sh} and the shell correction of its mirror nucleus E'_{sh} as follows [60]

$$\Delta E(Z, N, \beta) = c_1 E_{sh}(Z, N, \beta) + |I| E'_{sh}(Z, N, \beta), \quad (2.16)$$

the shell energy of a nucleus is computed at the same deformation of its mirror nuclei.

Some other residual corrections caused by the microscopic shell effect are written as a sum of three terms [19]

$$\Delta_{res}(Z, N) = \Delta_M(Z, N) + \Delta_p(Z, N) + \Delta_T(Z, N) \quad (2.17)$$

The first term, $\Delta_M(Z, N)$, further considers the mirror nuclei effect [60]. The second term, $\Delta_p(Z, N)$, considers the residual pairing corrections of nuclei, which may be phenomenologically given by the pairing gaps [19]. The third term, $\Delta_T(Z, N)$, accounts the influence of triaxial (or tetrahedral) deformation [60].

2.1.2.2.3. Final form. Finally in the WS mass formula, the total energy of a nucleus can be written as follows [19]:

$$\begin{aligned} E(Z, N, \beta) = -BE(Z, N, \beta) &= E_{mac}(Z, N, \beta) + \Delta E(Z, N, \beta) + \Delta_{res}(Z, N) \\ &= E_{LDM}(Z, N) \prod_{k \geq 2} (1 + b_k \beta_k^2) + \Delta E(Z, N, \beta) \\ &+ \Delta_M(Z, N) + \Delta_p(Z, N) + \Delta_T(Z, N) \end{aligned} \quad (2.18)$$

Their final expression contains only 16 parameters, and provides a root mean square deviation (RMS) of 336 keV [19] for the 2149 nuclei included in the atomic mass evaluation of 2003 [47]. Finally Wang & Liu [62] have improve the predictive power of their nuclear masses using image reconstruction techniques ([63]) but this time by using a radial basis function (for more details see [64, 65]) and the Garvey Kelson procedure ([66, 67, 68]), obtaining a RMS smaller than 200 keV for the fit of the 2149 measured nuclei and successfully satisfying the reliability tests introduced in [3] and [69].

2.1.3. Skyrme-Hartree-Fock-Bogoliubov (HFB) mass formulas

The HFB method, provides a generalized single-particle theory that unifies Hartree-Fock and BCS[33, 34]. It thus can be used to describe aspects of deformations (i.e. long range part of nucleon-nucleon force) as well as pairing correlations due to short ranged attraction [29]. HFB models have succeeded in going through the root mean square deviation, RMS~1 MeV barrier, which until very recently seemed unsurmountable, and have achieved RMS deviations smaller than 0.6 MeV [38]. The starting point of all their calculations is to choose a particularly suitable form of an effective force. In fact, the force used in the Hartree-Fock-Bogoliubov (HFB) mass model is an extended Skyrme force (containing t_4

and t_5 momentum dependent terms) ([39, 40, 41, 42, 43, 44]):

$$\begin{aligned}
 v_{ij} = & t_0(1 + x_0 P_\sigma) \delta(\mathbf{r}_{ij}) + t_1(1 + x_1 P_\sigma) \frac{1}{2\hbar^2} \times [p_{ij}^2 \delta(\mathbf{r}_{ij}) + H.c.] \\
 & + t_2(1 + x_2 P_\sigma) \frac{1}{\hbar^2} \mathbf{p}_{ij} \cdot \delta(\mathbf{r}_{ij}) \mathbf{p}_{ij} + \frac{1}{6} t_3(1 + x_3 P_\sigma) p^\gamma \delta(\mathbf{r}_{ij}) \\
 & + t_4(1 + x_4 P_\sigma) \frac{1}{2\hbar^2} \times [p_{ij}^2 \rho(\mathbf{R}_{ij}) \delta(\mathbf{r}_{ij}) + H.c.] \\
 & + t_5(1 + x_5 P_\sigma) \frac{1}{\hbar^2} \mathbf{p}_{ij} \cdot \delta(\mathbf{r}_{ij}) \mathbf{p}_{ij} \rho(\mathbf{R}_{i,j}) \\
 & + \frac{i}{\hbar^2} W_0 (\boldsymbol{\sigma}_i + \boldsymbol{\sigma}_j) \cdot \mathbf{p}_{ij} \times \delta(\mathbf{r}_{ij}) \mathbf{p}_{ij},
 \end{aligned} \tag{2.19}$$

In addition a 4-parameter delta-function pairing force adjusted to reproduce realistic N-N and 3N forces calculations of infinite nuclear and neutron matter [38, 45] is included. Pairing correlations are introduced in the framework of the Bogoliubov method. Deformations with axial and left-right symmetry are admitted. Finally, in their latest version a Wigner correction (2 additional parameters) is incorporated. The total binding energy is given by:

$$E_{tot} = E_{HFB} + E_W, \tag{2.20}$$

where, E_{HFB} is the HFB binding energy including a cranking correction to the rotational energy and a phenomenological vibration correction energy. The final parameter set, labelled BSk21, is determined by constraining the nuclear-matter symmetry coefficient to $J=30$ MeV and the isoscalar effective mass to $M_s^*/M=0.8$. Their latest mass table, from now on referred as HFB-21 [46] was fitted to the set of nuclei contained in the atomic mass evaluation of 2003 [47] with a remarkable root mean square deviation, $RMS = 0.577$ MeV. Finally, they predicted a total of 8389 nuclei with $Z, N \geq 8$ and $Z \leq 110$ lying between the proton and neutron driplines. For more details the reader is referred to [48].

2.1.4. Duflo-Zuker mass formula (DZ)

The Duflo-Zuker mass formula (from now on DZ) is a shell model inspired mass model. The DZ mass model provides an attractive combination of simplicity and microscopic components. Since its initial formulation [70, 71, 20], there have been efforts to communicate its philosophy [72, 73]. There are two versions available in the market, the one with 31 parameters (from now on DZ31) and its simplest version with 10 parameters (from now on DZ10). The last one contains the basic ingredients and still has an acceptable $RMS \approx 600$ KeV. Due to its relevance for the present work, in what follows we present a brief description of its simplest version, starting from its building blocks. For the interested reader a detailed analysis is available in [74].

The DZ mass model, is a functional of the shell occupancies that proceeds on the possibility to guess the form of the solutions of a many body Schrödinger equation, assuming perfect potentials that reproduce the data. There are four ingredients [75]:

- A) A monopole part in charge of correct LDM asymptotics and produces at the same time shell effects i.e., Harmonic Oscillator (HO) closures. To achieve this, DZ borrows from the realistic interactions a “master term” (see section 2.1.4.2) that leads to the bulk energy of nuclear matter and to HO closures (see section 2.1.4.1).

2.1. NUCLEAR MASS MODELS

- B) A mechanism that transforms HO closures into the observed Extruder-Intruder (EI) ones. To fix ideas: the HO closures at $N, Z = 40, 70$ associated to the g_{ds} shell of principal quantum number $p = 4$ must transform into (extruder-intruder, EI) closures at $N, Z = 50, 82$ by replacing the extruded $g_{9/2}$ shell by the $h_{11/2}$ intruder from the $p = 5$, h_{pf} shell. We have no rigorous information about the mechanism that effects the HO-EI transition (see section 2.1.4.3) to the observed closures at $N, Z = 28, 50, 126$ and $184(?)$. The present consensus is that it must involve three body forces [74, 76, 77].
- C) Correlation terms that simulate configuration mixing in the EI spaces defined by the monopole part. They contain a three-body contribution that should probably be ascribed to B). They are crucial but poorly understood as they owe as much to luck as to physical insight. They are extensively discussed in [74]. They have no counterpart in FRDM [18] and HFB21 [46].
- D) Terms that describe strongly deformed nuclei, They demand going beyond the EI spaces through a mechanism vindicated by later work [78, 72].

2.1.4.1. Master terms. Asymptotic behaviour

In their original paper Duflo and Zuker [20] assumed (guessed) that realistic two body interactions generate two collective terms (see Eq. 2.21, from now on Master terms) solely responsible for the leading liquid drop contributions. The same result can be obtained, assuming N nucleons occupying a series of levels whose energy separation is characterised by $\hbar\omega$, the energy should go as:

$$M_A = \frac{\hbar\omega}{\hbar\omega_0} \left(\sum_p \frac{m_p}{\sqrt{D_p}} \right)^2, \quad M_T = \frac{\hbar\omega}{\hbar\omega_0} \left(\sum_p \frac{t_p}{\sqrt{D_p}} \right)^2 \quad (2.21)$$

where $\hbar\omega \approx 40A^{-1/3}$ is the harmonic oscillator frequency [79], $\hbar\omega_0$ is left as a free parameter, $D_p = (p+1)(p+2)$ is the degeneracy (size) of the major Harmonic Oscillator (HO) shell of principal quantum number p , $m_p = n_p + z_p$, $t_p = n_p - z_p$, where n_p, z_p are number operators for neutrons and protons respectively. In what follows, a method to obtain the asymptotic values for the master terms M_A and M_T is discussed. Replacing $\hbar\omega/\hbar\omega_0$ by the scaling factor $1/\rho$. Using Boole's notation, i.e., $p^{(3)} \equiv p(p-1)(p-2)$ and summing up to the neutron (proton) Fermi shell p_{f_v} (p_{f_π}) which will be associated with the total number of neutrons N (protons Z) [79] we obtain:

$$\begin{aligned} N &= \sum_{p=0}^{p_{f_v}} n_p = \sum_{p=0}^{p_{f_v}} D_p = \sum_{p=0}^{p_{f_v}} (p+1)(p+2) \\ &= \frac{(p_{f_v} + 3)^{(3)}}{3} \approx \frac{(p_{f_v} + 2)^3}{3} \\ \implies p_{f_v} + 2 &\approx (3N)^{1/3}. \text{ analogously } p_{f_\pi} + 2 = (3Z)^{1/3} \end{aligned} \quad (2.22)$$

Approximating $\sqrt{D_p} \approx p + 3/2$, leads to

$$\begin{aligned} \sum_p^{p_{f_v}} \frac{n_p}{\sqrt{D_p}} &= \sum_p^{p_{f_v}} \sqrt{D_p} \approx \sum_p^{p_{f_v}} \left(p + \frac{3}{2}\right) \\ &= \frac{p_{f_v}(p_{f_v} + 4)}{2} + \frac{3}{2} \approx \frac{(p_{f_v} + 2)^2}{2}, \end{aligned} \quad (2.23)$$

introducing the operator M_N as the master term for neutrons,

$$\begin{aligned} M_N &\equiv \frac{1}{\rho} \left(\sum_{p=0}^{p_{f_v}} \frac{n_p}{\sqrt{D_p}} \right)^2 \\ &\approx \frac{(p_{f_v} + 2)^4}{4\rho} \approx \frac{(3N)^{4/3}}{4A^{1/3}} \text{ analogously } M_Z \approx \frac{(3Z)^{4/3}}{4A^{1/3}}, \end{aligned} \quad (2.24)$$

using M_N and M_Z one can rewrite eq. (2.21),

$$M_A \equiv M_N + M_Z + 2\sqrt{M_N}\sqrt{M_Z}, \quad M_T \equiv M_N + M_Z - 2\sqrt{M_N}\sqrt{M_Z}. \quad (2.25)$$

Proceeding with the calculation for M_A ,

$$\begin{aligned} M_A &= \frac{3^{4/3}}{4A^{1/3}} \left[N^{4/3} + Z^{4/3} + 2(NZ)^{2/3} \right] \\ &= \frac{3^{4/3}A}{4} \left[\left(\frac{N}{A}\right)^{4/3} + \left(\frac{Z}{A}\right)^{4/3} + 2\left(\frac{NZ}{A^2}\right)^{2/3} \right], \end{aligned} \quad (2.26)$$

introducing the following variables $\eta = \frac{N}{A} = \frac{1+\tau}{2}$ and $\zeta = \frac{Z}{A} = \frac{1-\tau}{2}$, where $\tau = \eta - \zeta = \frac{t}{A}$ and $1 = \eta + \zeta$. Eq. (2.26) in terms of the new variable τ is equal to

$$M_A = \frac{1}{4} \left(\frac{3}{2}\right)^{4/3} A \left[(1+\tau)^{4/3} + (1-\tau)^{4/3} + 2(1-\tau^2)^{2/3} \right]. \quad (2.27)$$

Expanding in taylor series up to the second order in τ , the leading asymptotic estimates become

$$M_A \asymp \left(\frac{3}{2}\right)^{4/3} A \left[1 - \frac{2}{9}\tau^2 \right]. \quad (2.28)$$

Following the same procedure,

$$M_T \asymp \left(\frac{3}{2}\right)^{4/3} A \left[\frac{2}{3}\tau \right]^2. \quad (2.29)$$

It is remarkable that $M_A \asymp A$ up to a small correction in τ , in other words the two collective terms ($M_A + M_T$) are solely responsible for the leading LD contributions.

2.1. NUCLEAR MASS MODELS

2.1.4.2. Origin of the master terms. Scaling

The Hamiltonian is written as:

$$H = K + \frac{1}{2} \sum_{rstu} W_{rstu}^{JT} Z_{rsJT}^\dagger \cdot Z_{tuJT} + \dots = H_m + H_M, \quad (2.30)$$

where K is the kinetic energy, W_{rstu}^{JT} represent the two-body interaction matrix elements, $Z_{a\Gamma}^\dagger (Z_{a\Gamma})$ create (annihilate) pairs ($a \equiv rs$) of particles in orbits a , coupled to $\Gamma = JT$.

For illustrative purposes in the discussion that follows, we are going to constrain H only to a two-body interaction. Following [72, 85], the strategy is to define a good unperturbed monopole Hamiltonian, H_m , which contains K and all quadratic forms in the scalar products of operators in $\Omega \equiv \hat{m}(\hat{t})$ for number operator (isospin operator), while the multipole Hamiltonian, H_M contain the rest. Starting with a set of matrix elements in an isospin representation

$$W_{rstu}^{JT} = V_{rstu}^{JT} - \delta_{rt} \delta_{su} V_{rs}^T \quad (2.31)$$

from which the centroids have been extracted

$$V_{rs}^T = \frac{\sum_J V_{rsrs}^{JT} (2J+1) [1 - (-)^{J+T} \delta_{rs}]}{(2j_r+1)(2j_s+1) [1 - (-)^T \delta_{rs}]} \quad (2.32)$$

In the neutron-proton representation (np) scheme each orbit r goes into two r_n and r_p and the centroids can be obtained through ($x, y = n$ or p , $x \neq y$)

$$V_{r_x r_y} = \frac{1}{2} \left[V_{rs}^1 \left(1 - \frac{\delta_{rs}}{2j_r+1} \right) + V_{rs}^0 \left(1 + \frac{\delta_{rs}}{2j_r+1} \right) \right] \quad (2.33)$$

$$V_{r_x s_x} = V_{rs}^1. \quad (2.34)$$

H_m has a diagonal part, H_m^d , given by

$$H_m^d = K^d + V_m^d = K^d + \frac{1}{2} \sum_{x,\alpha} V_{x\alpha} \Omega_x^\dagger \cdot \Omega_\alpha, \quad (2.35)$$

in an isospin representation, H_m^d can be written in terms of quadratic forms in $\Omega \equiv \hat{m}(\hat{t})$ for number operator (isospin operator),

$$H_{mJT}^d = K^d + \sum_{s \leq t} (a_{rs} m_{rs} + b_{rs} T_{rs}) \quad (2.36)$$

where

$$m_{rs} = \frac{1}{1 + \delta_{rs}} m_r (m_s - \delta_{rs}), \quad (2.37)$$

$$T_{rs} = \frac{1}{1 + \delta_{rs}} \left(T_r \cdot T_s - \frac{3}{4} m_r \delta_{rs} \right), \quad (2.38)$$

for a detailed discussion concerning to derivations, the interested reader is referred to [80, 72].

In order to investigate the microscopic derivation of the master term, the key step involves reduction to a sum of factorable forms valid for any interaction [80].

$$\sum_{x,\alpha} V_{x\alpha} \Omega_x \cdot \Omega_\alpha = \sum_{\mu} E_{\mu} \left(\sum_k \Omega_k U_{k\mu} \sum_{\beta} \Omega_{\beta} U_{\beta\mu} \right), \quad (2.39)$$

where V are symmetric matrices diagonalized by unitary transformations U and $\Omega \equiv \hat{m}(\hat{t})$ for isoscalar (isovector) number operators. As an example, consider the result of diagonalizing the isoscalar monopole interaction for the first 8 major oscillator shells for the chiral N3LO interaction [81] regulated by the V_{lowk} procedure [82]. There are 36 subshells and as many eigenvalues. One of them turns out to be strongly dominant. Within a very good approximation its value is proportional to $\hbar\omega \equiv 1/\rho \approx A^{1/3}$ and its eigenvector is independent of it. In [72], it is shown that the calculated amplitudes, $U_{p\mu}$, turns out to be proportional to $D_p^{-1/2}$.

2.1.4.3. The HO-EI transition

In DZ implementations [20] the combination $M \rightarrow M_A + M_T$ is employed, explicitly

$$M = \frac{1}{2A^{1/3}} \left[\left(\sum_{p=0}^{p_f} \frac{m_p}{\sqrt{D_p}} \right)^2 + \left(\sum_{p=0}^{p_f} \frac{t_p}{\sqrt{D_p}} \right)^2 \right], \quad (2.40)$$

The M term raises one of the outstanding problems in nuclear physics: realistic interactions fail to produce the observed closures [77]. Fig.2.2a, indicates what has to be done: "change the harmonic oscillator closures (HO) at $N, Z=8, 20, 70, \dots$, into the observed extruder-intruder (EI) ones at $N, Z=28, 50, 82$ and 126 ".

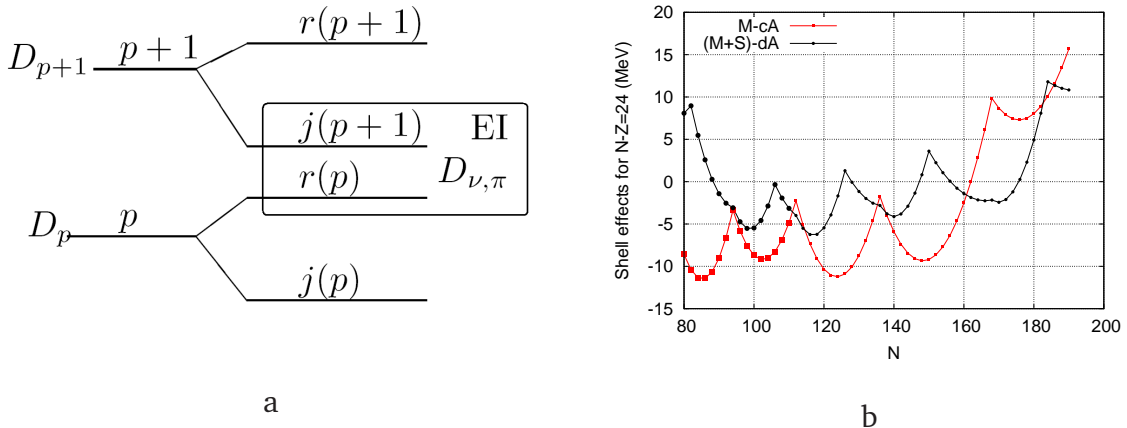


Figure 2.2: (a) Harmonic oscillator and extruder-intruder (EI) shells. (b) The evolution from HO (dots) to EI (squares) shell effects for $N - Z = 24$. Heavier marks for existing data.

The only relevant operators must separate orbit $j(p)$ of degeneracy $D_{j(p)} = 2(p+1)$ from its partners $r(p)$ of degeneracy $D_{r(p)} = p(p+1)$. The only one body operators that cancel at the harmonic oscillator closures and therefore give no asymptotic LD contribution are:

$$s_{\nu p} = \left[\frac{pn_{j_p} - 2n_{r_p}}{2(p+1)} \right], \quad s_{\pi p} = \left[\frac{pz_{j_p} - 2z_{r_p}}{2(p+1)} \right], \quad (2.41)$$

2.1. NUCLEAR MASS MODELS

the great merit of Jean Duflo was to introduce sophisticated combinations of Eq. (2.41), namely:

$$\begin{aligned}
 S_v &= \sum_p^{p_v} s_{vp} \frac{p^2 + 4p - 5}{\sqrt{D_p}(p+2)} + \sum_p^{p_v} n_p s_{vp} \frac{p^2 - 4p + 5}{D_p(p+2)}, \\
 S_\pi &= \sum_p^{p_\pi} s_{\pi p} \frac{p^2 + 4p - 5}{\sqrt{D_p}(p+2)} + \sum_p^{p_\pi} z_p s_{\pi p} \frac{p^2 - 4p + 5}{D_p(p+2)}, \\
 S &= \frac{S_v + S_\pi}{A^{1/3}},
 \end{aligned} \tag{2.42}$$

which leads to the remarkable result in Fig 2.2b (the choice of the $N - Z = 24$ is arbitrary):

- The HO closures are practically erased to give way to EI ones.
- The peaks, from left to right, correspond to $N = 82$, $N = 106(Z = 82)$, $N = 126$, $N = 150(Z = 126)$ and $N = 184$.

2.1.4.4. Macroscopic sector

Six terms define the macroscopic contribution to the energy (minus the binding energy):

$$\langle H_m \rangle = a_1 (M + S) - a_2 \frac{M}{A^{1/3}} - a_3 V_C - a_4 V_T + a_5 V_{TS} + a_6 V_p. \tag{2.43}$$

The last four terms have very much the usual LD except for some refinements. The pairing term goes as $1/\rho \approx A^{-1/3}$ and has also a correction in $T/A = |N - Z|/2A$ for even number of protons. It mocks the quenching (anti-pairing) effect due to Coulomb [74].

2.1.4.5. Microscopic sector

The EI spaces defined by the macroscopic (macro) sector are treated as model spaces in which to perform Shell Model calculations. To this we must add the effect of spherical correlations (correlations should cancel at shell closures). In [71] it is shown how to invoke perturbation theory or coupled cluster theory and average to obtain terms of type

$$\frac{m_v \bar{m}_v}{D_v A^{1/3}}, \quad \frac{m_v \bar{m}_v (m_v - \bar{m}_v)}{D_v^2 A^{1/3}}, \quad \frac{m_v^{(2)} \bar{m}_v^{(2)}}{D_v^3 A^{1/3}} \tag{2.44}$$

using the notations $m_v^{(2)} = m_v(m_v - 1)$ and $\bar{m}_v = D_v - m_v$ (representing holes) to write the form of the possible contributions in a valence space v of degeneracy D_v , the denominators are chosen so as to ensure correct $A^{1/3}$ scalings. The microscopic contributions are estimated including 3-body and 4-body terms evaluated with the spherical occupation numbers, with a 4-body term evaluated employing the deformed occupancies.

2.1.4.6. Spherical nuclei

For the spherical nuclei, the 3-body term is

$$s_3 = \frac{1}{A^{1/3}} \left[\frac{n_v \bar{n}_v (n_v - \bar{n}_v)}{D_v} + \frac{n_\pi \bar{n}_\pi (n_\pi - \bar{n}_\pi)}{D_\pi} \right], \tag{2.45}$$

and the 4-body term is

$$s_4 = \frac{1}{A^{1/3}} \left[2^{(\sqrt{n_p} + \sqrt{z_p})} \cdot \left(\frac{n_\nu \bar{n}_\nu}{D_\nu} \right) \cdot \left(\frac{n_\pi \bar{n}_\pi}{D_\pi} \right) \right], \quad (2.46)$$

The spherical contributions to the binding energies are then

$$\langle H_s \rangle = a_7 s_3 - a_8 \frac{s_3}{A^{1/3}} + a_9 s_4. \quad (2.47)$$

2.1.4.7. Deformed nuclei

The deformation is associated with the promotion of four neutrons and four protons to the next major shell *provided* both of them lie in the normal parity r -orbits, the last statement is something that can be seen from Nilsson diagrams as pointed out in [71]. The loss of macroscopic (monopole) energy is upset by the gain due to the quadrupole force, simulated by a specific quartic term. Calling generically $n' = n - 4$, the operator in charge of deformation is

$$d_4 = \frac{1}{A^{1/3}} \left[\left(\frac{n'_\nu \bar{n}'_\nu}{D_\nu^{3/2}} \right) \cdot \left(\frac{n'_\pi \bar{n}'_\pi}{D_\pi^{3/2}} \right) \right], \quad \langle H_d \rangle = a_{10} d_4. \quad (2.48)$$

2.1.4.8. Final form

In order to compute the energy (minus the binding energy), two calculations are made for each nucleus. Both include the macroscopic contribution plus either the spherical terms or the deformed one.

$$E_{DZ} = \langle H_m \rangle + \langle H_s \rangle \quad \text{if } Z < 50$$

$$E_{DZ} = \langle H_m \rangle + \max(\langle H_s \rangle, \langle H_d \rangle) \quad \text{if } Z \geq 50 \quad (2.49)$$

Despite of its simplicity, DZ10 reproduces the 2353 nuclei contained in the latest atomic mass evaluation (AME12 [32]) with a RMS deviation of 585 keV. The version with 31 parameters (DZ31) has a RMS deviation of around 390 keV.

2.2. Exploring systematics

In order to understand the current status of the available data for nuclear masses and those needed to perform nucleosynthesis calculations, we display the nuclear landscape (N-Z plane), in Fig. 2.3. The plot shows all the experimentally available nuclear masses (lime color dots) plus all those predicted by theoretical models (yellowed region), as a function of neutron number N (proton number Z) on the x axis (on the y axis). To guide the eye, lines are included and located at the position of the magic numbers (N,Z= 8,14,28,50,82,126,184). The aforementioned plot will be a frequently used tool along this chapter. In such plot each square represents a nucleus, the valley of stability is shown by red boxes, as you move away from such valley, the nuclei begin to get more and more unstable, up to the point when either protons or neutrons will become completely unbound. The point where this happens is known as the nuclear drip line (blue boxes in fig. 2.3), because it is as if the extra nucleons drip right off the nucleus. The drip lines are model dependent, and for their determination one computes the one neutron (proton) separation

2.2. EXPLORING SYSTEMATICS

energy $S_n(Z, N)$ ($S_p(Z, N)$) which is defined as the amount of energy required to remove a neutron (proton) from the nucleus:

$$S_n(Z, N) = BE(Z, N) - BE(Z, N - 1), \quad S_p(Z, N) = BE(Z, N) - BE(Z - 1, N). \quad (2.50)$$

In other words, the neutron (proton) drip lines are defined such that $S_n(Z, N) > 0$ ($S_p(Z, N) > 0$).

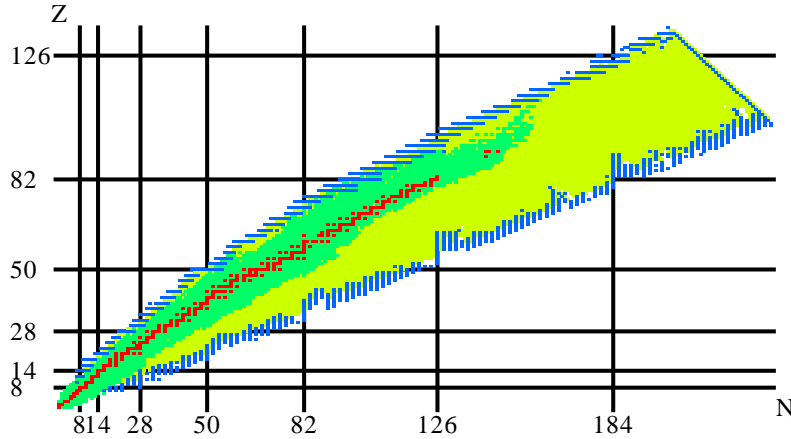


Figure 2.3: Nuclear Landscape for the binding energies. The lime color area corresponds to the measured nuclei taken from [32], the yellow region represents extrapolations based on the Finite Range Drop Model (FRDM) [18] up to its drip lines (blue boxes). The red boxes denote the valley of stability.

2.2.1. Tests of reliability

In the first part of this chapter, the theoretical foundations of a number of models for the calculation of ground state properties of nuclei in particular their nuclear masses had been discussed, what remains to be done is to compare them with the available experimental information. Starting from this section a number of systematic studies are going to be performed over the different set of nuclear mass models to be explored in the present work. The root mean square deviation (RMSD from now on) has been often used as the criterium to establish the error model, which in the case of the nuclear masses is given by:

$$RMSD = \sqrt{\frac{1}{n} \sum_{i=1}^n (\Delta_i(Z, N))^2}, \quad \Delta_i(Z, N) = BE_i^{exp}(Z, N) - BE_i^{th}(Z, N), \quad (2.51)$$

where $BE_i^{exp}(Z, N)$ is the corresponding binding energy taken from the latest atomic mass evaluation [32], $BE_i^{th}(Z, N)$ is the calculated theoretical binding energy, $\Delta_i(Z, N)$ represent the residuals or errors between the measured binding energies and those computed by the theoretical model and n is the number of nuclei with already measured mass values.

The AME95-03 test was introduced in [3] to test the ability of nuclear mass models to extrapolate. The test consisted in fitting the subset of nuclei with measured masses in the Atomic mass evaluation of 1995 (AME95)[83] and predict the new available nuclei included in the compilation of 2003 (AME03)[47]. In this work we present an upgraded version of the same to be denoted as the AME03-12 test, because instead of using the set

of nuclei based on AME95 (AME03) we are going to use the nuclei from AME03 (AME12). In all cases, the full set consists of the measured nuclear masses taken from the latest Atomic mass evaluation from 2012 (AME12)[32]. This set is then partitioned in two, one is used to fit the model parameters (In the case of FRDM [18], the model parameters were adjusted to the AME95 compilation [83]) and the remainder to compare measured masses with those predicted by extrapolation. The following models are analysed:

- Finite range drop model (FRDM [18]).
- Hartree-Fock-Bogoliubov (HFB21 [46]).
- Skyrme-Weisäcker model (WS3 [19]).
- Duflo-Zuker mass formula with 10 parameters (DZ10 [84]).
- Duflo-Zuker mass formula with 31 parameters (DZ31 [20]).

2.2.1.1. Results

Table 2.2, shows the comparison of the RMSD for the fit and prediction of the different mass models to be explored in this thesis. The first thing to be stressed is that all the models have a good agreement with the measured values ($\text{RMSD} < 0.7 \text{ MeV}$) for the fitted 2149 nuclei taken from AME03 [47] (blue region in Fig 2.4). Secondly by comparing the predictions over the new 219 nuclei included in AME12 [32] (red region in Fig 2.4), only the WS3 model [19] presents a $\text{RMSD} < 0.5 \text{ MeV}$, in the rest of the models the RMSD grows significantly. In particular, in the Duflo-Zuker models [20, 84] the RMSD increases by 300 keV. If we compare the two latest compilations (see column 2 and 4) the RMSD are comparable.

Table 2.2: RMSD in MeV, for the fits and predictions for different mass models.

MODEL	fit	prediction	full set
FRDM	0.655	0.765	0.666
HFB21	0.576	0.646	0.584
WS3	0.336	0.424	0.345
DZ10	0.551	0.880	0.588
DZ31	0.363	0.665	0.400

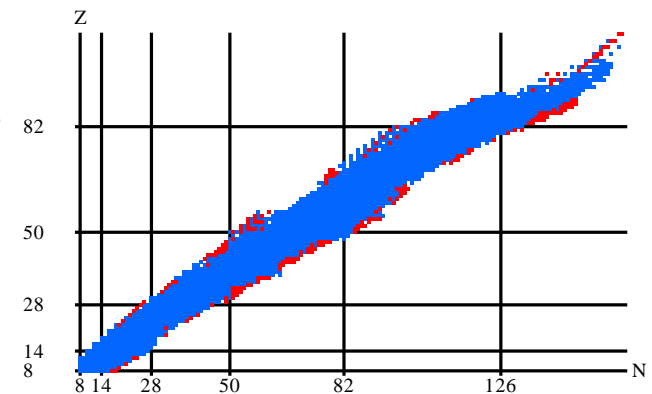


Figure 2.4: Set of nuclei used for the reliability test. The blue region represent the fitted ones and red dots the predicted ones.

2.2.1.2. Remarks

Before proceeding to the next sections, It is worth to mention that some models used in the present work share certain features by construction. For instance the two different versions of Duflo-Zuker, differ mostly in their treatments of the deformation (see section 2.1.4.5) and the transition from harmonic oscillator closures to the Extruder-Intruder ones, i.e.,

2.2. EXPLORING SYSTEMATICS

the so called HO-EI transition (see section 2.1.4.3). In its simplest version (DZ10) there is only one term to consider the deformation. It is remarkable that DZ10 has a RMSD of 550 keV however at the time of the extrapolation its RMS increases to 880 keV. The WS3 mass model shares the same philosophy with FRDM in the sense that both of them are macroscopic-microscopic approaches (a liquid drop model + shell corrections) however their treatment of pairing and deformation differ significantly. On the one hand FRDM considers pairing corrections treated in the Lipkin-Nogami variation of the BCS method (see section 2.1.2.1.2) and the deformation parameters come from a full energy minimisation (see section 2.1.2.1.3). On the other hand WS3 considers the same treatment of the pairing as in the Duflo-Zuker model [20] and it considers a semi-empirical treatment of deformation (see section 2.1.2.2.1). The WS3 mass model, with a RMSD=424 KeV for the most recent masses, turns out to be the most reliable one to perform extrapolations.

2.2.2. Global trends

Once one has understood the importance of theoretical models for the prediction of the nuclear masses, the next step is to establish their strengths and weaknesses when compared not only to the measured information but also between themselves. The RMSD is not the bottom line when judging the reliability of a given theoretical model to predict the binding energies of nuclei, another way to get some insight, is by :

- Exploring the pattern of the residuals, $\Delta_i(Z, N)$, as defined in Eq. 2.51.
- Study systematic trends in relative quantities like the so called shell corrections (SC) defined as,

$$SC(Z, N) = BE_{th}(Z, N) - BE_{LDM}(Z, N), \quad (2.52)$$

i.e., differences between a theoretical model, when referred to a liquid drop (LDM) like model, as there is no unique nor a universal liquid drop model. In the present work we choose to use the following version of the LDM given by [85]):

$$BE_{LDM}(Z, N) = 15.5A - 17.8A^{2/3} - 28.6 \frac{4T(T+1)}{A} + 40.2 \frac{4T(T+1)}{A^{4/3}} - 0.7 \frac{Z(Z-1)}{A^{1/3}}, \quad (2.53)$$

where the mass number is given by $A = Z + N$ and the isospin by $T = |N - Z|/2$.

- Analysing relative quantities between the model itself, like the one-neutron and two-neutrons separation energies, S_n and S_{2n} respectively,

$$S_{2n}(Z, N)/2 = [BE(Z, N) - BE(Z, N - 2)]/2, \quad (2.54)$$

the one-neutron separation energy S_n is defined in Eq. 2.50, in the case of the two-neutrons separation energies S_{2n} , we have divided this quantity by 2.

These patterns reflect global features missed or artificially introduced by a model and are useful for understanding the theoretical extrapolations to regions far away from the measured data.

2.2.3. Residuals patterns

The systematics behind the residual patterns for a number of mass models used in the present work when compared to the latest Atomic Mass Evaluation (AME12 [32]) are shown on the left hand side panels in Fig. 2.5. We have decided to display the results on a landscape using a color code bar with fixed lower and upper limits, allowing for easier comparison. The main similarity shared between most of the models is that their largest discrepancies when compared with measured nuclei occur in regions around the mid shell closures, in particular at $N \approx 70$ and $N \approx 90$ (see lime and red color spots on the left hand side of Fig. 2.5). Figure 2.5a displays the residual pattern for the case of FRDM. The largest discrepancies occur in the region of the lightest nuclei ($A < 60$). Nuclei around $N \approx 70$ and $N \geq 130$ are underbound (see red color spots on Fig. 2.5a), the opposite is true for nuclei around $N \approx 90$ (see lime color spots on Fig 2.5a) in both regions odd-even effects are observed (jumps in the residuals pattern on Fig 2.5a). Figure 2.5c shows the residual pattern for the case of HFB21. The pairing fluctuations can be seen everywhere on the landscape. Regions right after the neutron magic number $N=50, 82, 126$ and their corresponding mid shell closures in Z are underbound (see red color spots on Fig. 2.5c). The opposite is true for regions around $N \geq 70, N \approx 90$ and $Z \geq 70$ (see lime color spots on Fig 2.5c). The residual pattern corresponding to DZ10 is shown in Fig. 2.5e. Most of the nuclei in the neutron-deficient side in the region $40 < Z < 82$ and some nuclei around the mid shell closures are underbound (see red color spots on Fig 2.5e). In addition, DZ10 tends to produce overbind nuclei with $N \approx 70$ (see lime color spots on Fig 2.5e) and the pairing fluctuations appear around $N \approx 40, 70, 90$. For DZ31 (see Fig. 2.5g) and WS3 (see Fig. 2.5i), which are the most precise models when fitting all available measured masses (see table 2.2), it is difficult to describe a clear trend, because most of the residuals are fluctuating around 0. As DZ31 and WS3 have the same description of pairing than DZ10, the pairing fluctuation are expected to occur for the same regions than in DZ10. For the sake of comparison, on the right hand side of Fig. 2.5, we also display the residuals between the two-neutron separation energies (S_{2n}) for a number of theoretical models. The largest discrepancies (reddish and yellowish regions) occur right before and after the neutron shell closures. In particular among the different models explored in the present work, FRDM present the largest discrepancies. The region $N \sim 90$ turns out to be the region in which all models differ the most between each other, because the onset of deformation. Additionally, Table 2.3 shows the number of predicted nuclei contained in various intervals in the one-neutron separation energy S_n for a number of mass models. The considered intervals are: $0 < S_n < 2$, $2 < S_n < 4$ and $S_n > 4$. The total number of nuclei between the driplines is also displayed. To fix ideas, a recent paper exploring the limits of the nuclear landscape [86] via the nuclear density functional theory (DFT) [87], predicts a total number of 6900 ± 500 nuclei with $Z \leq 120$ bound to proton and neutron emission.

Table 2.3: Number of nuclei predicted in various intervals of the one-neutron separation energy S_n for all mentioned number of mass models

MODEL	$0 < S_n < 2$	$2 < S_n < 4$	$S_n > 4$	driplines
FRDM	1606	1776	4066	7448
HFB21	1718	1681	3495	6894
WS3	1993	2077	4149	8219
DZ10	1789	2054	4662	8505
DZ31	1768	2171	4640	8579

2.2. EXPLORING SYSTEMATICS

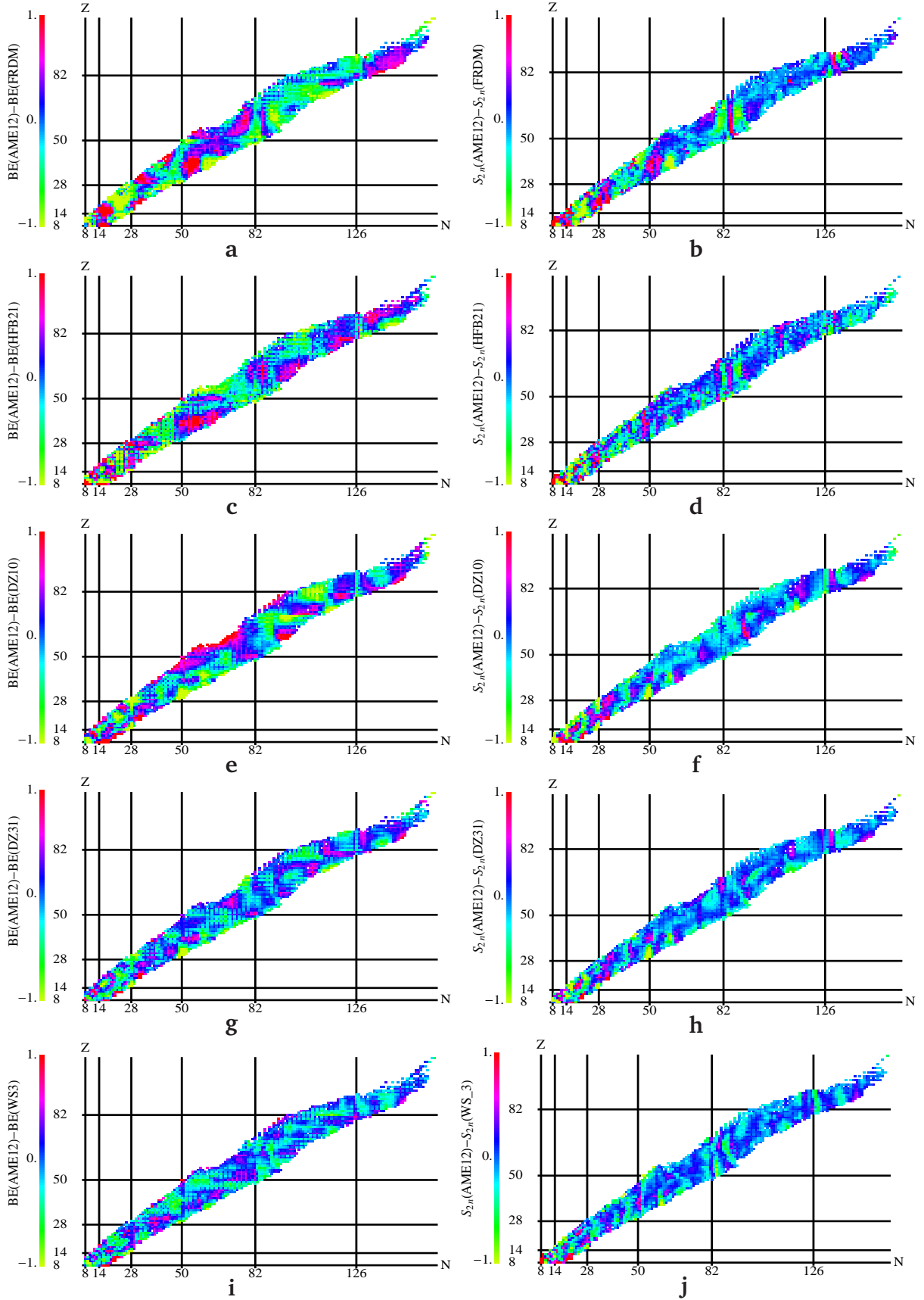


Figure 2.5: Residuals differences between $BE_{EXP} - BE_i$ for all nuclei included in AME12 [32] (l.h.s.). Residuals differences between $S_{2n}^{EXP} - S_{2n}^i$ for all nuclei included in AME12 (r.h.s.). The results for the different mass models used in the present work are displayed in the above panels as follows: a,b \rightarrow FRDM; c,d \rightarrow HFB21; e,f \rightarrow DZ10; g,h \rightarrow DZ31; i,j \rightarrow WS3.

2.2.4. Shell corrections

This section is dedicated to the analysis of the so-called shell corrections. As we have avoided any reference to pairing in equation 2.53, in order to properly display the shell correction surface, we must divide it in four sheets; i.e., even Z - even N, even Z - odd N, odd Z - even N and odd Z - odd N respectively. However as the information coming from any of the four sheets is basically the same, we choose to show only the even Z - even N nuclei.

In Fig. 2.6 we display the shell corrections for even-even nuclei as defined by Eq. 2.52 (see black lines in Fig. 2.6) as a function of the neutron number N for the isotopic chains ranging from $30 \leq Z \leq 83$ (this range of isotopic chains was selected due to their relevance for the forthcoming calculations in the present work). The shell corrections are based either on the set of measured nuclei taken from [32] or on sets of nuclei from different mass models used in the present work (see section 2.2.1). On the x-axis of Fig. 2.6, tics have been added at the position of the magic numbers ($N = 28, 50, 82$ and 126). At these numbers, it is observed that the liquid drop model (LDM) is always underestimating the binding energy, i.e., a pike like structure develops. In particular, a notorious difference among the models comes from the prediction of a strong shell closure at $N=184$ for HFB21 which is absent in the rest of the models. The amplitude of the shell corrections at a given magic number is similar for all models including the respective set of measured nuclei and it grows as a function of the neutron (mass) number, N (A), in general it grows as $N^{1/3}$ ($A^{1/3}$). Because the symmetry energy is also different among the models, we observe that the shell corrections are mostly positive for nuclei with $N < 50$. In the same fashion, the set of measured nuclei and those based on HFB21 (except in the region $50 < N < 82$) and FRDM (except for $N \geq 126$) follow this trend. On the other hand, for sets of nuclei based on the WS3 and the Duflo-Zuker mass formulas, the selected LDM (see 2.53) starts to overestimate the binding energy for nuclei in between the shell closures, thus the observed shell corrections become negative.

2.2.4.1. Region of deformation

Another important feature of all the models used in the present work is the deformation. To identify the well deformed nuclei, we are going to use nuclei, for which the deformation parameter $\beta_2 \geq 0.2$ for sets of nuclei based on FRDM, HFB21 and WS3. In the case of the Duflo-Zuker mass models as explained in section 2.1.4.5, the final form of the same goes as $E(N, Z)_{DZ} = \langle H_m \rangle + \max(\langle H_s \rangle, \langle H_d \rangle)$ if $Z \geq 50$. In this case we have selected only the cases in which the deformed sector ($\langle H_m \rangle + \langle H_d \rangle$) is favoured. In order to show the regions of deformation, we have decided to add red lines on top of the black lines (spherical nuclei) in Fig. 2.6. The predictions concerning to the transition from spherical to deformed nuclei are different in most of the models. Three deformation regions are identified at $N \approx 70, 90$ and 140 in Fig. 2.6. It is observed that the appearance of deformation introduce a change in the trends. For instance, the emergence of certain flat regions at places where such transition takes place. In other regions, the deformation spreads wider. The issue of deformation, in particular in the region around $N \approx 90$ will be considered in forthcoming chapters.

2.2. EXPLORING SYSTEMATICS

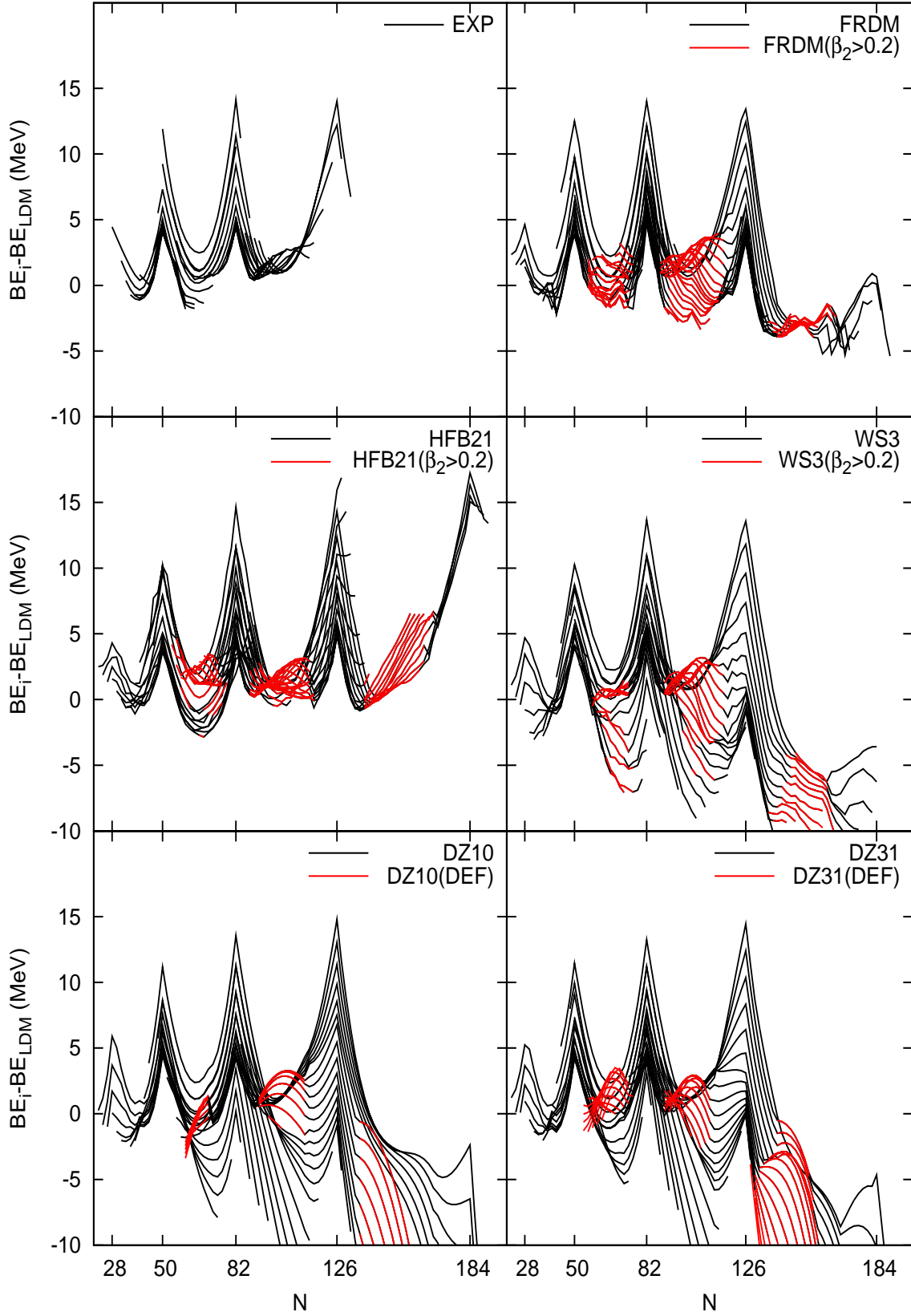


Figure 2.6: Shell corrections for even-even nuclei for a number of Isotopic chains ($30 < Z < 83$) for the set of nuclear masses based on AME12 up to the nuclear drip lines for the following theoretical models: FRDM, HFB21, DZ10 and DZ31 (black lines). The set of deformed nuclei predicted for a number of models is displayed by red lines (for further details see section 2.2.4.1).

2.2.5. Shell gaps

One of the systematics that is most often shown in nuclear masses related works, is the one of the two-neutrons separation energies S_{2n} which involves the differences in the binding energies between two isotopes in jumps of two units (see Eq. 2.54). In this way, odd-even effects are avoided by definition. The resulting surface of the two-neutrons separation energies S_{2n} , is smoother and decreases steadily with increasing neutron number N . A sudden drop in such surface is observed for the magic neutron numbers and also for regions of transition from spherical to deformed nuclei. In this section, the two-neutrons separation energies divided by two ($S_{2n}/2$) are analyzed in more detail. A representation of the strength of the shell gaps can be obtained, by taking the differences between the two-neutrons separation energies of two neighbor isotones (nuclides having the same number of neutrons N but different proton number Z), considering only even neutron number:

$$2 \cdot \Delta(Z, N_c) = S_{2n}(Z, N_c) - S_{2n}(Z, N_c + 2), \quad (2.55)$$

where $N_c = 50, 82, 126$ represent the neutron shell closure. Physically, decreasing Z for a given N in Eq. 2.55 drives the system deeper into the regime of exotic nuclei and $S_{2n}/2$ shrinks accordingly [88].

2.2.5.1. Behaviour of the shell gaps near experimental region

To begin with, we are going to compare how well different models reproduce the known shell gaps near the region of r-process. Fig. 2.7 show the shell as defined by Eq. 2.55, for different neutron shell closures, N_c . The upper panel of Fig. 2.7 exhibit the shell gap at $N_c= 50$. The middle panel of Fig. 2.7 the shell gap at $N_c= 82$. And finally, the bottom panel display the shell gap at $N_c= 126$.

2.2.5.1.1. N=50 shell gap The observed shell gap is reproduced satisfactorily by FRDM, WS3 and HFB21 model, the gaps based on DZ like mass model tend to be roughly constant, underestimated the observed gaps around $Z \sim 40$ and overestimated the those with $Z < 36$. The observed shell gaps have a maximum at $Z = 39$ and a minimum at $Z = 32$ which suggest that the gap would start to rise again in the region of unknown masses. For the region of extrapolation, DZ10 predicts by far the largest gap, in addition DZ10 predicts a symmetric gap with a cusp at $Z=28$, gaps based on FRDM and WS3 present a maximum at $Z=28$ and those DZ31 a minimum at $Z=28$.

2.2.5.1.2. N=82 shell gap The observed gap is best reproduced by DZ10, and to a certain degree by DZ31, the gap based FRDM remains roughly constant and the one based on HFB21 present many jumps. In general a maximum occurs at $Z=50$ in most of the models. The observed $N=82$ gap presents a kink at $Z=64$, which is only present in the gap based on WS3. There is not enough information to establish an expected trend in the region of extrapolation. For the region where the experimental information is no longer available, all the explored models but FRDM, predict an shrink in the shell gap, the DZ like mass models predicts a symmetrical gap with a cusp at $Z=50$ and a minimum at $Z \sim 40$. The gap predicted by FRDM is by far the strongest one and presents a maximum at $Z=42$.

2.2. EXPLORING SYSTEMATICS

2.2.5.1.3. N=126 shell gap The observed gap present a symmetric behaviour with maximum at Z=82 and its in a good agreement with gaps based on DZ31 and HFB21, the gap based on DZ10 is overestimated and the ones based on FRDM and WS3 tend to remain constant. Based on the available information, its expected that the shell gap tends to shrink, which is agreement with the predictions based on DZ like mass formulas and the WS3, where a minimum occurs at Z=70. The predicted gap based on both FRDM and HFB21 tend to become bigger.

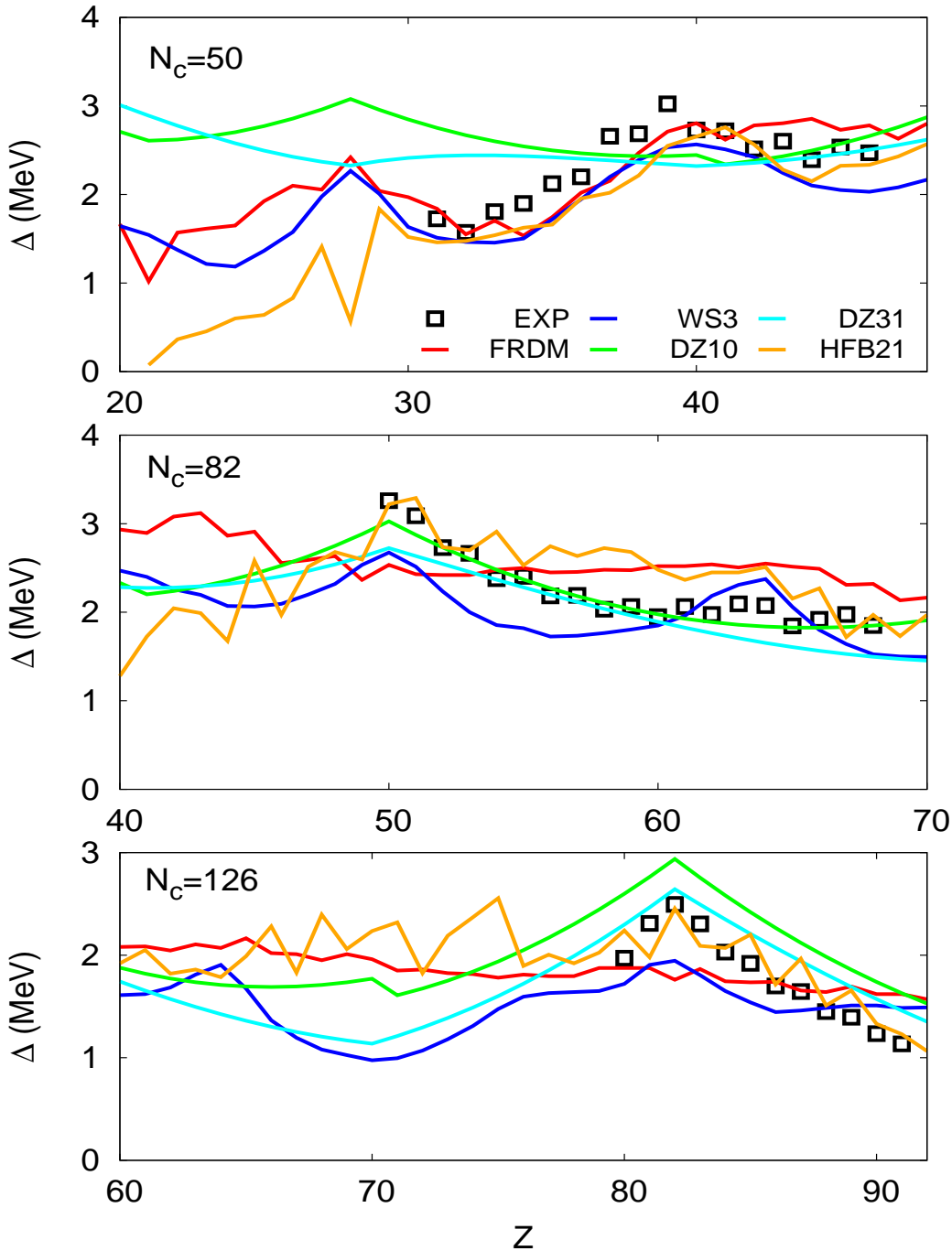


Figure 2.7: Shell gaps for the neutron shell closures at $N= 50$ (upper panel), 82 (middle panel) and 126 (bottom panel). For the mass models used in present work: FRDM (red lines), WS3 (blue line), DZ10 (green lines), DZ31 (cyan lines), HFB21 (orange lines) and also for the set of experimentally available nuclei, AME12 (black empty boxes).

2.2.5.2. Behaviour of the shell gaps for regions far away from stability

The right hand side panels of Figs. 2.8 to 2.12 display $S_{2n}/2$ as a function of the neutron number N (tics on the x-axis are added to identify neutron magic numbers at $N=50, 82$ and 126) for isotopic chains ranging from $30 < Z < 83$. The experimental value of $S_{2n}/2$ is always included when available, and displayed by red lines. In the absence of experimental information, the theoretical values are displayed by black lines. As in Fig. 2.6, the predicted deformed regions (see section 2.2.5 for more details) are added and identified by green lines on top of the theoretical value of $S_{2n}/2$. Finally every 5 isotopic chains bluish lines are included only to guide the eye. The left hand side panels of Figs. 2.8 to 2.12, display $S_{2n}/2$ as a function of the proton number Z for even-isotonic chains ranging from $40 < N < 184$. The experimental value of $S_{2n}/2$ are always displayed by red lines, the theoretical ones by black lines and the predicted deformed regions by green lines on top of the theoretical $S_{2n}/2$. Finally the shell gaps at $N=50, 82$ and 126 , are represented by bluish shadowed regions, to guide the eye, labels are added on top of the same. The experimental $S_{2n}/2$ surfaces (red lines in Figs. 2.8 to 2.12) present an smooth behaviour with discontinuities at the magic numbers ($N= 50, 82$ and 126) and certain irregularities at $N \approx 60$, $N \approx 90$ (a region of transition is expected there) and $N \approx 112$. Concerning the experimental shell gaps, the $N = 50$ shell gap turns out to be the only one, for which there is enough experimental information available to establish a trend. The shell gap at $N = 82$ is partially know up to $Z > 50$, but more experimental information is needed to establish a trend. Finally, the shell gap at $N = 126$ is completely unknown. For our purposes, the shell gaps at $N=82$ and 126 are the only ones with a potential impact on our r -process nucleosynthesis calculations (this point will become clear in the upcoming chapters). To stress the need of theoretical predictions and as a remainder, let us consider the waiting point approximation (see section 5.1.1), assuming typical r -process conditions, i.e., $T_9 = 1$ GK and $n_n = 10^{24} \text{ cm}^{-3}$, we obtain an r -process path of $S_n^0 = S_{2n}/2 \approx 2.8 \text{ MeV}$, and as we can see from the reddish lines in Figs. 2.8 to 2.12, most of the experimentally available $S_{2n}/2$ reach values of at least 4 MeV , this means that in order to perform r -process calculations, one needs to rely most of the time on the theoretical predictions.

Let us start with a discussion concerning the predicted $S_{2n}/2$ surfaces (see black and green lines in Figs. 2.8 to 2.12). The first thing to glimpse the eye is the extremely irregular behaviour of the predicted surfaces by HFB21 (see Fig. 2.9) and FRDM (see Fig. 2.8) in comparison to those of WS3 (Fig 2.10) and DZ (Figs. 2.11 and 2.12).

The FRDM model predicts a region of deformation at $N \approx 70$ and $N \approx 90$. The largest region of deformation predicted by FRDM spans nuclei from $90 < N < 110$. It presents notorious discontinuities before and after the neutron shell closures at $N=82$ and $N=126$ (see r.h.s of Fig. 2.8). Concerning the shell gaps:

1. The shell gap at $N = 82$ is kept in the same strength, however we can distinguish that certain surfaces starting with $N \approx 72$ overlap with the region of the shell gap.
2. The shell gap at $N=126$ is also kept with the same amplitude in this case there are also certain surfaces overlapping with the shell gap region for isotonic chains at $N \approx 130$ (see r.h.s of Fig. 2.8).

The already identified discontinuities, right before and after the magic numbers, as we will learn in forthcoming sections, are critical in the evolution of our r -process calculations.

2.2. EXPLORING SYSTEMATICS

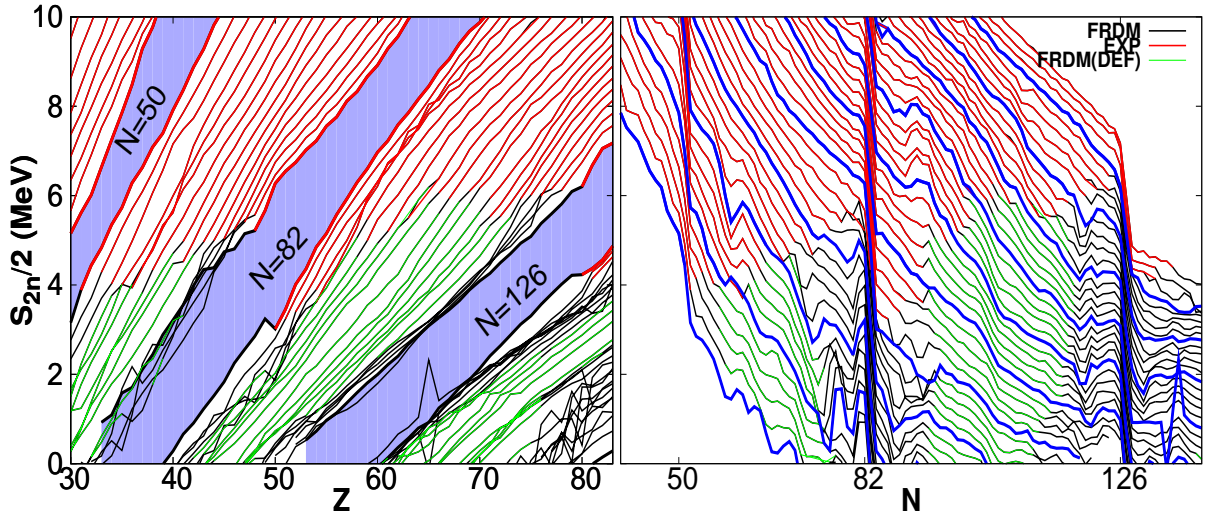


Figure 2.8: $S_{2n}/2$ for a number of isotonic (isotopic) chains $40 < N < 184$ ($30 < Z < 83$) on the l.h.s. (r.h.s.) based on the Finite Range Drop Model (FRDM) up to the neutron drip lines. Experimental data is always shown with red lines. Nuclei for which $\beta_2 \geq 0.2$ are displayed with green lines. On the l.h.s. only isotonic chains with N even are shown. The neutron shell gaps at $N=50$, 82 and 126 are represented by bluish shadowed regions with labels on top of the same. On the l.h.s. blue lines are added every five isotopic chains to guide the eye.

The HFB21 mass model presents the strongest fluctuations among the predicted $S_{2n}/2$ surfaces (fluctuations start for nuclei with $N > 60$). Its prediction for a deformation region at $N \approx 70$ involves a limited number of nuclei. On the other hand, the second region of deformation predicted ($90 < N < 110$) involves similar nuclei than in FRDM. However, its resulting surface presents an anomalous behaviour which seems rather a numerical effect of the minimisation procedure intrinsic to mean field models since such violent jumps result suspicious, as they are mostly absent in the rest of the mass models (see l.h.s. in Fig.2.9). Starting from $Z < 50$, the shell gap predicted for $N=82$ tends to be narrower than the one predicted by FRDM. On the other hand, the shell gap at $N=126$ mostly maintains the same amplitude (see r.h.s. in Fig.2.9).

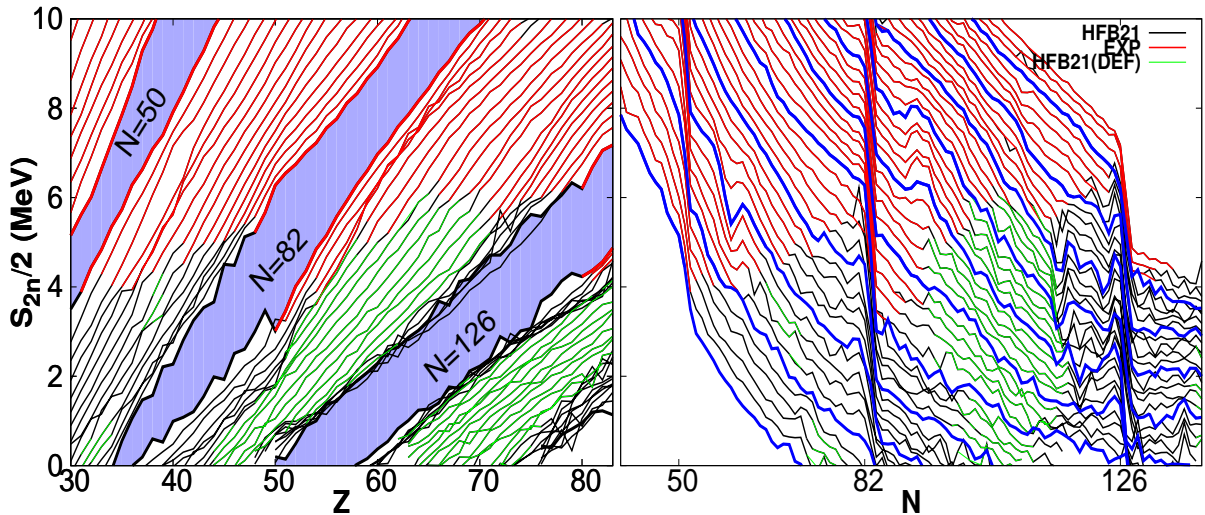


Figure 2.9: Same as in Fig.2.8 but for the HFB21 model.

The WS3 mass model predicts the same two deformation regions as FRDM, although less populated, i.e., they involve a smaller number of nuclei. There are also certain discontinuities before and after the shell closures at $N=82$ and $N=126$. Its resulting $S_{2n}/2$ surface is therefore smoother than the one of FRDM (see l.h.s. in Fig.2.10). The most remarkable difference comes from the prediction on the shell gaps (see r.h.s. in Fig.2.10):

1. The gap $N=82$ begins to reduce its strength for $Z \approx 40$.
2. The shell gap at $N=126$ present a more dramatic feature, its seems to shrink but only for the region $64 < Z < 82$ and afterwards it starts to recover part of its strength.

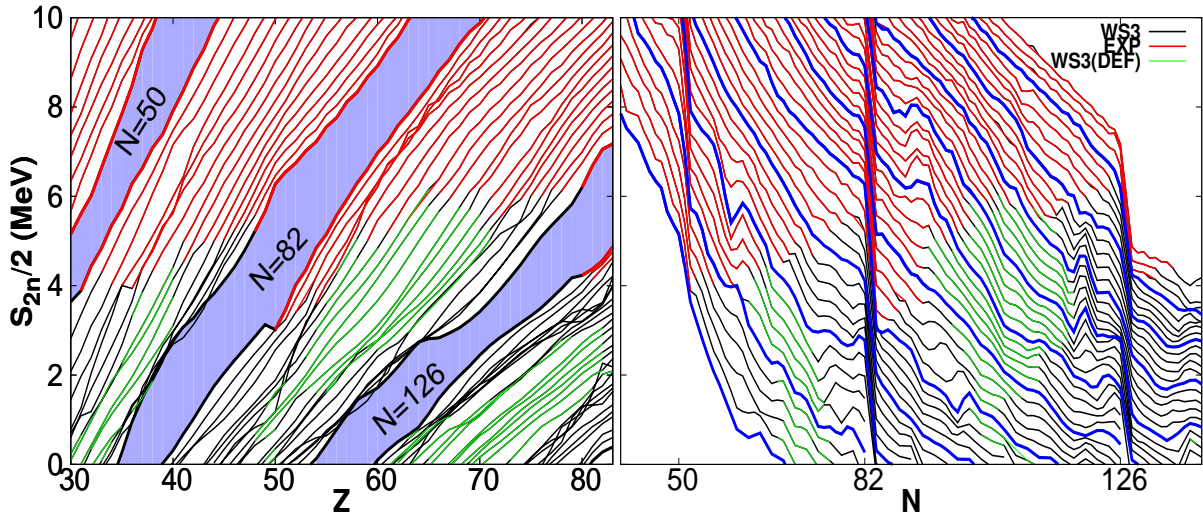


Figure 2.10: Same as in Fig 2.8 but for the WS3 model.

The predicted $S_{2n}/2$ surfaces by the Duflo-Zuker mass models are always the smoother ones (see Figs.2.11 and 2.12). Both models present discontinuities at $N=70$ and $N=112$. Such discontinuities are inherent to the way DZ builds the transition from harmonic oscillator closures ($N,Z=20,40,70,112$) to the magic numbers ($N,Z=28,50,82,126$), the so-called HO-EI transition (for more details the reader is referred to section 2.1.4.3). Concerning the deformation, both models predict similar deformation regions at $N \approx 90$ and at $N \approx 130$. The difference is that the predicted region is wider in the case of DZ31 than in DZ10. This is because in the case of DZ10 there is only one term in charge of the deformation and consequently only a dozen of nuclei are identified as deformed ones. The trends for the predicted shell gap at $N=82$ are similar in both Duflo-Zuker mass models. The predicted shell gap at $N=126$ for DZ31 is less strong (it gets weaker at $Z=70$) than the one of DZ10. In fact, in the case of DZ31 there are a number of surfaces overlapping with the shell gap (coming from $N \approx 130$).

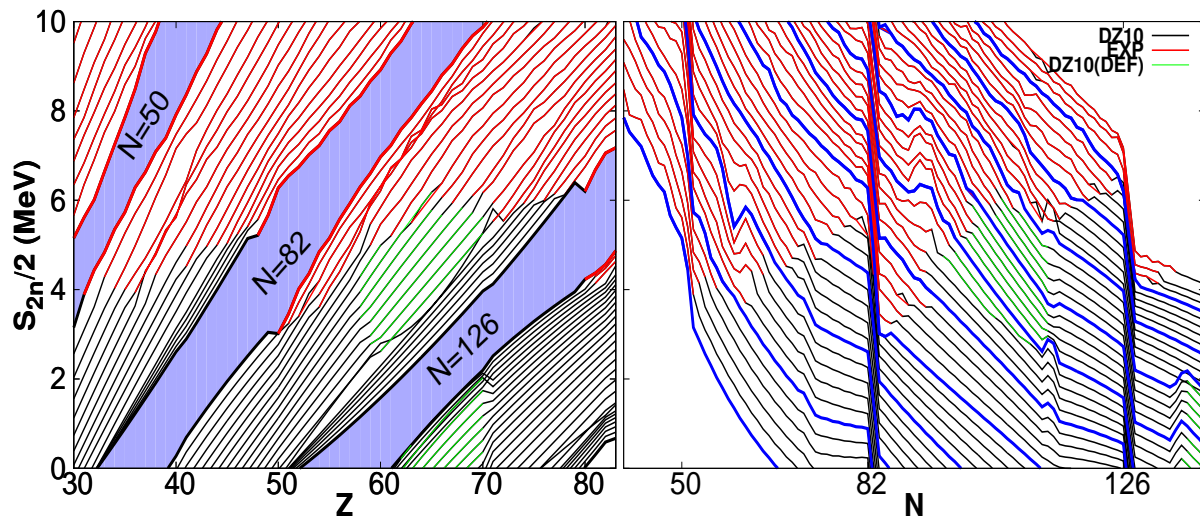


Figure 2.11: Same as in Fig 2.8 but for the DZ10 model.

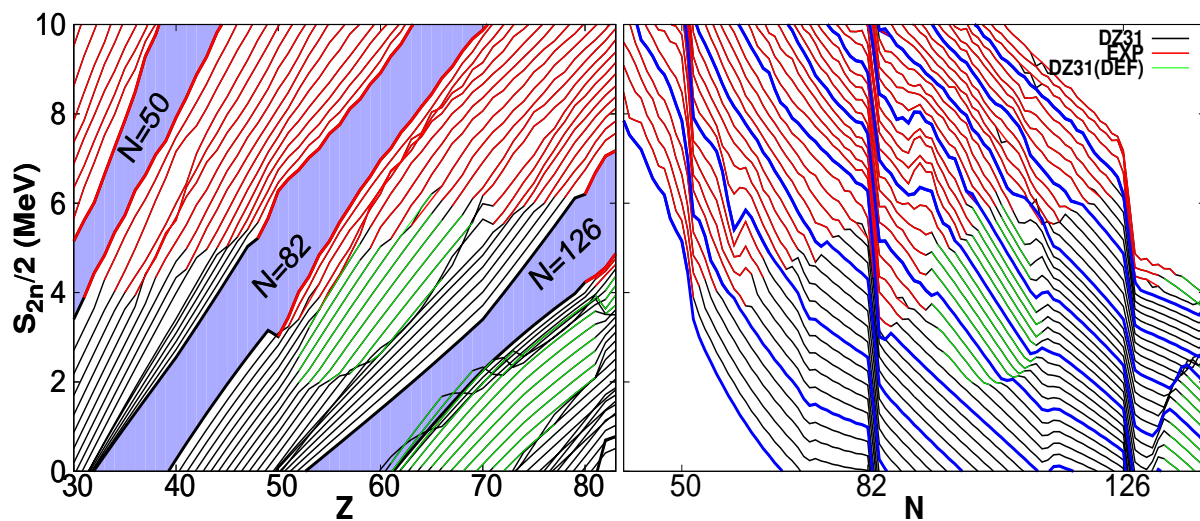


Figure 2.12: Same as in Fig 2.8 but for the DZ31 model.

r-process Nucleosynthesis

Since the seminal work of Burbidge, Burbidge, Fowler, and Hoyle (also known as *B²FH* [6]) and Cameron [89], the mechanism responsible for the production of heavy elements beyond Fe was identified. This mechanism consists in a series of neutron captures followed by a β -decays, these neutron capture processes are divided into rapid (*r*-process) and slow (*s*-process) depending on the time it takes a nucleus to capture a neutron (τ_n) compared to the time it takes the same nucleus to undergo a β -decay (τ_β). Strong support for this view is provided by Fig. 3.1, in which the solar system abundances of heavy elements produced by *r*-process and *s*-process neutron capture. The splitting of the abundance peaks in the mass regions $A=80-90$, $130-140$, and $190-200$, in fact, reveals signatures of two distinct neutron fluxes. This has led historically to the definition of two nucleosynthesis processes that are identified with quite different astrophysical environments [6, 89, 90]. Abundance peaks are caused by maximum τ_β or minimal *n*-capture at the neutron shell closures corresponding to neutron numbers $N = 50, 82, \text{ and } 126$. Because the *r*-process carries nuclei farther from the valley of stability than does the *s*-process, it encounters each closed shell at slightly lower mass number [7]. Hence the *r*-process peaks are offset to lower A . During the present chapter, we are going to explore only the *r*-process requirements and its possible astrophysical sites.

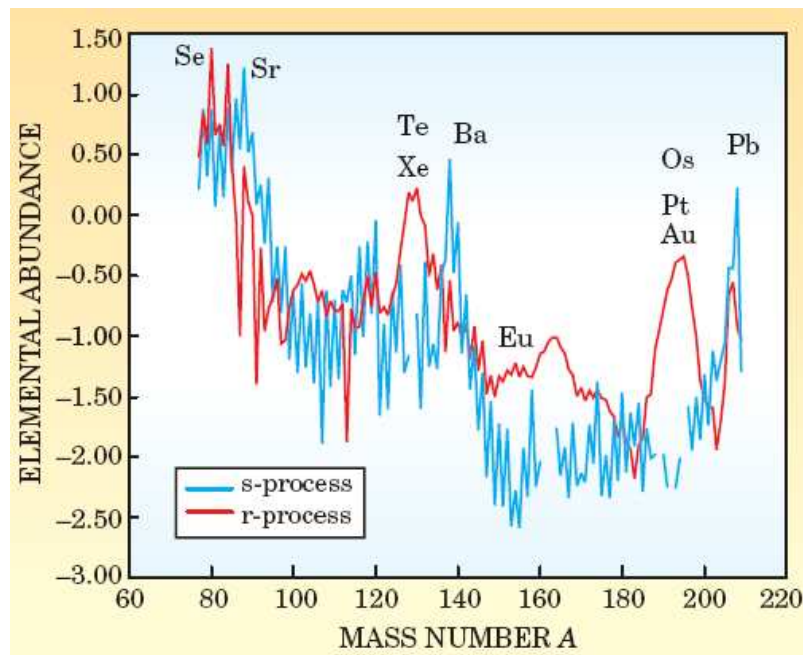


Figure 3.1: Solar system abundances of heavy elements produced by *r*-process and *s*-process neutron captures. Plotted values are $12 + \log_{10}$ of abundance relative to hydrogen. Taken from [7] (Adapted from [91]).

Note that in Fig. 3.1, the curves are not renormalised; the two process really have contributed about equally to the solar system inventory of heavy elements. The elements that compose the materials of the solar system contain admixtures of both r -process and s -process neutron capture, interestingly, nothing that would appear to be from any astrophysical process intermediate between the two[7].

3.1. Requirements for the r-process

Roughly one half of the isotopes heavier than the iron group show evidence of having been produced on a very rapid time scale (of the order of one second) in a high temperature environment by a very high flux of neutrons (more than 10^{20}cm^{-3} , at temperatures greater than 10^9K)[92]. These are referred to as the r -process nuclei (where 'r' stands for rapid neutron capture). The necessary conditions can only be achieved in explosive situations, and it has long been thought that supernovae are the most likely production site, although a frequently mentioned alternative is merging neutron stars. When subtracting s -process abundances (quite well understood via neutron captures in stellar evolution and nuclear physics at and close to stability [101, 102, 103]), the r -process emerges as a process with a path far on the neutron-rich side of stability, requiring explosive environments with large neutron-to-seed-nuclei-ratios (see Fig. 3.2).

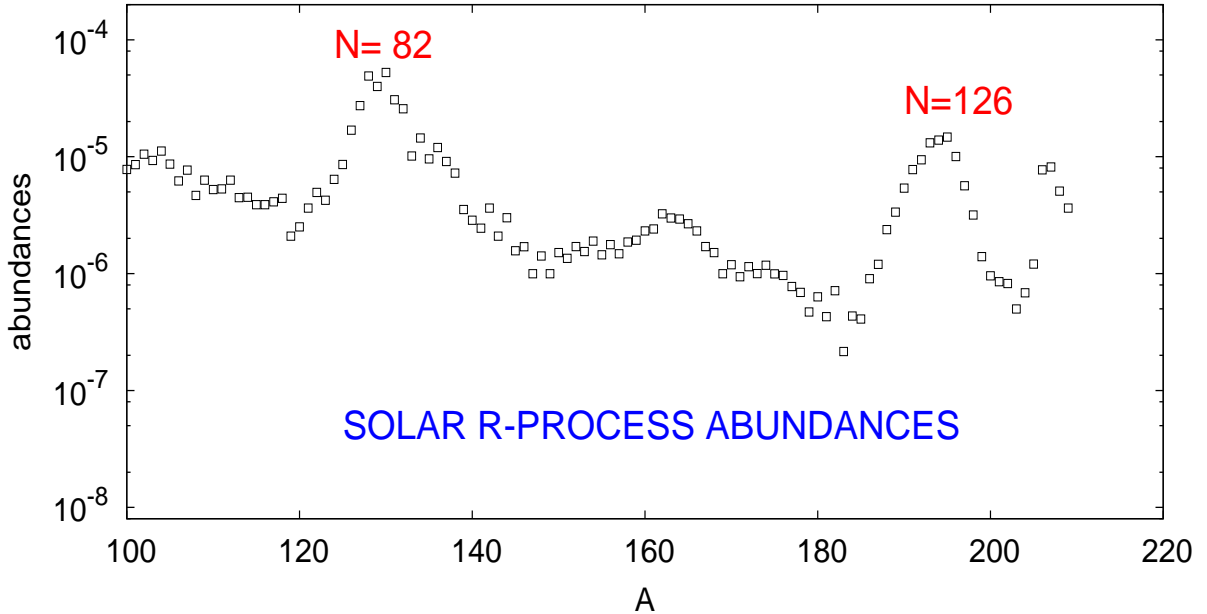


Figure 3.2: Solar r -process abundances. These abundances are obtained by subtracting the s -process contributions calculated from (a) the phenomenological approach and (b) models of two AGB stars. See [101, 102, 103] for details.

Regardless of the astrophysical site, there are two provisions needed for the r -process[93]:

- A flux of free neutrons.
- An abundance of seed-nuclei.

To determine the astrophysical conditions, we are going to closely follow [94]. The evolution of the neutron number density, n_n , in an r -process event can be described in terms of

3.1. REQUIREMENTS FOR THE R-PROCESS

the neutron-to-seed ratio

$$R_{n/s}(t) = \frac{Y_n(t)}{Y_h(t_0)}, \quad (3.1)$$

where $Y_n(t)$ is the neutron abundance at time t and $Y_h(t_0)$ is the initial abundance of seed nuclei. If fission can be ignored, conservation of mass and the total number of nuclei gives

$$Y_n(t) + \sum_{(Z,A)} A \cdot Y(Z,A) = Y_n(t_0) + \langle A_h \rangle Y_h(t_0), \quad (3.2)$$

$$\sum_{(Z,A)} Y(Z,A) = Y_h(t_0), \quad (3.3)$$

where $\langle A_h \rangle$ is the average mass number of the seed nucleus and the sums extend over all the nuclei with $\langle A \rangle \geq \langle A_h \rangle$. Equations (3.2) and (3.3) can be rewritten as

$$\langle A(t) \rangle + R_{n/s}(t) = \langle A_h \rangle + R_{n/s}(t_0), \quad (3.4)$$

where $\langle A(t) \rangle = \sum_{(Z,A)} A \cdot Y(Z,A) / \sum_{(Z,A)} Y(Z,A)$ is the average mass number of the nuclei with $\langle A \rangle \geq \langle A_h \rangle$ that are in the r -process network at time t . In general, when the r -process freezes out at $t = t_{\text{FO}}$, $R_{n/s}(t_{\text{FO}}) \lesssim 1$ and $\langle A(t_{\text{FO}}) \rangle \approx \langle A_h \rangle + R_{n/s}(t_0)$. Thus, the outcome of an r -process event can be simply estimated from the initial neutron-to-seed ratio and the mass number of the seed nucleus.

The initial neutron-to-seed ratio $R_{n/s}(t_0)$ not only provides a convenient means to characterise an r -process event but also highlights two important issues: (see [94])

- **Where do the seed nuclei come from?**

Observations of abundances in a large number of metal-poor stars as well as detailed studies covering many elements individual stars have been carried out by a number of groups (e.g., [104]–[114]), showed that the r -process already occurred in the early history of the Galaxy. This suggests that an r -process event cannot rely on some previous astrophysical events to provide the seed nuclei and must produce the seed nuclei within the event itself.

- **How is $R_{n/s}(t_0)$ determined?**

The production of the seed nuclei and the determination of $R_{n/s}(t_0)$ in an r -process event can be illustrated by considering a rather generic scenario in which neutron-rich material adiabatically expands from high temperature and density. The parameters characterising the expansion that results in a successful r -process can be taken as a new measure of the astrophysical conditions for the r -process.

The combinations of Y_e , S , and τ_{dyn} shown in Fig. 3.3 are considered to represent the conditions for an r -process that can produce the nuclei with $\langle A \rangle \sim 195$ from the seed nuclei with $\langle A_h \rangle \sim 90$, see [115] for details. Similar results were also obtained in [116, 117, 118]. The combinations of Y_e and S required to produce the nuclei with $\langle A \rangle \sim 130$ would lie to the left of the curves shown in Fig. 3.3 for fixed values of τ_{dyn} . Illustrative r -process calculations with different combinations of Y_e , S , and τ_{dyn} were carried out in [116, 117] and [119, 120].

Qualitatively, a low Y_e , a high S_0 , and a short τ_{dyn} favor a high neutron-to-seed ratio for the r process [115]. The lower Y_e is, the more neutrons are available. The shorter τ_{dyn} is, the less time there is for consuming neutrons and making seed nuclei.

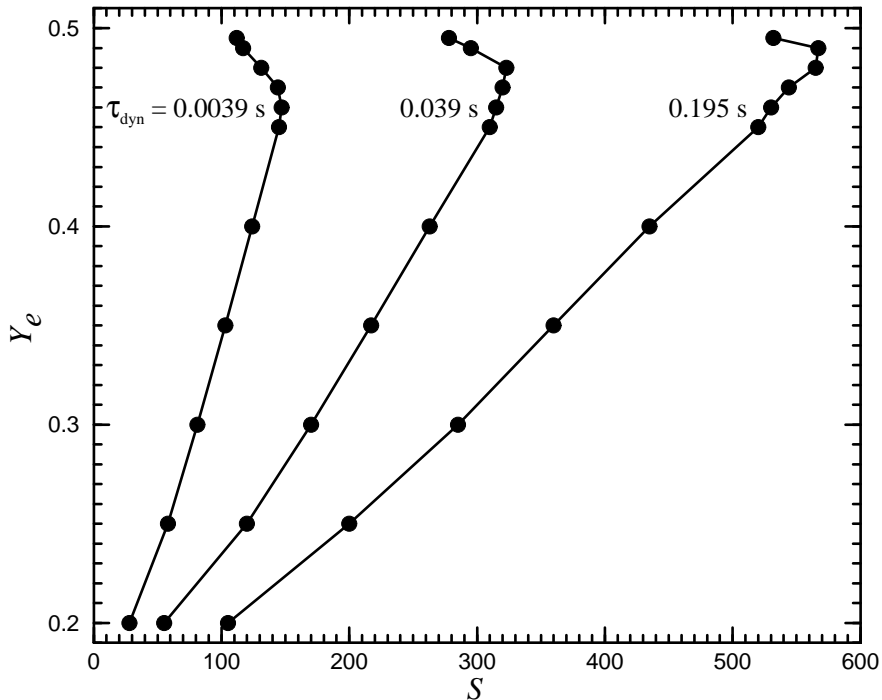


Figure 3.3: Combinations of Y_e , S , and τ_{dyn} giving rise to an initial neutron-to-seed ratio of $R_{n/s}(t_0) \approx 100$ for the r -process in adiabatically expanding matter. Production of nuclei with $A \sim 195$ is expected. Plot taken from [115].

3.2. Astrophysical sites for the r -process

The two major candidate astrophysical environments for the r -process to be discussed in the present work are characterised by $S \sim 100$ (neutrino-driven wind from core-collapse supernovae [8, 9, 10]) and $S \lesssim 10$ (matter that becomes gravitationally unbound from neutron star merger [11, 12, 13, 14, 15, 16]), respectively. Before enter in details of the two potential sites for r -process nucleosynthesis, we are going to briefly sketch the evolution and explosion of massive stars, by which we shall mean those that are born with initial masses of more than about $8 M_{\odot}$ (where M_{\odot} is the solar mass), the minimum mass for single stars to explode as supernova.

3.2.1. Massive star evolution and explosion

The life of a star can be pictured as a continuous struggle between the force of gravity (which is always trying to squeeze the system) and the pressure generated by nuclear reactions in its interior (which is radiating energy away and counteracting against the gravity), such reactions can occur only by altering its composition, so that the structure of the star changes with time. This process works because self-gravitating systems, i.e., non-degenerate stars have a negative heat capacity, this means that if the system loses energy, for example by radiating energy away into space, the average kinetic energy and with it the average temperature actually increases. Thus the exhaustion of one fuel, e.g., hydrogen, leads to the ignition of the next, e.g., helium, helium to carbon and oxygen, then carbon, neon, oxygen and silicon burning, until finally an inert core of iron is formed (in the case of a massive star), from which no further energy can be gained by nuclear burning [95]. Fig. 3.4 display an artistic representation of the above mentioned burning stages.

3.2. ASTROPHYSICAL SITES FOR THE R-PROCESS

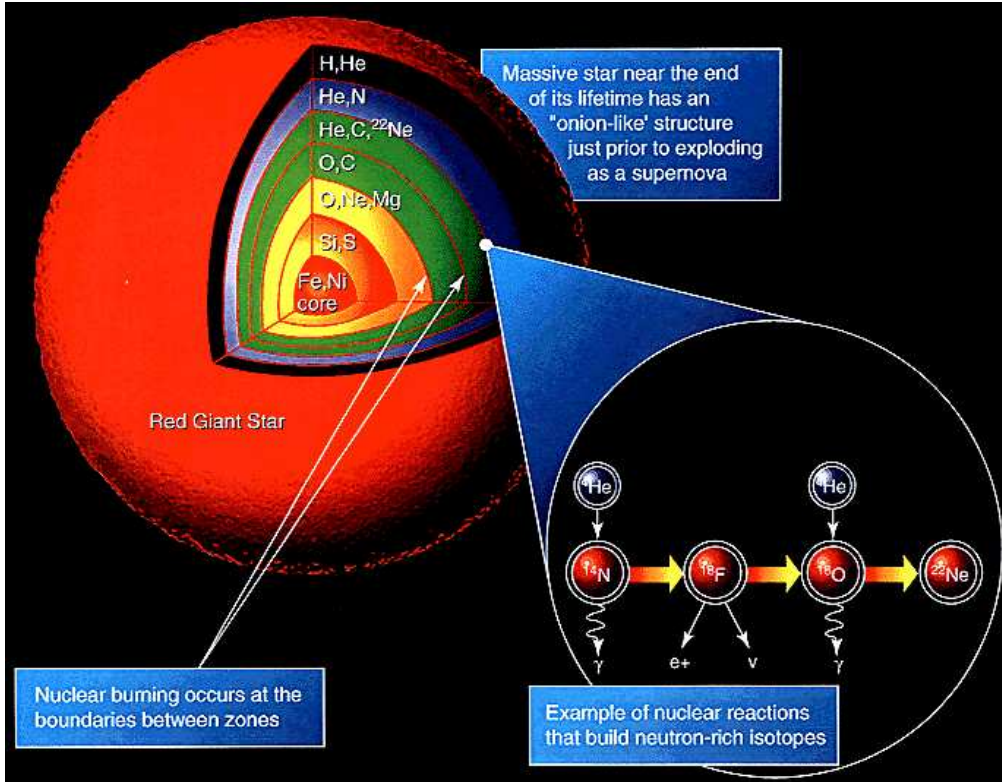


Figure 3.4: Structure of a massive star at the end of its evolution. Taken from [121].

When the iron and nickel core formed in the center of the massive star grows by silicon shell burning to a mass around the Chandrasekhar mass limit of about $1.44 M_{\odot}$, due to the high temperatures and densities, besides the energy losses via the released neutrinos, two other process namely the electron capture and the photo-disintegration start to rob the iron core of the energy it needs to maintain its pressure and avoid collapse. The situation becomes even worse, at densities above $10^{10} \text{ g cm}^{-3}$, electrons are squeezed to iron-group nuclei and electron degeneracy pressure cannot longer stabilise the core and it collapses. This starts what is called a core-collapse supernova in course of which the star explodes and parts of the star's heavy-element core and of its outer shells are ejected into the Interstellar Medium [97]. As a result a neutron star or a black hole is born.

The mechanism behind the supernova explosion is not fully understood yet, however for the discussion that follows, we are going to assume that a supernova explosion takes place.

3.2.2. Neutrino-driven winds from protoneutron stars

A well-studied model of nucleosynthesis in material adiabatically expanding from NSE concerns neutrino-driven winds from protoneutron stars (PNSs) produced in core-collapse supernovae (CCSNe) [8, 9, 10]). In what follows a brief summary of the same is given.

Core-collapse supernova occur at the end of the evolution of massive stars when the core collapses to form a proto neutron star (PNS) [122, 97]. The energy gain during the collapse corresponds to the gravitational binding energy of the PNS, $\approx 3 \times 10^{53}$ ergs, and is emitted as neutrino radiation on time scales of tens of seconds during which the central PNS cools,

deleptonizes and contracts to the final neutron star (see Fig. 3.5). A PNS cools by emitting neutrinos, i.e., ν_e , $\bar{\nu}_e$, ν_μ , $\bar{\nu}_\mu$, ν_τ , and $\bar{\nu}_\tau$. As these neutrinos pass through the hot material predominantly consisting of free nucleons immediately outside the PNS, a fraction of the ν_e and $\bar{\nu}_e$ can be absorbed through



On average, a nucleon obtains ~ 20 MeV from each interaction with ν_e or $\bar{\nu}_e$. In order to escape from the protoneutron star gravitational potential of $GM_{\text{NS}}m_u/R_{\text{NS}} \sim 200$ MeV, a nucleon in the wind must interact with ν_e and $\bar{\nu}_e$ for ~ 10 times. The result is a baryonic outflow that expands with supersonic velocities and is known as the **neutrino-driven wind** [123]. Eventually, the neutrino-driven wind collides with the slow, early supernova ejecta resulting in a wind termination shock or reverse shock [125, 126, 127, 21, 128]. The above reactions (see Eq. 3.5) also interconvert neutrons and protons, thereby determining the Y_e in the wind [100].

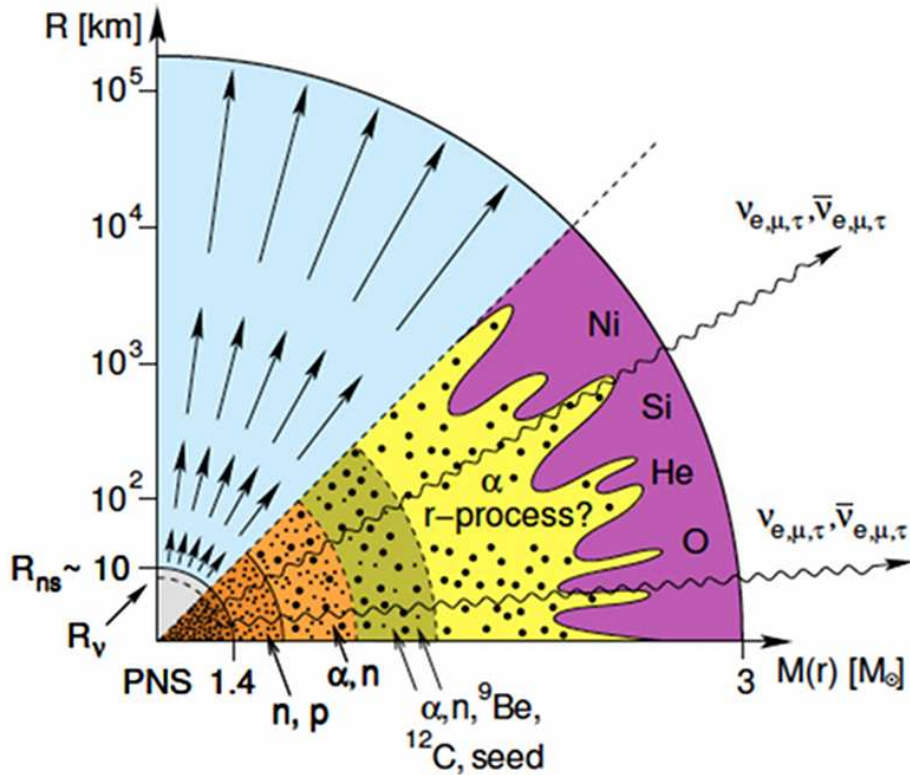


Figure 3.5: ν -driven wind from surface of the recently born proto neutron star (PNS). Taken from [97]

This neutrino-driven wind is a promising site for different nucleosynthesis processes and was proposed as the main host for the r-process. The general conditions required for the r-process were investigated both via analytical [8] and via steady-state [172, 129] models of neutrino-driven winds.

3.2. ASTROPHYSICAL SITES FOR THE R-PROCESS

3.2.2.1. Observational constrains and current status

In order to account for the solar r -process abundances associated with the peaks at $A = 130$ and 195, each supernova must eject $\sim 10^{-6}$ – $10^{-5} M_{\odot}$ of r -process material. Although the current neutrino-driven wind models have difficulty in providing the r -process conditions, the wind naturally ejects $\sim 10^{-6}$ – $10^{-5} M_{\odot}$ of material over a period of ~ 1 s [94]. This is because the small heating rate due to the weakness of neutrino interaction permits material to escape from the deep gravitational potential of the protoneutron star at a typical rate of $\sim 10^{-6}$ – $10^{-5} M_{\odot} \text{ s}^{-1}$ [8, 129]. Indeed, the ability to eject a tiny but interesting amount of material was recognized as an attractive feature of the neutrino-driven wind model of the r -process (e.g., [119]).

Current models fail to provide the conditions for an r -process to occur in the wind. For instance, the production of heavy r -process elements ($A > 130$), requires a high neutron-to-seed ratio. This can be achieved by the following conditions [8, 115, 172, 129]: high entropy, fast expansions, or low electron fraction. However, as Arcones and Martinez-Pinedo [10] remark, these conditions are not yet realized in hydrodynamical simulations that follow the outflow evolution during the first seconds of the wind phase after the explosion [21, 128]. This failure may simply reflect the uncertainties in the models and can be remedied when better physical input is used.

3.2.3. Neutron star mergers

Early in the development of the theory of nucleosynthesis, an alternative site for the origin of r -process nuclei was proposed by Tsuruta and Cameron [130]. It relies on the fact that at high densities (typically $\rho > 10^{10} \text{ g cm}^3$) matter tends to be composed of nuclei lying on the neutron rich-side of the valley of nuclear stability as a result of endothermic free-electron captures [15]. Such conditions are found in the decompression of cold, neutronized matter ejected by tidal effects of a black hole on a neutron star companion and also in the merger of two neutron stars, this site was firstly explored by Lattimer and Schramm [11, 12]. It was estimated that $\lesssim 5\%$ of the original neutron star mass may be ejected during tidal disruption of the neutron star in an NS-BH merger [11, 12]. Recent estimates for the amount of cold neutron star matter ejected during an NS-NS merger range from $\sim 10^{-3} M_{\odot}$ to $\sim 10^{-2} M_{\odot}$ [15]. As can be seen in Fig. 3.6 (taken from [16]), most of the ejecta originate from the contact interface between the colliding binary components, which get deformed into drop-like shapes prior to the merging. For the 1.35-1.35 M_{\odot} binary the ejecta in the shear interface between the stars are separate into two components, each being fed (nearly) symmetrically by material from both colliding stars.

3.2.3.1. Observational constrains and current status

Two binary neutron star (NS-NS) systems, PSR 1913+16 [132] and PSR 1534+12 [133], were observed in the Galaxy. The neutron stars in an NS-NS binary eventually merge due to orbital decay caused by gravitational radiation. The total time from birth to merger is $\approx 4 \times 10^8$ yr for PSR 1913+16 and $\approx 3 \times 10^9$ yr for PSR 1534+12 [134]. Estimates for the rate of NS-NS mergers in the Galaxy range from $\sim 10^{-6}$ to $\sim 3 \times 10^{-4} \text{ yr}^{-1}$ with the best guess being $\sim 10^{-5} \text{ yr}^{-1}$ (e.g., [134]–[135]). The birth rates of neutron star-black hole (NS-BH) and NS-NS binaries are comparable. However, the fraction of NS-BH binaries having the appropriate orbital periods for merging within the age of the universe ($\sim 10^{10}$

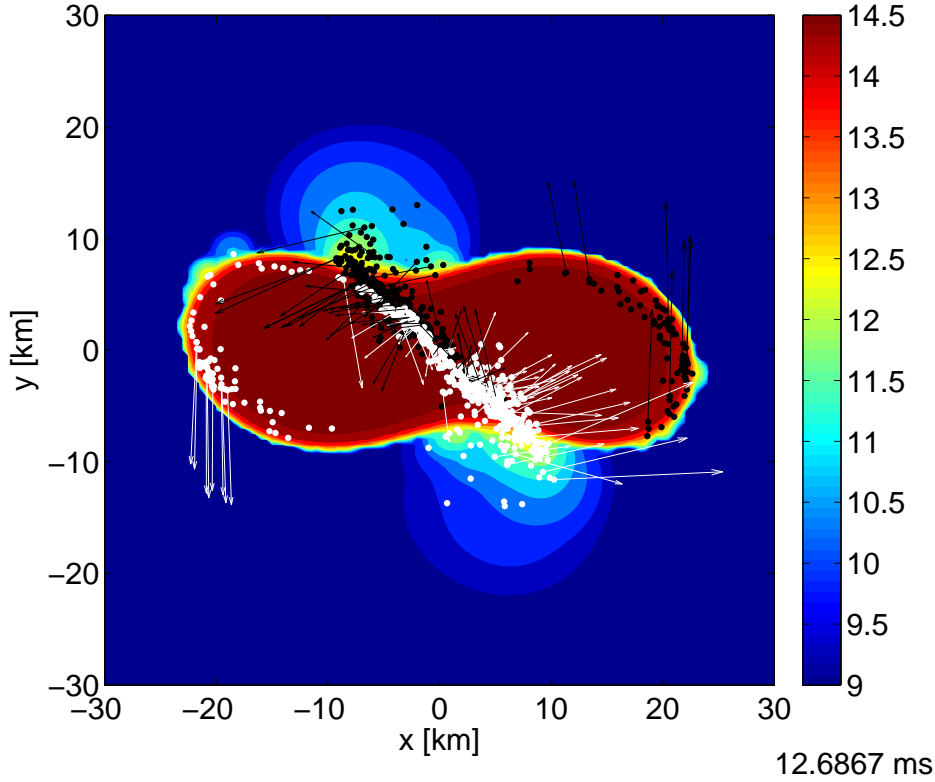


Figure 3.6: Merger and mass ejection dynamics of the $1.35\text{-}1.35 M_{\odot}$ binary with the DD2 EoS, visualized by the color-coded conserved rest-mass density (logarithmically plotted in g/cm^3) in the equatorial plane. The dots mark SPH particles which represent ultimately gravitationally unbound matter (taken from [16]).

yr) is uncertain due to their complicated evolution involving mass exchange [134]. In any case, the total rate of neutron star (including NS-NS and NS-BH) mergers in the Galaxy is perhaps $\sim 10^{-5} \text{ yr}^{-1}$, which is $\sim 10^3$ times smaller than the Galactic rate of SNe II [136]. This means that each merger must eject $\gtrsim 10^{-3} M_{\odot}$ of r -process material if neutron star mergers were solely responsible for the solar r -process abundances associated with the peaks at $A = 130$ and 195 ($\sim 10^{-6}\text{-}10^{-5} M_{\odot}$ of r -process material is required from each event in the case of core-collapse supernovae) [94].

More recent studies used detailed hydrodynamic simulations of mergers of two neutron stars and found robust production of r -process nuclei with $A \gtrsim 130$ (e.g., [14, 16]). Based on these studies, the extremely neutron-rich ejecta is heated by β -decay during its decompression and can also be shocked to high temperatures during its dynamic ejection. Due to the very high initial density of the ejecta, heavy nuclei are already present during the NSE phase of the expansion. The subsequent hot r -process undergoes fission cycling, thereby producing a stable abundance pattern for $A \gtrsim 130$.

Rates

Nuclear reactions generate energy in nuclear reactors, in stars, and are responsible for the existence of all elements heavier than hydrogen in the universe [137]. A key ingredient in any astrophysical calculations is the knowledge of the thermonuclear reaction rates via their cross sections; as they measure the probability of reactions between a target nucleus and incoming projectiles under astrophysical conditions. During the present work, we have mainly focused on the calculation of n-capture rates $N_A \langle \sigma v \rangle^*$ and their corresponding inverse rates, the so-called photodissociation rates, $\lambda_{\gamma,n}$ for a range of physical conditions established by hydrodynamical simulations corresponding to the possible astrophysical scenarios for r-process nucleosynthesis. We have chosen the statistical model or Hauser-Feshbach approach (see section 4.1.2) to accomplish such task. The first part of this chapter is intended to present a short review to the calculation of nuclear cross sections and in particular in the frame of the statistical model, for more details concerning to the field of reaction theory the interested reader is referred to [31]. The second part of the same deals with a summary of results for the calculations of n-capture rates, $N_A \langle \sigma v \rangle^*$, using the code MOD-SMOKER (see [154, 17] for more details).

4.1. Nuclear reaction cross sections

The reaction cross section is defined as follows:

$$\sigma = \frac{\text{number of reaction per target/sec}}{\text{flux of incoming particles}}, \quad (4.1)$$

Since the flux of incoming particles is measured in $cm^{-2} \cdot s^{-1}$, $\sigma [=] cm^2$. For instance all the particles passing through a region of area σ will undergo a reaction; then what σ measures is the probability of a reaction to occur. Introductory quantum mechanics relates the cross section to the sum of transmission coefficients over all possible angular momenta, i.e.,

$$\sigma = \frac{\pi}{k^2} \sum_{l=0}^{\infty} (2l+1) T_l, \quad (4.2)$$

where l , denotes the angular momentum and T_l the transmission coefficient of the incoming particles. The transmission coefficients (T_l) give the probability of the penetration of the potential barrier and can be computed using an optical model.

For the following derivations, we have decided to closely follow [90], our task is to derive an expression resulting from a general treatment of the scattering problem, describing

- an incoming plane wave(the projectile)

- scattering in all directions
- penetration into the nucleus.

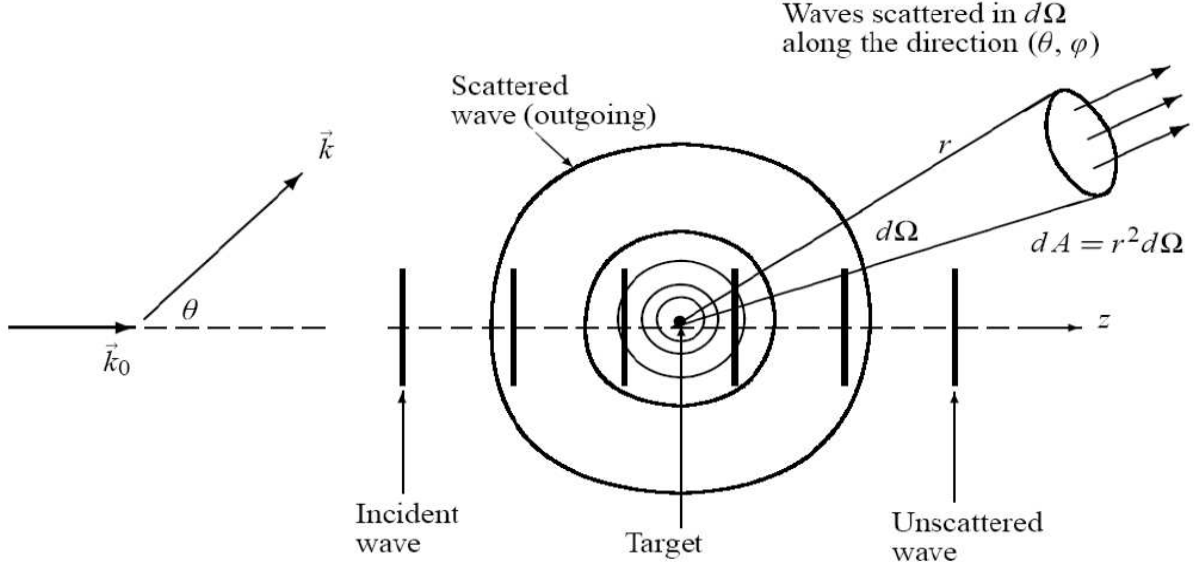


Figure 4.1: Geometry of the scattering problem.

The geometry of the scattering problem is depicted in Fig. 4.1. Let's start, assuming that the projectile is a plane wave moving in the z -direction, i.e.

$$\begin{aligned}\psi_{in} = e^{ikz} &= e^{ikr \cos \theta} \\ &= \sqrt{4\pi} \sum_{l=0}^{\infty} \sqrt{(2l+1)} i^l j_l(kr) Y_{l,0}(\theta).\end{aligned}\quad (4.3)$$

Since the spherical Bessel functions have an asymptotic behaviour,

$$j_l(kr) \xrightarrow{r \rightarrow \infty} \frac{\sin(kr - \frac{l\pi}{2})}{kr},$$

and using the following identity

$$\sin(x) = \frac{i}{2}(e^{-ix} - e^{ix}),$$

a plane wave in z -direction can be written for a large kr as follows

$$\psi_{in} = e^{ikz} = \sqrt{\pi} \sum_{l=0}^{\infty} \sqrt{(2l+1)} i^{l+1} \left[\frac{e^{-i(kr - \frac{l\pi}{2})}}{kr} - \frac{e^{i(kr - \frac{l\pi}{2})}}{kr} \right] Y_{l,0}.\quad (4.4)$$

Physically, this solution can be interpreted as a sum of incoming ($\frac{e^{-ikr}}{r}$) and outgoing ($\frac{e^{ikr}}{r}$) radial waves for $l = 0$, in the case of $l > 0$ they also carry angular momentum. If a reaction occurs, the outgoing wave will be reduced in amplitude (because not all of the incoming wave is scattered and reflected, part of it is transmitted into the nucleus and remains there). Thus the wave function for the total problem is:

$$\psi_{tot} = \frac{\sqrt{\pi}}{kr} \sum_{l=0}^{\infty} \sqrt{(2l+1)} i^{l+1} \left[e^{-i(kr - \frac{l\pi}{2})} - \eta_l e^{i(kr - \frac{l\pi}{2})} \right] Y_{l,0}.\quad (4.5)$$

4.1. NUCLEAR REACTION CROSS SECTIONS

In quantum mechanics the flux is defined by

$$\vec{j} = \frac{\hbar}{2mi} (\psi^* \vec{\nabla} \psi - \psi \vec{\nabla} \psi^*). \quad (4.6)$$

To determine the number of particles leaving ($+\vec{e}_r$) or entering ($-\vec{e}_r$) a spherical surface ($dA = r^2 d\Omega \vec{e}_r$, $d\Omega = \sin \theta d\theta d\phi$) one has to solve the following integral,

$$\int_0^{2\pi} \int_0^\pi \vec{e}_r \vec{j}_r r^2 \sin \theta d\theta d\phi \quad (4.7)$$

In the case of plane waves, we have $\vec{j}_{in} = \hbar k/m \vec{e}_z$ and the previous integral is equal to 0, because the number of particles leaving and entering that sphere is equal. This is no longer the case for ψ_{tot} (see Eq 4.5) where the outgoing waves are reduced by a factor η_l . Consequently $-\int_0^{2\pi} \int_0^\pi \vec{e}_r \vec{j}_r r^2 \sin \theta d\theta d\phi$ is equal to the number of particles per second that penetrate the nucleus for a reaction, i.e. the number of reactions per target per second. Due to the scalar product with \vec{e}_r , only the radial components of $\vec{\nabla}$ have to be calculated,

$$-\int_0^{2\pi} \int_0^\pi \vec{e}_r \vec{j}_{tot} r^2 \sin \theta d\theta d\phi = \frac{\hbar}{2mi} \int_0^{2\pi} \int_0^\pi \left(\psi_{tot}^* \frac{\partial}{\partial r} \psi_{tot} - \psi_{tot} \frac{\partial}{\partial r} \psi_{tot}^* \right) r^2 \sin \theta d\theta d\phi.$$

While computing the previous integral the orthonormality relation of the spherical harmonics will be useful, i.e. $\int_0^{2\pi} \int_0^\pi Y_{l,0} Y_{l',0} \sin \theta d\theta d\phi = \delta_{ll'}$. As final results one obtains the following expression for the number of reactions per target per second (the numerator of Eq 4.1)

$$-\int_0^{2\pi} \int_0^\pi \vec{e}_r \vec{j}_{tot} r^2 \sin \theta d\theta d\phi = \frac{\hbar \pi}{mk} \sum_{l=0}^{\infty} (2l+1)(1-|\eta_l|^2)$$

the flux of incoming particles is given by $|\vec{j}_i n| = \frac{\hbar k}{m}$.

From Eq. 4.1 one obtains a expression for the nuclear reaction cross section:

$$\sigma = \frac{-\int_0^{2\pi} \int_0^\pi \vec{e}_r \vec{j}_{tot} r^2 \sin \theta d\theta d\phi}{|\vec{j}_i n|} = \frac{\pi}{k^2} \sum_{l=0}^{\infty} (2l+1)(1-|\eta_l|^2), \quad (4.8)$$

where η_l can be interpreted as the coefficient of the reflected (R) wave function. And because of the conservation of probability, the transmission plus the reflexion probability must be equal to unity, $1 = T + R$ or $T = 1 - R = 1 - |\eta_l|^2$, then the reaction cross section becomes,

$$\sigma = \frac{\pi}{k^2} \sum_{l=0}^{\infty} (2l+1) T_l. \quad (4.9)$$

This is the cross section for the successful production of a compound nucleus at an excitation energy

$$E^* = E_a + Q,$$

where Q represents the reaction Q-value and E_a is the relative kinetic energy of the projectile (in the center-of-mass system).

4.1.1. Compound nucleus (formation and conservation laws)

Before going into more detail, let's introduce a compact notation for a binary reaction as follows $\mathbf{A(a,b)F}$, where a represents the projectile, A the target, b the ejectile and F the residual or daughter nucleus. Redefining our notation for the previous reaction we can illustrate the formation of the compound nucleus as follows,



where C^* represents the compound nucleus as intermediary stage of the reaction. As shown, this excited state (C^*) can again decay into other states via electromagnetic transitions into lower states of the compound nucleus (γ -decay) or via particle emission into another nucleus (in the final stage the compound nucleus can evaporate one or more particles). In most cases for low energy projectiles, no other decay channel is open, then γ -transitions and in particular s-waves ($l = 0$) will dominate, in such case, the transmission coefficients describe central collisions, where no angular momentum is involved.

The reaction previously introduced in Eq. 4.10 has to fulfill the following conservation laws,

$$\begin{aligned} E_A + E_a &= E_C = E_F + E_b && \text{total energy conservation,} \\ \vec{p}_A + \vec{p}_a &= \vec{p}_F + \vec{p}_b && \text{total momentum conservation,} \\ \vec{\ell}_a + \vec{s}_a + \vec{I}_A &= \vec{J}_C = \vec{\ell}_b + \vec{s}_b + \vec{I}_F && \text{total angular momentum conservation,} \\ (-)^{\ell_a} \pi_A \pi_a &= \pi_C = (-)^{\ell_b} \pi_F \pi_b && \text{total parity conservation,} \end{aligned} \quad (4.11)$$

where $E_i, \vec{p}_i, \vec{\ell}_i, \vec{s}_i, \vec{I}_i, \vec{J}_i, \pi_i$ represent the energy, momentum, angular momentum, intrinsic angular momentum, total angular momentum and parity of the species involved in the reaction respectively. Because of the conservation laws, the excitation energy E_C , total angular momentum \vec{J}_C and the parity π_C of the compound nucleus, are identical for the initial system (projectile + target) and for final system (ejectile + residual nucleus).

A relevant quantity to determine whether or not a reaction is allowed, is the so-called Q-value, defined as the difference between the initial and final masses of the involved nuclei, i.e.,

$$Q = m_a + m_A - (m_b + m_F), \quad (4.12)$$

the reaction is energetically allowed (forbidden) for a positive (negative) Q-value.

4.1.1.1. Compound nucleus cross section (spin dependence)

The reaction cross section for the production of a compound nucleus (see Eq. 4.9) was derived for spinless particles. However in a reaction, where target and projectile have spins \vec{I}_A and \vec{s}_a , they form the channel spin $\vec{S} = \vec{s}_a + \vec{I}_A$, as the total number of channel spin orientations is equal to the product of the individuals spin orientations, one has

$$\sum_{S=|I_A-s_a|}^{I_A+s_a} (2S+1) = \frac{(2I_A+1)(2s_a+1)}{(1+\delta_{Aa})}. \quad (4.13)$$

4.1. NUCLEAR REACTION CROSS SECTIONS

where the δ_{Aa} accounts for identical projectiles and targets, i.e., $A = a$. In such case, only even channel spins S are allowed as the wave function has to be symmetric.

The compound nuclear state with spin J is formed by coupling the channel spin S and the angular momentum l , $\vec{J} = \vec{S} + \vec{l}$. In this more general case, the summation over l in Eq. 4.9 should be replaced by a summation over J

$$\sum_J (2J + 1) = \sum_{l=|J-S|}^{J+S} (2l + 1) \sum_{S=|I_A-s_a|}^{I_A+s_a} (2S + 1). \quad (4.14)$$

In the last expression, a summation over all possible initial spin states of both projectile and target is included. In reality, however, we are interested in an average cross section (obtained by averaging over all possible spin states, i.e., we have to divide by Eq. 4.13). Additionally, it will be useful to define a transmission coefficient for fusions which produce the compound state at excitation energy E , with spin J and parity π via all possible channel spin and angular momentum combinations as

$$T(E, J, \pi) = \sum_{l=|J-S|}^{J+S} \sum_{S=|I_A-s_a|}^{I_A+s_a} T_{lS}(E) \quad (4.15)$$

Finally we can rewrite Eq. 4.9 as

$$\sigma(E) = \frac{\pi}{k^2} \frac{(1 + \delta_{Aa})}{(2I_A + 1)(2s_a + 1)} \sum_{J, \pi} (2J + 1) T(E, J, \pi), \quad (4.16)$$

notice that both the cross section for the production of the compound nucleus, $\sigma(E)$, and the wave-number, k ($k = \sqrt{2\mu E}/\hbar$, where μ is the reduced-mass for the initial system) are expressed in the center-of-mass system.

4.1.2. Statistical model

Along this thesis we are going to use the so called statistical (compound nucleus) model of nuclear reactions which will be described in this section.

4.1.2.1. Hauser-Feshbach Model

The statistical model assumes the formation of a compound nucleus at high excitation energy, so that many states maybe excited by the interaction of the projectile a with the target nucleus A . We have borrowed from [138] a scheme (see Fig 4.2) showing the energetics and transitions between nuclear levels in the involved nuclei for a reaction $a + A \rightarrow b + F$ (this can also be the compound nucleus C if the ejectile b is a photon). Moreover, the incident energy of the projectile a is shared between the individual components of the nucleus which fully equilibrates before decay takes place [139]. The de-excitation process is not necessarily immediate and the excited nucleus can live a relatively long time, if this the case the compound nucleus lives long enough to "forget" how it was formed and the de-excitation to the final products b and F only depends on the energy, total angular momentum and parity of the quantum state in the compound nucleus [137]. This picture implies the Bohr independence hypothesis in other words there is no correlation between the formation and the decay of the compound nucleus [140, 139], Bohr's hypothesis has been

experimentally verified [141]. The occurrence of a nuclear reaction in two stages allows the reaction cross section for a process from an initial channel α in the compound nucleus to a final channel β to be written as follows

$$\sigma_{\alpha,\beta} = \sigma_{\alpha} P_{\beta}, \quad (4.17)$$

where P_{β} is the probability that the compound nucleus decays into a channel β . The sum over all decay probabilities has to be unity,

$$\sum_{\beta'} P_{\beta'} = 1, \quad (4.18)$$

moreover from basic quantum mechanics we know that time-reversal symmetry gives us the so-called principle of detailed balance [142], i.e.,

$$\sigma_{\alpha,\beta} k_{\alpha}^2 = \sigma_{\beta,\alpha} k_{\beta}^2, \quad (4.19)$$

substituting Eq. 4.17 in Eq. 4.19 one obtains

$$\frac{\sigma_{\alpha} k_{\alpha}^2}{P_{\alpha}} = \frac{\sigma_{\beta} k_{\beta}^2}{P_{\beta}}, \quad (4.20)$$

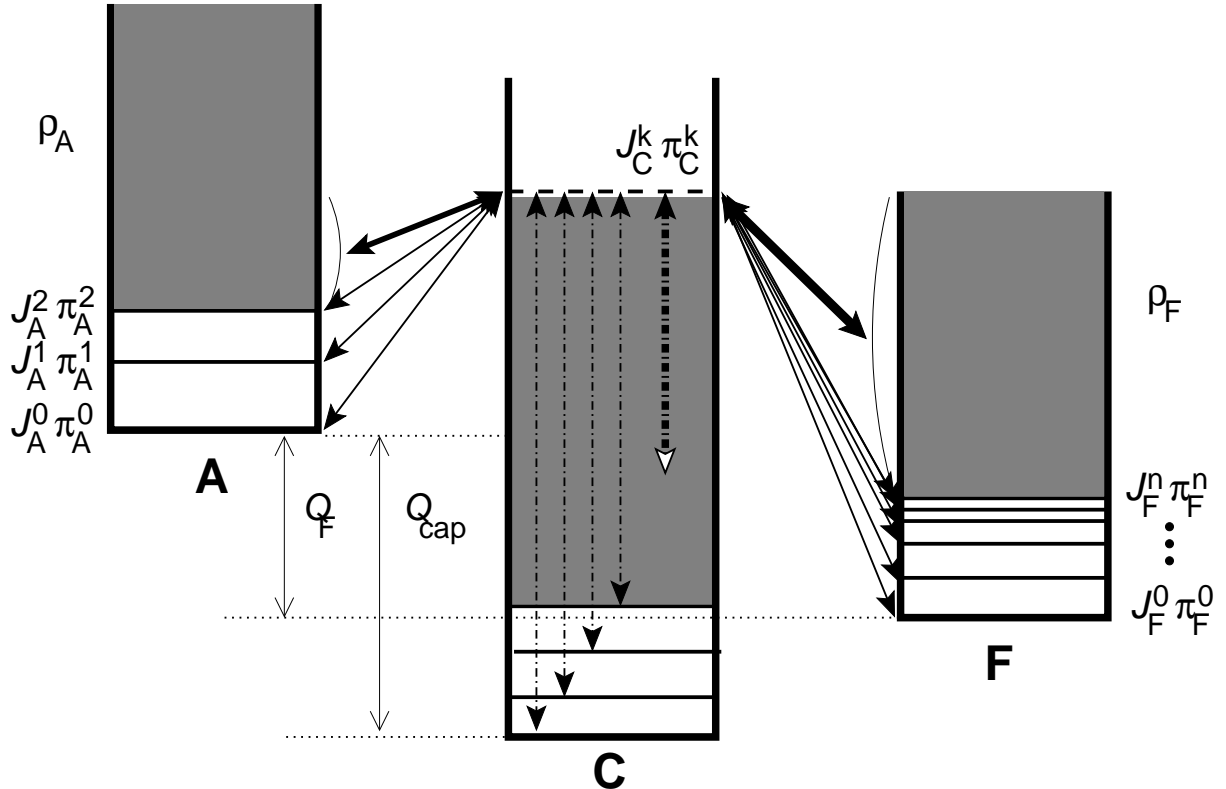


Figure 4.2: Schematic view of the transitions (full arrows denote particle transitions, dashed arrows are γ -transitions) in a compound reaction involving the nuclei A and F and proceeding via a compound state (horizontal dashed line) with spin J_C^k and parity π_C^k in the compound nucleus C. The reaction Q values for the capture reaction (Q_{cap}) and the reaction $A \rightarrow F$ ($Q_F = Q_{Aa}$) are given by the mass differences of the involved nuclei. Above the last state, transitions can be computed by integrating over nuclear level densities (shaded areas). Taken from [138]

4.1. NUCLEAR REACTION CROSS SECTIONS

making use of Eq. 4.2 and Eq. 4.18 in the previous equation, one finds a familiar result,

$$P_\beta = \frac{T_\beta}{\sum_\eta T_\eta}, \quad (4.21)$$

which is nothing that the probability of an specific outgoing channel β . Finally, inserting Eq. 4.21 in Eq. 4.17 one obtains the Hauser-Feshbach formula:

$$\sigma_{\alpha,\beta}^{HF}(E) = \frac{\pi\hbar^2}{2\mu E} \frac{(1 + \delta_{Aa})}{(2I_A + 1)(2s_a + 1)} \sum_{J,\pi} (2J + 1) \frac{T_\alpha(E, J, \pi) T_\beta(E, J, \pi)}{\sum_\eta T_\eta(E, J, \pi)}, \quad (4.22)$$

also known as the statistical model formula, since it implies a purely statistical probability of the decay in the outgoing channel (see [143]).

At low energies individual energies can dominate the cross section. The so-called Breit-Wigner resonance formula describes the cross section due to a particular resonance in the form of a Lorentz function

$$\sigma_{\alpha,\beta}^{BW}(E) = \frac{\pi\hbar^2}{2\mu E} \frac{(1 + \delta_{Aa})}{(2I_A + 1)(2s_a + 1)} \sum_n (2J_n + 1) \frac{\Gamma_{\alpha,n}(E, J, \pi) \Gamma_{\beta,n}(E, J, \pi)}{(E - E_n)^2 + (\Gamma_n(E, J, \pi)/2)^2}, \quad (4.23)$$

the width, Γ_n , of a resonant state n is the sum over the partial widths of the individual decay channels $\Gamma_n = \Gamma_{\alpha,n} + \Gamma_{\beta,n} + \dots$. This measures the stability of a state, since a level having width Γ can only exist for a time interval τ , where Γ and τ are related via the Heisenberg uncertainty principle $\Gamma \cdot \tau \approx \hbar$.

Note that the energy integral over a single term in the sum in Eq. 4.23 is

$$\int_{-\infty}^{+\infty} \frac{\Gamma_{\alpha,n}(E, J, \pi) \Gamma_{\beta,n}(E, J, \pi) dE}{(E - E_n)^2 + (\Gamma_n(E, J, \pi)/2)^2} = 2\pi \frac{\Gamma_{\alpha,n}(J, \pi) \Gamma_{\beta,n}(J, \pi)}{\Gamma_n(J, \pi)},$$

and after averaging over many resonances

$$\begin{aligned} \langle \sigma_{\alpha,\beta}^{BW}(E) \rangle &= \frac{\pi\hbar^2}{2\mu E} \frac{(1 + \delta_{Aa})}{(2I_A + 1)(2s_a + 1)} \\ &\times \sum_{J,\pi} 2\pi(2J + 1) \rho(E, J, \pi) \left\langle \frac{\Gamma_\alpha(J, \pi) \Gamma_\beta(J, \pi)}{\Gamma(J, \pi)} \right\rangle \end{aligned} \quad (4.24)$$

where $\rho(E, J, \pi) = \frac{\Delta n(J, \pi)}{\Delta E} = \frac{1}{D(E, J, \pi)}$ represents the level density, i.e., the number of levels per energy interval and $D(E, J, \pi)$ is the average spacing of resonances. Thus Eq. 4.24 can be rewritten as:

$$\begin{aligned} \langle \sigma_{\alpha,\beta}^{BW}(E) \rangle &= \frac{\pi\hbar^2}{2\mu E} \frac{(1 + \delta_{Aa})}{(2I_A + 1)(2s_a + 1)} \\ &\times \sum_{J,\pi} (2J + 1) \cdot W_{\alpha,\beta}(J, \pi) \cdot \frac{\frac{2\pi}{D(E, J, \pi)} \langle \Gamma_\alpha(J, \pi) \rangle \frac{2\pi}{D(E, J, \pi)} \langle \Gamma_\beta(J, \pi) \rangle}{\frac{2\pi}{D(E, J, \pi)} \langle \Gamma(J, \pi) \rangle} \\ &= \sigma_{\alpha,\beta}^{HF}(E) \end{aligned} \quad (4.25)$$

The last result can be obtained if we identify:

$$T_j(E, J, \pi) = 2\pi \cdot \rho(E, J, \pi) \cdot \langle \Gamma_j(J, \pi) \rangle = \frac{2\pi}{D(E, J, \pi)} \cdot \langle \Gamma_j(J, \pi) \rangle \quad \text{and} \quad (4.26)$$

$$W_{\alpha, \beta}(J, \pi) = \left\langle \frac{\Gamma_\alpha(J, \pi) \Gamma_\beta(J, \pi)}{\Gamma(J, \pi)} \right\rangle \cdot \frac{\langle \Gamma(J, \pi) \rangle}{\langle \Gamma_\alpha(J, \pi) \rangle \langle \Gamma_\beta(J, \pi) \rangle}, \quad (4.27)$$

where $W_{\alpha, \beta}(J, \pi)$ is known as the width fluctuation correction which correlates the incoming and outgoing channels, provided that the transmission coefficients T_j and the decay widths Γ_j are related via either the level density, $\rho(E, J, \pi)$ or its inverse, the level spacing, $D(E, J, \pi)$. In a completely statistical case, when no correlations exist $W_{\alpha, \beta}(E, J, \pi) = 1$.

4.1.2.2. Reaction rates from Statistical model

We are going to proceed the derivations in general lines, however it worth to be mentioned that during the present thesis, we are going to consider reactions involving target nuclei in the range $30 \leq Z \leq 83$ in the temperature range from 0.01 GK to 10 GK. We are mainly interested in (n, γ) reactions and in such reactions the residual and the compound nucleus are the same. The Hauser-Feshbach expression for the cross-section of an $A^\mu(a, b)F^\nu$ reaction proceeding from the target nucleus A in a state μ with spin J_A^μ and parity π_A^μ to a final state ν with spin J_F^ν and parity π_F^ν in the residual nucleus F via a compound state with excitation energy E, spin J, and parity π is given by (see also [144, 145, 155, 17, 154, 146])

$$\begin{aligned} \sigma_{a,b}^{\mu\nu}(E) &= \frac{\pi \hbar^2}{2\mu E} \frac{(1 + \delta_{A,a})}{(2I_A^\mu + 1)(2s_a + 1)} \sum_{J, \pi} (2J + 1) \\ &\times \frac{T_a^\mu(E, J, \pi; E_A^\mu, J_A^\mu, \pi_A^\mu) T_b^\nu(E, J, \pi; E_F^\nu, J_F^\nu, \pi_F^\nu)}{T_{tot}(E, J, \pi)}, \end{aligned} \quad (4.28)$$

where E and μ are the center-of-mass energy and the reduced mass for the initial system, All the relevant particle (neutron) and γ -transmission coefficients are schematically depicted in Fig 4.2, where full arrows denote particle transitions and dashed arrows represent γ -transitions. $T_{tot}(E, J, \pi)$ represents the sum of the transmission coefficients into all possible bound and unbound states over all energetically accessible exit-channels [17]. Experiments measure only transitions from the ground state in the target nucleus A to excited states in the final nucleus F, i.e. $\sigma^{lab} = \sum_\nu \sigma^{0,\nu}(E)$. Nevertheless in our case we are dealing with in an astrophysical plasma at temperature T^* , so that the target A has thermally populated states μ , consequently the astrophysical cross section σ^* is given by (see also [17])

$$\sigma_{A,a}^*(E) = \frac{\sum_\mu (2I_A^\mu + 1) \exp\left(\frac{-E_A^\mu}{kT^*}\right) \sum_\nu \sigma_{a,b}^{\mu\nu}(E)}{\sum_\mu (2J_A^\mu + 1) \exp\left(\frac{-E_A^\mu}{kT^*}\right)}, \quad (4.29)$$

k being the Boltzmann constant. Eq. 4.29 implies that one must replace the particle and γ -transmission ($T_a^\mu(E, J, \pi)$) coefficients in Eq. 4.28 by the total transmission coefficients ($T_a(E, J, \pi)$) into the exit channel due to the fact that for any initial state we want the decay

4.1. NUCLEAR REACTION CROSS SECTIONS

to all bound states, i.e.,

$$T_a(E, J, \pi) = \sum_{\mu=0}^{\kappa} T_n^{\mu}(E, J, \pi; E_A^{\mu}, J_A^{\mu}, \pi_A^{\mu}) + \int_{E_A^{\kappa}}^{E-S_a} \sum_{J_A \pi_A} T_n(E, J, \pi; E_A, J_A, \pi_A) \times \rho(E_A, J_A, \pi_A) dE_A, \quad (4.30)$$

where E_A^{κ} is the excitation energy of the last experimentally known state, κ , in the nucleus A. Above E_A^{κ} , transitions can be computed by integrating over nuclear level densities, $\rho(E_A, J_A, \pi_A)$, up to the channel separation energy S_a . An expression for $T_b(E, J, \pi)$ is obtained analogously. The single particle transmission coefficients $T_{lS}(E)$ (see Eq. 4.15) are calculated by solving the Schrödinger equation with an optical potential for the particle-nucleus interaction, for the case of neutrons we employ the optical potential given by [147]. The dominant γ -transitions ($E1$ and $M1$) have to be included in the calculation of the photon width [148]. The smaller, and therefore less important, $M1$ transitions via a single particle approach ($T_{M1} \propto E^3$ [149]). The $E1$ transitions are usually calculated on the basis of the Lorentzian representation of the giant dipole resonance (GDR) [148, 53]. For a detailed description of the approach utilised to calculate the γ -transmission coefficients for the cross section determination, the reader is referred to [145].

4.1.2.3. Applicability of the Statistical Model

In order to be able to apply the Hauser-Feshbach model, one needs a sufficiently large number of levels within the compound nucleus in a certain energy interval. The states in this interval can act as “doorway” states to the formation of the compound nucleus. In other words, The Hauser-Feshbach model is only valid if the nucleus to be describe contains many overlapping resonances at the compound excitation energy so that you can treat it statistically, i.e., it is required that $\Delta E \gg D$ or $\Delta E \cdot \rho \gg 1$. The critical level density is usually estimated between 5 and 10 levels per MeV [148]. Furthermore, the compound nucleus picture will only dominate when the energy of the incident particle is low enough (<20 MeV) [17]. In case of neutron capture, this energy range is around the compound nucleus excitation energy given by the sum of the incident neutron’s kinetic energy E_n plus the neutron separation energy S_n in the compound, i.e.

$$E_{CN}^* = E_n + S_n \quad (4.31)$$

Intuitively, the Statistical Model cannot be applied to describe:

- light nuclei, as they contain rather small number of levels ($A \leq 60$)
- magic nuclei, as they exhibit particularly small level densities due to the shell-gaps.
- very exotic nuclei for which the separation energy becomes too low, (S_n) ≈ 0 .

In the aforementioned cases, single resonances or direct capture will become significant and have to be treated individually, this goes beyond of the scope of the current research. For the interested reader, the range applicability of the statistical model for all nuclei relevant for the so called r-process nucleosynthesis has been extensively studied by Rauscher et al. [148].

4.1.2.4. Level densities

In what follows a brief description of the calculation of level densities is given stressing the relevance of the knowledge of the nuclear masses through the binding energies $BE(N, Z)$. For the most simplest system with A particles with an excitation energy E , the number of levels per energy interval, i.e., the level densities is given by

$$\rho(A, E) = \frac{dN(A, E)}{dE} \quad (4.32)$$

Starting from the experimental observations at low energies, it is well known that level densities should grow exponentially with the excitation energy E moreover by using the Fermi gas model and adding an empirical correction for pairing correlations one finds the following expression:

$$\rho(E, J, \pi) = \frac{1}{2} \times \frac{\sqrt{\pi} \exp[2\sqrt{a(E - \Delta)}]}{12 a^{1/4}(E - \Delta)^{5/4}} \times \frac{2J + 1}{2\sqrt{2\pi}\sigma^3} \exp\left[-\frac{(J + 1/2)^2}{2\sigma^2}\right], \quad (4.33)$$

where $\Delta(N, Z) = \frac{1}{4}(4BE(N, Z) - [BE(N-1, Z) + BE(N+1, Z) + BE(N, Z-1) + BE(N, Z+1)])$ defines the pairing gap, σ is the spin cutoff parameter and the so-called level density parameter including shell corrections via the Ignatuk formula [150] is given by

$$a(N, Z, E) = (\alpha A + \beta A^{2/3}) \times \left[1 + BE_{th}^{mic}(N, Z) \frac{1 - \exp(-\gamma E)}{E} \right], \quad (4.34)$$

α , β and γ are parameters to be obtained from fitting to experimental data. In the previous expression the variation of a with the excitation energy is completely govern by the sign of the shell corrections $BE_{th}^{mic}(N, Z)$ which presents by far the largest uncertainties in the description of nuclear reaction rates in the statistical model [17, 148]. By taking the shell corrections from FRDM [18] we can extend the calculation of the same for any theoretical model as follows:

$$BE_{th}^{mic}(N, Z) = [BE_{th}(N, Z) - BE_{FRDM}(N, Z) + BE_{FRDM}^{mic}(N, Z)], \quad (4.35)$$

with $BE_{FRDM}^{mic}(N, Z) = [BE_{FRDM}(N, Z) - BE_{FRDM}^{mac}(N, Z)]$.

4.2. Astrophysical Reaction Rates

In general, a target, a , and a projectile, A , follow some distribution of velocities, in which case the number of reactions per cm^3 and per second, i.e., the rate $r_{A,a}$, for the process depicted in Eq. 4.10 is given by [151]

$$r_{A,a} = \int \sigma(v_{A,a}) v_{A,a} d^3 n_A d^3 n_a, \quad (4.36)$$

where $v_{A,a} = |v_A - v_a|$ is the relative velocity of particles A and a . The evaluation of this integral depends of the type of particles and distributions involved. Nuclei A and a in an astrophysical plasma follow a Maxwell-Boltzmann distribution, thus

$$d^3 n = n \left(\frac{m}{2\pi kT} \right)^{3/2} \exp \left(-\frac{mv^2}{2kT} \right) d^3 v, \quad (4.37)$$

4.2.1. Reactions with particles of similar mass

when the mass of the particles that participate in the reaction is similar, one can rewrite Eq. 4.38 as

$$r_{A,a} = \langle \sigma v \rangle_{A,a} n_A n_a \equiv \langle A, a \rangle n_A n_a, \quad (4.38)$$

where $\langle \sigma v \rangle_{A,a}$ is the velocity integrated cross section. In other words the nuclear reaction rate per particle pair, at a given stellar temperature T^* is determined by folding the reaction cross section with the Maxwell-Boltzmann (MB) velocity distribution of the projectiles [152, 153]

$$\begin{aligned} \frac{r_{A,a}}{n_A n_a} &= \langle \sigma^* v \rangle_{A,a} \equiv \langle A, a \rangle^* \\ &= \left(\frac{8}{\pi \mu_{A,a}} \right)^{1/2} \frac{1}{(kT^*)^{3/2}} \int_0^\infty E \sigma_{a,b}^*(E) \exp(-E/kT^*) dE, \end{aligned} \quad (4.39)$$

For charged particle interactions, the reaction cross section depends critically in the Coulomb barrier and for low energies the reaction is only possible via the tunnel effect, the quantum mechanical penetration through a barrier at a classically forbidden energy. [156].

4.2.2. Photodissociation, decays and weak interaction rates

When the particle a in Eq. 4.38 is a photon, its distribution is given by the Plank distribution,

$$d^3 n_\gamma = \left(\frac{8\pi}{c^3 \hbar^3} \right) \frac{E_\gamma^2}{\exp(E_\gamma/kT^*) - 1} dE_\gamma. \quad (4.40)$$

Furthermore, its relative velocity is always c and the number of reactions per cm^3 and per second is simply

$$r_A = \frac{\int d^3 n_A}{\pi^2 (c\hbar)^3} \int_0^\infty \frac{c \sigma(E_\gamma) E_\gamma^2}{\exp(E_\gamma/kT^*) - 1} dE_\gamma \equiv \lambda_{A,\gamma}(T) n_A. \quad (4.41)$$

Luckily there is, no need to directly evaluate the photo-disintegration cross sections, because they can be expressed by detailed balance in terms of the capture cross section for

the inverse reaction, i.e., $b + B \rightarrow M + \gamma$ see [17, 152]. In the last expression “A” was replaced by “M” to avoid confusions in further derivations.

$$\lambda_{M,\gamma}(T) = \left(\frac{G_B G_b}{G_M} \right) \left(\frac{A_B A_b}{A_M} \right)^{3/2} \frac{(2j_B + 1)(2j_b + 1)}{(2j_M + 1)} \times (T^*)^{3/2} \cdot F \\ \times N_A \langle b, B \rangle^* \cdot \exp(-Q_{Bb}/kT^*), \quad (4.42)$$

where $G_k = \sum_i (2J_i + 1) \exp(-E_i/kT^*)$ is the so called partition function, which account for the population of the excited states in the nucleus, k is the Boltzmann constant, N_A is Avogadro’s number, J and A are spins and masses A (in atomic mass units u) of the particles involved in the reaction, T^* the temperature, $N_A \langle b, B \rangle^*$ the inverse reaction rate and $Q_{bB} = (m_b + m_B - m_j)c^2$ the reaction Q-value. In order to express the photodissociation rate, $\lambda_{M,\gamma}$, in s^{-1} , using the usual practical units, i.e. temperatures $T_9 = T^*/10^9$ K and $N_A \langle b, B \rangle^*$ in $\text{cm}^3 \text{s}^{-1} \text{mole}^{-1}$, one obtains the following numerical value for factor F in the above equation:

$$(T^*)^{3/2} \cdot F = \left(\frac{ukT^*}{2\pi\hbar^2} \right)^{3/2} \frac{1}{N_A} = T_9^{3/2} \cdot 9.8685 \times 10^9 \text{mole cm}^{-3} \quad . \quad (4.43)$$

We can follow a similar procedure to that for Eq. 4.42 to obtain electrons/positrons capture rates by nuclei (for positrons in thermal equilibrium with photons, electron and nuclei), because the electron is almost 2000 times less massive than a nucleon. The resulting electron capture rates will depend on the Temperature, T , and the electron number density, n_e , because depending on the astrophysical conditions the distribution of velocities of the electrons can be assumed to be Maxwellian, Boltzmann or even a degenerate Fermi distribution, i.e.,

$$r_{M,e} = n_M \int \sigma_e(v_e) v_e dn_e = \lambda_{M,e}(T, n_e) n_M. \quad (4.44)$$

In the case of normal decays, i.e., β or α -decay, with a characteristic half life $\tau_{1/2}$, Eqs. 4.41 and 4.44 also applies with the decay constant $\lambda = \ln 2 / \tau_{1/2}$ [151].

At densities of the order of $\rho \sim 10^{13} \text{g/cm}^3$, even though the size of the ν -scattering cross section on nuclei and electrons is very small, enough scattering events occur to thermalize the neutrino distribution. Under such conditions the inverse process of electron-capture, i.e., neutrino capture can occur in significant numbers, and such rates can be computed via Eq. 4.44, integrating over the thermal neutrino distribution or determining them via detailed balance from the electron and positron capture rates. In the same way, one can express the rates for inelastic neutrino scattering [90, 151].

4.2.3. Stellar enhancement factor

As laboratory cross sections always consider the target being in the ground state, for astrophysical applications, we have to correct them for the stellar enhancement effect due to thermal excitation of the target [17]. The stellar enhancement factors (SEF) f^* are defined by

$$f^* = \frac{\sigma^*}{\sigma_{lab}}, \quad (4.45)$$

and they are given in tables for a range of temperatures for nuclei close to stability.

4.3. Results: MOD-SMOKER

This section deals with results of the calculations of n-capture rates, $N_A \langle \sigma v \rangle^*$, using the code MOD-SMOKER (see [154] which includes changes and updates from the code NON-SMOKER due to Rauscher and Thielemann [17] which itself is derived from the well-known SMOKER code originally developed by Thielemann [155]). The following results involve calculations over more than 4000 targets, spanning from Zr (Z=40) to Bi (Z=83).

4.3.1. Preliminary details

The advantage of using the code NON-SMOKER/MOD-SMOKER is that it contains all the experimental information available for the calculation of the astrophysical reaction rates; i.e., nuclear masses and experimental levels. The additional information needed for the code MOD-SMOKER to compute the neutron capture rates is the following:

1. For the known experimental levels and the description of the E1 component of the γ -width we used the Reference Input Parameter Library (RIPL2 [157] and RIPL3 [158]).
2. The optical potentials for neutrons were taken from [147].
3. Nuclear level density (from [148]). Assuming that parity is evenly distributed, i.e., at each excitation energy there are equal number of states of positive and negative parity, for more details see [146].
4. Different mass models were used:
 - Finite range drop model (FRDM [18]).
 - Hartree-Fock-Bogoliubov (HFB21 [46]).
 - Skyrme-Weisäcker model (WS3 [19]).
 - Duflo-Zuker mass formula with 10 parameters (DZ10 [84]).
 - Duflo-Zuker mass formula with 31 parameters (DZ31 [20]).

4.3.2. Analytic neutron capture rate fits

Neutron capture rates have been computed, for a temperature grid of 24 points: $T_9 = 0.1, 0.15, 0.2, 0.3, 0.4, 0.5, 0.6, 0.7, 0.8, 0.9, 1.0, 1.5, 2.0, 2.5, 3.0, 3.5, 4.0, 4.5, 5.0, 6.0, 7.0, 8.0, 9.0$ and 10.0 , which were fitted by the following seven parameters expression [17]:

$$N_A \langle \sigma v \rangle^* \left. \vphantom{N_A \langle \sigma v \rangle^*} \right\} \lambda_{\gamma,n} = \exp \left(a_0 + a_1 T_9^{-1} + a_2 T_9^{-1/3} + a_3 T_9^{1/3} + a_4 T_9 + a_5 T_9^{5/3} + a_6 \ln T_9 \right), \quad (4.46)$$

where a_i are free parameters and the stellar temperature T_9 is given in 10^9 K. This parametrization proves to be flexible enough to accommodate the different temperature dependencies of the various reaction types across the fitted temperature range of $0.1 \leq T_9 \leq 10$. [17]. To make sure that the parametrization will be valid for our needs, we decided to add $T_9(n=0) = 0.01$ and $T_9(n=25) = 100$ to the grid as follows (from now on, n represent the n-th point in the grid):

- For $T_9(n=0) = 0.01$ we simple take $N_A \langle \sigma v \rangle^* \Big|_{T_9(0)} = N_A \langle \sigma v \rangle^* \Big|_{T_9(1)}$

- For $T_9(n = 25) = 100$, we have to assure that the reaction rates don't diverge. We implemented a linear extrapolation to obtain the $\text{Log}_{10} \left[N_A \langle \sigma v \rangle^* \Big|_{T_9(25)} \right]$.

4.3.3. Parameters for the photodissociation rates

As already mentioned in section 4.2.2, one can rely on detailed balance to calculate the reverse rate of the n-capture rate, $N_A \langle \sigma v \rangle^*$, i.e. the photodissociation rate, $\lambda_{\gamma,n}$, Eq. (4.46) is employed and the seven parameters $a_0^{\text{rev}} - a_6^{\text{rev}}$ for the reverse rate are determined as follows:

$$\begin{aligned}
 a_0^{\text{rev}} &= a_0 + \log \left[F \cdot \frac{(2j_B + 1)(2j_n + 1)}{(2j_M + 1)} \cdot \left(\frac{A_B A_n}{A_M} \right) \right] \\
 &= a_0 + \log \left[9.8685 \cdot \frac{(2j_B + 1)(2j_n + 1)}{(2j_M + 1)} \cdot \left(\frac{A_B \cdot 1.008664 \text{ u}}{A_M} \right) \right] \\
 a_1^{\text{rev}} &= a_1 - Q_{nB}/k = a_1 - 11.6045 \cdot Q_{nB} \\
 a_2^{\text{rev}} &= a_2 \\
 a_3^{\text{rev}} &= a_3 \\
 a_4^{\text{rev}} &= a_4 \\
 a_5^{\text{rev}} &= a_5 \\
 a_6^{\text{rev}} &= a_6 + 1.5
 \end{aligned} \tag{4.47}$$

The above relations are derived from Eqs. (4.39) and (4.42), using Eq. (4.46) and taking the logarithms on both sides. A_B (A_M) stands for the mass A of the residual (target) nucleus (in atomic mass units u) and $Q_{nB} = (m_n + m_B - m_M)c^2$ the reaction Q-value. Finally, for the reverse reaction case, *the value found by application of Eqs. (4.46) and (4.47) has to be multiplied by the ratio of the partition functions for residual and target nucleus G_B/G_M .*

4.3.4. Computed rate sets

In chapter 2, it was shown that most of the theoretical models for calculation of nuclear masses predict different trends for exotic nuclei, i.e., deformations, shell corrections and shell gaps. In addition, in previous sections in this chapter we learned that the knowledge of the nuclear masses is required to perform calculations of the neutron capture rates. In order to explore the role of the nuclear masses, four different sets of neutron capture rates have been calculated. They differ in the mass model used, which enters into the computation of the separation energies and Q-values as well as into the microscopic input to the level density calculation (see section 4.1.2.4). It is worth to be mentioned, that to perform the calculation of the n-capture rates we used experimental masses taken from [32] whenever available. For those regions in which there is no experimental information, the calculations are based on the sets of masses previously explored in chapter 2, corresponding to the FRDM, WS3, DZ10 and DZ31 mass models respectively. As the DZ10 and DZ31 mass models don't provide any deformation parameters, in order to perform the calculations we took the set of deformation parameters provided by FRDM.

4.3. RESULTS: MOD-SMOKER

4.3.4.1. Global features

In order to compare the results obtained in the present work with previous calculations available in the literature, we have chosen to display the following ratio between different set of n-capture rates, i.e.,

$$\Gamma_{i,SMOKER} = \frac{N_A \langle \sigma v \rangle_i^*}{N_A \langle \sigma v \rangle_{SMOKER}^*} \quad (4.48)$$

where i , represents the different mass models used in the present work, and SMOKER stands for the calculation performed by Rauscher [17], where the set of FRDM masses was used. The grid point corresponding to a temperature of $T=1\text{GK}$ was selected due to its relevance in the evolution of the r-process.

It was already mentioned, that because of some changes and updates in both the MOD-SMOKER code and its inputs, it is expected that even when using the same set of masses, the comparison between our results and those taken from [17] will differ. Most of the updated input data were taken from the Reference Input Parameter Library (RIPL2 [157] and RIPL3 [158]). For a summary of changes and updates to MOD-SMOKER/NON-SMOKER, the interested reader is referred to [154].

The uppermost panel of Fig. 4.3), display a comparison between the two sets of neutron capture rates based on the set FRDM masses, showing that our calculations, tend to overestimate the original neutron capture rates for nuclei with $N=Z$ (redish boxes) and also those in the neutron deficient side (greenish boxes).

On the other hand, when a comparison of the computed n-capture rates is done between different set of masses, we notice that similarly to the upper panel of Fig. 4.3, our calculations tend to overestimate the original neutron capture rates for nuclei with $N=Z$ (redish boxes) and also those in the neutron deficient side (greenish boxes). Most of the calculated rates based on DZ10, DZ31 and WS3 are smaller when compared to those of Rauscher et al. [17] at the n-rich side (dark blue region in the three lower panels in Fig. 4.3). However, there are certain regions, in particular right before and after the $N=82$ and $N=126$ shell closures and around $N \approx 164$ (see redish and greenish regions), in which our rates present larger values than those of the set of Rauscher [17]. This feature seems to be related with an anomalous behaviour appearing before and after the shell closures at $N=82$ and 126 in the systematics of $S_{2n}/2$ based on the FRDM masses (see section 2.2.5, in particular Fig. 2.8).

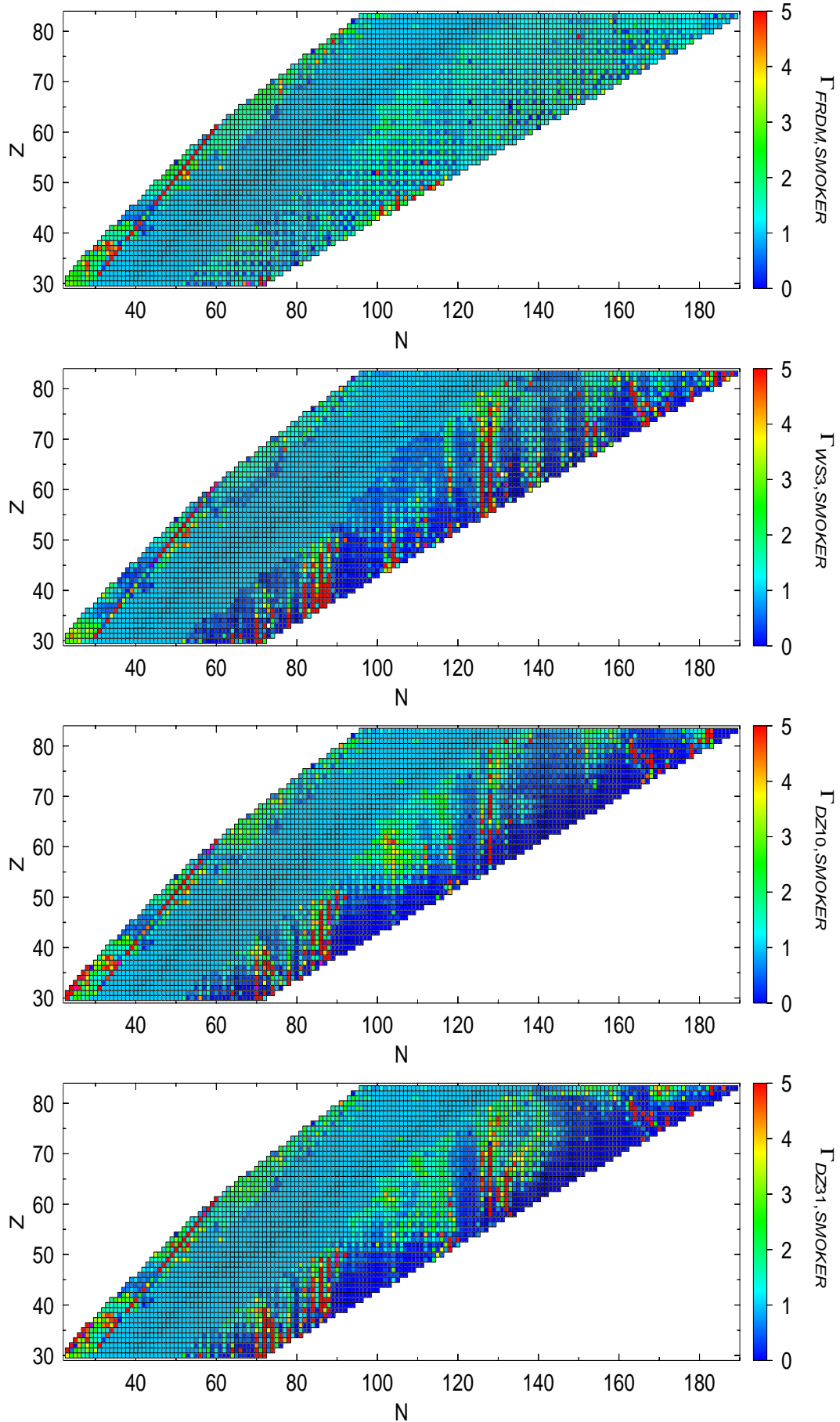


Figure 4.3: Ratio of n-capture rates of 4 investigated mass models (FRDM, WS3, DZ10 and DZ31) to those from [155] at a temperature $T = 1\text{GK}$. Experimental masses were used when available.

4.3.4.2. Local features

Fig. 4.4 displays a comparison of n-capture rates (at a temperature $T=1\text{GK}$) and the one-neutron separation energies for a number of representative isotopic chains in the region of relevance for the r-process, i.e., Pd ($Z=46$), Ag ($Z=47$) and Cd ($Z=48$). The comparison is done, using the following mass models: FRDM (black lines), WS3 (blue lines), DZ10 (red lines), DZ31 (orange lines) and the previously n-capture rates computed in [155] are shown by dashed lines. Only to guide the eye, dotted lines are added at $S_{1n} = 0$. For illustrative purposes, in each isotopic chain an r-process region is also shown. This region is arbitrarily defined to contain only those nuclei with one-neutron separation energies spanning from $0 < S_{1n} < 3\text{ MeV}$, for isotopic chains based on FRDM such definition is meaningless (see below).

Let us first consider the results for the isotopic chains of Pd, Ag and Cd based on the set of FRDM masses. Our calculations (black filled lines) and those obtained by Rauscher et al (back dashed lines) are in agreement between each other and suggest that the capture of the free available neutrons in the r-process region is hindered due to the anomalous behaviour of the one-neutron separation energies, S_{1n} , around $N \sim 90$ (see Fig. 2.8). In fact, when the one-neutron separation energy becomes negative, a drop of four orders of magnitude in the neutron capture rate is observed. In upcoming sections we will learn that such a feature has important consequences in the evolution and the final distribution of the abundances in an r-process.

Moreover, we notice by looking at the systematics of S_{1n} for mass models different than FRDM displayed in Fig. 4.4, that such a feature in S_{1n} around $N \sim 90$, is absent, allowing them to continue capturing the free available neutrons in the ambient up to the point when the one-neutron separation energy turns negative favouring the neutron emission channel. The similar behaviour in the systematics for the one-neutron separation energies, S_{1n} , between the DZ like mass models translate in similar neutron-capture rates. The S_{1n} of WS3 present a slightly different behaviour than those of DZ mass models, for instance, in the Cd isotopes, one clearly noticed that the neutron-capture rates based on WS3 (blue line in the lowermost panel in Fig. 4.4) are always smaller than those of DZ mass models for the region $88 < N < 96$.

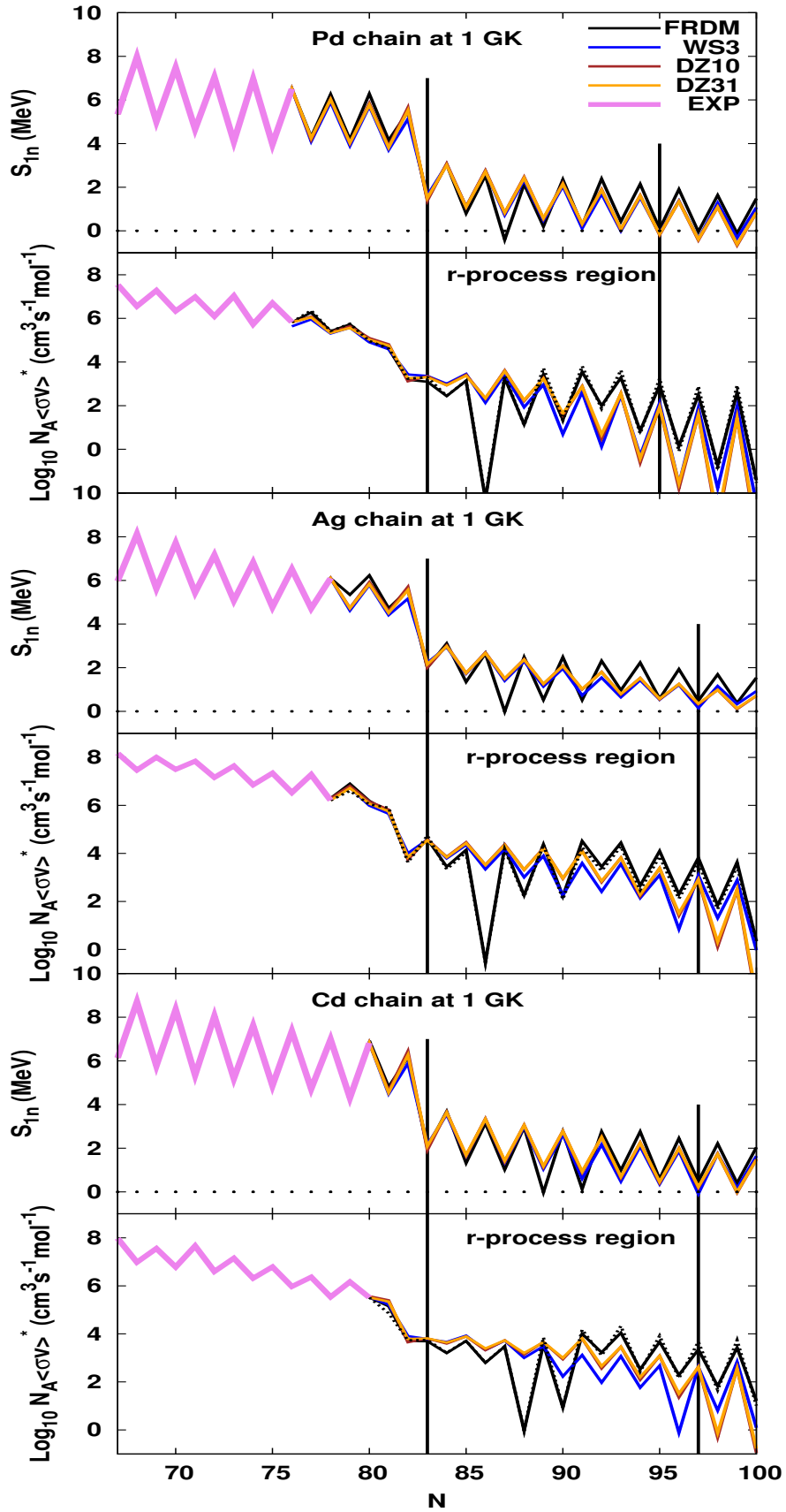


Figure 4.4: Comparison of the n-capture rates for a number of representative isotopic chains in the region of relevance for the r-process nucleosynthesis calculations, the rates are based on different mass models. The previously n-capture rates computed in [155] are shown by dashed lines.

Nuclear reaction network

In astrophysical simulations, it is required to track changes in the abundances of the participating nuclei due to thermonuclear reactions. These changes translate into an energy generation and nucleosynthesis. In order to simulate such changes, it is convenient to perform large scale network calculations. As we will see in this chapter, a nuclear reaction network is a set of coupled ordinary differential equations that links all participating nuclei.

For a given astrophysical environment, a whole variety of different reactions can occur simultaneously. For convenience, we divide all reactions into three categories based on their number of reactants. Decays, electron/positron captures, photodissociations, and neutrino induced reactions depend only on the number density of the targets nuclei. Fusion and radiative capture reactions involve two reactants, thus their reaction rates depend on the number density of both target and projectile nucleus. Reactions involving three nucleons are rare, but nonetheless important, such as the triple- α -process. Hence, we can write the change of the number density of each nuclear species i , in terms of the corresponding reaction rates, r , as [151]:

$$\left. \frac{\partial n_i}{\partial t} \right|_{\rho=\text{const}} = \sum_j \mathcal{N}_i(j)r_j + \sum_{j,k} \mathcal{N}_i(j,k)r_{j,k} + \sum_{j,k,l} \mathcal{N}_i(j,k,l)r_{j,k,l}, \quad (5.1)$$

where the coefficients \mathcal{N}_i 's are provided for properly accounting of the number of nuclei and are given by:

$$\begin{aligned} \mathcal{N}_i(j) &= \pm N_i, \\ \mathcal{N}_i(j,k) &= \pm \frac{N_i}{(|N_j|!|N_k|!)}, \\ \mathcal{N}_i(j,k,l) &= \pm \frac{N_i}{(|N_j|!|N_k|!|N_l|!)}. \end{aligned} \quad (5.2)$$

The numerator in Eqs. 5.2 quantifies how many particles of species i are created (+) or destroyed (-) in the reaction. The denominator avoids double counting of reactions when identical particles react.

As we are only interested in changes caused by reactions, not in density variations, it results convenient to introduce the abundance of species i as $Y_i = \frac{n_i}{\rho N_A}$, where N_A is Avogadro's number, and ρ the mass density, respectively. Moreover, we express the involved rates as follows:

- In the case of one body reactions, i.e. decays, photo-disintegration, electron and positron capture reactions via $r_i = \lambda_i Y_i$

- For the two and three particle reactions (fusion, radiative capture, etc.) via $r_{i,j} = N_A^2 \rho^2 \langle i, j \rangle Y_i Y_j$ and $r_{i,j,k} = N_A^3 \rho^3 \langle i, j, k \rangle Y_i Y_j Y_k$.

Finally, one obtain , the rate of change of nuclear abundances Y_i :

$$\begin{aligned} \dot{Y}_i = \frac{dY_i}{dt} &= \sum_j \mathcal{N}_i(j) \lambda_j Y_j + \sum_{j,k} \mathcal{N}_i(j,k) \rho N_A \langle j, k \rangle Y_j Y_k \\ &+ \sum_{j,k,l} \mathcal{N}_i(j,k,l) \rho^2 N_A^2 \langle j, k, l \rangle Y_j Y_k Y_l. \end{aligned} \quad (5.3)$$

The above expression represents our reaction network equations, which are constrained to fullfil mass conservation (5.4):

$$\sum_i A_i Y_i = 1. \quad (5.4)$$

5.1. Application: r-process nucleosynthesis

In the present thesis, we are mostly interested in r-process nucleosynthesis. In this case, the evolution of the abundances is mainly determined by neutron capture, photo-disintegration and β -decay processes. The reaction network equation that determines the change of the abundance of a nucleus with charge Z and mass number A is given by [10]:

$$\begin{aligned} \frac{dY(Z,A)}{dt} &= n_n \langle \sigma v \rangle_{n,\gamma}(Z,A-1) Y(Z,A-1) + \lambda_\gamma(Z,A+1) Y(Z,A+1) \\ &+ \sum_{j=0}^J \lambda_{\beta j n}(Z-1,A+j) Y(Z-1,A+j) \\ &- \left(n_n \langle \sigma v \rangle_{n,\gamma}(Z,A) + \lambda_\gamma(Z,A) + \sum_{j=0}^J \lambda_{\beta j n}(Z,A) \right) Y(Z,A), \end{aligned} \quad (5.5)$$

where $n_n = \rho N_A Y_n$ is the neutron number density, $\langle \sigma v \rangle_{n,\gamma}(Z,A)$ is the thermally averaged neutron-capture rate and $\lambda_\gamma(Z,A)$ represents the photodissociation rate for a nucleus ${}^A Z$, while $\lambda_{\beta j n}(Z,A)$ is the β^- decay rate of ${}^A Z$ with the emission of j delayed neutrons (up to a maximum of J). Note, that the photodissociation rate is related to the neutron capture rate by detailed balance (Eq. 4.42). This yields the following relation:

$$\lambda_\gamma(Z,A+1) = \langle \sigma v \rangle_{n,\gamma}(Z,A) \left(\frac{m_u k T}{2\pi \hbar^2} \right)^{3/2} \left(\frac{2G(Z,A)}{G(Z,A+1)} \right) \left(\frac{A}{A+1} \right)^{3/2} \exp(-S_n(Z,A+1)/kT), \quad (5.6)$$

where G 's are the partition functions and the neutron separation energies are expressed by

$$S_n(Z,A+1) = m_n + M(Z,A) - M(Z,A+1) = BE(Z,A+1) - BE(Z,A), \quad (5.7)$$

with m_n the neutron mass and $M(Z,A)$ the mass of the nucleus ${}^A Z$, In the last equation we have used the definition of the binding energy of a nucleus ${}^A Z$, i.e., $BE(Z,A) = Z m_p + (A-Z) m_n - M(Z,A)$.

Assuming that the neutron abundance Y_n varies slowly enough, i.e., the neutron density n_n is constant over a time step, then each isotopic chain in the network can be solved sequentially, beginning with the lowest Z [159]. Unfortunately, this approximation becomes

5.1. APPLICATION: R-PROCESS NUCLEOSYNTHESIS

unstable when the neutron abundances becomes small ($Y_n \leq 10^{-5}$). Therefore, it is advisable to include in the set of differential equations the one determining the change of the neutron abundance:

$$\frac{dY_n}{dt} = \sum_{Z,A} \left[\lambda_\gamma(Z,A) + \left(\sum_{j=1}^J j \lambda_{\beta j n}(Z,A) \right) - n_n \langle \sigma v \rangle_{n,\gamma}(Z,A) \right] Y(A,Z). \quad (5.8)$$

Eqs. 5.5 and 5.8 allow for several approximations which are valid depending on the astrophysical conditions. These approximations will be briefly covered in the sections 5.1.1 and 5.1.2.

5.1.1. The waiting point approximation

In the classical r-process calculations [6], the main assumption was the $(n, \gamma) \rightleftharpoons (\gamma, n)$ equilibrium, provided that neutron-densities ($n_n \gtrsim 10^{20} \text{ cm}^{-3}$) and temperatures ($T \gtrsim 1 \text{ GK}$) [159] are large enough to ensure that both neutron-capture and photodissociation rates are of the same order and much larger than the β -decay rates (time scales) for all the participating nuclei in the network, i.e., $\rho N_A \langle \sigma v \rangle \approx \lambda_\gamma \gg \lambda_\beta$ ($\tau_{n,\gamma} \approx \tau_{\gamma,n} \ll \tau_\beta$). Under such conditions, the typical time scales of neutron-captures are of the order of 10^{-4} s, whereas β -decays of the most abundant nuclei act on timescales of 10^{-1} to 10^{-3} s. Neglecting the small β -decay rates, the evolution of the system (Eq. 5.5) reduces to:

$$\frac{dY(Z,A)}{dt} = \lambda_\gamma(Z,A+1)Y(Z,A+1) - n_n \langle \sigma v \rangle_{Z,A} Y(Z,A). \quad (5.9)$$

Since nuclear reactions occur much faster than hydrodynamical processes, an equilibrium is expected to happen within an Isotopic chain,

$$\frac{dY(Z,A)}{dt} = 0 \implies \frac{Y(Z,A+1)}{Y(Z,A)} = \frac{n_n \langle \sigma v \rangle_{Z,A}}{\lambda_{Z,A+1}}, \quad (5.10)$$

As pointed out before, this approximation is known as $(n, \gamma) \rightleftharpoons (\gamma, n)$ equilibrium or “*waiting point approximation*”. Moreover, invoking the detailed balance principle (see Eq. ??), Eq. 5.10 can be written as:

$$\frac{Y(Z,A+1)}{Y(Z,A)} = n_n \left(\frac{2\pi\hbar^2}{m_u kT} \right)^{3/2} \left(\frac{A+1}{A} \right)^{3/2} \frac{G(Z,A+1)}{2G(Z,A)} \exp [S_n(Z,A+1)/kT], \quad (5.11)$$

which relates the abundance ratio of two neighbouring isotopes within one isotopic chain. An additional feature is that under the *waiting point approximation* no detailed knowledge of the capture or photodissociation rates is required. The only nuclear input required, are the nuclear masses through the neutron separation energies (S_n), due to its exponential behaviour in Eq. 5.11, the abundance maxima within an isotopic chain is very sharp. This abundance maxima in turn determines the *waiting points*. In fact, the set of waiting point nuclei constitutes the **r-process path**. The rest of abundances within an isotopic chain depends on the astrophysical conditions. However, due to the pairing effect, the most abundant isotopes are always those with an even number of neutrons.

By setting the left hand side of Eq. 5.11 to 1 and neglecting any small difference in both mass numbers and partitions functions, one finds the most abundant isotope within an

isotopic chain, which results in a value of S_n^0 which is the same for all abundance maxima in each isotopic chain for a given neutron density, n_n and temperature, T [10]:

$$S_n^0 \approx kT \cdot \log \left(\frac{2}{n_n} \left(\frac{m_u kT}{2\pi\hbar^2} \right)^{3/2} \right) = \frac{T_9}{5.09} \left(34.075 - \log(n_n) + \frac{3}{2} \log(T_9) \right), \quad (5.12)$$

where T_9 is the temperature in units of 10^9 K and n_n the neutron number density in cm^{-3} . Eq. 5.12, implies that the r-process proceeds along lines of constant separation energies towards heavy nuclei. Plugging typical r-process conditions, i.e., $T_9 = 1$ GK and $n_n = 10^{24} cm^{-3}$ one obtains $S_n^0 \approx 2.8$ MeV. Following [159], it may be more appropriate to characterise the most abundant isotope as having a two neutron separation energy given by

$$S_{2n} = 2 \cdot S_n^0. \quad (5.13)$$

This is possible because we can always write $S_{2n}(Z, A) = S_n(Z, A+2) + S_n(Z, A)$, and assume that $S_n(Z, A+2) \sim S_n(Z, A)$. Then we obtain Eq. 5.13. The nice features of using S_{2n} 's is that the pairing effect is no longer present and the large jumps in the S_{2n} 's are correlated with the presence of the magic numbers. In fact, we will show later that the r-process nuclei near the magic numbers have a neutron separation energies much larger than the typical S_n^0 , which means that the r-process path moves closer to stable nuclei.

Up to this point, we have only described the time-evolution within one isotopic chain, neglecting the fact that isotopic chains are connected by β -decays. In order to illustrate this flow, and following [93], let us introduce the total abundance for each chain by

$$Y(Z) = \sum_A Y(Z, A), \quad (5.14)$$

where the individual abundances $Y(Z, A)$ can be expressed via

$$Y(Z, A) = P(Z, A)Y(Z), \quad (5.15)$$

where $P(Z, A)$, stands for the so-called individual population coefficients, which can be calculated from the equilibrium condition given by Eq. 5.11 (normalised to one). In the waiting point approximation Eqn. 5.5 can be finally written as:

$$\begin{aligned} \frac{dY(Z)}{dt} &= Y(Z-1) \sum_A P(Z-1, A) \lambda_\beta(Z-1, A) - Y(Z) \sum_A P(Z, A) \lambda_\beta(Z, A) \\ &= \lambda_\beta^{eff}(Z-1)Y(Z-1) - \lambda_\beta^{eff}(Z)Y(Z), \end{aligned} \quad (5.16)$$

where the effective β -decay rates have been introduced as:

$$\lambda_\beta^{eff}(Z) = \sum_A P(Z, A) \lambda_\beta(Z, A) = \frac{\sum_A \lambda_\beta(Z, A) Y(Z, A)}{\sum_A Y(Z, A)}. \quad (5.17)$$

In this case the r-process evolution is independent of the neutron capture and photodisso- ciation rates, only β -decay rates are needed in Eq. 5.16 and nuclear masses in Eq. 5.11.

5.1. APPLICATION: R-PROCESS NUCLEOSYNTHESIS

Looking at Eq. 5.16, it becomes clear that in the *waiting point approximation*, the solution of the full reaction network is no longer required, therefore the size of the system decreases to the number of different isotopic chains involved [93, 90]. The neutron number density is governed by the fact that the total number of nucleons, free and bound in nuclei, is constant in time, i.e.:

$$Y_n (= \frac{n_n}{\rho N_A}) + \sum_{Z,A} AY(Z,A) = \text{constant} \quad (5.18)$$

5.1.2. Steady flow approximation

If the r-process proceeds in $(n, \gamma) \rightleftharpoons (\gamma, n)$ equilibrium and if its duration is larger than the β -decay lifetimes of the nuclei present, after a sufficient time, all nuclei in the network will approach a steady state abundance, denoted as steady β -flow [92] that satisfies, the following condition:

$$\frac{dY(Z)}{dt} = 0 \implies \lambda_{\beta}^{eff}(Z-1)Y(Z-1) = \lambda_{\beta}^{eff}(Z)Y(Z) \quad (5.19)$$

The steady β -flow has an important role in r-process calculations, which will be discussed in the upcoming chapters.

The r-process can also operate under conditions where the temperatures are so low that the photodissociation rates in Eq. 4.38 become negligible. Under these conditions the r-process operates under a competition of neutron captures and beta decays. If one neglects beta-delayed neutron emission, Eq. 4.38 can be reduced to two independent equations that govern the evolution of the total abundance along an isotopic change, $Y(Z) = \sum_A Y(Z,A)$ and along an isobaric chain, $Y(A) = \sum_Z Y(Z,A)$ [10]:

$$\frac{dY(Z)}{dt} = \lambda_{\beta}^{eff}(Z-1)Y(Z-1) - \lambda_{\beta}^{eff}(Z)Y(Z), \quad (5.20a)$$

$$\frac{dY(A)}{dt} = n_n \langle \sigma v \rangle_{n,\gamma}^{eff}(A-1)Y(A-1) - n_n \langle \sigma v \rangle_{n,\gamma}^{eff}(A)Y(A), \quad (5.20b)$$

where

$$\langle \sigma v \rangle_{n,\gamma}^{eff}(A) = \frac{\sum_Z \langle \sigma v \rangle_{n,\gamma}(Z,A)Y(Z,A)}{\sum_Z Y(Z,A)}. \quad (5.20c)$$

If the r-process duration is longer than β -decay and neutron-capture lifetimes, Eqs. 5.20a and 5.20b reaches an equilibrium denoted as steady flow that satisfies for each Z and A:

$$\frac{dY(Z)}{dt} = 0 \implies \lambda_{\beta}^{eff}(Z-1)Y(Z-1) = \lambda_{\beta}^{eff}(Z)Y(Z), \quad (5.21a)$$

$$\frac{dY(A)}{dt} = 0 \implies \langle \sigma v \rangle_{n,\gamma}^{eff}(A-1)Y(A-1) = \langle \sigma v \rangle_{n,\gamma}^{eff}(A)Y(A), \quad (5.21b)$$

In addition, as the r-process occurs under a competition of beta-decays and neutron captures we obtain:

$$n_n \langle \sigma v \rangle_{n,\gamma}^{eff}(A)Y(A) \approx \lambda_{\beta}^{eff}(Z)Y(Z). \quad (5.22)$$

As the abundances along an isotopic and isobaric chain are dominated by a single nucleus this condition determines also the nuclei that participate in the r-process, i.e. the r-process path [10]. While the steady flow approximation is not applicable as a fully dynamical calculation, it can be applied for calculations in which the neutron density only changes on time scales long in comparison to beta decay half lives [90].

5.1.3. Dynamic calculations

Dynamic models are required for the study of r-process conditions over a wide range of neutron number densities and temperatures. In such calculations, $(n, \gamma) \rightleftharpoons (\gamma, n)$ equilibrium is not assumed and the steady flow approximation is not used. The r-process path is determined by the competition between neutron captures and β -decay rates, which are determined for each nucleus as a function of the density and temperature. The r-process path therefore is affected both by the astrophysical conditions and by the nuclear properties of each nucleus participating in the network.

5.1.3.1. Numerical solution of the reaction network

Given an initial set of abundances $\vec{Y}(t_0) = \{Y_i(t_0)\}$, temperature $T(t_0)$ and density $\rho(t_0)$ the network equations can be integrated numerically, prior discretisation of Eq. 5.5

$$\frac{d\vec{Y}}{dt} = F(\vec{Y}), \quad (5.23)$$

the vector of abundances after a network time step, Δt , is given by $\vec{Y}(t_0 + \Delta t) = \vec{Y}_i(t_0) + \delta\vec{Y}$, where $\delta\vec{Y}$ represents a small change in the abundances. However, because of the wide range in time-scales between processes spanning strong, electromagnetic and weak reactions, the nuclear networks form an extraordinarily stiff system. For a stiff set of non-linear differential equations which forms most of the nuclear networks, a fully implicit treatment is generally most successful [160]. The implicit Euler-backward-differentiation method for our reaction network can be written as:

$$\frac{\delta\vec{Y}}{\Delta t} = F(\vec{Y} + \delta\vec{Y}), \quad (5.24)$$

eq. 5.24 is equivalent to finding the zeros of the set of non-linear equations:

$$G(\vec{Y}) = F(\vec{Y} + \delta\vec{Y}) - \frac{\delta\vec{Y}}{\Delta t} = 0. \quad (5.25)$$

This is done via the Newton-Raphson method, which is based on the Taylor series expansion of $F(\vec{Y} + \delta\vec{Y})$, with the trial change in abundances given by $\delta\vec{Y}$,

$$F(\vec{Y}) + \frac{\partial F(\vec{Y})}{\partial \vec{Y}} \delta\vec{Y} - \frac{\delta\vec{Y}}{\Delta t} = 0, \quad (5.26)$$

where $\frac{\partial F_i}{\partial Y_k}$ is the so-called Jacobian Matrix. The iteration procedure continues until a pre-determined level of convergence ($|\delta\vec{Y}| \leq \epsilon$) is achieved.

For larger networks, the Newton-Raphson method requires the solution of a moderately large matrix equation. However, as not every species reacts with each other, thus with

5.2. APPLICATION: ENERGY GENERATION

a few important exceptions, the dominant reactions involves the capture or release of n, p, α, γ [151]. In summary, as most entries in the Jacobian matrix are zero, such matrix belongs to a type known as “sparse matrices”. Consequently, the system of linear equations can be solved via a sparse matrix solver. As in [161], the PARallel sparse DIrect linear SOLver (PARDISO) has been applied in this work.

5.2. Application: Energy generation

All reactions occurring in an astrophysical plasma must conserve total energy and total momentum of the particles involved. However due to the fact that the rest mass energy of the particles involved is different for initial and final species, their kinetic energy must change. It is precisely, the change of kinetic energy what determines the energy liberated by the reaction [162].

Since the nuclear energy release is uniquely determined by the abundance changes, the rate of thermonuclear energy release, $\dot{\epsilon}$ is given by

$$\dot{\epsilon} = - \sum_i N_A m_i c^2 \frac{dY_i}{dt} = - \sum_i \frac{m_i c^2}{m_u} \frac{dY_i}{dt} \quad (\text{in units of MeVg}^{-1}\text{s}^{-1}) \quad (5.27)$$

where $m_i c^2$ is the rest mass energy of species i in MeV, N_A is Avogadro’s number and m_u is the atomic mass unit. The entropy change per unit time is given by [163]

$$T \frac{ds}{dt} = \frac{1}{k_B \cdot N_A} \left(\dot{\epsilon} - \sum_i \mu_i \frac{d}{dt} \left(\frac{n_i}{\rho} \right) \right) \quad (5.28)$$

where k_B is the Boltzmann constant. In this way the entropy, s , is given in units of k_B^{-1} baryon $^{-1}$, μ_i and n_i are the chemical potential and the number density of the i -th species, respectively. Inserting 5.27 in 5.28 and recasting terms, we obtain an entropy source term caused by nuclear reactions:

$$\frac{ds}{dt} = - \frac{1}{k_B T} \sum_i (m_i c^2 + \mu_i) \frac{dY_i}{dt} \quad (5.29)$$

From the previos expression, we conclude that as long as there are no transmutations of nuclei, $ds = 0$. Otherwise, nuclear binding energy is released and heats up the material. Adiabaticity implies Eq. 5.29.

Part II

Results

r-process network calculations: General features

The major goal of the present work is to study the role of the nuclear masses in r -process nucleosynthesis calculations. To accomplish such goal we have to merge a fully dynamical r -process network code with hydrodynamical simulations from different astrophysical sites, which are considered as r -process candidates.

This chapter is intended to be a short introduction for the upcoming chapters, in which results on the interplay between the different astrophysical sites and the different nuclear mass models are going to be presented. We start with a brief description of our network.

6.1. Description of the network

We use a dynamical r -process network that includes:

1. Neutron captures and photodissociation rates computed in the framework of the statistical model approach [155].
2. The theoretical β -decay rates were taken from [164].
3. We used the Viola-Seaburg formula to estimate the theoretical α -decay rates [165].
4. For the fission reactions, we included contributions from neutron-induced fission, β -delayed fission and spontaneous fission (see [166]). The fission yields were taken from [167, 168].

It's important to stress that we have always used experimental information when available. The resulting rates have been implemented in a fully implicit network, that includes 7362 nuclei from nucleons up to ^{213}Ds . The set of differential equations is linearized and solved using the Newton-Raphson method [151]. As in [161], the PARallel sparse Direct linear SOLver (PARDISO) is used to solve the resulting linear system of equations.

6.2. Hydrodynamical trajectories

In this thesis, the physical conditions to perform r -process calculations were taken from hydrodynamical trajectories from both high entropy ν -driven winds from CCSNe simulations [21] and the matter that becomes gravitationally unbound from the neutron star merger (NSM) simulations [22]. The evolution of such trajectories will be shown in the upcoming chapters.

6.2.1. Extrapolation to late times

For times that are larger than the hydrodynamical trajectory, an analytical expression is used. To obtain an analytical description of the ejecta, we assume a constant mass outflow rate

$$\dot{M} = 4\pi\rho r^2 \frac{dr}{dt} = \text{constant}. \quad (6.1)$$

This corresponds to the assumption that matter reaches an asymptotic constant velocity [169]. Under the further assumption that the density decreases as

$$\rho(t) = \rho(t_n) \left[\frac{\Delta + t_n}{\Delta + t} \right]^2, \quad \text{where } \Delta = -\frac{\sum_{i=n-10}^n \left(\frac{2}{\frac{d \ln \rho_i}{dt_i} + t_i} \right)}{10}, \quad (6.2)$$

where $\rho(t_n)$ and t_n represent the last values for the density and time taken from a given trajectory. The parameter Δ represents an average over the last ten values to guarantee a smooth transition from the original trajectory to the extrapolated one. Eq. 6.2 arises from the analysis of current simulation (e.g. [21]), in which it is observed that the density behaves almost constant for a short period of time and then decreases with t^{-2} [170, 169].

When energy generation is considered (see sections 5.2, all heating is self-consistently added to the entropy of the fluid (see 8.1). Finally, the system evolves up to time scales of the order of tens of Gigayears (around the age of the universe). For more details on network calculations the reader is referred to chapter 5 and to the literature [151].

6.3. Performing network calculations

6.3.1. Expansion from NSE

In addition to $\rho(t)$, the initial temperature T , electron fraction Y_e and seed properties ($\langle Z \rangle, \langle A \rangle$) are specified for a given calculation. In all our r-process network calculations the initial distribution of nuclei is found by starting from nuclear statistical equilibrium (NSE). A generic model for an r-process is based on the expansion of a material from high temperature T and high (mass) density ρ , for which all strong and electromagnetic reactions among free nucleons and nuclei occur so fast that the relative abundances of nuclei are given by NSE independently of the detailed dynamics of these reactions. This initial composition and the subsequent evolution of temperature and density determine the neutron-to-seed ratio ($R_{n/s} = \frac{Y_n}{Y_h}$) and ultimately the abundance pattern produce by the r-process [94]. In NSE, the abundance of $Y(Z, A)$ is given by:

$$Y(Z, A) = \frac{G(Z, A) A^{3/2}}{2^A} Y_n^{A-Z} Y_p^Z \times \left(\frac{2\pi\hbar^2}{m_u kT} \right)^{3(A-1)/2} \left(\frac{\rho}{m_u} \right)^{A-1} \exp \left[\frac{B(Z, A)}{kT} \right], \quad (6.3)$$

where $G(Z, A)$ and $B(Z, A)$ are the partition functions and binding energies of a given nucleus, Y_n and Y_p are the number fraction of neutron and protons, respectively, \hbar the Plank constant, m_u is the atomic mass unit, k is the bolzmann constant. The composition under NSE is subjected to constraints from conservation of baryon number and electric

6.3. PERFORMING NETWORK CALCULATIONS

charge:

$$Y_n + Y_p + 4 \cdot Y_\alpha + \sum_{Z,A} AY(Z,A) = 1 \quad \text{and} \quad Y_p + 2 \cdot Y_\alpha + \sum_{Z,A} ZY(Z,A) = Y_e \quad (6.4)$$

The summation runs from $Z > 2$ and $A > 4$ to avoid double counting of free nucleons and α particles. Y_e represents the electron fraction and $Y_\alpha = Y_{4\text{He}}$ is the fraction of α particles or ${}^4\text{He}$ nuclei.

6.3.2. Relevant variables and stages of the evolution

The evolution of the composition is followed with a dynamical r-process network. A crucial step is then to decide which variables besides the temperature (T) and neutron number density (n_n) deserve to be analysed in more detail and also which are the most relevant stages of the evolution of an r-process. Before starting this discussion and only for illustrative purposes, Fig. 6.1 displays an example of the evolution of relevant variables and stages for an arbitrary trajectory and an arbitrary mass model.

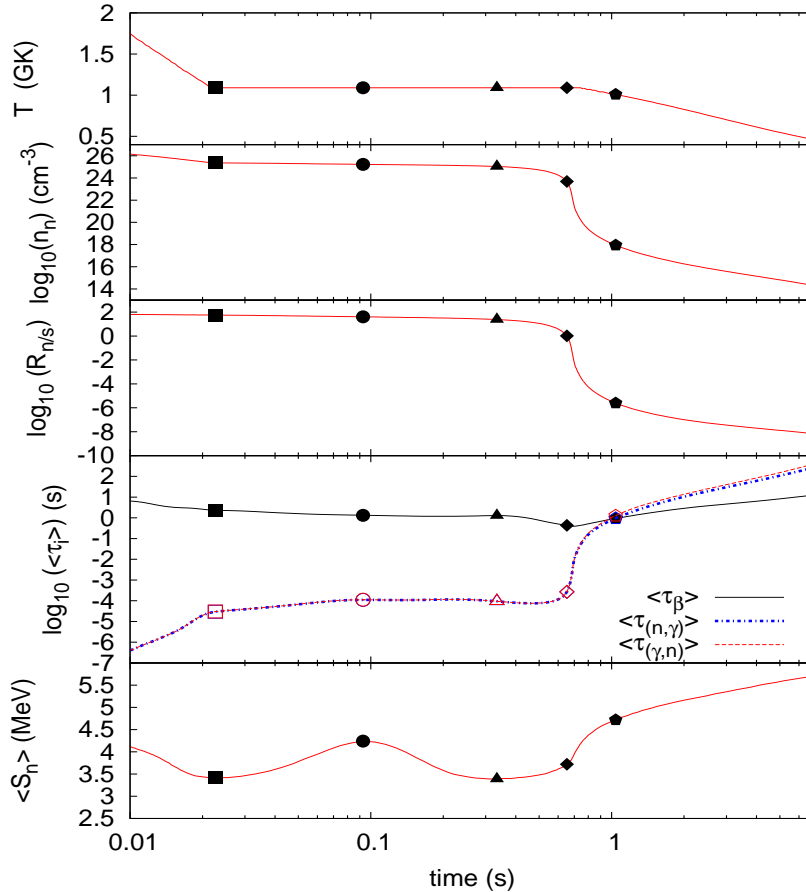


Figure 6.1: Evolution of the temperature T , the neutron number density n_n , the neutron-to-seed-ratio Y_n/Y_h , the average one-neutron separation energy $\langle S_n \rangle$ and the characteristic time-scales involving in the r-process, i.e., n-capture $\langle\tau_{(n,\gamma)}\rangle$ (dotted lines), photodissociation $\langle\tau_{(\gamma,n)}\rangle$ (dashed lines) and β -decay $\langle\tau_\beta\rangle$ (continuous lines). This results correspond to an arbitrary trajectory and an arbitrary mass model. Symbols are added on top of the lines that follow the evolution of the relevant variables to denote relevant stages in the evolution of the r-process (for further details see text).

First of all, it is convenient to find an average nucleus ($\langle Z \rangle$, $\langle A \rangle$), i.e. the most representative nucleus at any stage of the evolution of our system. Such nuclei is going to be defined as follows:

$$\langle Z \rangle = \frac{\sum_{Z,A} ZY(Z,A)}{\sum_{Z,A} Y(Z,A)}, \quad \langle A \rangle = \frac{\sum_{Z,A} AY(Z,A)}{\sum_{Z,A} Y(Z,A)}, \quad Y_h = \sum_{Z,A} Y(Z,A), \quad (6.5)$$

where the summation runs from $Z > 2$ and $A > 4$ and Y_h identify the fraction of heavy nuclei in the system (nuclei heavier than ${}^4\text{He}$ nuclei).

As in the present work we are mainly interested in the build-up of heavy nuclei by the so called ‘‘r-process’’, which involves a series of rapid neutron captures followed by β -decays, it results convenient to follow the evolution of the different characteristic time-scales occurring during the r-process, i.e., neutron capture, photodissociation, and beta decay which are defined, respectively as [10]:

$$\left\langle \frac{1}{\tau_{(n,\gamma)}} \right\rangle = \frac{\sum_{Z,A} n_n \langle \sigma v \rangle_{n,\gamma}(Z,A) Y(Z,A)}{\sum_{Z,A} Y(Z,A)}, \quad (6.6)$$

$$\left\langle \frac{1}{\tau_{(\gamma,n)}} \right\rangle = \frac{\sum_{Z,A} \lambda_\gamma(Z,A) Y(Z,A)}{\sum_{Z,A} Y(Z,A)}, \quad (6.7)$$

$$\left\langle \frac{1}{\tau_\beta} \right\rangle = \frac{\sum_{Z,A} \lambda_\beta(Z,A) Y(Z,A)}{\sum_{Z,A} Y(Z,A)}, \quad (6.8)$$

where n_n is the neutron density, $\langle \sigma v \rangle_{n,\gamma}(Z,A)$ the neutron capture or (n, γ) rate, $\lambda_\gamma(Z,A)$ the photodissociation or (γ, n) rate and $\lambda_\beta(Z,A)$ the β -decay rate (a generic evolution of the different characteristic time-scales occurring during the r-process is shown in Fig. 6.1). A relevant stage of the evolution to be identified is the ‘‘end of the r-process’’ which occurs when the neutron capture rates start to be overcome by the β -decay rates; i.e., when $\langle \tau_{(n,\gamma)} \rangle > \langle \tau_\beta \rangle$, because afterwards the β -decay rates dominate and the system decays back to the valley of stability (see pentagon like symbols in Fig. 6.1).

Another relevant quantity for our subsequent studies is the already introduced neutron-to-seed ratio, $R_{n/s}$ (see Eq. 3.1 and Fig. 6.1). In general, when the r-process freezes out at $t = t_{\text{FO}}$, $R_{n/s}(t_{\text{FO}}) = 1$, since afterwards the flux of available neutrons decrease dramatically and so does the probability to capture neutrons (see diamond like symbols in Fig. 6.1).

And last but not least relevant is the average one-neutron separation energy defined as,

$$\langle S_n \rangle = \frac{\sum_{Z,A} S_n(Z,A) Y(Z,A)}{\sum_{Z,A} Y(Z,A)}, \quad (6.9)$$

where $S_n(Z,A)$ is the one-neutron separation energy of a nucleus with mass number A and charge number Z . The evolution of this variable is relevant because it encodes the nuclear

6.3. PERFORMING NETWORK CALCULATIONS

structure features of each mass model; i.e. shell closures and transition regions from spherical to deformed nuclei. Also it is well known that smaller neutron separation energies are expected for nuclei far from stability, as their neutrons becomes less bound. It is worth to mention that along the present work the behaviour around $\langle S_n \rangle$ extrema (maxima and minima) were chosen as significant stages, because the rest of the r-process evolution depends dramatically on such stages; this point will be clear later on when a detailed analysis will be presented. Finally, by detecting the minimum of $\langle S_n \rangle$ we are also tracking how far from stability one can reach by using say a particular set of nuclear masses at a given astrophysical conditions.

In summary the relevant stages of the evolution of the r-process are displayed on Fig. 6.1, and identified as follows:

- Squared shape symbols identify the 1st minimum in the average one-neutron separation energy $\langle S_n \rangle$. Matter reaching the neutron shell closure at $N = 82$.
- Circular shape symbols identify the 1st maximum in the average one-neutron separation energy $\langle S_n \rangle$. Matter overcoming the neutron shell closure $N = 82$.
- Triangular shape symbols identify the 2nd minimum in the average one-neutron separation energy $\langle S_n \rangle$. Matter reaching the neutron shell closure at $N = 126$.
- Diamond like symbols identify the neutron exhaustion. i.e., when $R_{n/s}(t_{FO}) = 1$.
- Pentagon like symbols identify the end of the r-process. i.e., when $\langle \tau_{(n,\gamma)} \rangle = \langle \tau_\beta \rangle$.

r-process network calculations: ν -driven wind conditions

This chapter is mainly focused in exploring the neutrino-driven wind (see section 3.2.2) as a potential site for r-process nucleosynthesis. The general conditions required for the r-process were investigated both via analytical [8] and via steady-state [172, 129] models of neutrino-driven winds. Three parameters were identified to determine the possibility of r-process nucleosynthesis in the neutrino-wind environment: the electron fraction Y_e ; the expansion timescale, τ , which decides how fast the temperature and density of the outflowing matter drop; and the wind entropy per nucleon, s , as a measure of the photon-to-baryon ratio of the environment [8, 115, 118]. These wind parameters depend on the neutron star properties, namely, its mass and radius, and on the neutrino emission of the neutron star, i.e., the time-dependent luminosities and spectra of the radiated neutrino [8]. The entropy of the neutrino driven wind required for a successful r-process is of the order of several times $100k_B$, making the wind environment a candidate for the so-called high-entropy r-process [119, 171].

We have performed dynamical r-process network calculations (see section 5.1.3). The physical conditions are given by hydrodynamical trajectories from neutrino-driven wind simulations and in particular a trajectory ejected at 8 seconds after bounce in an explosion of a $15M_\odot$ progenitor (for more details the reader is referred to [21]). As it was pointed out in [173] such trajectory doesn't allow the synthesis of heavy r-process elements to occur because the neutron-to-seed ratio after the freeze-out of charged-particle reactions is too low ($Y_n/Y_h \sim 10^{-2}$). A way to obtain a higher Y_n/Y_h is to increase the entropy, this can be achieved reducing the density by a factor of two to obtain a higher neutron-to-seed ratio ($Y_n/Y_h \sim 70$) which is enough to produce the third r-process peak [10].

Another aspect that deserve to recall our attention is the wind termination or reverse shock, which is produced when the neutrino-driven wind collides with the slower moving ejecta behind the supernova shock [125, 126, 127, 21, 128]. For that reason and following the same lines as in [10] the impact of the reverse shock on the r-process abundances and dynamics has been explored too.

The temperature and density evolution of the trajectories used in the current work are shown in fig. 7.1, where three different trajectories can be identified as follows:

- The label “cold” at fig. 7.1 from now on will be used to denote the trajectory in which the position of the reverse shock is taken from Ref. [21] but as previously mentioned the density is overall reduced by a factor of two. Since the position of the shock is at low temperatures, the neutron emission by photodissociation does not play a role so that such environment is commonly referred as a “cold r-process”.

- The label “hot” at fig. 7.1 refers to the situation in which the reverse shock is assumed to take place at a temperature of around 1 GK. This temperature is high enough to maintain the (quasi) $(n, \gamma) - (\gamma, n)$ equilibrium during the major r-process phase (hereafter “hot r-process”).
- The label “nors” at fig. 7.1, reproduces a case without reverse shock, where matter expands without colliding with the slow, early supernova ejecta [10].

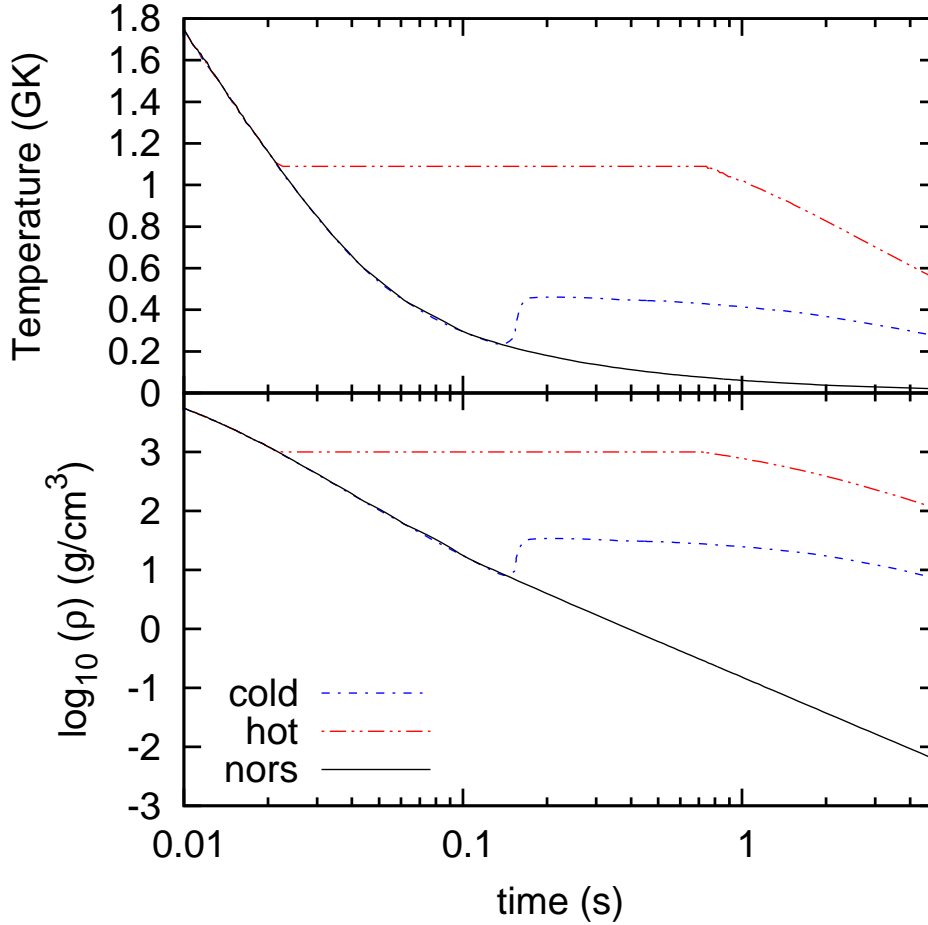


Figure 7.1: Temperature and density evolution

In the following section the results of different r-process physical conditions in the ν -driven wind scenario denoted by “hot r-process”, “cold r-process”, “no-reverse shock r-process” and their interplay with different mass models are shown. In order to have exactly the same distribution of seed nuclei, we start all our nucleosynthesis calculations at the same conditions, a temperature of around 3 GK and a density of the order of 10^4 g cm^{-3} , where nuclei in the region of $A \sim 90$ are favoured. This is shown in the upper panel of fig. 7.2 where the Abundances (Y) are displayed as a function of the mass number (A), while the bottom panel contains the same information in the N - Z plane. The stable isotopes are included and indicated by empty black box symbols and in order to guide the eye a color bar representing $\text{Log}_{10} Y(N, Z)$ is displayed on the right hand side.

7.1. R-PROCESS DYNAMICS

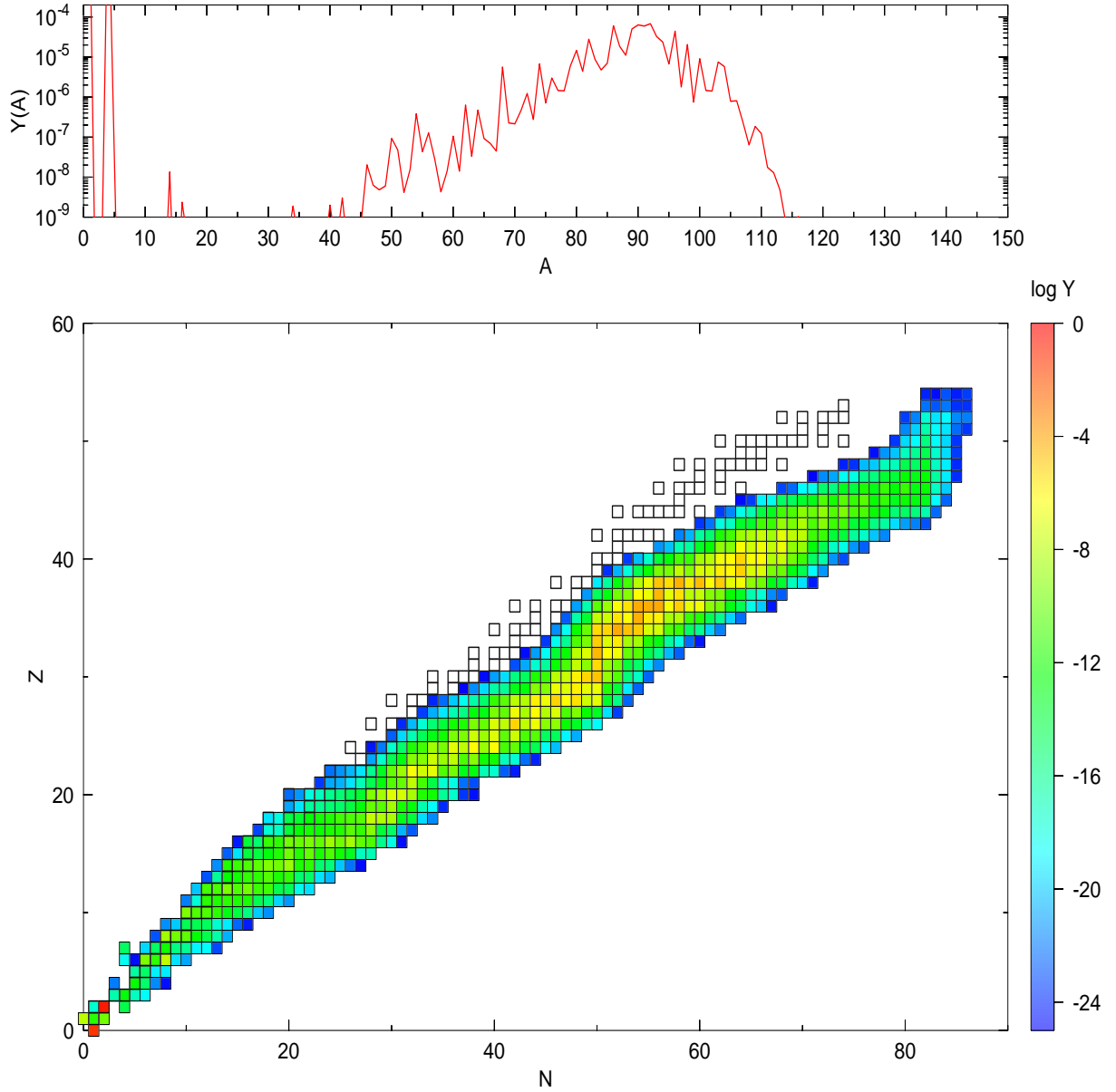


Figure 7.2: Initial composition obtained via a network calculation (see section 6.3.1) for a temperature $T=3$ GK and a density of the order of 10^4 g cm^{-3} . The initial composition favours nuclei in the region of $A \sim 90$

7.1. r -process dynamics

In this section, the relevant physics concerning to the different stages of the r -process evolution is analysed. The results concerning the evolution of the relevant variables for a number of r -process physical conditions in the ν -driven wind scenario denoted by “hot r -process”, “cold r -process”, “no-reverse shock r -process” are displayed in Figs. 7.3 to 7.5. On time scales of interest for covering the relevant stages (see section 6.3.2) of our r -process calculations. To identify these stages, symbols are added on top of the lines that follows the evolution of the relevant variables (see section 6.3.2). In particular the evolution of the average one-neutron separation energy $\langle S_{1n} \rangle$ exhibits certain inflexion points that deserve to be understood in more detail.

7.1.1. General features

7.1.1.1. Evolution of a hot r-process

To explore a “hot r-process” that assumes $(n, \gamma) \rightleftharpoons (\gamma, n)$ equilibrium, we will consider a trajectory with a reverse shock at a temperature of 1 GK (see uppermost panel of Fig. 7.3) that forces the system to remain in this equilibrium during most of the r-process evolution. In the beginning the system expands very fast (see panel concerning the evolution of the neutron number density n_n in Fig. 7.3) up to the point when matter reaches the N=82 shell closure and it gets blocked there. At this moment a minimum is developed in the average one-neutron separation energy $\langle S_{1n} \rangle$ (see panel on the evolution of the $\langle S_{1n} \rangle$ in Fig. 7.3, squared symbols are added to identify this stage). In fact, when matter reaches any neutron magic number, there are two reasons that prevent the system from going any further away from stability. On the one hand, the abrupt drop of individual one-neutron separation energies and on the other hand the higher photodissociation rates. As a consequence, the system has to wait to β -decay in order to continue capturing the free available neutrons. After the matter overcomes the N=82 shell closure, a local maximum in the average one-neutron separation energy $\langle S_{1n} \rangle$ is developed (see circular shape symbols in Fig. 7.3). Then the r-process path moves further from stability (see panel concerning the evolution of the $\langle S_{1n} \rangle$) until it reaches the N=126 shell closure and a 2^{nd} minimum in the $\langle S_{1n} \rangle$ is developed (triangular like symbols). Again, the system has to wait for β -decay, and soon afterwards the freeze-out of neutrons occurs, this happens when the so called neutron-to-seed ratio $R_{n/s}(t = t_{FO}) = 1$ (see diamond like symbols in the evolution of neutron number density n_n and the neutron-to-seed ratio $R_{n/s}$). In order to understand the relation between the neutron-exhaustion and the end of the r-process, let us define the inverse of the average time scale for neutron depletion (i.e., the average neutron depletion rate): as follows:

$$\left\langle \frac{1}{\tau_{n,dep}} \right\rangle = \left| \frac{1}{Y_n} \frac{dY_n}{dt} \right|. \quad (7.1)$$

Furthermore, assuming that only neutron capture processes determine the change of neutron abundance, i.e.,

$$\frac{dY_n}{dt} = \sum_{Z,A} n_n \langle \sigma v \rangle_{Z,A} Y_{Z,A} = \frac{\sum_{Z,A} Y(Z,A)}{\langle \tau_{(n,\gamma)} \rangle}. \quad (7.2)$$

The last equality follows from equation 6.6. The resulting expression for the characteristic time scale for neutron depletion is then:

$$\langle \tau_{n,dep} \rangle = R_{n/s} \langle \tau_{(n,\gamma)} \rangle. \quad (7.3)$$

From the previous equation, we see that at freeze-out $R_{n/s}(t_{FO}) = 1$, both the characteristic time scale for n-captures ($\langle \tau_{(n,\gamma)} \rangle$) and the characteristic time scale for neutron depletion ($\langle \tau_{n,dep} \rangle$) becomes of the same order. Afterwards, as the neutron number density n_n drops faster (see panel concerning the evolution of the neutron number density n_n), i.e., $R_{n/s}(t > t_{FO}) \ll 1$ and consequently $\langle \tau_{n,dep} \rangle \ll \langle \tau_{(n,\gamma)} \rangle$ (the probability for capturing a neutron decreases dramatically). Then end of the r-process occurs when both the characteristic time scale for neutron capture $\langle \tau_{(n,\gamma)} \rangle$ and the one for β -decay $\langle \tau_\beta \rangle$ becomes of the same order (see pentagon like symbols). When the r-process finishes, the system decays back to stability (see panel concerning the evolution on the average one-neutron separation energy $\langle S_{1n} \rangle$).

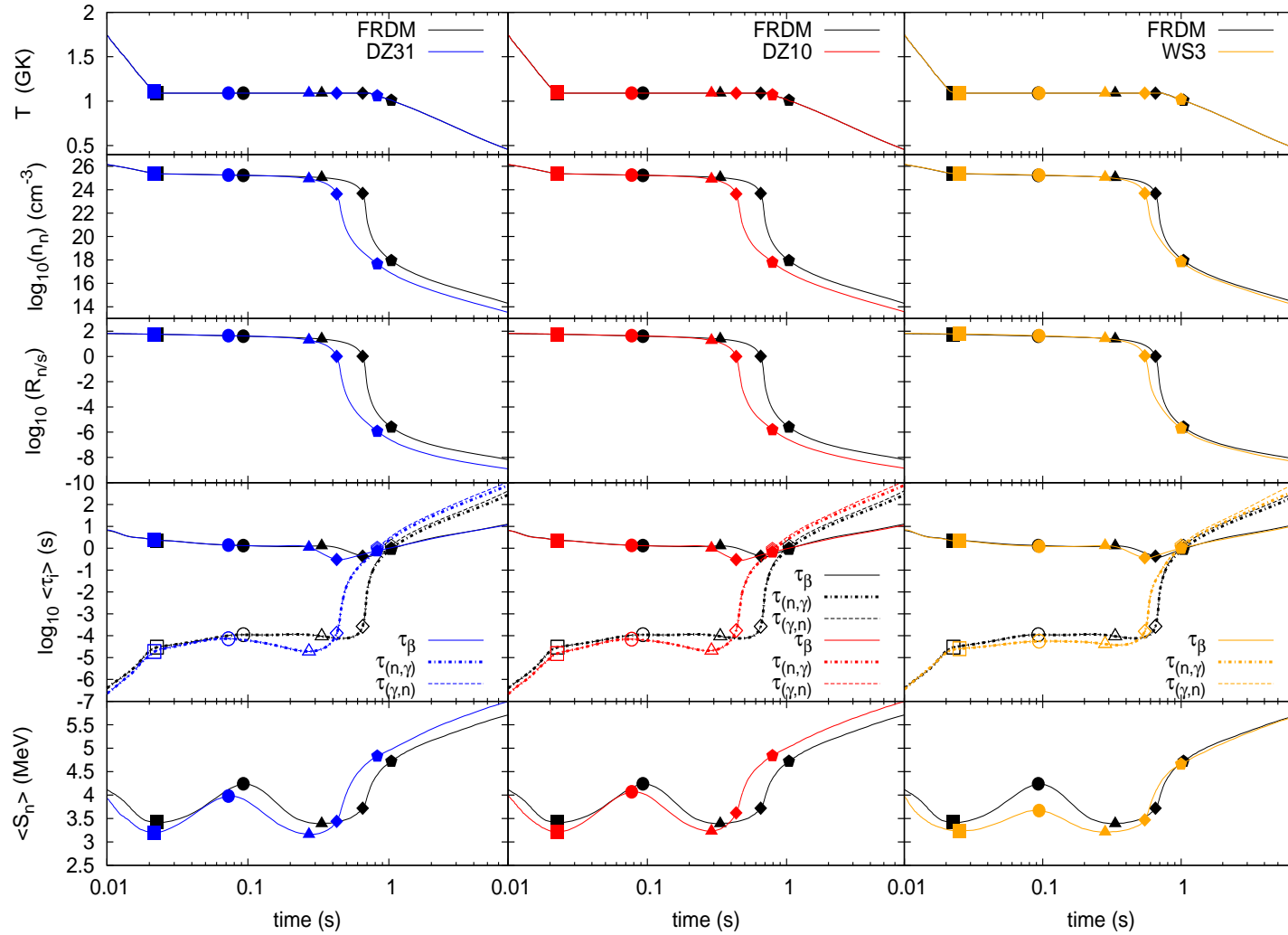


Figure 7.3: Evolution of the temperature T , the neutron number density n_n , the neutron-to-seed-ratio Y_n/Y_h , the average one-neutron separation energy $\langle S_{1n} \rangle$ and the characteristic time-scales involving in the r-process, i.e., n-capture $\langle \tau_{(n,\gamma)} \rangle$ (dotted lines), photodissociation $\langle \tau_{(\gamma,n)} \rangle$ (dashed lines) and β -decay $\langle \tau_\beta \rangle$ (continuous lines). These results correspond to a hot r-process for the different mass models used in the present work: FRDM (black lines on all the panels), DZ31 (bluish lines), DZ10 (reddish lines) and WS3 (orange lines), we choose to use FRDM as a reference. Symbols are added on top of the lines to denote relevant stages in the evolution of the r-process.

7.1.1.2. Evolution of a cold r-process

A generical “cold r-process” runs at lower temperatures, where the above mentioned $(n, \gamma) \rightleftharpoons (\gamma, n)$ equilibrium breaks down. This happens because the characteristic time scale for neutron-emission via photodissociations, $\langle \tau_{\gamma, n} \rangle$, becomes so slow that it does not play a significant role. As a consequence the r-process runs mainly in a competition between β -decay and neutron capture processes ([11]). In the following, we are going to explore a “cold r-process”, with a reverse shock at lower temperatures (at $T_0 \sim 0.2$), such that the photodissociation process can be neglected. One has to keep in mind that in a “cold r-process”, when the equilibrium breaks down, the neutron number density, n_n , drops faster. Since the characteristic time scale for n-captures, $\langle \tau_{(n, \gamma)} \rangle$, is inversely proportional to n_n (see Eq. 6.6), then $\langle \tau_{(n, \gamma)} \rangle$ becomes slower at earlier times. Thus a “cold r-process” is faster than a “hot r-process”. The evolution of relevant variables and relevant stages is displayed in Fig. 7.4.

During the first stage of the evolution of our cold r-process calculations, i.e., when the evolving system reaches the N=82 shell closure, the temperature is still high $T \sim 1$ GK (see square symbols in the upper most panel in Fig. 7.4), so that the behaviour is similar to the one previously described for a hot r-process (see section 7.1.1.1). Afterwards, as for $T \sim 0.5$ GK the photodissociation are smaller, then the characteristic time scale for n-captures $\langle \tau_{(n, \gamma)} \rangle$ becomes the dominant one and the system overcomes the N=82 closure faster than if it were running under hot r-process conditions (see the panels on the evolution of characteristic time scales $\langle \tau_i \rangle$ and the average one-neutron separation energy $\langle S_{1n} \rangle$ in Fig 7.4, where full circular symbols are added to denote the second stage of the evolution of a cold r-process).

The next stage in the evolution of a cold r-process is identified by the presence of a reverse shock, which occurs when the expanding matter collides with the slow early supernova ejecta. It has the following consequences: the system is heated up from $T \sim 0.2$ GK to $T \sim 0.5$ GK and the expansion of the system gets slower, due to the fact that even when the photodissociation are smaller, they are no longer negligible. At the same time the system finally reaches the N=126 (see triangle symbols in Fig 7.4). It is observed that at this stage, a cold r-process moves matter further from stability, i.e., the 2nd minimum in the average one-neutron separation energy $\langle S_{1n} \rangle$ is smaller than the corresponding one for a hot r-process (compare position of triangles in $\langle S_{1n} \rangle$ in both figures 7.3 and 7.4).

The neutron exhaustion stage, i.e. when the neutron-to-seed ratio $R_{n/s} \sim 1$ occurs soon after the system has reached the N=126 closure. But as already mentioned under cold r-process conditions this occurs at earlier times than in a hot r-process. In fact at the time when the system reaches $R_{n/s} \sim 1$, the characteristic time scale for β -decay $\langle \tau_\beta \rangle$ is already comparable to the one of the n-captures $\langle \tau_{(n, \gamma)} \rangle$ (see diamond like symbols on the evolution of Y_n/Y_h and the characteristic time scales $\langle \tau_i \rangle$ in Fig 7.4). Consequently, the n-capture process becomes less efficient, at earlier times than a hot r-process, due to the fact that it has to compete sooner with the β -decay. As a consequence, the end of the r-process occur at earlier times than in hot r-process conditions (compare position of pentagon like symbols in both Figs. 7.4 and 7.3).

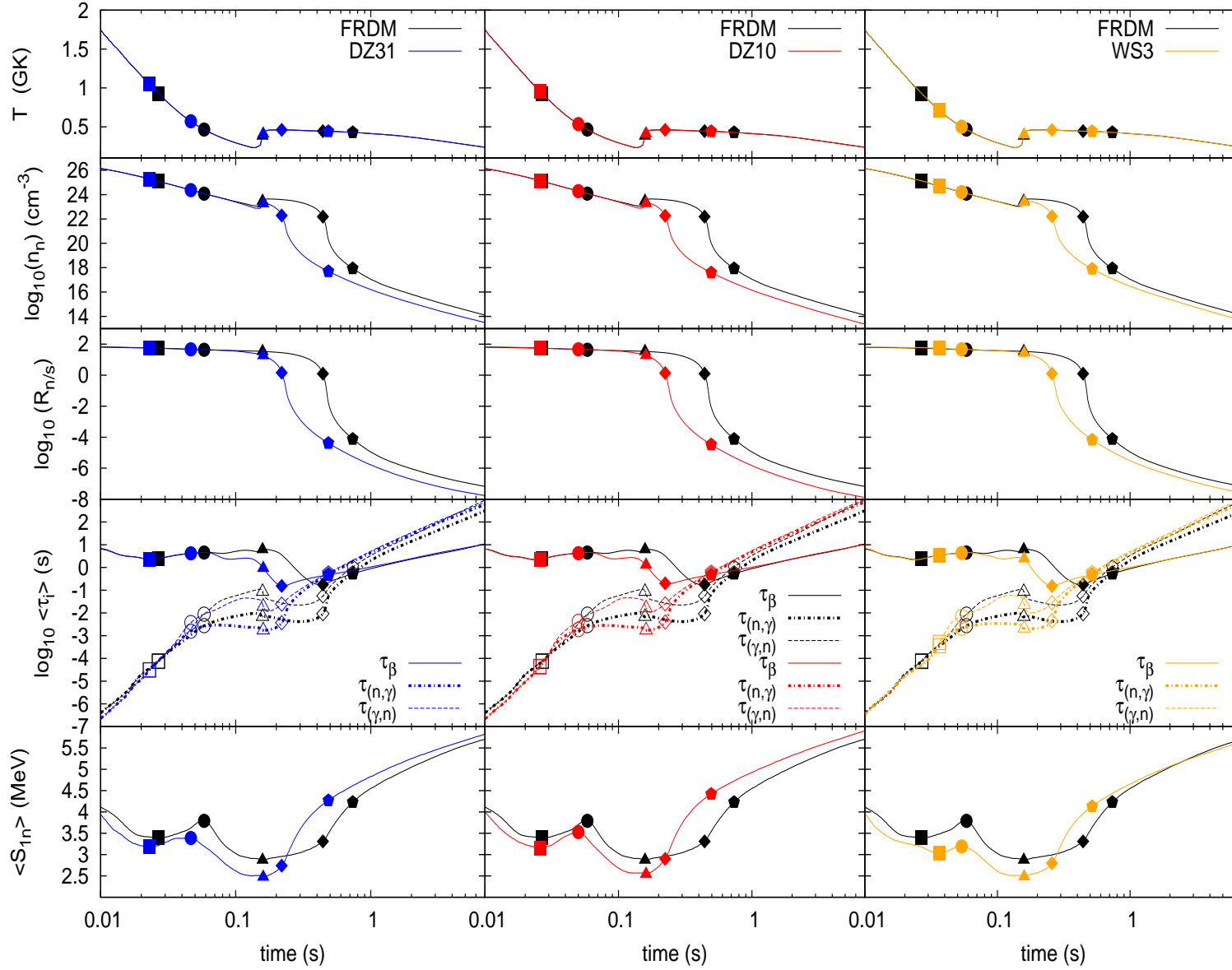


Figure 7.4: Evolution of the temperature T , the neutron number density n_n , the neutron-to-seed-ratio Y_n/Y_h , the average one-neutron separation energy $\langle S_{1n} \rangle$ and the characteristic time-scales involving in the r-process, i.e., n-capture $\langle \tau_{(n,\gamma)} \rangle$ (dotted lines), photodissociation $\langle \tau_{(\gamma,n)} \rangle$ (dashed lines) and β -decay $\langle \tau_\beta \rangle$ (continuous lines). These results correspond to a cold r-process for the different mass models used in the present work: FRDM (black lines on all the panels), DZ31 (bluish lines), DZ10 (reddish lines) and WS3 (orange lines), we choose to use FRDM as a reference. Symbols are added on top of the lines to denote relevant stages in the evolution of the r-process.

7.1.1.3. Evolution of an r-process without a reverse shock

So far we have explored situations in which the ν -driven wind trajectories experience a reverse shock, either at high temperatures (see section 7.1.1.1) or at lower temperatures (see section 7.1.1.2). In this section an r-process without a reverse shock is explored. Under such conditions the ν -driven wind expands without colliding with the earlier ejecta from CCSNe. The evolution of the relevant variables and stages is displayed in Fig. 7.5. The results for the first two stages for the r-process evolution are the same as those previously discussed in section 7.1.1.2 (see squared and circular symbols in Fig. 7.5), the rest of the evolution is different. Due to the absence of a reverse shock the neutron density drops very fast and then the efficiency of the n-capture process decreases dramatically, i.e., the characteristic time scale for n-captures $\langle\tau_{(n,\gamma)}\rangle$ (see triangles and diamonds in Fig. 7.5) is almost an order of magnitude slower than the one when a reverse shock present at lower temperatures (see triangles and diamonds like symbols in the panels on the evolution of $\langle\tau_{(n,\gamma)}\rangle$ in Fig. 7.4). Such $\langle\tau_{(n,\gamma)}\rangle$ quickly becomes comparable to the time scale for the expansion of the system so that at the end of the r-process, the amount of free available neutrons in the system is still large.

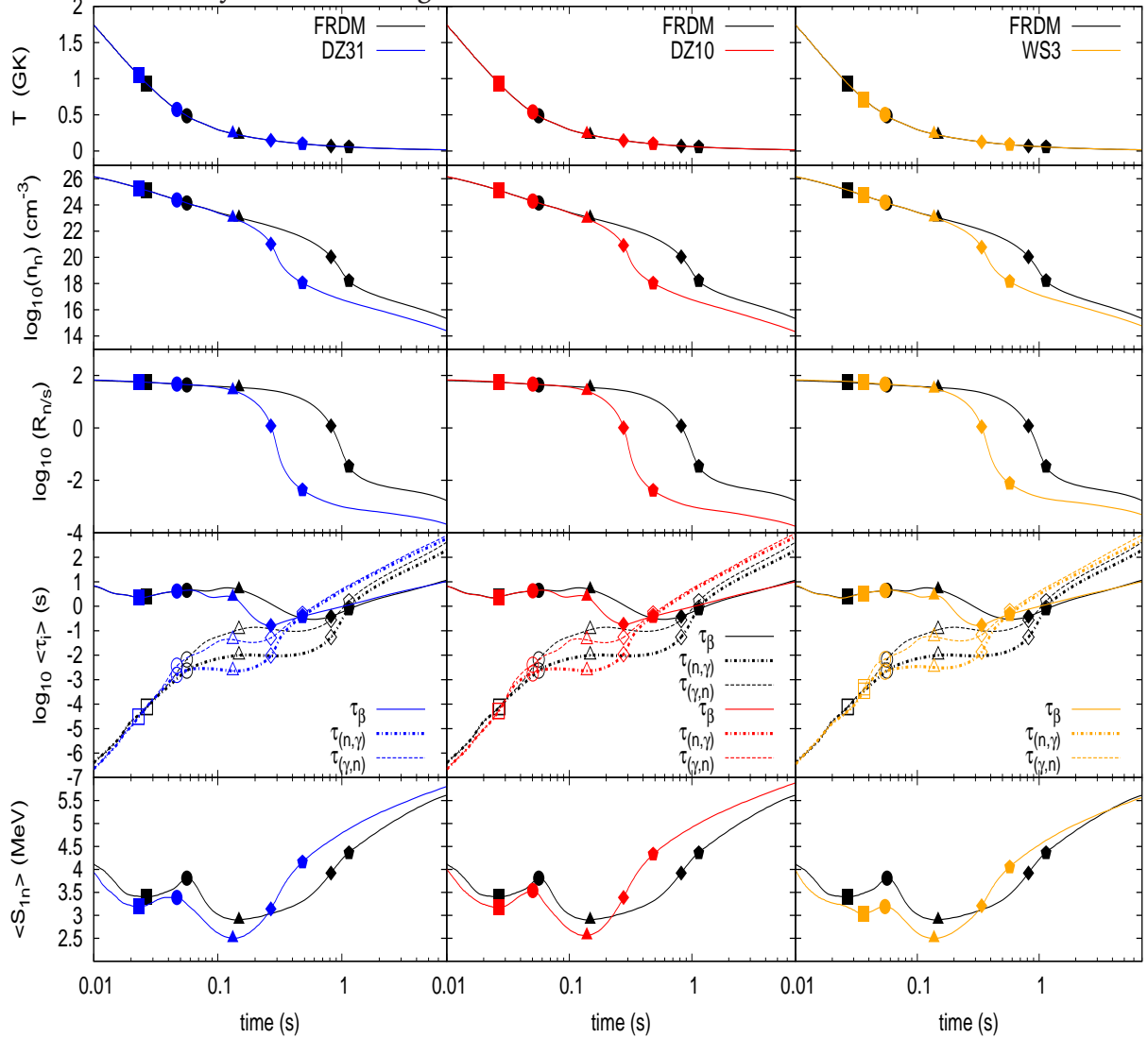


Figure 7.5: Same as in Fig. 7.3 but this time, the evolution is referring to an r-process without a reverse shock (for further details see text).

7.1.2. Sensitivity to the nuclear physics input

Up to now, details concerning the role of the nuclear physics input have been avoided and we have described the evolution of different r-process running under a number of ν -driven wind conditions. In this section, we focus mainly on difference among mass models and their impact on r-process dynamics. For the discussion that follows, we are going to make use of the results found in section 2.2.2, and also of Figs. 7.3 to 7.5.

In the previous section we have identified 5 relevant stages in the evolution of a generical r-process, now let us describe the evolution of the same in terms of the nuclear physics input:

- **1st minimum in the average one-neutron separation energy $\langle S_{1n} \rangle$ (reaching the $N=82$ shell closure).** In the first stage of a generical r-process evolution the system reaches the $N=82$ shell closure, but before that happens, depending on the set of n-capture rates used, the system has to overcome either an onset of deformation around $N \approx 70$ (the FRDM and the WS3 mass models exhibit different predictions concerning the onset of deformation, see Figs. 2.6, 2.8 and 2.10) or an harmonic oscillator closure at $N=70$ in the case of the Duflo-Zuker models (see Figs. 2.11 and 2.12). As the deformation spans a larger region of nuclei, matter spends more time there, and consequently the FRDM and the WS3 models reach the 1st minimum in $\langle S_{1n} \rangle$ at slightly late times in comparison to the DZ models (see lowermost panels in Figs. 7.3 to 7.5). In addition to the onset of deformation, the WS3 mass model presents an additional feature at $Z=40$ (see Fig. 2.10) which translates in an additional kink just before the $N=82$ shell closure. This effect is more noticeable in trajectories with a reverse shock at lower temperatures and without a reverse shock (see orange squared symbols in Figs. 7.4 and 7.5). As the systematics before $N=82$ for the Duflo-Zuker models are similar, so are the observed $\langle S_{1n} \rangle$.
- **1st maximum in the average one-neutron separation energy $\langle S_{1n} \rangle$ (overcoming the $N=82$ shell closure).** After reaching the $N=82$ shell closure, the system has to wait to β -decay in order to continue capturing the free available neutrons, and depending of the strength of the shell gap at $N=82$ (see left hand side in Figs. 2.8 to 2.12) the system starts to move closer to the region of stability. If the shell gap at $N=82$ is weaker (as in the case of the WS3 mass model, see Fig. 2.10), matter easily overcomes the region around $N=82$; i.e., only a few β -decays can occur and then the system moves farther from stability (lower $\langle S_{1n} \rangle$, see orange circular filled symbols on the evolution of $\langle S_{1n} \rangle$ in Figs. 7.3 to 7.5) than when the shell gap at $N=82$ is stronger like in the case of FRDM (see black circular filled symbols in $\langle S_{1n} \rangle$ in Figs. 7.3 to 7.5). Since photodissociation rates are smaller or negligible in trajectories with a reverse shock at lower temperatures or no reverse shock at all. In average matter overcomes faster the $N=82$ shell closure and moves farther from stability.
- **2nd minimum in the average one-neutron separation energy $\langle S_{1n} \rangle$ (reaching the $N=126$ shell closure).** The following step in the evolution of an r-process starts when matter finally overcomes the $N=82$ shell closure, and it is moving in its way to the $N=126$ shell closure. Before doing so, it has to overcome two obstacles, on the one hand an onset of deformation predicted at $N \approx 90$ and on the other hand a deformation shell closure at $N \approx 112$ which is present in most of the mass models (see Fig. 2.8 to 2.12). As previously mentioned in section 2.2.5, among the models

FRDM predicts the largest region of deformation and also the most irregular S_{2n} surface (see Fig. 2.8). Especially there are kinks right after the $N=82$ (at $N\approx 90$) and before the $N=126$ (at $N\approx 112$) shell closures. Such features, as we will learn in the next sections, have important consequences in the final pattern of r-process abundances. WS3 presents a similar deformation region than FRDM, but does a better job by smoothing the S_{2n} surface, however the already mentioned kinks are still there (see Fig. 2.10). The DZ mass formulas display the smoothest behaviour for the S_{2n} surfaces and a deformation region smaller than WS3 and FRDM, however they display a strong harmonic oscillator shell closure at $N=112$ (see Fig. 2.11 and 2.12). All the above mentioned features can be identified when comparing the characteristic time scales for n-capture $\langle\tau_{(n,\gamma)}\rangle$ on going from the 1st maximum in $\langle S_{1n}\rangle$ to the 2nd minimum of the same, one can notice that $\langle\tau_{(n,\gamma)}\rangle$ gets an order of magnitude faster and this feature is driving the system further from stability (most of the models but FRDM present such a feature). The WS3 and the DZ models due to their smoother behaviour in the S_{2n} surfaces move matter farther away from stability than FRDM.

- **Neutron exhaustion (neutron-to-seed ratio $Y_n/Y_h \approx 1$).** When matter reaches the $N=126$, it has to wait longer for β -decay, the situation being similar to the one found in the second stage of the r-process evolution (at 1st maximum in the $\langle S_{1n}\rangle$), in the sense that the strength of the shell gap will determine how many β -decays are allowed. However, the big difference is that in this stage, the neutron number density, n_n , drops faster than in the previous stages (see diamond like symbols in Figs. 7.3 to 7.5). In fact, the neutron exhaustion ($R_{n/s} \sim 1$) occurs when characteristic time scale for neutron depletion for the system $\langle\tau_{(dep)}\rangle$ becomes comparable with the characteristic time scale for n-captures $\langle\tau_{(n,\gamma)}\rangle$ (see Eq. 7.3). Among all the analysed mass models, FRDM presents the strongest shell gap at $N=126$ (see Fig. 2.8); followed by DZ10, WS3 and DZ31 respectively. For that reason it is observed that when used n-capture rates based on WS3 and DZ31, the system is effectively moving at lower $\langle S_{1n}\rangle$ (in the a region of more exotic nuclei) than for FRDM and DZ10.
- **End of the r-process ($\langle\tau_{(n,\gamma)}\rangle > \langle\tau_{\beta}\rangle$).** In the final stage the neutron number density, n_n , drops six orders of magnitude compared to the previous stage of the r-process evolution (see diamond and pentagon like symbols in n_n in Figs. 7.3 to 7.5). It is observed that independently of the conditions in the ν -driven wind scenario, the n-capture rates based on FRDM always produce the slowest r-processes, the reason is the r-process path for FRDM, involves nuclei with larger half lives, i.e., the r-process path of FRDM moves closer to the stability than for the rest of the models.

The whole evolution of an r-process depends on the nuclear physics input. We have learnt that the knowledge of the nuclear masses are of major relevance in the so called hot r-process. On the other hand, in the so called cold r-process, the knowledge of both n-capture and β -decay rates is required. Following the evolution of the average one-neutron separation energy $\langle S_{1n}\rangle$ and correlating its behaviour with the systematics of the two-neutrons separation energies ($S_{2n}/2$), results an useful tool to make a qualitative analysis of the dynamics of the whole r-process. Such systematics encode the nuclear structure features of each mass model; i.e. shell closures, shell gaps and transition regions from spherical to deformed nuclei.

7.2. Final r -process abundance pattern

Along this section, we are going to trace back in previous sections to investigate the origin of the differences in the final pattern of r -process abundances, based on what we have learnt on the systematics of the mass models (see section 2.2.2) and the relevant stages of the r -process evolution (see section 7.1).

7.2.1. General features

Fig. 7.6, shows the impact of the reverse shock on the final r -process abundances, In this figure we have displayed the final pattern of r -process abundances by choosing a given set of neutron capture rates (we have four choices: FRDM, WS3, DZ10 and DZ31 mass models) and varying the conditions in the ν -driven wind scenario. The so-called solar r -process abundances are always added as a reference. Let us start by identifying the global features in the final r -process abundances due to various physical conditions in the ν -driven wind scenario, denoted as hot, cold and no reverse shock r -process:

- As in [10], none of our calculations reproduce the second r -process peak (region around $A \approx 130$), since we have chosen conditions which produce mainly the 3rd r -process peak ($A \approx 195$). However, it is remarkable that some of our calculations also reproduce the so-called “rare earth peak (REP)” (region around $A \approx 165$). This issue is treated in more detail in section 7.2.2.3.
- The cold r -process final abundances present always a broader distribution around the 3rd r -process peak (no matter which set of neutron capture rates have been used). This is because the free available neutrons get more efficiently captured around the region $170 < A < 200$. This feature is discussed in 7.2.2.2.
- The cold r -process without a reverse shock is the fastest and the most inefficient in capturing neutrons. Even so, its final r -process abundances around the 3rd r -process peak seem similar to those of the cold r -process. However around the “REP” their abundances largely differ, this is because photodissociation rates are relevant to build the “REP”. And in a cold r -process without a reverse shock they are always neglected.
- The hot r -process final abundances around the 3rd r -process peak, are slightly shifted to the right when compared to the rest of the trajectories explored in present work. This is because, as shown by [10], for a hot r -process, even at $Y_n/Y_h \approx 10^{-5}$ there are still some late time n -captures happening.

7.2.2. Sensitivity to the nuclear physics input

The relevance of the present work is the understanding of the impact of the nuclear physics input in r -process calculations, and this section is intended to accomplish such goal. Fig. 7.7, displays the pattern of final r -process abundances, but this time we have fixed the conditions in the ν -driven wind scenario and varying the set of the neutron capture rates (FRDM, WS3, DZ10 and DZ31 mass models). Such figure shows the sensitivity of nuclear physics input on the final r -process abundances.

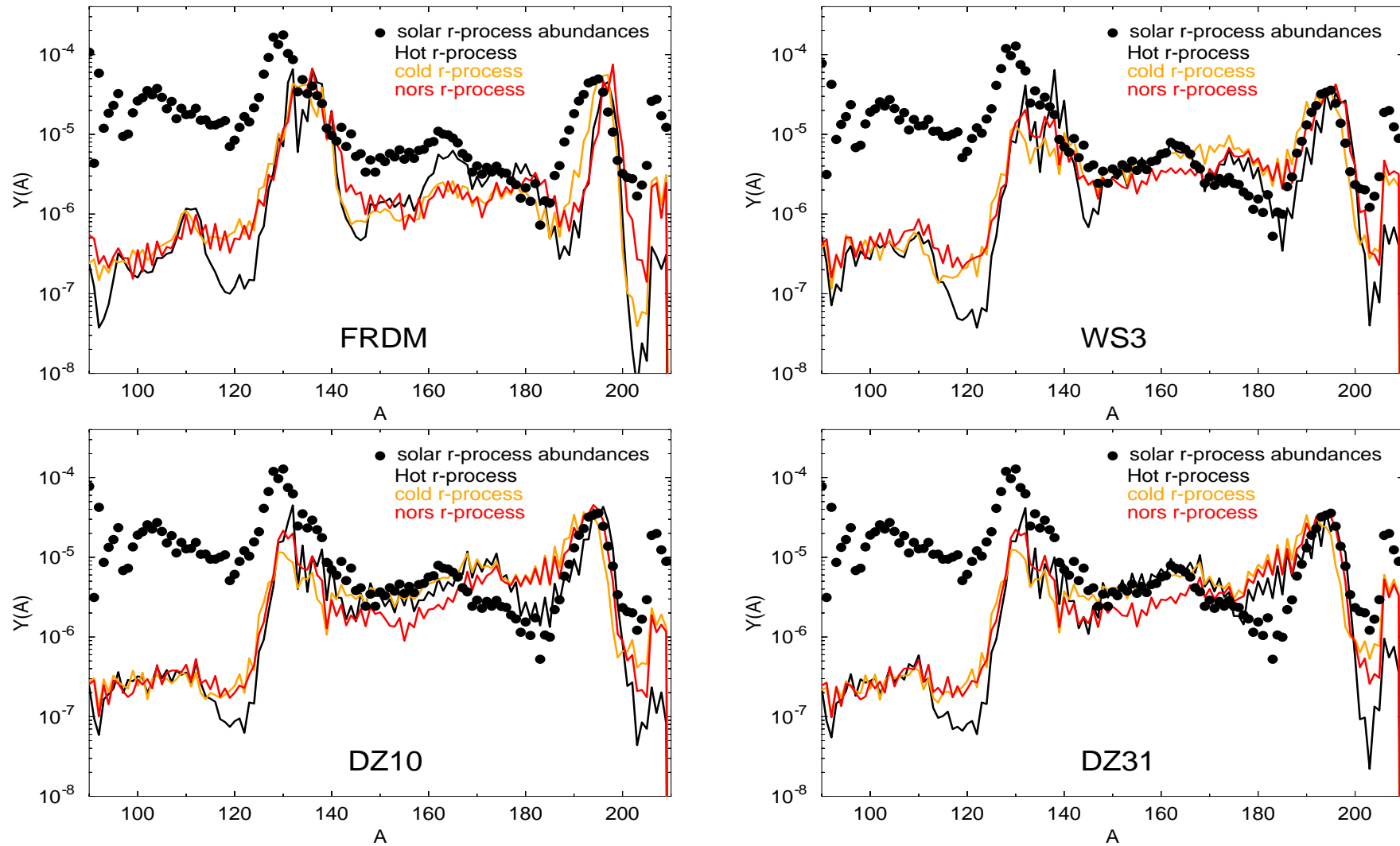


Figure 7.6: Final r-process abundances as a function of the mass number A , for various conditions in the ν -driven wind scenario: hot r-process (Black lines), cold r-process (orange lines) and for an r-process without a reverse shock (red lines). Bullet symbols representing the solar r-process abundances are added to guide the eye. The displayed results correspond to a set of rates based on: FRDM, WS3, DZ10 and DZ31 mass model.

7.2. FINAL R-PROCESS ABUNDANCE PATTERN

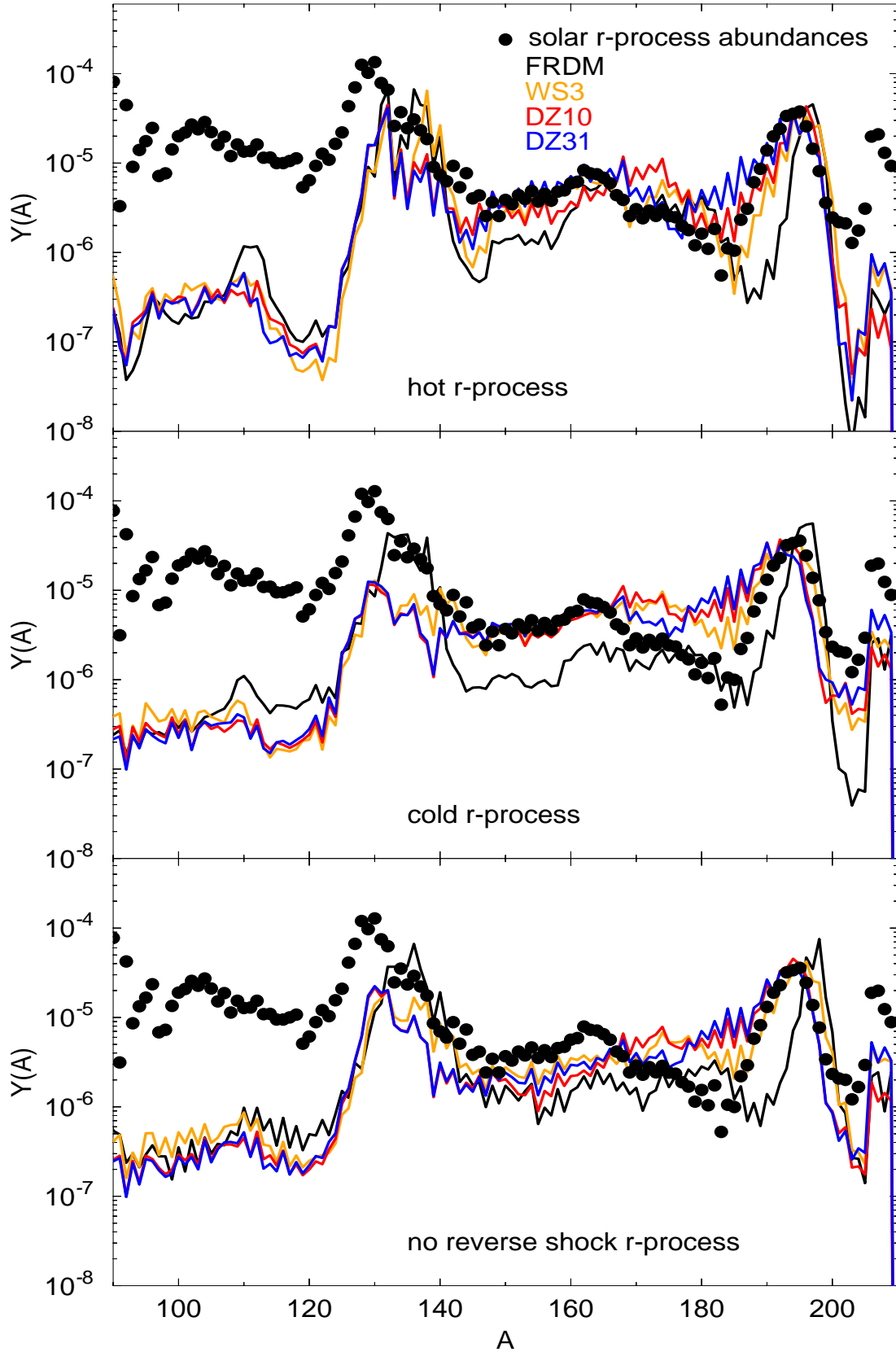


Figure 7.7: Final r-process abundances as a function of the mass number A , for a number of mass models: FRDM (Black lines), WS3 (orange lines), DZ10 (red lines), DZ31 (blue lines). Bullet symbols representing the solar r-process abundances are added to guide the eye. The uppermost panel shows the results corresponding to a hot r-process, the middle panel exhibits the results of a cold r-process and the lower one, results for an r-process without a reverse shock.

7.2.2.1. Anatomy of a hot r -process

In order to get a glimpse of the impact of the nuclear physics input on the final r -process abundances, we have selected 3 representative stages of the r -process evolution. Figs. 7.8 to 7.10, show the behaviour of a hot r -process around the 2nd minimum in the $\langle S_{1n} \rangle$, at the n -exhaustion ($Y_n/Y_h \approx 1$) and at end of the r -process ($\tau_{n,\gamma} \gg \tau_\beta$), respectively, for all the sets of rates used in the current work (FRDM, WS3, DZ10 and DZ31 mass models). The behaviour of a given mass model, is described via 3 subpanels organised as follows:

- The upper panel displays the dynamical r -process path at a given set of conditions (the position of the dots represent the most abundant isotope for a given isotopic chain Z), for different isotopic chains ranging from Zn ($Z=30$) to Bi ($Z=83$) as a function of the mass number A . Every 5 isotopic chains thick brown lines are added to guide the eye. Reddish lines stand for the experimentally available $S_{2n}/2$. Black lines represent the predicted $S_{2n}/2$ for a given model.
- The middle panel displays both the abundances as a function of the mass number A for a given model at the selected stage and solar r -process abundances as a reference.
- The bottom panel contain a label with the physical conditions at the selected stage; i.e., temperature, T (GK), the density, ρ (g cm^{-3}), neutron number density, n_n (cm^{-3}), neutron-to-seed ratio, Y_n/Y_h , and the average one-neutron separation energy, $\langle S_{1n} \rangle$ (MeV). The abundances are also displayed, but this time in the N - Z plane, stable isotopes are included and indicated by empty black box symbols and again a color bar representing $\text{Log}_{10}Y$ is displayed on the right hand side.

As explained in section 7.1, the second minimum in $\langle S_{1n} \rangle$ occurs once matter overcomes the $N=82$ shell closure and its moving through the region of deformation (around $N \approx 90$) in its way to reach the $N=126$ shell closure. The uppermost panel in Fig. 7.8, shows an abrupt drop in the S_{2n} at the magic numbers $N=82$ and $N=126$ leading to an accumulation of matter at these neutron numbers (see yellowish boxes in the lowermost panels of the same figure) and to the formation of peaks at $A \approx 130$ and $A \approx 190$ in the abundance distribution (see middle panel of the same figure). The afore mentioned features are common to all the mass models. In addition to the behaviour at the neutron shell closures $N=82$ and $N=126$, there are two other notorious features identified in the uppermost panel in Fig. 7.8. Both of them, are related to kinks in the systematics of the $S_{2n}/2$. First of all, FRDM and WS3 exhibit a kink right after the $N=82$ shell closure, around $N \approx 90$ (at the onset of deformation), such feature is absent in the Duflo-Zuker mass models. Secondly, an additional feature is identified for all of the models before the $N=126$ shell closure. In both FRDM and WS3 it occurs when the predicted deformed region ends around $N \approx 118$, and in the DZ mass models occurs it at $N=112$ due to an harmonic oscillator shell closure. The observed consequences of such features are troughs in the abundances, which also translate in troughs in the r -process path. On the one hand, the 1st kink produces a trough ranging from $A=140$ to $A=150$ and on the other hand, the 2nd kink produces a trough around $A \approx 180$ in the case of FRDM and WS3. DZ10 presents an small version of the same and its effect on DZ31 is negligible. The afore mentioned harmonic oscillator closure at $N=112$ has an stronger effect in DZ10 than in DZ31. In fact a peak appears at $A=172$ in the abundances of DZ10. The next snapshot (see Fig. 7.9), shows the behaviour at the neutron exhaustion stage. In the phase of the freeze-out, the few available neutrons are not equally captured in all regions [10]. Because of its stronger shell gap at $N=126$ (see

7.2. FINAL R-PROCESS ABUNDANCE PATTERN

figure 2.8) and the afore mentioned deformation region at $N \approx 118$, FRDM presents the largest trough around $A \approx 180$, when comparing with the rest of the models. In WS3, the trough around $A \approx 180$ is partially filled due to matter movements caused by saddle points in the s_{2n} , such features generate changes in the r-process path. In the DZ mass models, as matter has to overcome a deformation region and also an harmonic oscillator closure at $N=112$ before reaching the $N=126$ shell closure, this stage already shows some differences between both DZ10 and DZ31. In particular, in the region between $170 < A < 190$, DZ31 allows more n-captures and so the distribution around the 3^{rd} r-process peak starts to become broader than DZ10, this is because on the one hand the shell gap at $N=126$ in DZ10 is stronger than in DZ31 and on the other hand, as already mentioned the kink at $N=112$ produce a peak in DZ10 at $A=172$, which it is absent in DZ31. When the r-process path reaches the deformation region, an additional feature appears at $A \approx 160$ ($N=104$) in the systematics of the $S_{2n}/2$ for all models, in particular in FRDM and WS3, such feature creates an small trough at ($A \approx 160$) in the abundances distribution, this feature was already identified in [174], as necessary condition for the rare earth peak (region around $A \approx 165$) formation. The late issue will be discussed in section 7.2.2.3. Fig. 7.10, displays an snapshot at the moment when the β -decay rates overcome the n-capture rates. This occurs because as was already mentioned, after the neutron exhaustion stage ($Y_n/Y_h \approx 1$), the neutron number density, n_n , drops six orders of magnitude. As the characteristic time scale for n-capture rates, $\langle \tau_{(n,\gamma)} \rangle$, is inversely proportional to this quantity, it grows larger, until it becomes of the order of the characteristic time scale for β -decay, $\langle \tau_\beta \rangle$. The uppermost panel shows that for regions before the $N=82$ shell closure the r-process path is already running at regions where the experimental information is available for $S_{2n}/2$. The rest of the r-process path is running over the predicted deformation region until it reaches the $N=126$ shell closure. The largest difference with respect to the previous stages is that, n_n is way too small, so the system will most likely β -decay back to stability without substantially changing the mass number. The large fluctuations presented in the abundances of all the models at the neutron exhaustion stage have been considerably smoothed in the end of the r-process stage. However, as shown by [10], even at $Y_n/Y_h \approx 10^{-5}$ there are still some late time n-captures happening, with a non negligible impact in the final r-process abundances. Both FRDM and WS3 r-process paths are still running under the influence of the already identified kink around $A \approx 160$.

Remark: Once a significant trough is developed, it stays there until the end of the r-process. This means that the right shifted 3^{rd} r-process peak observed for both WS3 and FRDM has an origin related with the behaviour around $A \approx 180$ found at the 2^{nd} minimum of the r-process evolution. If the trough is not too deep, it can be partially filled by matter movements due to saddle points in the $S_{2n}/2$. As in the DZ models, there is no waiting point at such place, neutron captures can move matter from that region trough higher mass numbers and as consequence the 3^{rd} r-process peak gets broader. The difference in the final r-process abundances between DZ10 and DZ31 has to deal with an afore mentioned feature at $N=112$ (at the region of transition from HO-EI, see section 2.1.4.3). DZ10 presents a flat region right after the rare earth peak spanning from $168 < A < 175$ (see uppermost panel in Fig. 7.7). In summary, the observed kinks at $N \approx 90$ in FRDM and WS3, produce waiting points; in which matter has to wait for β -decay in order to continue capturing the free available neutrons, and as a consequence matter starts to accumulate there (see yellowish boxes in the lowermost panel Figs. 7.8 to 7.10).

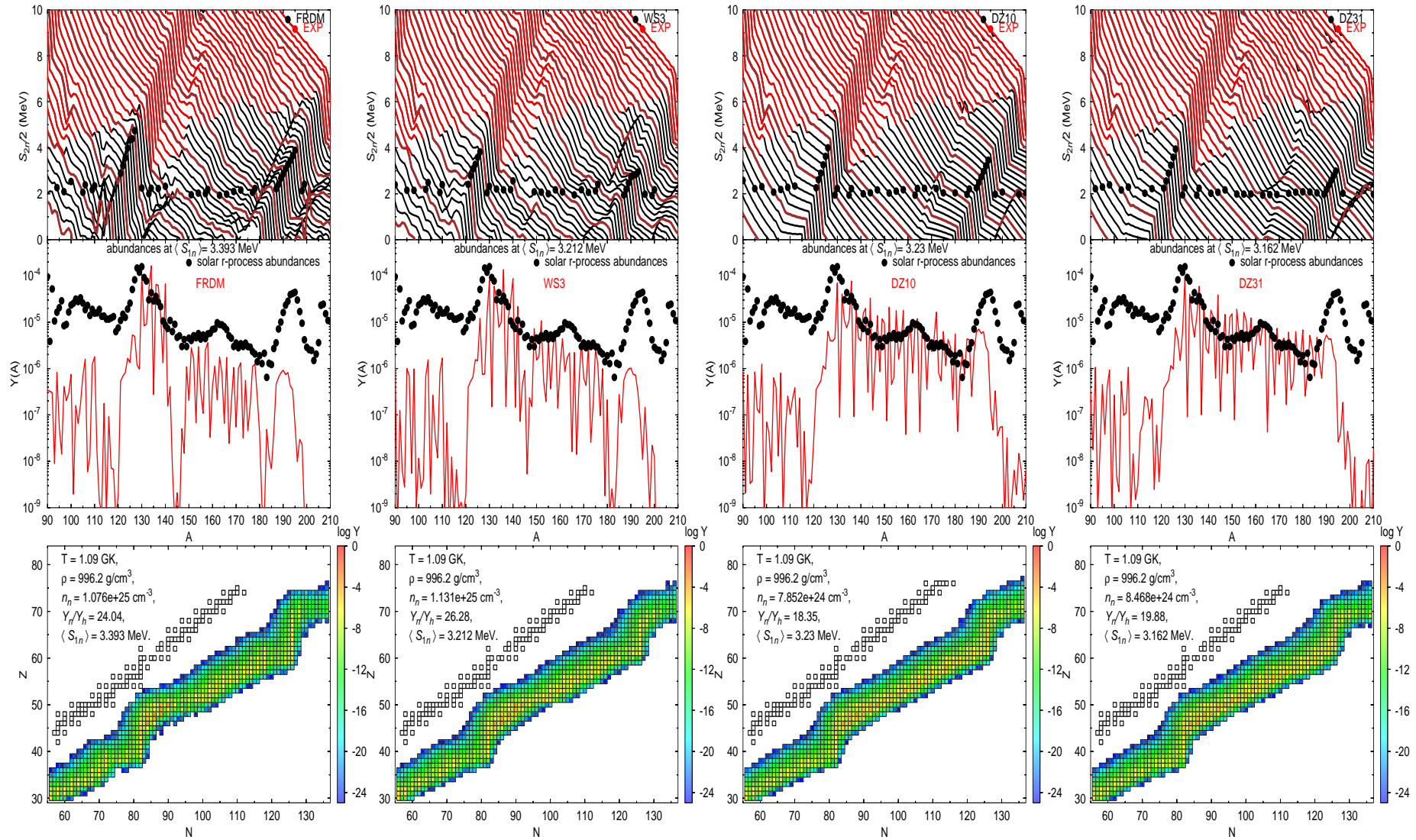


Figure 7.8: Behaviour around the second minimum in the average neutron separation energy $\langle S_{1n} \rangle$ (See triangular shape symbols in Fig. 7.3) for a hot r-process (see Fig. 7.1). From the left hand to the right hand side panels, one can distinguish results involving rates based on FRDM, WS3, DZ10, DZ31 masses. The Uppermost panel display the $S_{2n}/2$ surface of the different models (the experimental information is always displayed), the middle zone shows the current abundances as a function of A and the bottom panel display the same on the N - Z landscape.

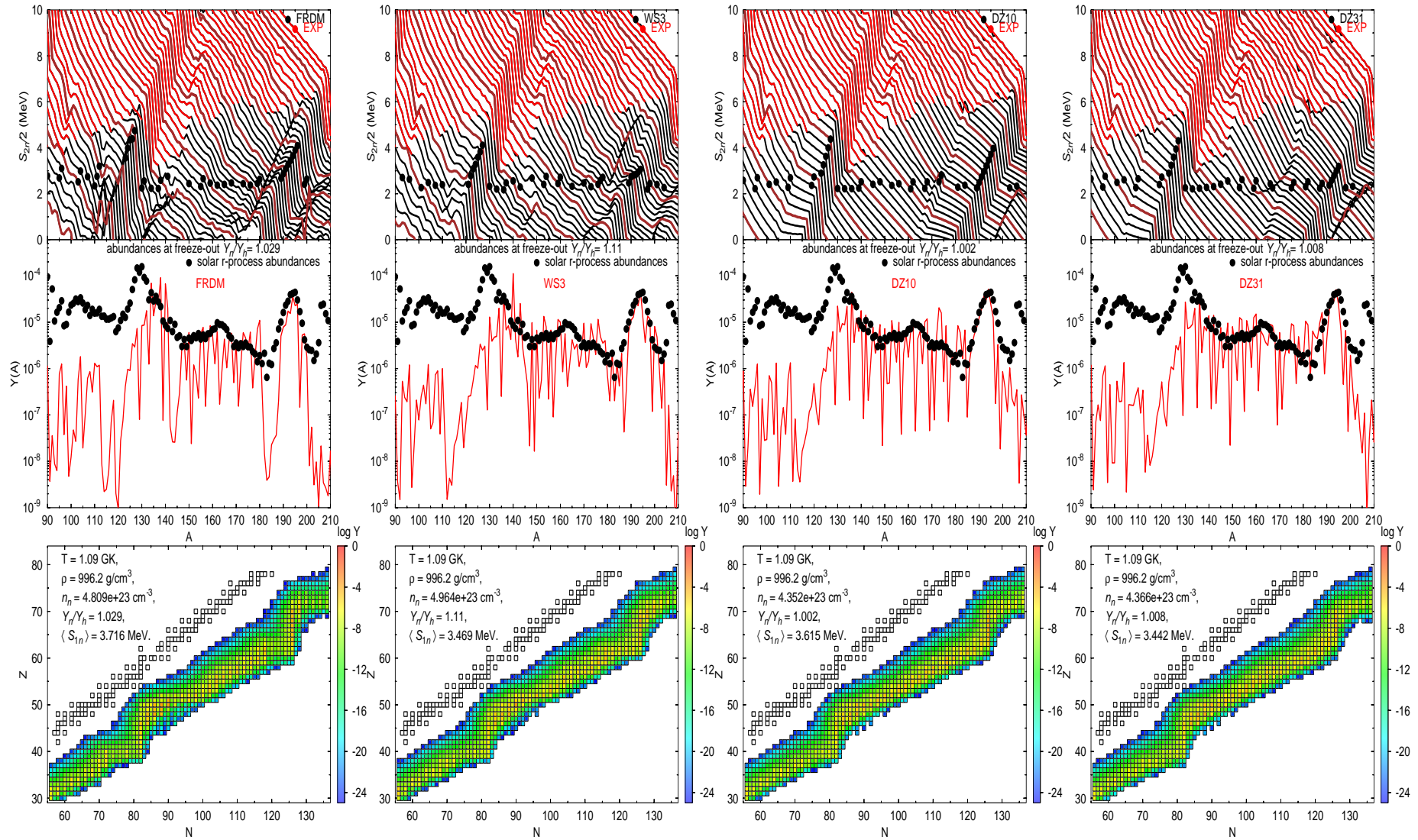


Figure 7.9: Behaviour at the time of the neutron exhaustion, i.e. when $Y_n/Y_h \approx 1$ (See diamond shape symbols in Fig. 7.3) for a hot r-process (see Fig. 7.1). From the left hand to the right hand side panels, one can distinguish results involving rates based on FRDM, WS3, DZ10, DZ31 masses. The Uppermost panel display the $S_{2n}/2$ surface of the different models (the experimental information is always displayed), the middle zone shows the current abundances as a function of A and the bottom panel display the same on the N - Z landscape.

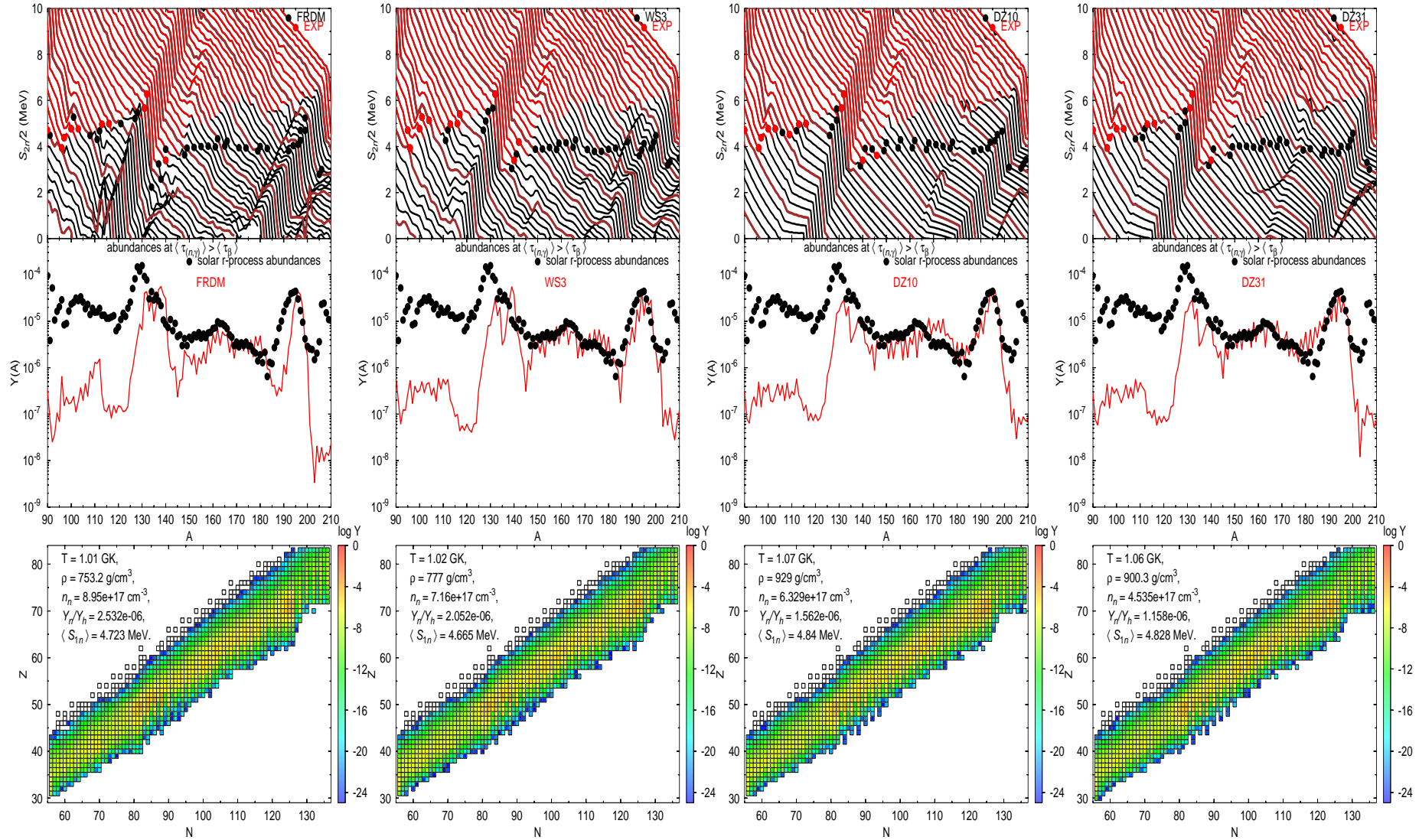


Figure 7.10: Behaviour at the time of end of the r-process, i.e. when $\tau_{n,\gamma} \gg \tau_{\beta}$ (See pentagon shape symbols in Fig. 7.3) for a hot r-process (see Fig. 7.1). From the left hand to the right hand side panels, one can distinguish results involving rates based on FRDM, WS3, DZ10, DZ31 masses. The Uppermost panel display the $S_{2n}/2$ surface of the different models (the experimental information is always displayed), the middle zone shows the current abundances as a function of A and the bottom panel display the same on the N - Z landscape.

7.2. FINAL R-PROCESS ABUNDANCE PATTERN

7.2.2.2. Anatomy of a cold r -process

As it was previously pointed out, the evolution of a “cold r -process” with a reverse shock at lower temperatures, is mainly running at $T_9 < 1$ GK, for which neutron-emission via photodissociation can be neglected and the r -process runs under a competition of beta-decays and neutron captures. Thus to understand its evolution and final abundance distribution, an explicit knowledge of both n -capture rates, $N_n \langle \sigma v \rangle^*$, and beta decays rates, λ_β , is required. To explore the role of the nuclear physics input in the final abundances under a cold r -process, we will closely follow [10], introducing the net neutron-capture flux and the β -decay flux to quantify the competition among these processes. The net neutron-capture flux is defined as follows:

$$F_n(Z, A) = Y(Z, A) N_n \langle \sigma v \rangle_{Z, A} - \lambda_\gamma(Z, A + 1) Y(Z, A + 1), \quad (7.4)$$

and the β -decay flux:

$$F_\beta(Z, A) = \lambda_\beta(Z, A) Y(Z, A). \quad (7.5)$$

To display the above mentioned fluxes, it is convenient to define the fluxes for an isobaric chain

$$F_\beta(A) = \sum_Z F_\beta(Z, A) \quad \text{and} \quad F_n(A) = \sum_Z F_n(Z, A) \quad (7.6)$$

and the fluxes for an isotopic chain

$$F_\beta(Z) = \sum_A F_\beta(Z, A) \quad \text{and} \quad F_n(Z) = \sum_A F_n(Z, A) \quad (7.7)$$

Fig. 7.11 displays the abundances $Y_i(A)$, the fluxes $F_n(A)$ and $F_\beta(A)$ vs the mass number A and the fluxes $F_n(Z)$ and $F_\beta(Z)$ vs Z , at the neutron-exhaustion stage ($Y_n/Y_h \approx 1$) and at the so-called end of the r -process stage ($\tau_{n,\gamma} \approx \tau_\beta$). We have also included the final abundances obtained in the last time step of our calculations and the solar r -process abundances as a reference.

Arcones and Martínez-Pinedo found in [10], that for a cold r -process running under the same conditions as the one used in the present work, the abundances at freeze-out stage reach an equilibrium that we will denote as steady flow that satisfies for each Z and A :

$$\lambda_\beta(Z - 1) Y(Z - 1) = \lambda_\beta(Z) Y(Z) \quad (7.8a)$$

$$N_n \langle \sigma v \rangle_{A-1}^* Y(A - 1) = N_n \langle \sigma v \rangle_A^* Y(A) \quad (7.8b)$$

This is clearly shown in Fig. 7.11 where for a cold r -process, both the $F_n(A)$ and $F_\beta(Z)$ become constant for the region spanning $140 < A < 190$ and $50 < Z < 65$ respectively. As the abundances along an isotopic and isobaric chain are dominated by a single nucleus this condition determines also the nuclei that participate in the r -process, i.e. the r -process path. Moreover, as a cold r -process runs under a competition of beta-decays and neutron captures one obtains that $N_n \langle \sigma v \rangle_A^* Y(A) \approx \lambda_\beta(Z) Y(Z)$. In the present work, we found that the latest condition is valid for the set of n -capture rates based on the FRDM, WS3, DZ10 and DZ31 masses as long as the time scale for both n -capture rates and β -decay are of the same order and faster than the r -process duration. Under such conditions, the peaks in the abundance distribution correspond not only to long beta decay lifetimes but also to long neutron capture lifetimes.

7.2. FINAL R-PROCESS ABUNDANCE PATTERN

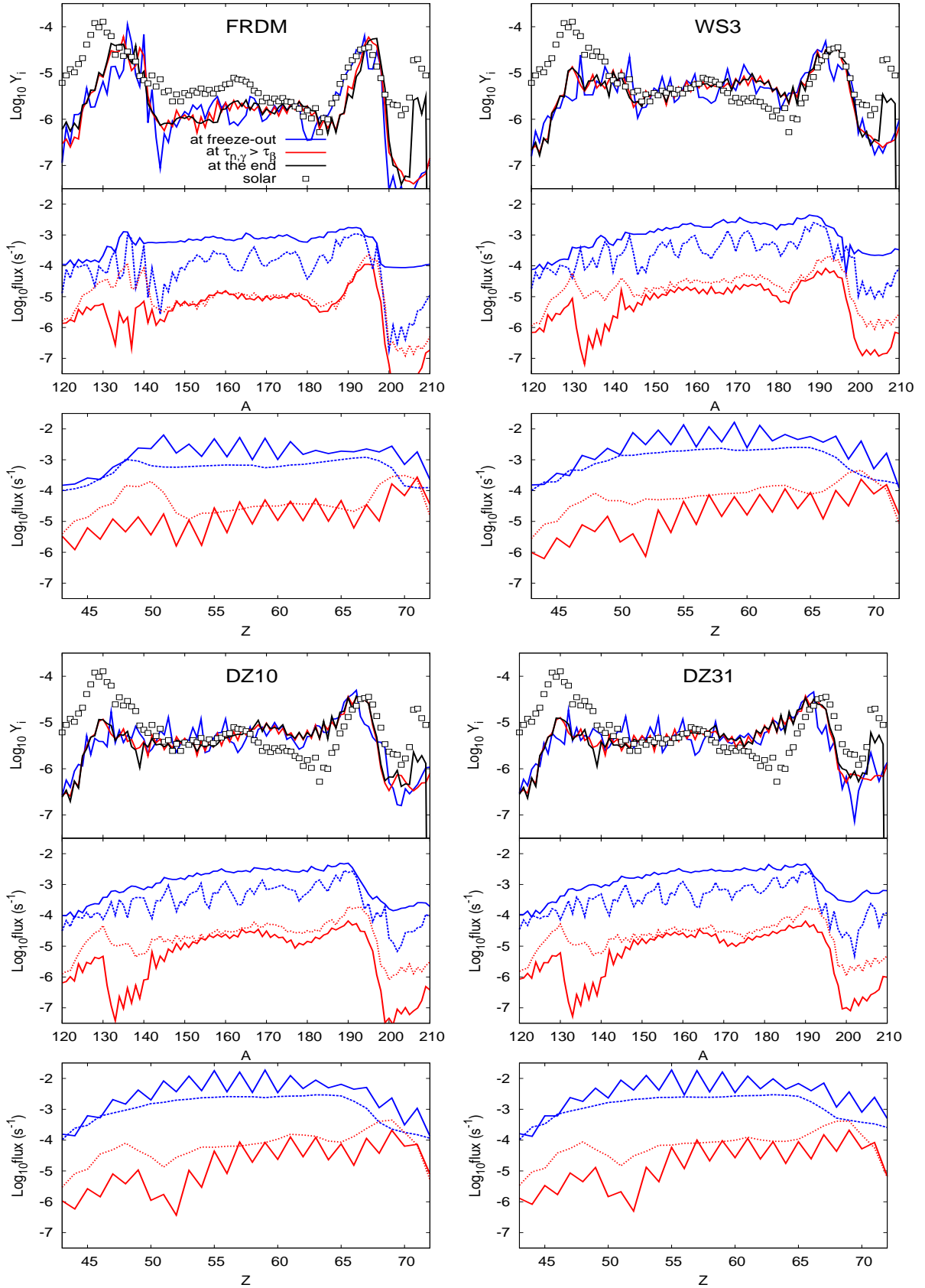


Figure 7.11: Evolution of the abundances $Y_i(A)$, and the fluxes (defined in Eqs. 7.6 and 7.7) vs A and Z for a cold r-process at the neutron-exhaustion stage (see bluish lines) and at the so-called end of the r-process stage (see reddish lines). The net neutron capture flux is represented by solid lines and the β -decay flux by dashed lines. The set of rates are based on the: a) FRDM mass model, b) WS3 mass model, c) DZ10 mass model and d) DZ31 mass model.

7.2. FINAL R-PROCESS ABUNDANCE PATTERN

The fluxes $F_n(A)$ and $F_\beta(A)$ present several features when $\tau_\beta \approx \tau_{(n,\gamma)}$ that can explain how matter is redistributed in the late time evolution [10]. Fig. 7.11 shows that for the set of rates based on FRDM, in regions with $A > 195$ where beta-decay dominates over n-captures, nuclei will beta decay without substantially changing the mass number and for regions where neutron capture becomes comparable or even the dominant process, the abundances will be shifted to higher mass numbers ($A = 185\text{--}195$). For the set of rates based on the WS3, DZ10 and DZ31, the β -decay flux dominates in most of the regions over the flux of n-captures, the exception are local regions around $A \approx 160$ for both DZ10 and DZ31 and around $A \approx 185$ for the WS3 mass model. In such regions the system is in a sort of equilibrium between n-capture and β -decay fluxes. In summary, in most of the cases after the freeze-out stage, the matter is mainly going to decay back to stability, with the exception of certain regions in which the system is either in a local equilibrium or favouring n-captures. The latest effect translates in shifted the abundances to higher mass number.

7.2.2.3. Formation of the rare earth peak ($A \sim 165$)

In what follows, we will show two cases with a successful formation of the so-called rare earth peak (region around $A \sim 165$), corresponding to the interplay between a hot r-process trajectory and rates based on the FRDM mass model and the WS3 mass model. Before we continue with the discussion, it is worth to be mentioned that the mechanism behind the formation of the rare earth process was previously been discussed by [174]. It was attributed to the fact that before β -decay takes over, the r-process path is moving through a deformation maximum or other nuclear structure effect that produce a kink around $A \sim 160$. Due to the fact that after the freeze-out the n-capture rates become of the same order as the β -decay rates, and moreover in a hot r-process the system is still running in $(n, \gamma) \rightleftharpoons (\gamma, n)$ equilibrium, we will make use of the above defined fluxes for isobaric chains, $F_n(A)$ and $F_\beta(A)$ to quantify the competition among these processes. Figs. 7.12 and 7.13 show snapshots of fluxes, abundances and r-process paths for a hot r-process during the neutron exhaustion stage, the final r-process stage and at the final time step of our nucleosynthesis calculations for the region $150 < A < 180$. Our results suggest that the rare earth process peak is still not formed at the neutron-exhaustion stage (at $Y_n/Y_h \approx 1$). However, it is important to realize that as the r-process path is moving through the above mentioned region of deformation, the interplay of this feature and the fact that the neutron number density, n_n , has been reduced considerably, make the β -decay flux becoming of the same order than the net flux of n-captures. A more radical behaviour was found with the WS3 model, where, negative net neutron capture fluxes appear at $A \sim 165$ and $A \sim 175$, because the n-emission by photodissociation becomes stronger than the n-capture process. All the above mentioned facts at the freeze-out stage make matter waiting longer to continue capturing the free available neutrons as certain thresholds are developed. On the final stage of the r-process evolution for both cases (rates based on FRDM and WS3 mass model), we observe that the rare earth peak is already present in the region $A \sim 165$. In FRDM, as the beta-decay and neutron-capture fluxes are very similar, in regions in which the latter dominates a net movement of matter to higher mass numbers is expected. As a consequence the peak will be slightly shifted to the right before β -decay takes over and the final abundances set up. On the other hand, for the WS3 mass model we found that the β -decay flux is already the dominant process but the n-captures flux is still competing in some regions, and so the final distribution of abundance will suffer some changes before the system β -decays to stability.

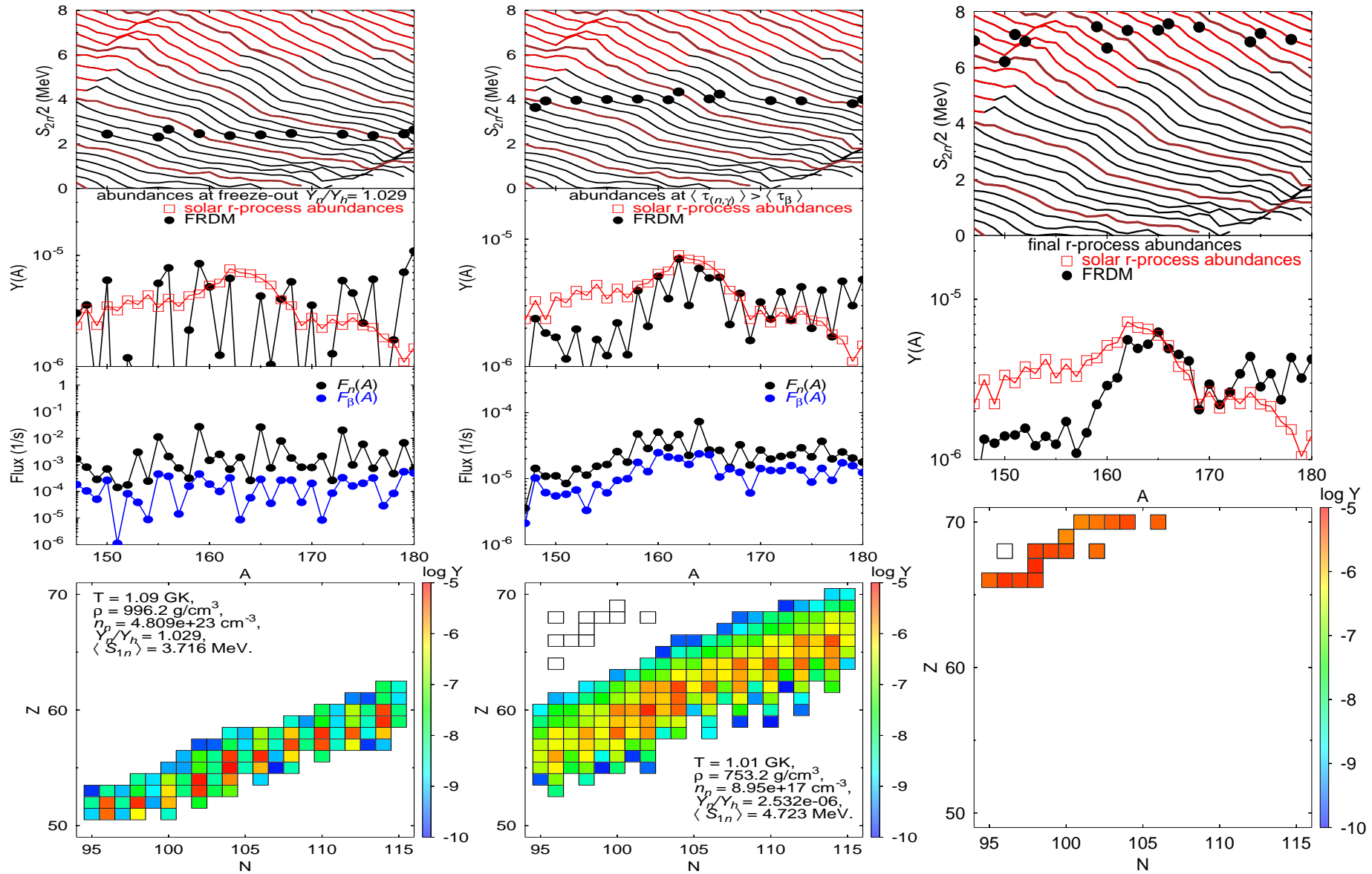


Figure 7.12: Understanding the formation of the rare earth peak (REP). Behaviour of the r-process path, distribution of abundances and the fluxes for neutron-capture (F_n) and β -decay (F_β) at various stages of the evolution of a hot r-process for rates based on the FRDM mass model.

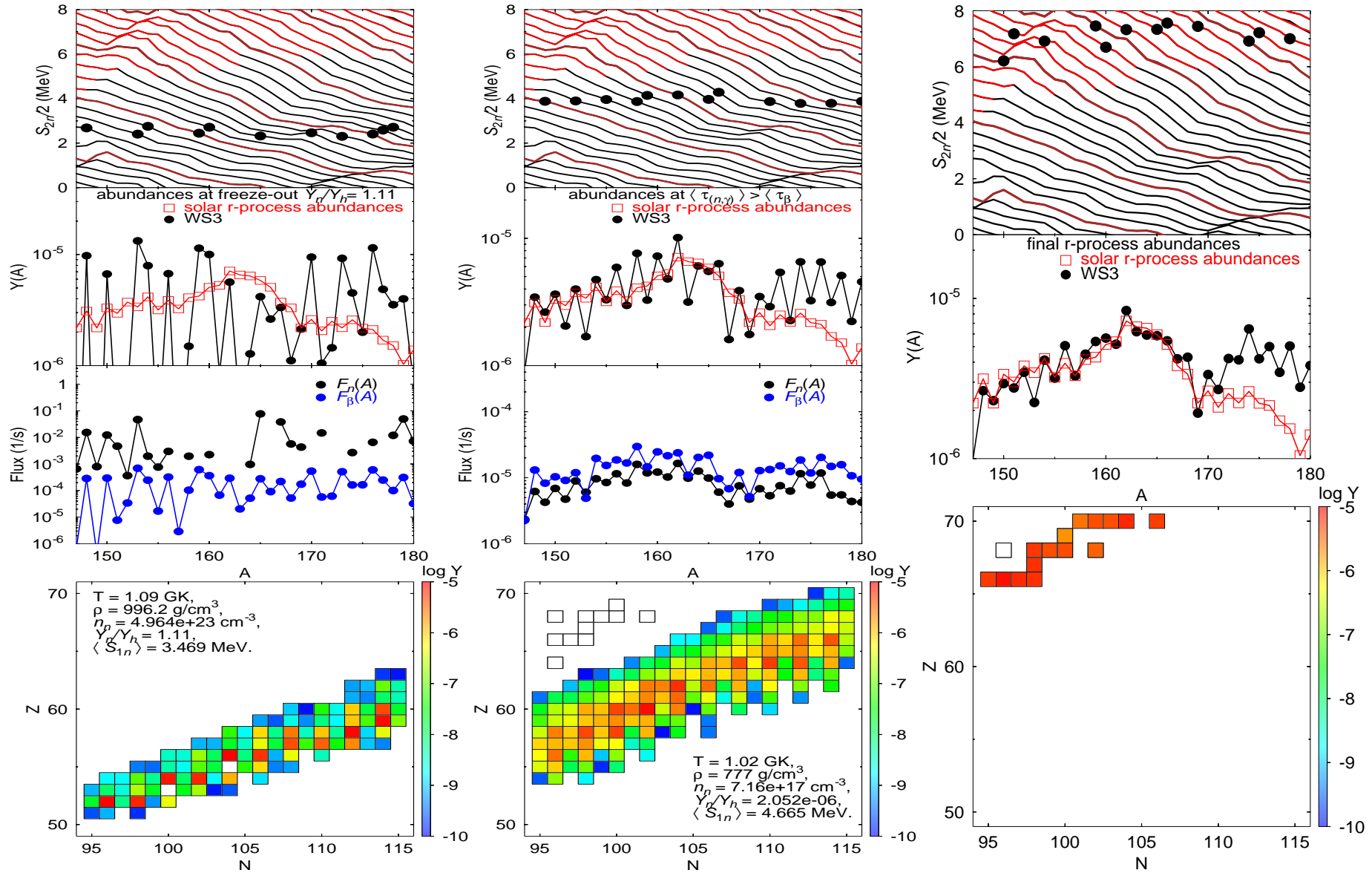


Figure 7.13: Understanding the formation of the rare earth peak (REP). Behaviour of the r-process path, distribution of abundances and the fluxes for neutron-capture (F_n) and β -decay (F_{β}) at various stages of the evolution of a hot r-process for rates based on the WS3 mass model.

7.2.3. Relevance of the deformation region at $N \sim 90$

In previous chapters we have stressed that the region around $N \sim 90$ is of relevance because a transition from spherical to deformed nuclei is predicted to take place in most of the mass models. Moreover, the lack of experimental information motivates the use of theoretical approaches and most of them predict different behaviour for nuclei around this region. It was shown in the previous section that the dynamical r-process path is running through the region $N \sim 90$ during some of the relevant stages of the r-process evolution. Consequently, it is expected that this region has an important role in the final distribution of r-process abundances.

As we have learnt from section 2.2.5, the FRDM mass model presents an anomalous behaviour right before and after the $N=82$ shell closure, in particular a strong kink is observed at the onset of deformation ($N \sim 90$). This feature has been smoothed in the WS3 mass model and it is absent in both DZ10 and DZ31 mass models. The consequence of such an anomalous trend is the presence of an artificial waiting point. This means that when the r-process path happens to reach that kink, matter has to wait longer to continue capturing the free available neutrons. A trough is developed in the abundances around that region and it remains there until the end of our nucleosynthesis calculations.

To explore the impact of the region $N \sim 90$, we have decided to build a number of “hybrid rates” as follows:

1. Take the set of FRDM masses.
2. Replace the masses of isotopic chains ranging from Pd ($Z=46$) to Xe ($Z=54$) by the ones based on the set of WS3, DZ10 and DZ31 masses. From now on, these sets of masses will be denote as “hybrid set of masses”
3. Compute the n-capture rates and their inverse rates based on the above mentioned set of “hybrid masses” via the statistical model (see chapter 4).

We have performed nucleosynthesis calculations based on the above mentioned sets of “hybrid rates”. In order to display the results, we have decided to used the same format employed in figures 7.8 to 7.10. Fig. 7.14 shows an snapshot of a hot r-process running at the neutron exhaustion stage (when $\frac{Y_n}{Y_h} \sim 1$). In the uppermost panel, bluish lines (dots) are added to identify the $S_{2n}/2$ (r-process path) corresponding to the set of the replaced region, black lines (dots) correspond to those based on FRDM masses. The first thing to be stressed is that the new $S_{2n}/2$ for the “hybrid sets of masses” are always smoother than the ones of FRDM in the region $N \sim 90$. The middle and lower panels, display the abundances at the current stage, black lines stands for abundances based on FRDM, bluish ones for a particular model to be compared with and reddish ones for the “hybrid set” (FRDM + replaced masses). We noticed that in the region $130 < A < 160$, the obtained abundances for the “hybrid sets” and those based on the set of replaced masses are basically the same (reddish lines are on top of the bluish ones) and no artificial waiting points around $A \sim 140$ is observed, i.e., the matter can move to regions of higher mass number without any significant accumulation at the onset of deformation. On the other hand, for the rest of regions the abundances of these “hybrid sets” correspond to those of the FRDM set of masses (reddish lines on top of black ones), consequently the trough around $A \sim 180$ is still present in the abundances.

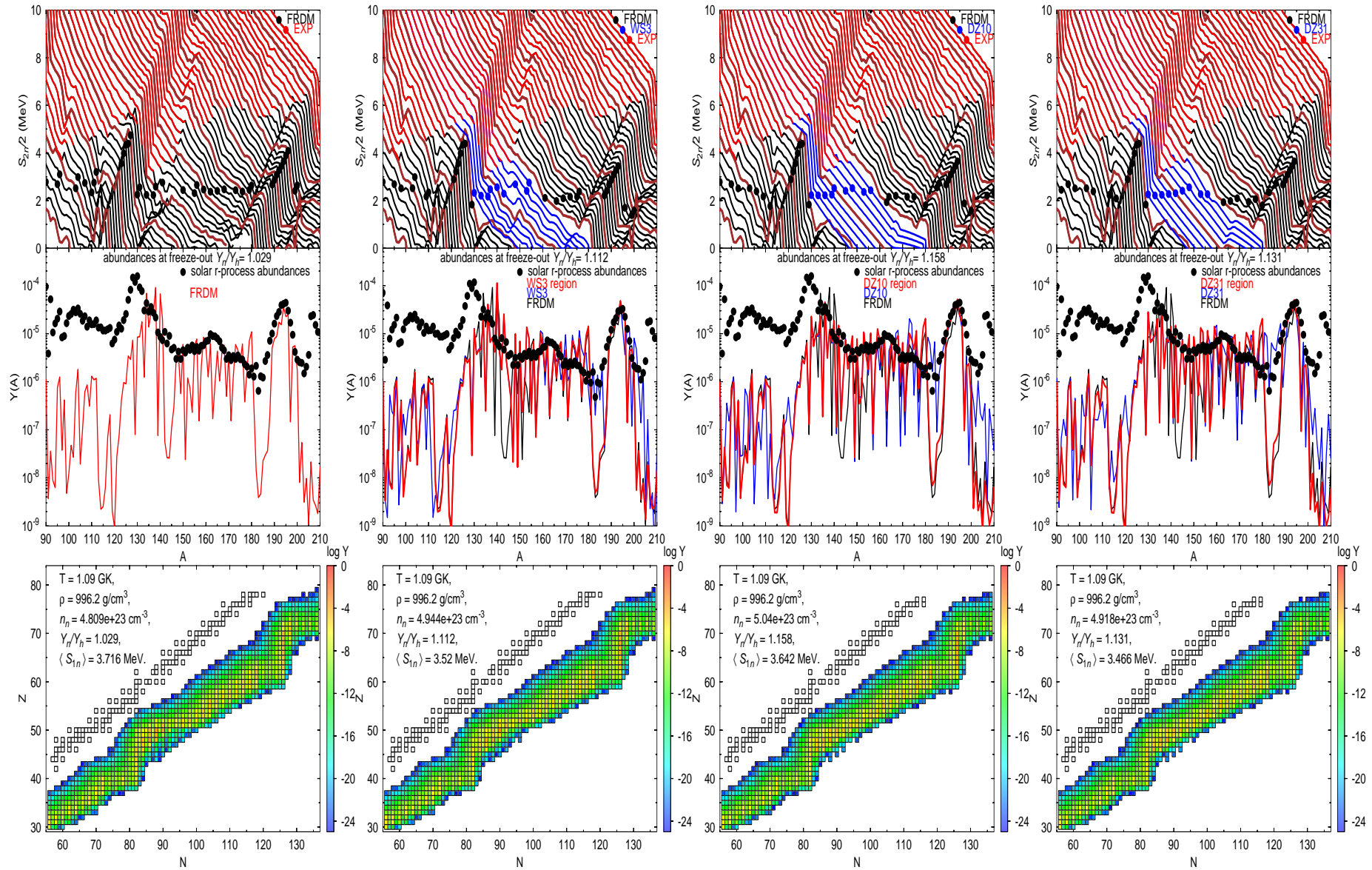


Figure 7.14: Same as Fig. 7.8, Impact of the region $N \sim 90$ under hot r-process conditions, at the time of the neutron exhaustion, i.e. when $Y_n/Y_h \sim 1$.

Fig. 7.15 displays, the final r-process abundances based on the above defined set of “hybrid rates”. Black lines are included to identify calculations based on FRDM and to guide the eye, the set of solar r-process abundances is represented by bullets.

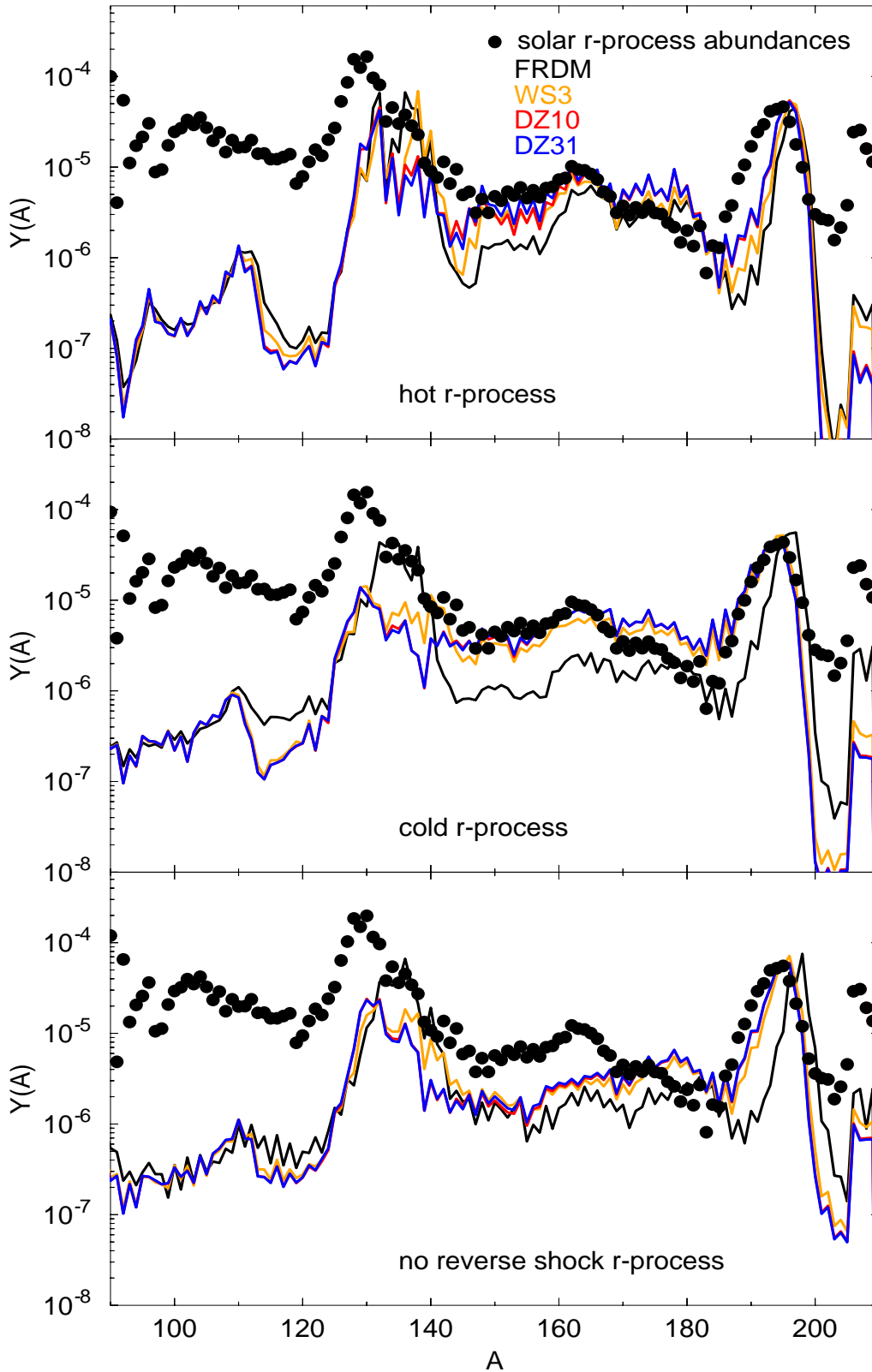


Figure 7.15: Same as in Fig. 7.7, but this time to explore the impact of the region $N \sim 90$ in the final r-process abundances.

7.2. FINAL R-PROCESS ABUNDANCE PATTERN

A comparison between the final r-process abundances based on the “original set of rates” (see Fig. 7.7) and the so-called “hybrid set of rates”, which were built by replacing FRDM masses around $N \sim 90$ (see Fig. 7.15), allows us to extract the following relevant remarks concerning to the role of the deformation region at $N \sim 90$:

- The origin of the trough around $A \sim 140$ (see Fig. 7.15) is related with an anomalous kink in the systematics of FRDM around $N \sim 90$ (see Fig. 2.8), consequently the obvious effect due to the “hybrid set of masses” is reduce/remove the trough around $A \sim 140$, because such feature is smoothed/absent in most of the mass models others than FRDM (see Figs. 2.10 to 2.12). As the final outcome (see Fig. 7.15) in the region $A \sim 140$ is mainly determined by the “replaced set of masses”, it is observed that the trough the final r-process abundances around $A \sim 140$ is notoriously reduced.
- Fig. 7.7 shows that when using sets of rates based on most of the models but FRDM, the final abundances for both hot and cold r-process in the region between the “REP” and the third r-process peak are always overestimated. In the case of a cold r-process a sort of “flat region” is observed. The effect of using the “sets of hybrid rates” (see Fig. 7.15) is that the final distribution of abundances around the third r-process peak region follow the behaviour of the set of rates based on FRDM. The following consequences are observed:
 - In the case of a hot r-process, the FRDM rates allow late time neutron captures around the region of the third r-process peak, shifting the peak to the right as a consequence.
 - When using a cold r-process, it is observed that the width of the third r-process peak is nicely reproduced for all the “hybrid set of rates”. This nice feature is the most remarkable consequence of the deformation region around $N \sim 90$ and comes from the interplay of the “replaced set of masses” which rule the behaviour around the region $N \sim 90$ and the “set of FRDM masses” which govern the behaviour around the third r-process peak region.
- A more detailed description of such “interplay” goes as follows: *due to the smooth behaviour of the “replaced set of masses”, more matter overcomes the region of deformation at $N \sim 90$, afterwards this matter will encounter a new deformation region before $N=126$ (due to FRDM) and as a consequence it will be partially blocked there, finally when matter manage to overcome such feature the width of the third r-process peak is correctly reproduced.*
- Fig. 7.7 displays, an additional advantage of using the “set of hybrid rates”, i.e., the region around the rare earth peak r-process peak ($A \sim 165$) is reproduced for both hot r-processes and cold r-process. This is again a consequence of the aforementioned interplay of “replaced set of masses” with the FRDM masses. As already mentioned, to produce the “REP”, there are 2 requirements [174, 10]:
 - A deformation region should exist in the systematics of the $S_{2n}/2$ at $A \sim 162$.
 - After the freeze-out stage, the r-process path should move around such feature. Namely, the “REP” will be produced as consequence of the late evolution of an r-process.

As the behaviour of the r-process abundances around $A > 160$ is governed by the FRDM set of mass the 1st requirement is fulfilled. For the second requirement, the systematics of the “replaced set of masses” ensure that enough matter will be moving through such feature at the late time evolution of an r-process. In the case of a hot r-process the above argument becomes more evident, as the evolution depends on the “set of masses” (see section 7.2.2.1). In the case of a cold r-process, the above argument has to be reinforced due to the fact that the evolution of the r-process depends on the competition of late time n-captures and β -decays (see section 7.2.2.2).

r-process network calculations: NSM conditions

In this chapter we explore the dynamically ejected matter from the merger of two neutron stars as a production site of neutron-rich heavy elements via rapid neutron captures (r-process). In order to do so, results from merger simulations and full network calculations are combined.

The thermodynamical trajectories were taken from three-dimensional relativistic simulations of a symmetric NS-NS mergers of $1.35M_{\odot}$ each; performed with a general relativistic smoothed particle hydrodynamics scheme [175, 22, 16]. The Einstein field equations were solved assuming a conformally flat spatial metric, for more details the reader is referred to [22]. In such simulations, about $6 \times 10^{-3}M_{\odot}$ were found to become gravitationally unbound, most of the ejected mass originates from the deep layers of the inner crust so that any contribution from near-surface layers remains minor.

The ejected matter is initially cold, but most of it gets shock-heated during the ejection to temperatures above 1 MeV. Note that the $1.35M_{\odot} - 1.35M_{\odot}$ case is of particular interest since, according to population synthesis studies and pulsar observations, it represents the most abundant system [176].

We use the dynamical r-process network described in sections 5.1.3 and 6.1. We follow a selected set of trajectories that cover the whole range of electron fractions, Y_e , found in the NSM simulations performed in [177]. We start our nucleosynthesis calculations when the density has dropped below the neutron drip density ($\rho_{drip} = 4 \cdot 10^{11} \text{ g cm}^{-3}$), since at higher densities, β -decays are Pauli-blocked and no heating to r-process like conditions may occur [14]. Fig 8.1, shows the set of trajectories used in the present work (see solid lines), for times that are larger than the hydrodynamic trajectories, we use an analytical expression (see dashed lines) for more details see section 6.2.1. We have added labels to denote its initial electron fraction Y_e .

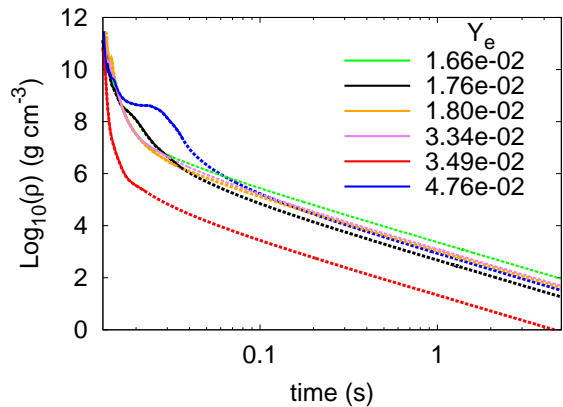


Figure 8.1: Density evolution of the NSM trajectories, starting when density has dropped below ρ_{drip} (see text).

A Network calculation has been performed (see section 6.3.1) to determine the initial composition before the material cools down by means of the expansion to the point at which Fermi blocking of β -decays ends and reheats sets in [14]. Figure 8.2 displays the initial composition for a number of NSM trajectories based on the masses from the WS3 mass model, its observed that the most representative nuclei lies near the magic numbers with $N=50$ ($A \approx 80$) and $N=82$ ($A \approx 120$). As mentioned above, we start our calculations when the NSM trajectories reach a density, $\rho \sim 10^{11} \text{gcm}^{-3}$, the distribution of seed nuclei will depend on both the nuclear structure features of the mass model and the thermodynamical conditions of the astrophysical scenario (NSM trajectories are characterised by their electron fraction, Y_e). A low Y_e implies that the scenario is highly neutron rich and consequently the neutron-to-seed ratio is large (the employed NSM trajectories reach neutron-to-seed ratios of the order of $Y_n/Y_h \sim 1500$) and the system is pushed far away from the valley of stability up to the neutron-driplines. In fact, the interplay of the Y_e with the temperature and the density of the ambient will determine the distribution of nuclei and how far away from stability the system is moving. If the system is running at higher temperatures, the dominant contribution to the total entropy is the radiation, so that the distribution will be shifted to lower mass numbers due to the photodissociation (predominantly to $A \sim 80$), on the other hand at low temperatures (low entropy), the system is moving farther from stability, i.e., the average one-neutron separation energy, $\langle S_{1n} \rangle$, reaches values of $\langle S_{1n} \rangle < 1$ MeV (favoring $A \sim 120$).

8.1. r-process heating

All heating is self-consistently added to the entropy of the fluid as follows:

1. Take the starting temperature and density from a given NSM trajectory.
2. At each time a dynamical r-process network code is used to determine the change in abundances (see section 5.1.3.1) and the nuclear energy generated (see Eq 5.27). From the energy generated we determine the change of entropy (see section 5.29).
3. Assuming that the density evolves as given by the NSM trajectory, a new temperature based on the increase of entropy can be obtained, i.e., $S(T, \rho) = S(t)$. The change of temperature was calculated from the Timmes EOS [178] that includes contributions from electrons, positrons, photons, nucleons, nuclei and the energy release resulting from nuclear transmutations. The entropy of the mixture is given by:

$$S(T, \rho) = S_\gamma + S_{e^+} + S_{e^-} + S_n + \sum_i S_i \quad (8.1)$$

Although our calculation does not explicitly account for the energy loss from β -decays into escaping neutrinos, we take this into account by artificially decreasing the heating rate by a factor 1/2. This is justified because as for neutron rich nuclei the β -decay Q-values are larger than the electron mass, most of the heating results from β -decays and the energy released is shared approximately equally between electrons (which thermalize) and neutrinos [179].

8.2. EVOLUTION OF AN R-PROCESS UNDER NSM CONDITIONS

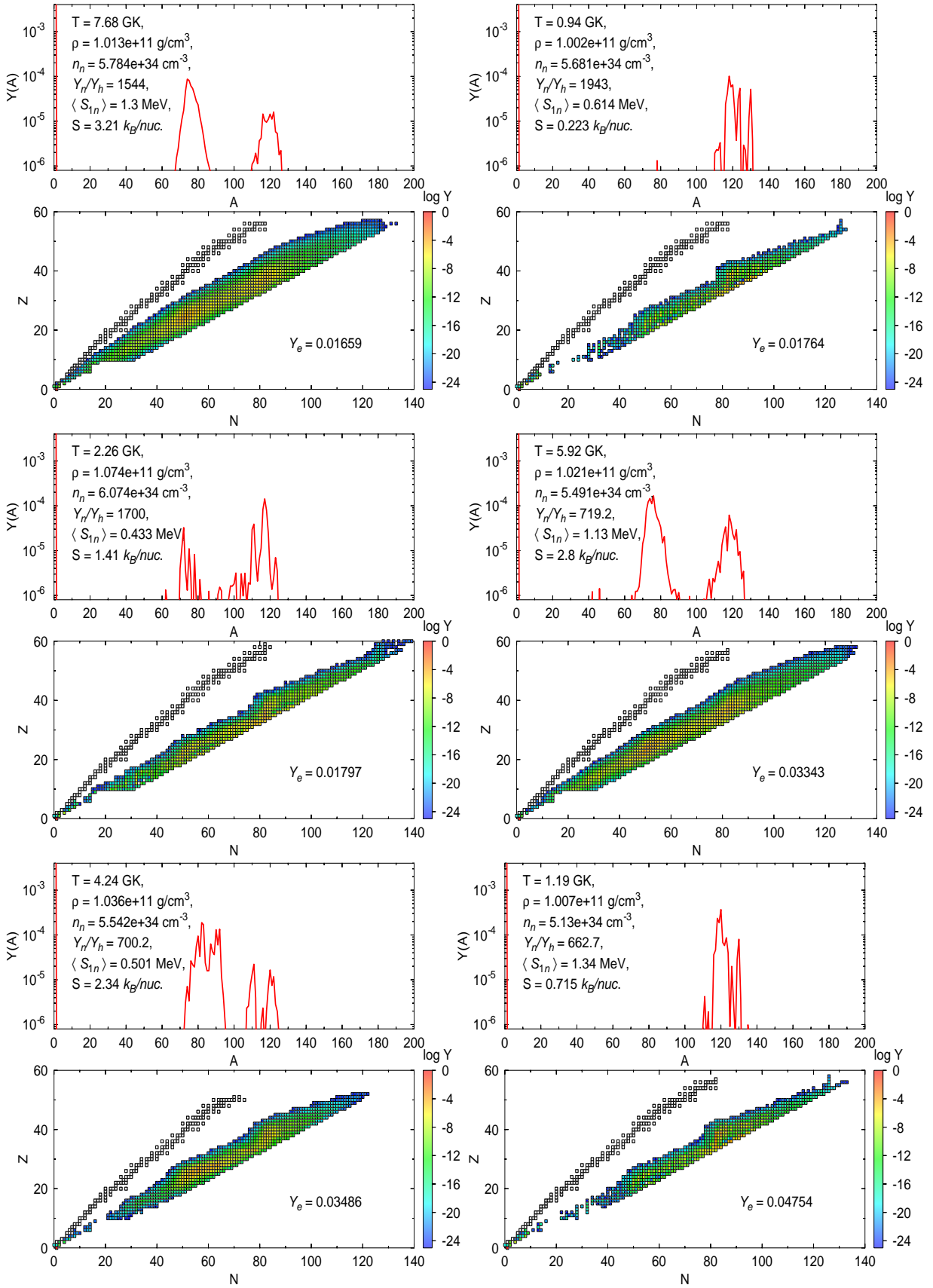


Figure 8.2: Initial composition based on the set of masses from the WS3 model for various NSM trajectories. Labels are added to identify the physical conditions, i.e., Temperature, T , density, ρ , neutron number density, n_n , neutron to seed ratio, Y_n/Y_h , entropy, S , and the electron fraction, Y_e .

8.2. Evolution of an r-process under NSM conditions

In order to gain additional insight, let us denote $\frac{dE}{dt}$ as the energy generation per unit of time and per nucleon. We have the following relation:

$$\frac{dE}{dt} = k_B T \frac{ds}{dt}, \quad (8.2)$$

where k_B is the Boltzmann constant. In this way the entropy, s , is given in units of k_B^{-1} baryon⁻¹. Furthermore let us assume that the entropy is a function of the temperature and density, i.e.,

$$s = s(T, \rho), \text{ in general, one obtains:} \quad (8.3)$$

$$\frac{dT}{dt} = \left(\frac{\frac{dE}{dt}}{k_B T} - \frac{\partial s}{\partial \rho} \frac{d\rho}{dt} \right) \left(\frac{\partial T}{\partial s} \right). \quad (8.4)$$

What Eq. 8.4 is telling us that in an adiabatic expansion, the rate of change of the Temperature will depend on the competition of the heating rate ($\frac{dE}{dt}$) and the expansion of the system ($\frac{d\rho}{dt}$).

Fig. 8.3 displays, the evolution of 3 variables: the density, ρ , the energy generation, $\frac{dE}{dt}$ and the temperature, T , for a number of NSM trajectories characterised by its electron fraction, Y_e . Each vertical panel display calculations based on: FRDM, WS3, DZ10 and DZ31 mass modes.

The lower most panels of Fig. 8.3, show that in general the heating rate, $\frac{dE}{dt}$, is independent of the uncertainties in the nuclear properties of unstable nuclei far from stability, i.e., no matter which mass model is employed, the heating rate display a similar behaviour. Concerning to the role of the energy heating in the evolution of an r-process under NSM conditions, one can extract the following important remarks by using both Fig. 8.3 and Eq. 8.4:

- Overall, it is observed that at the beginning the temperature of the system, drops faster as a consequence of the adiabatic expansion, soon afterwards the expansion rate decreases and the energy heating sets in, reheating the system up to temperatures of the order of $T \sim 1\text{GK}$. The energy generation doesn't last forever and it becomes inefficient with time, in particular $\frac{dE}{dt}$ sharply decreases once the neutrons are exhausted ($R_{n/s} \ll 1$) and the r-process is effectively complete [179]. The temperature of the system drops, once again following an adiabatic expansion.
- For certain NSM trajectories, the original adiabatic expansion after decompression stage, pushed the system to a very low temperature of the order of $T \leq 0.05\text{GK}$, and by the time that the energy generation rate becomes dominant, the system heats and reaches a temperature of $T \approx 0.25\text{GK}$.
- In more particular cases, it is observed that after initial period of decompression, certain NSM trajectories develop a sort of ‘‘plateau’’ in their evolution; i.e., the density behave like a constant for short period. Under such conditions all the energy generation us used to heated up the system, a sort of kinks appear in the Temperature evolution.

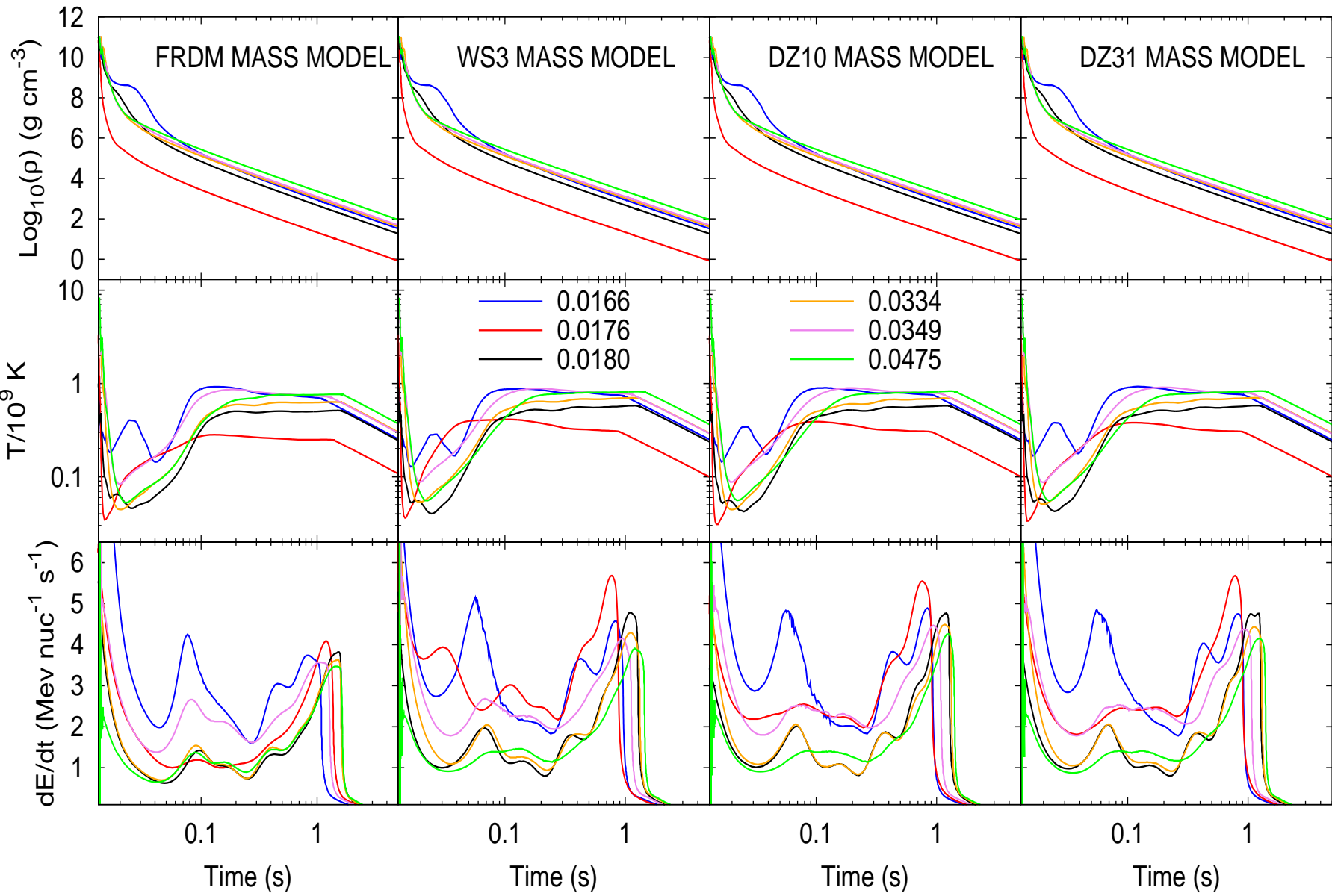


Figure 8.3: Evolution of relevant variables for the r-process.

8.3. Distribution of abundances for NSM trajectories at various stages

We have decided to display our results, as follows, keeping a set of masses and varying the trajectories, Figs. 8.4 to 8.7, show the distribution of the abundances, $Y(A)$, as a function of the mass number. Under Neutron Star Merger (NSM) conditions, the system is driven far away from stability. In order to explore the fission cycling, we have decided to display its abundances $Y(A)$ up to $A \sim 280$. Three snapshots of the abundances, $Y(A)$, are shown the uppermost panel at the time of the neutron exhaustion ($Y_n/Y_h = 1$), the middle panel at the end of the r-process ($\tau_{(n,\gamma)} = \tau_\beta$) and the lowermost panel at the final time step of our nucleosynthesis calculations.

Let us start describing generic features. As most of the NSM trajectories are still running under a hot r-process, we learned in section 7.2.2.1 that the knowledge of the nuclear masses is required to understand its evolution and distribution of abundance. Moreover, at the freeze-out stage, their abundances present a series of troughs, due to n-emission via photodissociation, the most dominant troughs appear due to waiting points located at saddle in the systematics of the S_{1n} . In addition, as the region $A \sim 280$ is reached, fission starts to feed back matter to the region around $A \sim 130$. Before the end of the r-process, the neutron-captures tend to favor even N (In particular around $A=130$ and $A=196$), as a consequence the abundances present a sort of staggering. A kink associated with the rare earth peak, REP, ($A \sim 165$) starts to emerge at the end of the r-process in most of the cases but DZ10. Finally, as the neutron number density is still large, in the late time evolution of our calculations, there are still some neutron-captures happening, but they are acting only on a limited number of regions, consequently smoothing the final distribution of abundances.

With the above facts in mind, we can explain the particular features of the mass models in the final abundance distribution:

- FRDM (see Fig. 8.4). The troughs developed at $A=140,180$ since the neutron exhaustion stage are still there, fission enters into the game and its mainly responsible for the peak $A \sim 130$. The late time neutron captures occur mainly in the region $a > 160$ and $A > 195$, this explain the shift to the right in the region of 3^{rd} peak of the r-process and the slightly reproduction of the REP ($A \sim 165$).
- WS3 (see Fig. 8.5). At the end of the r-process epoch, the width of the 3^{rd} r-process peak is reproduced, fission starts to feedback $A \sim 130$ and creates the 2^{nd} r-process peak, in addition the REP appears. In the end of the r-process only beta decays are happening and the distribution of abundances in the region $120 < A < 190$ is fixed.
- DZ10 (see Fig. 8.6). The distribution of abundances for $A > 200$ present a sort of plateau, i.e., almost a constant value and The 3^{rd} r-process peak is nicely form at the end of the r-process. Fission occurs soon afterwards an helps to built the 2^{nd} r-process peak. The rest of the evolution is governed mainly by β -decays.
- DZ31 (see Fig. 8.7). The width of the 3^{rd} r-process peak is overestimated because the systematics in the S_{1n} are “too smooth”, allowing matter to move to larger mass number A . The REP is nicely reproduced due to late time neutron captures in the region $A \sim 165$. Fission enter and reproduce the position and width of the 2^{nd} r-process peak.

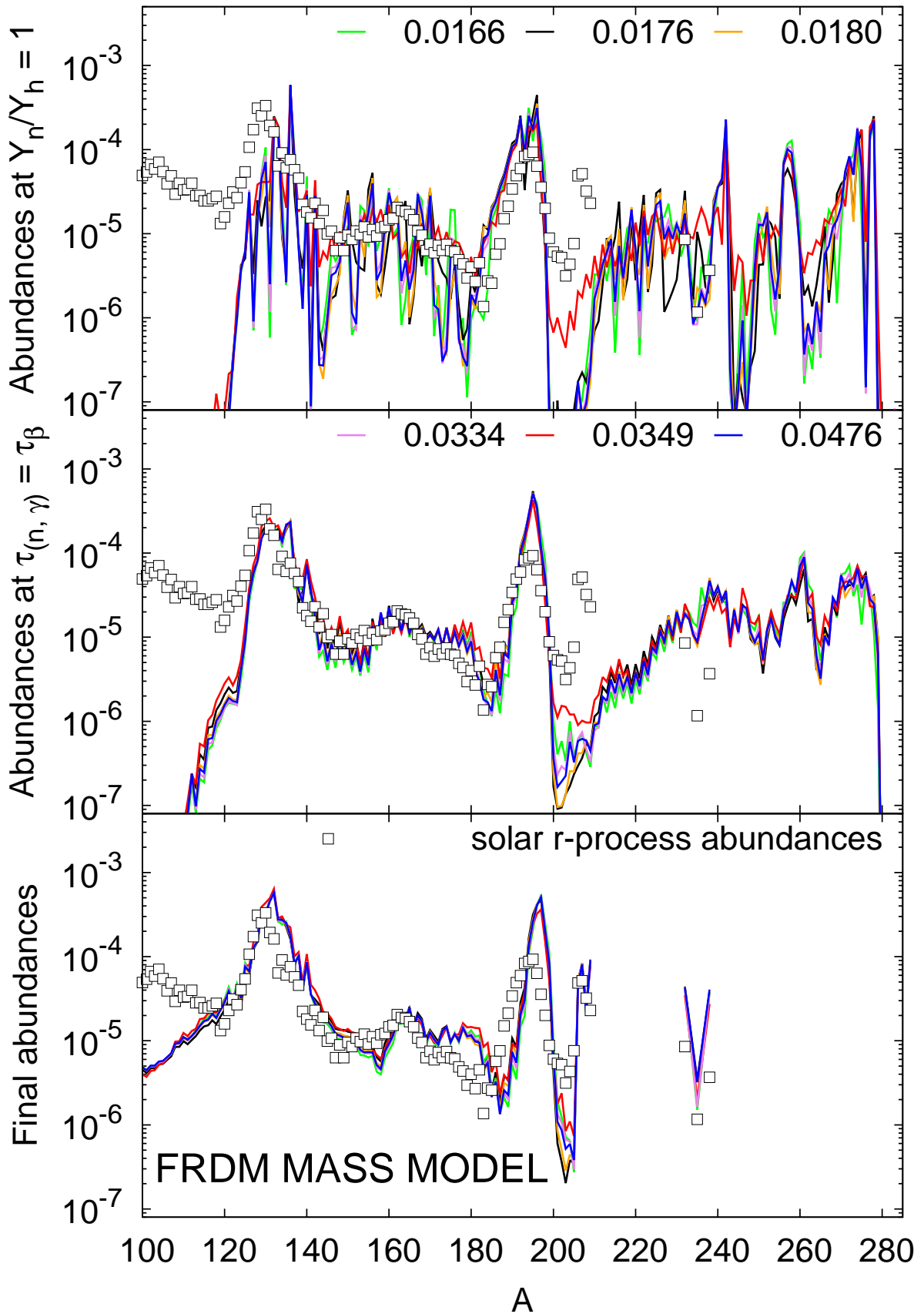


Figure 8.4: Distribution of abundances at various stages of the r-process as a function of the mass number A , for the FRDM mass model. Empty boxes symbols representing the solar r-process abundances are added just to guide the eye. Labels denote the electron fraction, Y_e , of a given trajectory.

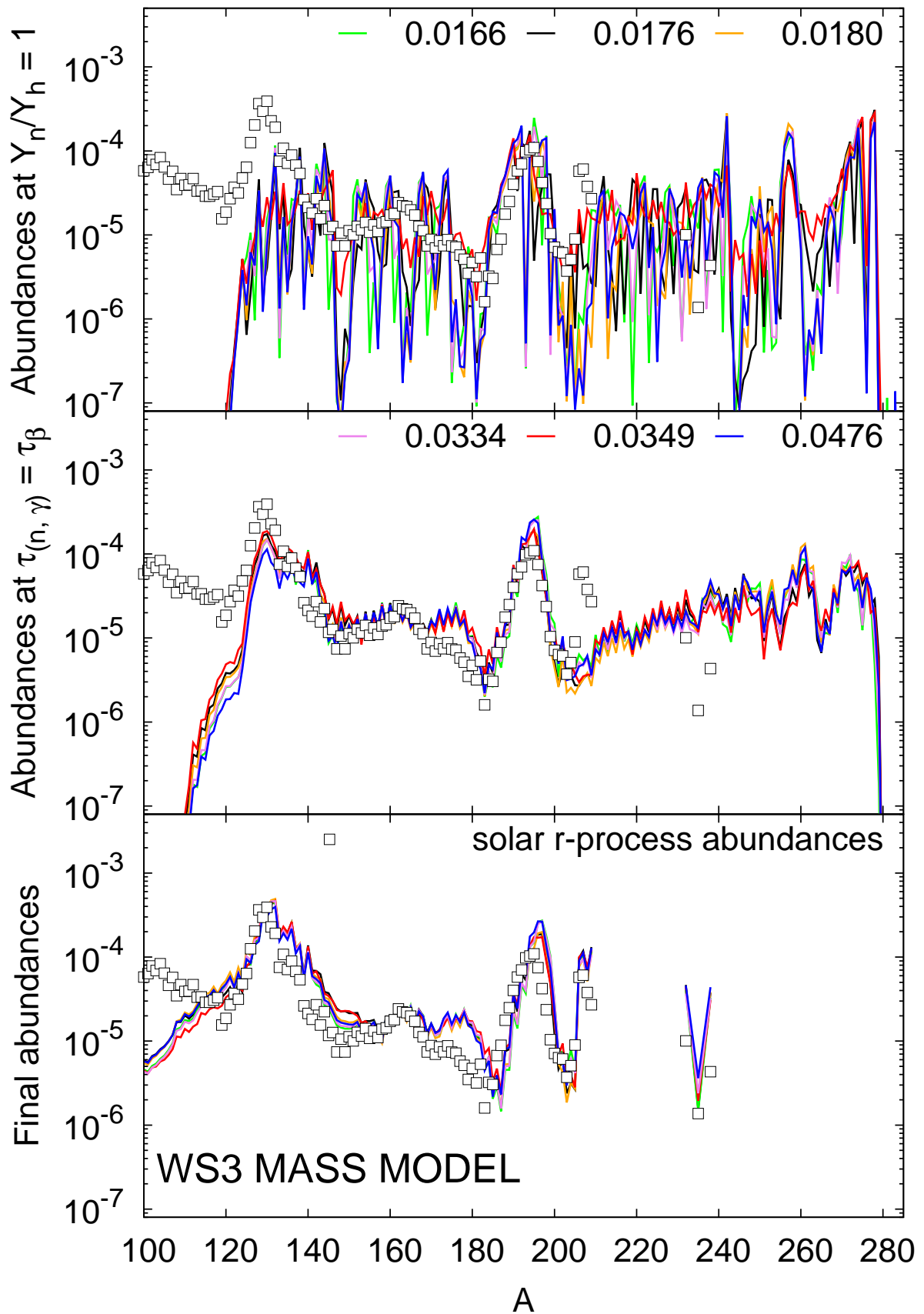


Figure 8.5: Distribution of abundances at various stages of the r-process as a function of the mass number A , for the WS3 mass model. Empty boxes symbols representing the solar r-process abundances are added just to guide the eye. Labels denote the electron fraction, Y_e , of a given trajectory.

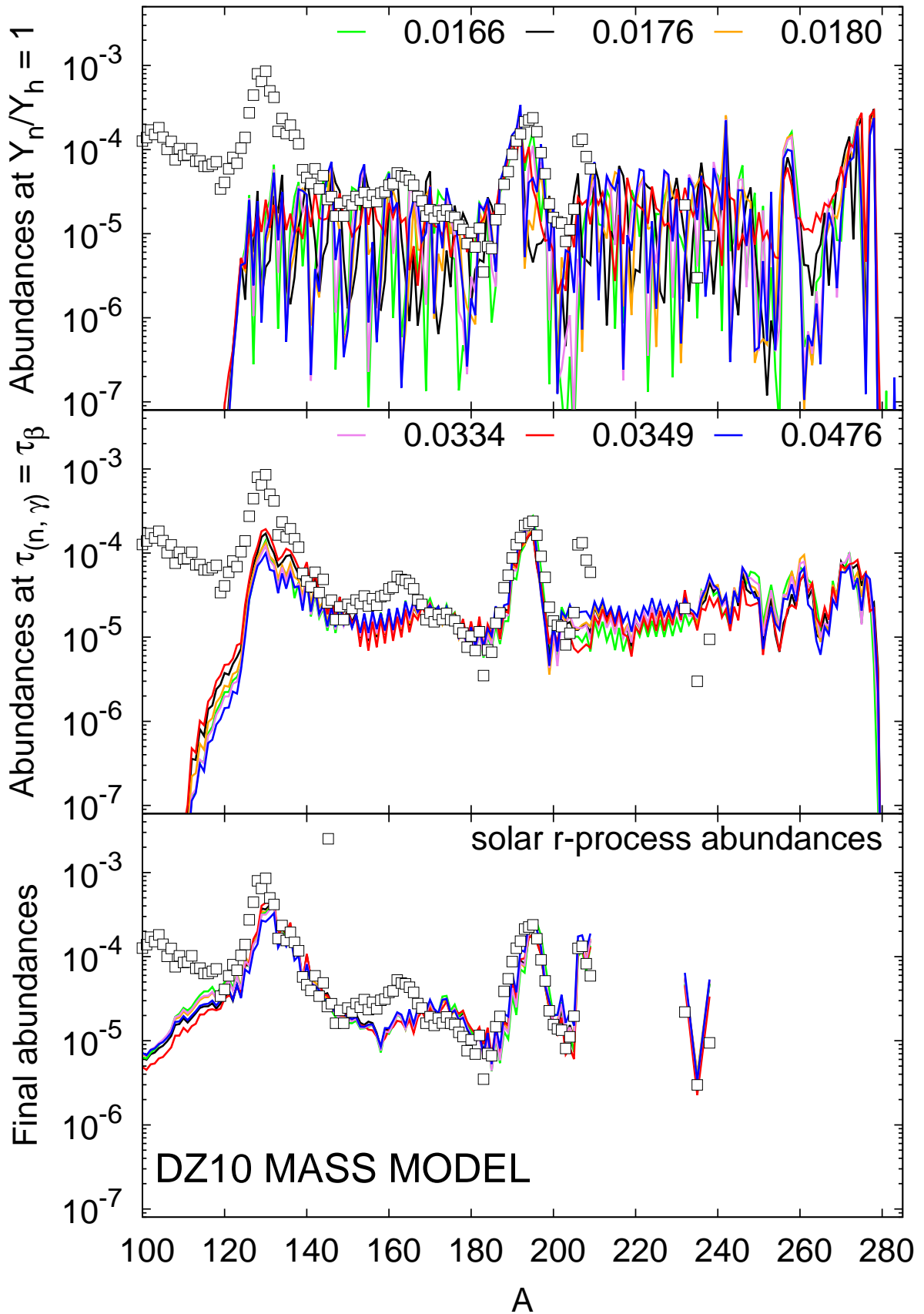


Figure 8.6: Distribution of abundances at various stages of the r-process as a function of the mass number A , for the DZ10 mass model. Empty boxes symbols representing the solar r-process abundances are added just to guide the eye. Labels denote the electron fraction, Y_e , of a given trajectory.

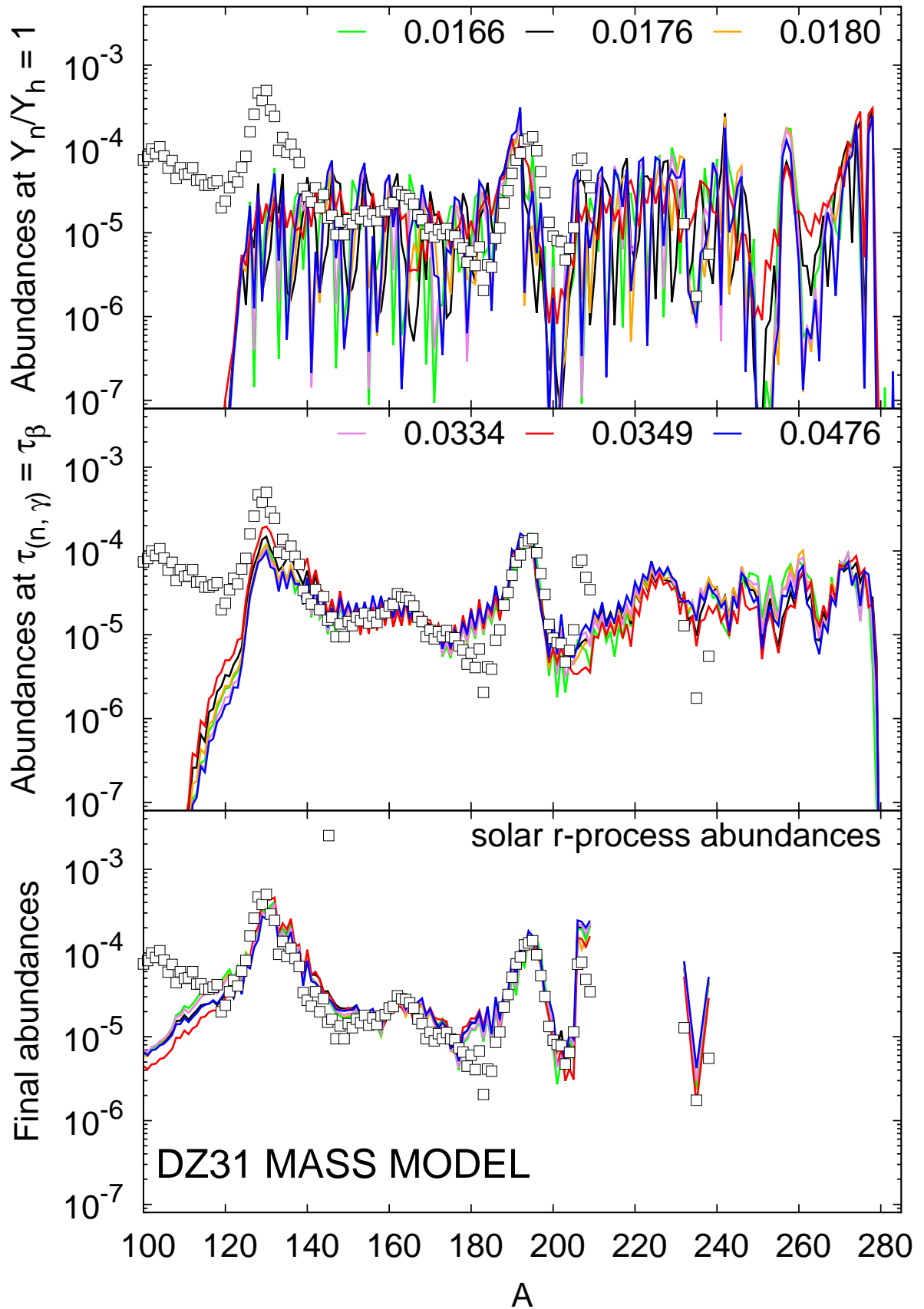


Figure 8.7: Distribution of abundances at various stages of the r-process as a function of the mass number A , for the DZ31 mass model. Empty boxes symbols representing the solar r-process abundances are added just to guide the eye. Labels denote the electron fraction, Y_e , of a given trajectory.

8.4. ROBUSTNESS IN THE OBSERVED FINAL PATTERN OF ABUNDANCES

In addition, the same aforementioned figures show that the REP is formed only, when either late neutron-captures occur around $A \sim 160$ or if neutron-emission occur at $A \sim 170$. In other words, as was found in [174] under a hot r-process like evolution the aforementioned process are effectively blocking the matter in the region $A \sim 165$.

8.3.1. Fission cycles

We have learned, that for the calculations involving NSM trajectories, the heating by nuclear processes during the r-process is not negligible, and the energy generation need to be consider (see section 5.2). Additionally, under the NSM scenario the matter will be pushed to conditions in which fission becomes important. In order to quantify the number of fission cycles, let us assume a bimodal distribution of the fission fragments, then at each fission cycle the final abundances of heavy nuclei increases by a factor 2. The number of fission cycles can be determined by:

$$Y_h^f = 2^{n_{cyc}} \cdot Y_h^0 \implies n_{cyc} = \text{Log}_2 \left(\frac{Y_h^f}{Y_h^0} \right), \quad (8.5)$$

$\frac{Y_h^f}{Y_h^0}$ can be estimated due to mass conservation:

$$\langle A \rangle^0 \cdot Y_h^0 + Y_n^0 = \langle A \rangle^f \cdot Y_h^f \implies \frac{Y_h^f}{Y_h^0} = \frac{\langle A \rangle^0 + \left(\frac{Y_n}{Y_h} \right)^0}{\langle A \rangle^f} = \frac{\langle A \rangle^0 + R_{n/seed}^0}{\langle A \rangle^f} \quad (8.6)$$

Table 8.1, shows that at the end of most of our r-process calculation we have found at least 2 fission cycles.

Table 8.1: number of fission cycles for a number of NSM trajectories, for n-capture rates based on: FRDM, WS3 and two variants of the DZ mass model.

Y_e	1.66e-02	1.76e-02	1.80e-02	3.34e-02	3.49e-02	4.75e-02
FRDM	3.64	3.70	3.69	2.52	2.79	2.25
WS3	3.42	3.79	3.62	2.42	2.39	2.36
DZ10	3.41	3.75	3.73	2.36	2.57	2,27
DZ31	3.38	3.73	3.54	2.29	2.41	2.23

Figs. 8.4 to 8.7, clearly show that the second peak of the r-process abundances ($A \sim 130$) originates via fission recycling, if a symmetric fission is assumed and furthermore if the fission takes place in the region $A \sim 280$.

8.4. Robustness in the observed final pattern of abundances

Fig. 8.8 summarizes the robustness in the observed final pattern of abundances for $A > 120$, i.e., the fact that the final abundances are independent of which NSM trajectory is used (in this case the neutron-to-seed ratio, $Y_{n/h}$, is shown instead of the electron fraction, Y_e , for a given trajectory). All the explored theoretical mass models exhibited the same behaviour. This is a consequence of the fission cycling, which in turn is redistributing matter from regions with $A \sim 280$ to regions with $A \sim 140$, this feedback of matter is responsible for the reproduction of the 2nd r-process peak.

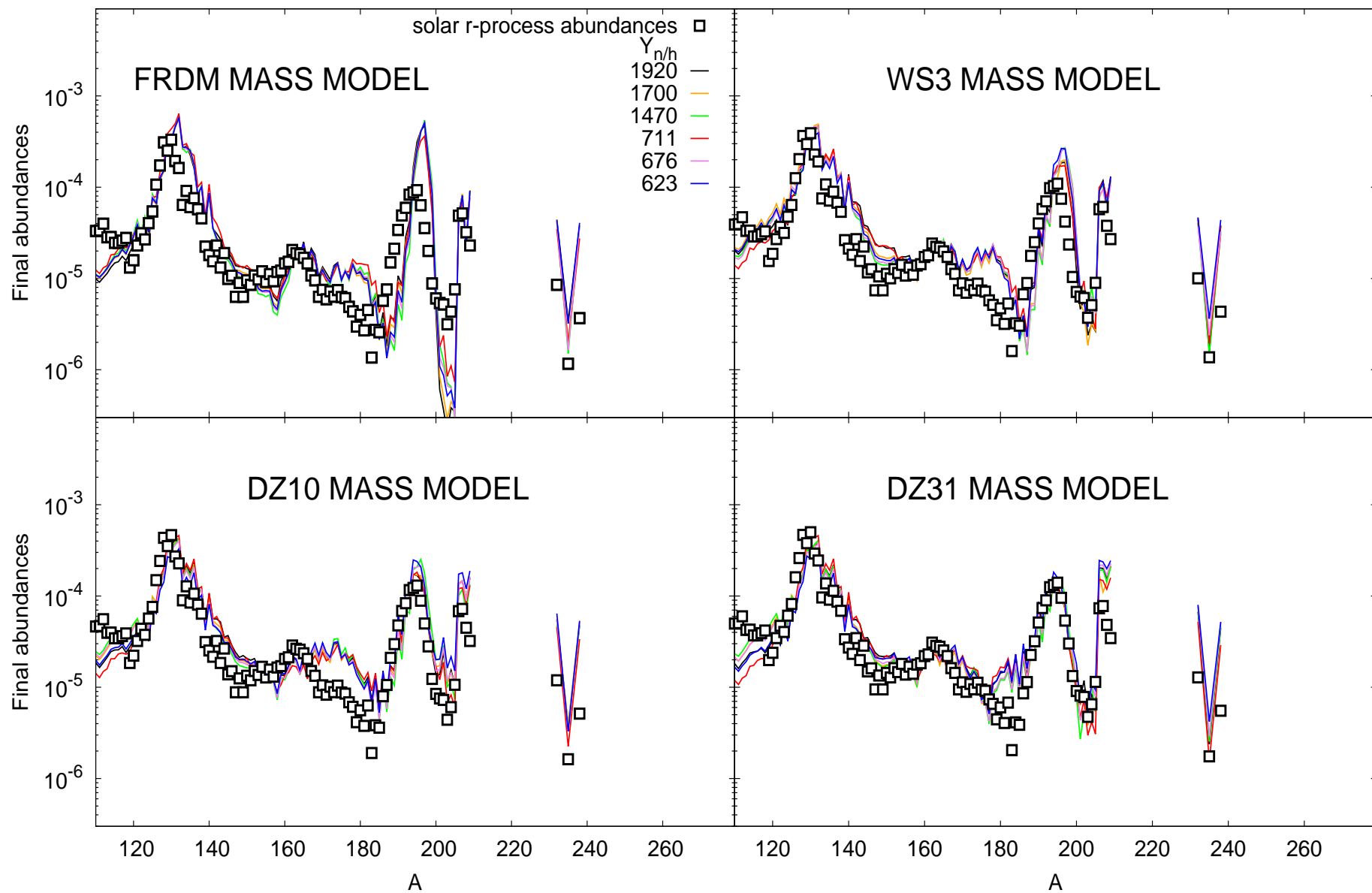


Figure 8.8: Robust pattern in the final r-process abundances for $A > 120$ due to fission cycling.

Part III

Summary and Outlook

Summary and Outlook

During the present Thesis, the role of the nuclear masses in r -process nucleosynthesis calculations have been explored. In order to accomplish this goal, we have computed neutron capture rates in the framework of the statistical model [154] for all relevant nuclei in the r -process regime, to be more specific, nuclei ranging from Zn ($Z=30$) to Bi ($Z=83$) and contained inside the model dependent driplines. We have use the currently available mass models that best reproduce the known masses with a root mean square deviation smaller than $\text{RMSD} < 600$ keV. This include the following set of mass models: Finite Range Droplet Model (FRDM) [18], Weizsäcker-Skyrme model (WS3) [19] and two variants of the Duflo-Zuker mass model [20], namely DZ10 and DZ31.

Our work was mainly devoted to perform tree tasks, namely:

1. Identify the systematics of the different mass models in terms of familiar nuclear structure quantities, like: one-neutron separation energies ($S_{1n}(Z, N)$), two-neutron separation energies ($S_{2n}(Z, N)$), shell gaps ($\Delta(Z, N)$), where Z denotes the number of protons and N the number of neutrons respectively. Additionally we also explored the residuals (differences between a given theoretical mass model and the set of measured masses) shell corrections (differences between a given mass model and a liquid drop model like mass formula).
2. Compute the neutron capture rates for the aforementioned models in the framework of the statistical model [17]. The resulting reaction library has been used to perform r -process network calculations.
3. Perform dynamical r -process network calculations with thermodynamical conditions taken from hydrodynamical simulations corresponding to high entropy neutrino winds from core collapse supernovae (SNe) and Neutron star mergers(NSM). In the case of the neutrino winds, we also explored the impact of the reverse shock on the r -process abundances and dynamics, this was done by introducing three different trajectories, which mainly differ in the position of the shock, allowing us to make the distinction of three different r -process, namely: hot r -process, cold r -process and a evolution without a reverse shock. In the case of the NSM calculations, as this scenario corresponds to a lower entropy site, one has to considered to compute the energy generation due to nuclear transmutations. Nucleosynthesis calculations were performed with a large reaction network which includes 7000 isotopes from nucleons up to $Z=110$ between the neutron drip line and the line of stability.

Detail analysis of the first and second items (systematics and n-capture rates based on different mass models) revealed, that the region of transition from spherical to deformed nuclei (at $N \sim 90$) is the region in which the models differ the most. To explore the impact of this particular region, we decided to build a number of “hybrid rates” as follows: Merge the set of FRDM masses with another set of masses at a time, this is done by replacing the masses of isotopic chains ranging from Pd ($Z=46$) to Xe ($Z=54$) by the ones based on the set of WS3, DZ10 and DZ31 masses. In this way the final outcome will be denote as “hybrid set of masses”. Compute the n-capture rates based on the aforementioned “hybrid set of masses” via the statistical model.

It is worth to mention that up to now, only the n-capture rates based on sets of masses based on the Extended Thomas Strutinsky Integral (ETFSI), FRDM computed via the statistical model [17] and those based on HFB mass models computed via the code TALIS [181] are available. In that sense, our calculations have added 3 new set of n-capture rates based on the WS3, DZ10 and DZ31 mass models. In comparison to previous studies to explore the impact of different mass models in r-process network calculations (e.g., [182]), we have obtained results which are self-consistent. This is because we have used the same set of masses as an input for the calculation of the n-capture rates.

After the r-process calculations are finished, we proceed to identify the sensitivity of the nuclear physics input in the evolution and the final distribution of r-process abundances. Our most important findings can be summarised as follows:

High entropy ν -driven wind trajectories. When considering the evolution of a hot r -process with a reverse shock at a temperature of 1 GK, the system is pushed to a (quasi) $(n, \gamma) - (\gamma, n)$ equilibrium during the major r-process phase. Under such conditions the evolution of the r-process only depends on the knowledge of the nuclear masses through their separation energies and interesting conclusions can be extracted from the analysis of its systematics. For instance, we found that the region of deformation at $N \sim 90$ ($N \sim 118$), identified right before (after) the neutron shell closure at $N=82$ ($N=126$) is of major relevance for the final distribution of abundances. In fact, the right shifted 3rd r-process peak observed for both WS3 and FRDM has an origin related with the behaviour around $A \approx 180$ ($N \approx 118$), because matter start to accumulate there an trough is developed. As this feature is absent in the DZ models, neutron captures can move matter from that region through higher mass numbers and as consequence the 3rd r-process peak gets broader. The above analysis is not possible when considered a “cold” r -process. To understand its evolution and final abundance distribution, an explicit knowledge of both n-capture rates, $N_n \langle \sigma v \rangle^*$, and beta decays rates, λ_β , is required. The r-process path for a cold r-process move matter to a region farther away from stability when compared to the one of a generic “hot r-process”, due to the fact that as the system is mainly running at $T_9 < 1$ GK, the neutron-emission via photodissociation can be neglected. As in [10], we found that the in the case of a “cold r-process”, late time n-captures, after the freeze-out stage, are still occurring and they produce not negligible changes in the final r-process abundances. In fact, it was found that for the case of set of rates based on FRDM, the final distribution of abundances will be shifted to higher mass numbers ($A = 185-195$) because of the late time n-captures in the regions with $A > 195$. In the rest of the mass models, beta-decay dominates over n-captures, nuclei will beta decay without substantially changing the mass number. We found that the formation of the so-called “rare earth peak” at $A \sim 165$, for a “hot r-process” depends

on the late time distribution of the r-process abundances, under a competition (after the freeze-out stage) of the three major process occurring in an r-process, namely: n-capture, n-emission via photodissociation and β -decay. The final r-process abundances based on the “set of hybrid rates”, present interesting properties, namely: removing/smoothing the artificial waiting point at $A \sim 140$, reproducing the width of the “third r-process peak” at $A \sim 195$ and in certain cases reproducing the “rare earth peak” at $a \sim 165$. All the already mentioned features, are due to the behaviour at $N \sim 90$ of the mass models explored.

Neutron star merger trajectories(NSM) In most of the NSM trajectories explored in the current work, the expansion time scale of NSM is not too fast, allowing the heating rate to drive the system up to a $T \sim 1\text{GK}$. Such scenario correspond to the already described “hot r-process”. However, there are differences between these “hot r-processes”, which are related to the densities and expansion time scales of the two processes. The NSM one involves densities orders of magnitude bigger than the ν -driven wind one; in addition the expansion time scale for NSM is faster when compared to the ν -driven wind. When using NSM trajectories, the calculated final r-process abundances seem to be independent of the original conditions, i.e., their final pattern of abundances is robust. The reason was attributed to fission cycling, which in turn is redistributing matter. In fact, our calculations found that the matter in NSM trajectories is subjected to up three fission cycles. As the neutron number densities are still large at the freeze-out stage, late time n-captures are also not negligible, this in turns produce a sort of smoothing in the final r-process abundances of the NSM trajectories. The physics behind the 2nd r-process peak ($A \sim 130$) is related to fission around $A \sim 280$. One has to keep in mind that regardless of the mass models employed, in a NSM trajectory even at earlier stages the system is pushed to a region were fission is already possible. The final r-process abundances are very sensitive to the theoretical masses. In particular the region $N \sim 90$ determine the mass flow from the second ($A \sim 130$) to third ($A \sim 195$) r-process peaks. The agreement with the position of “REP” ($A \sim 165$) is more complex to disentangle. And depends on the interplay of the dominant processes occurring in the late time evolution of the r-process.

Finally, the following things remain to be implemented:

- In certain NSM trajectories, it is observed that the r-process is moving at lower separation energies ($S_{1n} < 1 \text{ MeV}$), for which the statistical model description of the neutron capture rates may break down. In these cases, we must consider the direct neutron captures.
- Our calculations are currently using the set of β -decay rates of Moeller et al. [164], in the near future it will be interested to consider additional sets of β -decay rates.
- Implementation of different fission fragment yields.
- Study the sensitivity to the nuclear physics input and to the astrophysical sites for the production ratios of U and Th Cosmochronometers.

Bibliography

- [1] Aston, F. W., 1920, *Nature* (London) 105, 617.
- [2] Eddington, A. S., 1920, *Nature* (London) 106, 14.
- [3] Lunney, D.; Pearson, J. M. & Thibault C., 2003, *Rev. Mod. Phys.* 75, 3.
- [4] Rolfs C.E. & Rodney, W.S. 1988, *Cauldrons in the Cosmos* (Chicago IL: University of Chicago Press)
- [5] Blaum K. 2006, *Phys. Rep.* 425 1
- [6] Burbidge, E.M., Burbidge, G.R., Fowler, A.A. & Hoyle, F. 1957, *Rev. Mod. Phys.* 29, 547.
- [7] Cowan, J. J.; Thielemann, F-K. 2004, *Phys. Today* 57, 47.
- [8] Qian, Y.-Z., |& Woosley, S. E. 1996, *ApJ* 471, 331.
- [9] Qian, Y.-Z. 2000, *ApJ* 534 L67.
- [10] Arcones, A. & Martínez-Pinedo, G. 2011, *Phys. Rev. C* 83, 045809 (4).
- [11] J. M. Lattimer & D. N. Schramm. 1976, *Astrophys. J.* 210, 549-567.
- [12] J. M. Lattimer, F. Mackie, D. G. Ravenhall & D. N. Schramm. 1977, *Astrophys. J.* 213, 225-233.
- [13] D. Eichler, M. Livio, T. Piran & D. N. Schramm. 1989, *Nature* 340:126?128.
- [14] Freiburghaus, C., Rosswog, S., & Thielemann, F-K. 1999b, *ApJ* 525, L121.
- [15] Goriely, S., Bauswein, A. & Janka, H.-T. 2011, *ApJ lett.* 738:L32.
- [16] Bauswein, A. ,Goriely, S. & Janka, H.-T. 2013, *ApJ* 773, 78.
- [17] Rauscher, T. & Thielemann F-K. 2000, *At. Data Nucl. Data Tables* 75, 1.
- [18] Möller, P, Nix, J.R., Myers, W.D. & Swiatecki, W.J.. 1995, *At. Data Nucl. Data Tables* 59, 185. <http://ie.lbl.gov/txt/astab.txt>
- [19] Liu, M., Wang, N., Deng, Y. & Wu, X. 2011, *Phys. Rev. C* 84. <http://www.inqmd.com/mass/WS3.6.txt>

- [20] Duflo, J. & Zuker, A.P. 1995, *Phys. Rev. C* 52, 23.
- [21] Arcones A., Janka, H.-T. & Scheck L. 2007, *Astron. & Astrophys* 467 1227.
- [22] Bauswein, A., Janka, H.-T. & Oechslin R. 2010, *Phys. Rev. D* 82, 08404.
- [23] Goriely, S., Tondeur, F, Pearson, J.M. 2001, *Atom. Data Nucl. Data Tables* 77 311.
- [24] Gamow G., 1929, *Proc. Roy. Soc. [A]* 146, 386-387.
- [25] Gamow G., 1930, *Proc. Roy. Soc. [A]* 126, 632-644.
- [26] Rutherford, E., Chadwick J. & Ellis C. D. 1930 *Radiations from Radioactive Substances* (Macmillan and Cambridge University Press) pp 327.
- [27] Von Weizsäcker, C. F., 1935, *Zeit. f. Phys.* 96, 431-458.
- [28] Bethe, H. A. & Barcher, R. F. 1936, *Rev. Mod. Phys.* 8, 165-168.
- [29] Ring, P. and Schuck, P. 1980, *The Nuclear Many-Body Problem* (Springer-Verlag).
- [30] Bethe, H. A., 1999, *Rev. Mod. Phys.* 71, 2.
- [31] Krane, Kenneth S. 1987, *Introductory Nuclear Physics*, Wiley, 1987.
- [32] Audi, G., Wang, M., Wapstra, A.H., Kondev, F.G., MacCormick, M., Xu X & Pfeiffer, B. 2012, *Chin. Phys. C* 36.
- [33] Bardeen, J., Cooper, L. N. & Schrieffer, J. R. 1957, *Phys. Rev. Lett.* 108, 1175.
- [34] Bohr, Å., Mottelson, B. R. & Pines, D. 1958, *Phys. Rev.* 110, 936.
- [35] Myers, W.D. & Swiatecki, W.J. 1966, *Nucl. Phys.* 81, 1.
- [36] Wigner, E. 1937, *Phys. Rev.* 51, 106.
- [37] Van Isacker, P, Warner, D. & Brenner, D. S. 1995, *Phys. Rev. Lett.* 74, 4607.
- [38] Goriely, S., Chamel, N. & Pearson, J. M. 2009, *Phys. Rev. Lett* 102 152503.
- [39] Vautherin, D. & Brink, D. M. 1972, *Phys. Rev. C* 5, 626
- [40] Beiner, M., Flocard, H., Van Giai, N., and Quentin P. 1975, *Nucl. Phys. A* 238, 29.
- [41] Tondeur, F, Brack, M., Farine, M. & Pearson, J. M. 1984, *Nucl. Phys. A* 420, 297.
- [42] Brack, M., Guet, C. & Håkansson, H.-B. 1985, *Phys. Rep.* 123, 275.
- [43] Chabanat, E., Bonche, P, Haensel, P, Meyer, J. & Schaeffer, R. 1997, *Nucl. Phys. A* 627, 710.
- [44] Chabanat, E., Bonche, P, Haensel, P, Meyer, J. & Schaeffer, R. 1998, *Nucl. Phys. A* 635, 231.
- [45] Chamel, N., Goriely, S., & Pearson, J. M. 2008, *Nucl. Phys. A* 812 72.

BIBLIOGRAPHY

- [46] Goriely, S., Chamel, N. & Pearson, J. M. 2010, *Phys. Rev. C* 82 035804.
<http://www-astro.ulb.ac.be/bruslib/nucdata/hfb21-dat>
- [47] Audi, G., Wapstra, A.H. & Thibault, C. 2003 *Nucl. Phys. A* 729, 337.
- [48] <http://http://www.astro.ulb.ac.be/pmwiki/Bruslib/Hfb17>
- [49] Strutinsky, V. M. 1967, *Nucl. Phys. A* 95, 420.
- [50] Strutinsky, V. M. 1968, *Nucl. Phys. A* 122, 1.
- [51] Myers, W.D., & Swiatecki, W.J. 1969, *Ann. Phys.* 55, 395.
- [52] Myers, W.D., & Swiatecki, W.J. 1974, *Ann. Phys.* 84, 186.
- [53] Myers, W.D., Swiatecki, W.J., Kodama, T., El-Jaick, L.J. & Hilf, E.R. 1977, *Phys. Rev. C* 15, 2032.
- [54] Moller, P. & Nix, J.R. 1981, *Nucl. Phys A* 361, 117.
- [55] Treiner, J., Myers, W.D., Swiatecki, W.J. & Weiss, M. S. 1986, *Nucl. Phys A* 452, 93.
- [56] Audi, G., Midstream Atomic Mass Evaluation, private communication (1989), with four revisions.
- [57] Möller, P., Myers, W. D., Sagawa, H., Yoshida, S. 2012, *Phys. Rev. Lett* 108, 052501.
- [58] Wang, N., Liu, M. & Wu, X. 2010, *Phys. Rev. C* 81 044322.
- [59] Wang, N. & Liu, M. 2010, *Phys. Rev. C* 81 067302.
- [60] Wang, N., Liang, Z., Liu, M. & Wu, X. 2011, *Phys. Rev. C* 82 044304.
- [61] Liu, M., Wang N., et al. 2006, *Nucl. Phys. A* 768 80.
- [62] Wang, N. & Liu, M. 2011, *Phys. Rev. C* 84 051303(R).
- [63] Morales I. O., Van Isacker, P., Velázquez, V. I., Barea, J., Mendoza-Temis, J., López Vieyra, J. C., Hirsch, J.G. & Frank, A. 2010, *Phys. Rev. C* 81, 024304.
- [64] Hardy, L. 1971, *J. Geophys. Res.* 76 1905.
- [65] Buhmann, M. D. 2003, *Radial Basis Functions: Theory and Implementations* (Cambridge University Press, Cambridge UK)
- [66] Garvey, G.T. & Kelson, I. 1966, *Phys. Rev. Lett.* 16, 197.
- [67] Barea, J., Frank, A., Hirsch, J. G., Van Isacker, P., Pittel, S. & Velázquez, V. 2008, *Phys. Rev. C* 77 041304(R).
- [68] Morales, I. O., López Vieyra, J. C., Hirsch, J. G., Frank, A. 2009, *Nuc. Phys. A* 828 113.
- [69] Mendoza-Temis, J., Morales, I., Barea, J., Frank, A., Hirsch, J.G., López Vieyra, J. C., Van Isacker, P. & Velázquez, V. 2008, *Nuc. Phys. A* 812 28.

-
- [70] Duflo, J. 1994, *Nucl. Phys. A* 576 29.
- [71] Zuker, A.P. 1994, *Nucl. Phys. A* 576 65.
- [72] Caurier, E., Martínez-Pinedo, G., Nowacki, F., Poves, A. , Zuker, A.P. 2005, *Rev. Mod. Phys.* 77 427.
- [73] Zuker, A.P. 2008, *Rev. Mex. Fis.* S 54 129.
- [74] Mendoza-Temis, J., Hirsch, J.G. & Zuker, A.P. 2010, *Nucl. Phys A.* vol. 843, no. 1, pp. 14-36.
- [75] Zuker, A.P. 2009, *Private communication*.
- [76] Zuker, A.P. 2003, *Phys Rev. Lett.* 90, 042502.
- [77] Schwenk, A. & Zuker, A.P. 2006, *Phys. Rev. C* 74 061302(R).
- [78] Zuker, A.P., Retamosa, J., Poves, A. 1995, *Phys. Rev. C* 52 R1741.
- [79] Bohr, A. & Mottelson, B.R. 1998, *Nuclear Structure, vol. I: Single-Particle Motion*, (World Scientific, Singapore), Sections 2-4
- [80] Dufour, M. & Zuker, A.P. 1996, *Phys. Rev. C* 54 1641.
- [81] Entem, D.R. & Machleidt, V. 2003, *Phys. Rev. C* 68 041001.
- [82] Boegner, S.K., Kuo, T.S. & Schwenk, A. 2003, *Phys. Rep.* 386 1.
- [83] Audi, G., Wapstra, A.H. 1995 *Nucl. Phys. A*, 595, 409.
- [84] Zuker, A.P. 1995. Private Communication.
- [85] Zuker, A.P. 2008, *Rev. Mex. Fis.*, S 54, 129.
- [86] Erler, J., Birge N., Kortelainen, M., Nazarewicz, W., Olsen, E., Perhac A.M., Stoiso, M. 2012, *Nature*, 486, 509.
- [87] Bender, M., Hennen, P.H., Reinhard, P.G. 2003, *Rev. Mod. Phys* 75, 121-180.
- [88] Reiss, C., Bender, M., Reinhard, P.G. 1999, *Eur. Phys. J. A* 6, 157-165.
- [89] Cameron, A.G.W., 1957, *Chalk River rep. no. CRL-41*, Chalk River Labs, Chalk Rive, Ontario.
- [90] Cowan, J.J., Thielemann, F-K. & Truran, J.W. *Nuclear evolution of the universe* Forthcoming.
- [91] Sneaden, C. Cowan, J.J. 2003, *Science* 299, 70.
- [92] Kratz, K.-L., Bitouzet, F., Thielemann, F-K., Moeller, P & Pfeiffer, B. 1993, *Astrophys. J.*, 403, 216.
- [93] Mocalj, D., “Neutron-nd neutrino-induced reactions: their physical description and influence on r-process calculations.” PhD diss. Universität Basel, 2006.
-

BIBLIOGRAPHY

- [94] Qian, Y.-Z. 2003, *Prog. Part. Nucl. Phys* 50, 153-199.
- [95] Woosley, S. E. and Heger, A. and Weaver, T. A., 2002 *Rev. Mod. Phys.* 74, 1015-1071.
- [96] Heger, Alexander, Woosley, S.E., Fryer, C.L. & Langer, Norbert. 2003, *Massive Star Evolution Through the Ages* (Springer Berlin Heidelberg) 3-12.
- [97] Janka, H.-Th., Langanke, K., Marek, A., Martínez-Pinedo G. & Müller B. 2007 *Phys.Rept.* 442, 38-74
- [98] Fowler, W.A. & Hoyle F *Nucleosynthesis in Massive Stars and Supernovae*, Univ. of Chicago Press, Chicago, 1965.
- [99] Qian, Y.-Z. 2012, *AIP Conference Proceedings*, 1484, 201-208
- [100] Y.-Z. Qian, G. M. Fuller, G. J. Mathews, R. W. Mayle, J. R. Wilson, and S. E. Woosley, *Phys. Rev. Lett.* 71, 1965–1968 (1993).
- [101] E. Anders and N. Grevesse, *Geochim. Cosmochim. Acta* 53 (1989) 197
- [102] R. Gallino, C. Arlandini, M. Busso, M. Lugaro, C. Travaglio, O. Straniero, A. Chieffi and M. Limongi, *APJ* 497 (1998) 388
- [103] C. Arlandini, C., F. Käppeler, K. Wisshak, R. Gallino, M. Lugaro, M. Busso, and O. Straniero, *APJ* 525 (1999) 886
- [104] A. McWilliam, G. W. Preston, C. Sneden, and L. Searle, *AJ* 109 (1995) 2757
- [105] C. Sneden, A. McWilliam, G. W. Preston, J. J. Cowan, D. L. Burris, and B. J. Armosky, *Astrophys. J.* 467 (1996) 819
- [106] S. G. Ryan, J. E. Norris, and T. C. Beers, *Astrophys. J.* 471 (1996) 254
- [107] C. Sneden, J. J. Cowan, D. L. Burris, and J. W. Truran, *Astrophys. J.* 496 (1998) 235
- [108] J. Westin, C. Sneden, B. Gustafsson, and J. J. Cowan, *Astrophys. J.* 530 (2000) 783
- [109] C. Sneden, J. J. Cowan, I. I. Ivans, G. M. Fuller, S. Burles, T. C. Beers, and J. E. Lawler, *Astrophys. J.* 533 (2000) L139
- [110] D. L. Burris, C. A. Pilachowski, T. A. Armandroff, C. Sneden, J. J. Cowan, and H. Roe, *Astrophys. J.* 544 (2000) 302
- [111] J. A. Johnson and M. Bolte, *Astrophys. J.* 554 (2001) 888
- [112] V. Hill, et al., *Astron. Astrophys.* 387 (2002) 560
- [113] J. J. Cowan, C. Sneden, S. Burles, I. I. Ivans, T. C. Beers, J. W. Truran, J. E. Lawler, F. Primas, G. M. Fuller, B. Pfeiffer, and K.-L. Kratz, *Astrophys. J.* 572 (2002) 861
- [114] E. Carretta, R. Gratton, J. G. Cohen, T. C. Beers, and N. Christlieb, *Astron. J.* 124 (2002) 481
- [115] R. D. Hoffman, S. E. Woosley, and Y.-Z. Qian, *Astrophys. J.* 482 (1997) 951

- [116] B. S. Meyer and J. S. Brown, *Astrophys. J. Suppl. Ser.* 112 (1997) 199
- [117] C. Freiburghaus, J.-F. Rembges, T. Rauscher, E. Kolbe, F.-K. Thielemann, K.-L. Kratz, B. Pfeiffer, and J. J. Cowan, *Astrophys. J.* 516 (1999) 381
- [118] J. Witt, H.-T. Janka, and K. Takahashi, *Astron. Astrophys.* 286 (1994) 841
- [119] B. S. Meyer, G. J. Mathews, W. M. Howard, S. E. Woosley, and R. D. Hoffman, *Astrophys. J.* 399 (1992) 656 .
- [120] K. Takahashi, J. Witt, and H.-T. Janka, *Astron. Astrophys.* 286 (1994) 857
- [121] http://en.wikipedia.org/wiki/Portal:Astronomy/Picture/Week_46_2007
- [122] Bethe, H. A. 1990 *Rev. Mod. Phys.* **62** 801
- [123] Arcones A. & Thielemann F.-K. 2013 *Journal of Physics G: Nuclear and Particle Physics*, Volume 40, Issue 1.
- [124] R. C. Duncan, S. L. Shapiro, and I. Wasserman, *APJ*3091411986
- [125] A. Burrows, J. Hayes and B.A. Fryxell, *Ap.J.* **450** (1995) 830
- [126] H.-Th. Janka and E. Müller, *Astron. Astrophys.***306** (1996) 167
- [127] R. Buras, M. Rampp, H.-Th. Janka and K. Kifonidis, *Astron. Astrophys.* **447** (2006) 1049
- [128] Fischer T, Whitehouse S C, Mezzacappa A, Thielemann F K and Liebendörfer M 2010 *Astron. & Astrophys.* **517** A80
- [129] Thompson, T. A., Burrows, A., & Meyer, B. S. 2001, *ApJ*, 562, 887.
- [130] Tsuruta, S., & Cameron, A.G.W. 1965 *Can. J. Phys.*, 43, 2056.
- [131] Wanajo, S., Kajino, T, Mathews, G.J., & Otsuki, K. 2001, *APJ* 554, 578.
- [132] J. H. Taylor and J. M. Weisberg, *Astrophys. J.* 345 (1989) 434
- [133] A. Wolszczan, *Nature* 350 (1991) 688
- [134] E. S. Phinney, *Astrophys. J.* 380 (1991) L17
- [135] K. Belczynski, T. Bulik, and V. Kalogera, *Astrophys. J.* 571 (2002) L147
- [136] E. Cappellaro, R. Evans, M. Turatto, *Astron. Astrophys.* 351 (1999) 459
- [137] Bertulani, C. A. 2007 *Nuclear Physics in an Nutshells*, Princeton University Press, 1st edition.
- [138] Rauscher, T. 2011, *Int.J.Mod.Phys.* E20, 1071-1169.
- [139] Hilaire, S. 2001, *ICTP Lecture Notes Series*, Volume 5.
- [140] Bohr, N. 1936, *Nature*, 137, 334.

BIBLIOGRAPHY

- [141] Ghoshal, S. N. 1950, *Phys. Rev.* 80, 6, 939.
- [142] Fröbrich, P. & Lipperheide, R. 1996 *Theory of Nuclear Reactions*, Oxford Science Publications.
- [143] Gadioli, E. & Hodson, P.E. 1992, *Pre-Equilibrium Nuclear Reactions*, Clarendon Press, Oxford.
- [144] Holmes, J. A., Woosley, S. E., Fowler, W. A. & Zimmerman, B. A. 1976, *At. Data Nucl. Data Tables* 18, 305.
- [145] Cowan, J. J., Thielemann, F.-K. & Truran, J. W. 1991, *Phys. Rep.* 208, 267.
- [146] Loens, H. P., Langanke, K., Martínez-Pinedo G. & Sieja, K. 2012, *Eur. Phys. J. A* 48: 34.
- [147] Jeukenne, Lejeune, Mahaux. 1977, *Phys. Rev. C* 15, 10-28; 1848.
- [148] Rauscher, T., Thielemann, F.-K. & Kratz, K.-L. 1997, *Phys. Rev. C* 56, 1613.
- [149] Blatt, J.M., Weisskopf, V.F. 1952, *Theoretical Nuclear Physics*, Wiley, New York.
- [150] Ignatyuk, A.V., Smirenkin, G.N. & Tishin, A.S. 1975, *Yad. Phys.* 21 485.
- [151] Hix, W. R. and Thielemann F.-K. 1999, *Journal of Computational and Applied Mathematics*, 109, 321.
- [152] Fowler, W.A., Caughlan, G.E. & and Zimmerman, B.A. 1967, *Ann. Rev. Astron. Astrophys.* 5 525.
- [153] Fowler, W.A. 1974, *Quarterly Journ. Royal Astron. Soc.* 15, 82.
- [154] Loens, H. P., “Influence of parity-dependent nuclear level densities on astrophysical reactions.” Diploma thesis. Technische Universität Darmstadt, 2007.
- [155] Thielemann, F.-K., Arnould, M. & Truran, J.W., 1987 “Advances in Nuclear Astrophysics”, edited by Vangioni-Flam, et al. *Editions Frontiere, Gif sur Yvette* 525.
- [156] Martínez-Pinedo G. 2008, *Eur. Phys. J. Special Topics* 156, 123.
- [157] Belgia, T., Bersillon, O., Capote, R., Fukahori, T., Zhigang, G., Goriely, S., Herman, M., Ignatyuk, A.V., Kailas, S., Koning, A., Oblozinsky, P., Plujko, V. & Young, P. *Handbook for calculations of nuclear reaction data, RIPL-2* <http://www-nds.iaea.org/RIPL-2/>
- [158] Capote, R., Herman, M., Oblozinsky, P., Young, P.G., Goriely, S., Belgia, T., Ignatyuk, A.V., Koning, A.J., S. Hilaire, S., Plujko, V.A., Avrigeanu, M., Bersillon, O., Chadwick, M.B., Fukahori, T., Zhigang Ge, Yinlu Han, Kailas, S., Kopecky, J., Maslov, V.M., Reffo, G., Sin M., Soukhovitskii, E.Sh. & Talou, P. 2009, *Nucl. Data Sheets* 110, 3107-3214. <https://www-nds.iaea.org/RIPL-3/>
- [159] Cameron, A.G.W., Cowan, J.J., Truran, J.W. 1983, *Ap&SS*, vol. 91, 2, p. 235-243.
- [160] Arnett, W.D., Truran, J.W. 1969, *ApJ*, 157, 339; 1369.

-
- [161] Petermann, I., “Influence of fission processes on nucleosynthesis in r-process network calculations.” PhD diss. Technische Universität Darmstadt, 2010.
- [162] Martínez-Pinedo, G. 2013, *Lecture notes on Nuclear Astrophysics II* at the Technische Universität Darmstadt.
- [163] Sato, K. 1974, *Prog. Theor. Phys.*, 51 726-744.
- [164] Moeller, P, Pfeiffer B., Kratz K.-L. 2003, *Phys. Rev. C* 67, 055802.
- [165] Dong, T., Ren, Z. 2005, *EPJA* 26, 69-72.
- [166] Panov, I.V and Thielemann F.-K. 2004, *Astronomy Letters* 30, 647.
- [167] Gaimard, J. & Schmidt K. 1991, *Nuclear Physics A* 531, 709.
- [168] Kelic, A., Ricciardi, M.V. & Schmidt K. 2009, *Arxiv e-prints*, <http://2009arXiv0906.4193K>.
- [169] Hutter, L., “Nucleosynthesis in neutrino-driven winds.” PhD diss. Technische Universität Darmstadt, 2013.
- [170] Wanajo, S., Janka, H.-T., Kubono, S. 2011, *Astrophys. J.* 729 46.
- [171] Meyer, B. S. 1994, *Annual Review of Astronomy and Astrophysics* 32, 153.
- [172] Otsuki, K., Tagoshi, H., Kajino, T., & Wanajo, S. 2000, *ApJ*, 533, 424.
- [173] Arcones, A. and Montes, F. 2011, *ApJ*, 731,5.
- [174] Mumpower, M., McLaughlin, G., Surman, R. 2012, *Astrophys. J.* 752, 117.
- [175] Oechslin R., Janka, H.-T. & Marek, A. 2007, *A & A* 467, 395.
- [176] Belczynski, K., O’Shaughnessy R., Kalogera V. et al., *Astrophys. J.* 680 (2008) L129
- [177] Bauswein, A. 2012, *Private communication*.
- [178] Timmes, F.X. & Arnett, D. 1999, *ApJS* 125, 277.
- [179] Metzger, B.D., Arcones, A., Quataert, E. & Martínez-Pinedo, G. 2010, *Mon. Not. R. Astron. Soc.* 402, 2771.
- [180] Symbalisty, E.D.M., & Schramm, D. N. 1982, *Astrophys. Lett.* 22, 143.
- [181] Goriely, S., Hilaire, S. and Koning, A. J. 2008, *A & A*, 487, 767G.
- [182] Farouqi, K., Kratz, K., Pfeiffer, B., Rauscher, T., Thielemann, F.-K. & Truran, J.W. 2010, *Astrophys. J.* 712, 1359.
- [183] Wanajo, S., Goriely, S., Samyn, M. & Itoh N. 2004, *apj* 606, 1057.

Joel de Jesús Mendoza-Temis, M.Sc.(Physics)

CONTACT INFORMATION Technische Universität Darmstadt
Institut für Kernphysik
Theoretical Nuclear Astrophysics group
Theory center Room S2 | 11 103
Schlossgartenstrasse 2
64289 Darmstadt

Voice:
Mobile:(+49) 170 169 6988
Office:(+49) 6151 16 75663
E-mail:
J.MendozaTemis@gsi.de
temisnike@gmail.com

LANGUAGES Spanish and English *CITIZENSHIP:*Mexican.

PERSONAL OBJECTIVES Becoming a researcher dedicated to generate scientific knowledge and contribute in the technological development, to spread the seeds and ensure by myself that future generations will never extinguish the desire to explore the vast world of science.

RESEARCH INTERESTS Nuclear Structure, Nuclear Astrophysics, The many body problem in Quantum Mechanics, History of Art, Music and Sports.

EDUCATION **Technische Universität Darmstadt and GSI**, Darmstadt; Germany.

Ph. D., Nuclear Structure and Nuclear Astrophysics, 17.02.2014.

- Thesis Topic:“**Nuclear Masses and their impact in r-process nucleosynthesis**”

Advisors: Prof. Dr. Gabriel Martinez-Pinedo

Prof. Dr. Karlheinz Langanke

Area of Study: Nuclear Structure and Nuclear Astrophysics.

National University of Mexico, Mexico City; Mexico.

M.Sc., Nuclear Structure, 06.02.2008.

- Thesis Topic:“**Microscopic corrections to the Liquid Drop Model of Nuclear Masses**”

Advisor: Dr. Jorge G. Hirsch

Area of Study: Nuclear Physics.

Orizaba Institute of Technology, Orizaba, Veracruz; Mexico.

B.Sc., Chemical Engineering, 23.09.2004.

- Thesis Topic:“**Contribution in the experimental determination of the mass transfer coefficients for the process of batch cooling cristallization**”

Advisor: Dr. Eusebio Bolaños Reynoso

Area of Study: Chemical Engineering Applied in Industrial Processes.

SCHOLARSHIPS
AND AWARDS

GSI Darmstadt and TU Darmstadt, Germany

- PhD scholarship. 01.04.2010-31.07.2013.

HIC for FAIR and TU Darmstadt, Germany

- PhD scholarship. 01.04.2010-31.03.2013.

National System of Researchers, Mexico (SNI)

- Assistant Researcher(SNI-3) Fellow during 2007-2009.

National council for Science and Technology, Mexico (CONACYT)

- Fellowship of M.Sc. during 2005-2007.

National System of Researchers, Mexico (SNI)

- Assistant Researcher(SNI-3) Fellow during 2004-2005.

Council of the National System of Technological Education, Mexico (COSNET)

- Assistant Researcher Fellow during 2003-2004.

Orizaba Institute of Technology, Mexico

- Best Bachelor Student(class 1999-2003, Chemical Engineering).

Mexican Institute of Chemical Engineers(IMIQ)

- Former Secretary of the local student branch of the Mexican Institute of Chemical Engineers.

PARTICIPATION
IN RESEARCH
PROJECTS

Institut für Kernphysik at Technische Universität Darmstadt, Darmstadt, Germany .

PhD student

2010 –2014

- Nuclear Masses and their impact in r-process nucleosynthesis. under the direction of Profr. Dr. Gabriel Martínez-Pinedo.
- Member of the Theoretical Nuclear Astrophysics Group at TU Darmstadt.

Institute for Nuclear Sciences at UNAM, Mexico City, Mexico.

M.Sc.(Physics) and Graduate

2005 –2009

- Prediction of Nuclear Properties by using Image Reconstruction Techniques. under the direction of Dr. Jorge G. Hirsch and Dr. Alejandro Frank.
- Member of the Nuclear Masses Group in the Institute for Nuclear Sciences at UNAM.

Orizaba Institute of Technology, Orizaba, Veracruz; Mexico.

Bachelor and Undergraduate

2002–2004

- Optimization and Control of the process of batch cooling crystallization.
under the direction of Dr. Eusebio Bolaños Reynoso.
- Former member of the Pilot Plants Group at Orizaba Institute of Technology.

PUBLICATIONS
(1ST AUTHOR)

The anatomy of the simplest Duflo-Zuker mass formula

Joel Mendoza-Temis, Jorge G. Hirsch and Andrés P. Zuker
Nuclear Physics A, Volume 843, pp 14-36 (2010).

Testing the predictive power of nuclear mass models

J. Mendoza-Temis, A. Frank, J.G. Hirsch, J.C. López Vieyra, I. Morales, J. Barea, P. Van Isacker, and V. Velázquez.
Nuclear Physics A, Volume 812, pp 28-43 (2008).

Nuclear masses and the number of valence nucleons

J. Mendoza-Temis, I. Morales, J. Barea, A. Frank, J.G. Hirsch, J.C. López Vieyra, P. Van Isacker and V. Velázquez.
Nuclear Physics A, Volume 799, pp 84-93 (2008).

PUBLICATIONS
(CO-AUTHOR)

Microscopic mass estimations

Jorge G. Hirsch and Joel Mendoza-Temis.
J. Phys. G: Nucl. Part. Phys. 37 (2010) 064029

Image reconstruction techniques applied to nuclear mass models

Irving O. Morales, P. Van Isacker, V. Velázquez, J. Barea, J. Mendoza-Temis, J. BarJ.G. Hirsch, J.C. López Vieyra, and A. Frank.
Phys. Rev. C 81, 024304 (2010).

Image reconstruction of nuclear masses

I.O. Morales, J. Mendoza-Temis, J. Barea, A. Frank, J.G. Hirsch, J.C. López-Vieyra, P. Van Isacker and V. Velázquez.
Revista Mexicana de Física, Volume 55 (2), pp. 98-102 (2009).

Robust Calculation of Nuclear Masses by means of Image Reconstruction

I. Morales, J. Mendoza-Temis, J. Barea, J. G. Hirsch, J. C. López Vieyra, P. Van Isacker, V. Velazquez and A. Frank.
AIP Conference Proceedings, Volume 1090, pp. 246-252 (2009).

The art of predicting nuclear masses

Hirsch J .G., I. Morales, J. Mendoza-Temis, , A. Frank, J.C. López Vieyra, J. Barea, S. Pittel, P. Van Isacker and V. Velazquez.
International Journal of Modern Physics E, Volume 17, pp. 398-411

(2008).

Perspectives on nuclear mass formulae

J. Barea, A. Frank, J.G. Hirsch, P. Van Isacker, J.C. López-Vieyra, J. Mendoza-Temis, I. Morales, S. Pittel and V. Velazquez.
Revista Mexicana de Física, Volume 54 3, pp 5-10 (2008).

Exploring the Nuclear Landscape by Image Reconstruction Techniques

I. Morales, J. Mendoza Temis, J.C. López-Vieyra, José Barea, J.G. Hirsch, A.Frank and V. Velázquez.
Revista Mexicana de Física, Volume 53 s, pp 28-34 (2007).

Calculation of nuclear masses using image reconstruction techniques

Barea J., Frank A., Hirsch J.G., López J.C., Morales I., Mendoza J., Velázquez V.
AIP Conference Proceedings, Volume 947, pp. 348-355 (2007).

SOFTWARE AND PACKAGES Operating Systems: Mac OS X, Linux, Microsoft Windows XP/2000.

Programming: Fortran, Pascal, Basic, UNIX shell scripting and Python.

Applications: \LaTeX , Emacs, GNUplot, XM-grace, Gri, Origin, OpenOffice, Microsoft Office and other common productivity packages for Windows, OS X, and Linux platforms.

MATHEMATICA

MATLAB toolboxes: control system.